Electron-Ion Recombination of Low-Charged Heavy Atomic Ions at the Cryogenic Storage Ring

Dissertation

submitted for the degree of
Doctor of Natural Sciences

Leonard Isberner

2025

I. Physikalisches Institut
FB07 - Mathematik und Informatik, Physik, Geographie
Justus-Liebig-Universität Gießen

Gutachter:
Prof. Dr. Stefan Schippers
Prof. Dr. Markus Thoma

Datum der Disputation: 05.02.2025

Zusammenfassung

Elektron-Ion-Rekombination niedrig geladener schwerer atomarer Ionen am kryogenen Speicherring CSR

Für die Modellierung von Plasmen, z. B. in astrophysikalischen Umgebungen, werden verlässliche Daten zur Rekombination von atomaren Ionen mit freien Elektronen benötigt. Insbesondere niedrig geladene schwere Ionen, die ein hohes Masse-zu-Ladungs-Verhältnis m/q besitzen und z. B. in Kilonovae vorkommen, können eine komplexe elektronische Struktur aufweisen, weshalb die Rekombination dieser Ionen theoretisch schwer zu behandeln ist. Bisher gibt es keine experimentellen Daten zur Rekombination niedrig geladener schwerer Ionen. Aufgrund technischer Beschränkungen waren frühere Experimente zur Elektron-Ion-Rekombination in Speicherringen auf Ionen mit einem geringen Masse-zu-Ladungs-Verhältnis $m/q \leq 15$ beschränkt. Lediglich in extrem anspruchsvollen *single-pass*-Experimenten wurde die Rekombination eines Ions mit einem höheren $m/q = 24$ gemessen.

In dieser Arbeit wurden erste Experimente zur Elektron-Ion-Rekombination atomarer Ionen am kryogenen Speicherring CSR am Max-Planck-Institut für Kernphysik in Heidelberg durchgeführt. In zwei Experimenten wurden absolute Ratenkoeffizienten für die Rekombination in überlagerten Elektronen- und Ionenstrahlen für Ne^{2+}- und Xe^{3+}-Ionen gemessen. Radiative und dielektronische Rekombination wurden beobachtet. Das erste Experiment, durchgeführt mit Ne^{2+}-Ionen ($m/q = 10$), zeigt die grundsätzliche Durchführbarkeit von Elektron-Ion-Rekombinationsexperimenten mit atomaren Ionen am CSR. Das zweite Experiment, durchgeführt mit Xe^{3+}-Ionen, die ein hohes Masse-zu-Ladungs-Verhältnis von $m/q = 43$ aufweisen, belegt die Machbarkeit von Rekombinationsexperimenten mit *niedrig geladenen schweren* Ionen am CSR.

Die Experimente zeigen, dass die Rekombination von bisher nicht zugänglichen niedrig geladenen schweren atomaren Ionen in der kryogenen Umgebung des CSR untersucht werden kann.

Abstract

Electron-ion recombination of low-charged heavy atomic ions at the Cryogenic Storage Ring

For plasma modeling, e.g., in astrophysical environments, reliable data on the recombination of atomic ions with free electrons are required. Especially low-charged heavy ions, which have a high mass-to-charge ratio m/q, and which are found, e.g., in kilonovae, can have a complex electronic structure and therefore the recombination of these ions is difficult to treat theoretically. So far, no experimental data are available on the recombination of low-charged heavy ions. Due to technical limitations, previous electron-ion recombination experiments in storage rings were restricted to ions with a low mass-to-charge ratio $m/q \leq 15$. Only in extremely challenging single-pass experiments, recombination of an ion with a higher $m/q = 24$ was measured.

In this work, first experiments on electron-ion recombination of atomic ions were performed at the Cryogenic Storage Ring CSR at the Max-Planck-Institut für Kernphysik in Heidelberg. In two experiments, absolute merged-beams rate coefficients for electron-ion recombination were measured for Ne^{2+} and Xe^{3+} ions. Recombination features from radiative and dielectronic recombination have been observed. The first experiment, performed with Ne^{2+} ions ($m/q = 10$), demonstrates the general feasibility of electron-ion recombination experiments with atomic ions at CSR. The second experiment, performed with Xe^{3+} ions, which have a high mass-to-charge ratio of $m/q = 43$, proves the feasibility of recombination experiments with *low-charged heavy* ions at CSR.

The experiments show that recombination of previously not accessible low-charged heavy atomic ions can be studied in the cryogenic environment of CSR.

Contents

List of Figures

List of Tables

Acronyms

AGN Active Galactic Nucleus

AS *AUTOSTRUCTURE*

COMPACT Cold Movable Particle Counter

CSR Cryogenic Storage Ring

DC Dielectronic Capture

DR Dielectronic Recombination

EBIT Electron Beam Ion Trap

ECR Electron Cyclotron Resonance

FAC *Flexible Atomic Code*

FWHM Full Width at Half Maximum

MBRC Merged-Beams Rate Coefficient

MCP Microchannel Plate

MPIK Max-Planck-Institut für Kernphysik

NICE Neutral Imaging in Cold Environment

NIST National Institute of Standards and Technology

PHD Pulse Height Distribution

RF Radio Frequency

RR Radiative Recombination

TSR Test Storage Ring

Chapter 1

Introduction

About 99 % of all visible matter in the universe is thought to exist in the plasma state, where atoms and molecules are partially ionized, and free electrons are present. The physical conditions of these environments are governed by collision processes of the available particles. In particular, the charge-state distributions for the individual atomic species in the plasma are determined by ionization processes such as photoionization or electron-impact ionization, which compete with electron-ion recombination processes. To model and understand any plasma, whether in an astrophysical environment or man-made, knowledge of the cross sections for the fundamental collision processes is crucial [1].

Under conditions where the particle density is low and three-body collisions are unlikely, as it is the case in many cosmic plasmas [2], the recombination of atomic ions A^{q+} proceeds mainly in collisions with free electrons e^- via radiative mechanisms. The most relevant of these are the non-resonant Radiative Recombination (RR) and the resonant Dielectronic Recombination (DR). The RR process,

$$e^- + A^{q+} \rightarrow A^{(q-1)+} + h\nu, \tag{1.1}$$

where the excess energy upon electron capture is taken away by one or more photons $h\nu$, was first theoretically described by Kramers in 1923 [3]. The resonant process of DR,

$$e^- + A^{q+} \rightarrow \left(A^{(q-1)+}\right)^{**} \rightarrow A^{(q-1)+} + h\nu, \tag{1.2}$$

which involves the excitation of one of the bound electrons in the ion during the electron capture and thus the formation of a doubly excited ion, was first considered related to research on the Earth's ionosphere by Massey and Bates in 1942 [4], but ultimately found irrelevant in this context. Only after Burgess in 1964 [5] showed that DR plays a significant role in recombination processes in the corona of the Sun, the importance of DR in (astrophysical) plasmas was recognized. Still, it took almost 20 years before first laboratory experiments on electron-ion recombination were carried out [6–8].

In the late 1980s and early 1990s, heavy-ion storage rings like TSR in Heidelberg, ESR in Darmstadt, and CRYRING in Stockholm became operational. Their in-ring electron coolers were identified as an ideal environment for clean high-resolution recombination experiments of atomic ions with free electrons. The configuration of merged electron and ion beams in the storage rings enabled recombination studies at center-of-mass collision energies between almost 0 eV and several keV. Additionally, highly charged ions became accessible as the storage rings were connected to accelerator facilities. In the following decades, many recombination studies were carried out in storage rings. The experiments were mainly motivated by two fields of research: the derivation of cross sections or plasma rate coefficients for the use in plasma modeling (e.g., [9]), and fundamental atomic physics (e.g., [10]). The applications of DR concerning atomic physics are diverse. For example, DR can be employed to study the lifetimes of long-lived metastable levels [11] by tracing their recombination signal, which is unique for each (excited) level, over the storage time. From the resonance energies in the DR spectrum, the excitation energy of the initial ion A^{q+} can be deduced, permitting the application of DR experiments as a spectroscopic tool. For highly charged heavy ions with few electrons (Li-like, Be-like ions), this enables the test of QED theory (e.g., [10, 12–15]).

Recombination studies concerned with the generation of data for the use in plasma modeling were focused mostly on ions with complex electronic structures. For these systems, theoretical calculations of the DR signal are challenging and not always reliable, which is why experimental data is needed. For instance, the need for recombination data in fusion research triggered extensive experimental studies with open $4f$ shell tungsten ions $W^{18+\ldots21+}$ [16], revealing strong recombination features that have not been found in previous theoretical work. Many recombination experiments were motivated by astrophysical applications [2, 9, 17]. The large abundance of iron in space and the X-ray absorption in plasmas in the surroundings of Active Galactic Nuclei (AGNs) [2, 17] stimulated the investigation of recombination of iron ions in a wide range of charge states, $Fe^{7+\ldots22+}$ [18–20]. The given examples are just a selection of recombination measurements with astrophysically relevant ions.

Currently, storage rings are the most powerful machines for studying atomic recombination. However, the main challenge in the experiments lies in the background signal caused by charge transfer in collisions of the stored ions with residual-gas particles. To enable meaningful measurements, the background signal has to be suppressed sufficiently, which is especially difficult for low-charged heavy ions with a high mass-to-charge ratio m/q. Due to technical reasons, the storage ring recombination experiments have prior been limited to ions with rather low m/q. The highest m/q reported in a storage ring recombination experiment so far was $m/q = 15$ for Sc^{3+} [21, 22].

Nonetheless, data on the recombination of low-charged heavy ions with high m/q are relevant and important. For example, such data are needed for a complete understanding of the surroundings of AGNs [23]. Additionally, low-charged heavy ions have recently been found in kilonova events. Kilonovae [24] are transient phenomena occurring after

the merger of two heavy cosmic objects (such as two neutron stars or a neutron star and a black hole), and emit light in the optical and infrared parts of the electromagnetic spectrum. In 2017, the first kilonova directly correlated to the merger of two neutron stars was observed [25]. Such mergers are formation sites for heavy elements which can not be produced by nuclear fusion. Material ejected from the merger undergoes rapid neutron capture, leading to the formation of heavy elements like lanthanides [26]. The decay of radioactive isotopes formed in the merger powers the kilonova, which can last for several days. The ionic species contributing to the optical and infrared emission of the kilonova are assumed to exist in low charge states $q \lesssim 3$ [27]. So far, low-charged heavy ions like Sr^+ [28], Y^+ [29], Te^{2+} [30, 31] as well as lanthanide ions [32] have been tentatively identified in the spectra of kilonovae. Because these spectra are broad and consist of absorption and emission features from a multitude of elements, the identification of individual species is challenging, but more identifications are to be expected in the future. The modeling of the physical conditions in kilonovae will require recombination data on a wide range of low-charged heavy ions. Since these ions can possess complex electronic structures and therefore potentially show collective many-electron phenomena in the recombination process, theoretical calculations are challenging. To benchmark atomic theory, accurate experimental recombination data on the class of low-charged heavy ions are needed.

To enable recombination experiments with low-charged heavy ions, the background signal from electron-capture collisions of the ions with residual-gas particles must be suppressed more efficiently than was previously possible in storage rings for low-charged heavy ions. Promising conditions for such experiments exist in the Cryogenic Storage Ring (CSR) [33], located at the Max-Planck-Institut für Kernphysik (MPIK) in Heidelberg. CSR is a *cryogenic* storage ring and the main research focus lies on experiments with internally cold molecular ions, some of which are relevant for astrophysics [34]. CSR is the only cryogenic storage ring equipped with an electron cooler, and several electron-recombination studies with cold molecular ions have been performed [35–40]. The cryogenic environment facilitates a very low residual-gas pressure in CSR which is approximately two orders of magnitude lower than the pressure in conventional room-temperature storage rings. The unique conditions in CSR are expected to enable recombination studies with low-charged heavy atomic ions that have a high m/q.

The goal of this work was to establish experiments on the recombination of low-charged heavy atomic ions with free electrons at CSR. Therefore, two recombination studies have been performed with O-like Ne^{2+} and Sb-like Xe^{3+}. The experiment on $Ne^{2+} + e^- \rightarrow Ne^+$ was a first proof-of-principle to establish the general techniques. Ne^{2+} has a moderately low mass-to-charge ratio of $m/q = 10$, and its recombination has been measured at CRYRING@ESR in Darmstadt before [41]. Ne^{2+} was found in space, e.g., in AGN plasmas [42] and in H II regions [43]. The second experiment on $Xe^{3+} + e^- \rightarrow Xe^{2+}$ was meant to demonstrate the feasibility of recombination studies with low-charged heavy ions at CSR. Xe^{3+} has a mass-to-charge ratio of $m/q = 43$, which is by far higher than for any other ion in any previous recombination experiment.

Xe^{3+} has been found in space as well, e.g., in planetary nebulae [44] and in white dwarfs [45]. Furthermore, the photoionization spectrum of Xe^{2+} shows a broad 'giant resonance' correlated to collective many-electron effects in the $4d$ shell [46, 47]. Since recombination is the inverse of photoionization, such collective effects potentially occur in the electron-recombination process of Xe^{3+} as well. Still, both studies with Ne^{2+} and Xe^{3+} were test cases for the realization of first recombination experiments with low-charged heavy ions at CSR.

This thesis is structured in the following way: Chapter 2 provides an overview of electron recombination with atomic ions, corresponding experiments, and their limitations. The special conditions in CSR are highlighted. Chapter 3 presents the experimental setup at CSR. Chapter 4 introduces general methods and procedures employed in the experiments and in the data analysis. Chapter 5 focuses on the results from the recombination experiment with Ne^{2+}. The measured data are compared with the CRYRING@ESR experiment and with theoretical calculations. Chapter 6 reports the results from the recombination experiment with Xe^{3+} as well as a comparison of the experimental data with theoretical calculations. Chapter 7 summarizes the main findings of this thesis and gives an outlook on possible improvements for future experiments with low-charged heavy atomic ions at CSR.

Chapter 2

Electron-Ion Recombination

Electron-ion recombination belongs to the fundamental collision processes between atomic ions and free electrons. It is the inverse process to photoionization and can proceed via non-resonant and resonant pathways. In this chapter, the basic principles of radiative and dielectronic recombination are addressed. Storage ring recombination experiments are introduced. Finally, the limitations of previous experiments concerning the recombination of *low-charged heavy* ions are highlighted, as well as the unique and promising conditions in CSR.

2.1 Radiative Recombination and Dielectronic Recombination

The electron-ion recombination process

$$e^- + A^{q+} \rightarrow A^{(q-1)+} + h\nu \tag{2.1}$$

is also referred to as 'photorecombination', as one or more photons $h\nu$ are emitted. It can proceed either via a direct process, called Radiative Recombination (RR), or via indirect, resonant processes, the simplest of which is Dielectronic Recombination (DR). The processes of RR and DR are schematically depicted in figure 2.1.

RR involves the direct capture of a free electron into an ion. The excess energy is emitted in form of one photon in case the electron is captured into the lowest possible level, or several photons in case the electron is captured into a higher level and cascades down afterwards. RR is non-resonant, but its cross section depends on the electron-ion collision energy nonetheless. The first theoretical description was a semi-classical approach by Kramers [3]. Later, quantum-mechanically correct descriptions [48] involving relativistic [49] and QED effects [50] have been published. According to

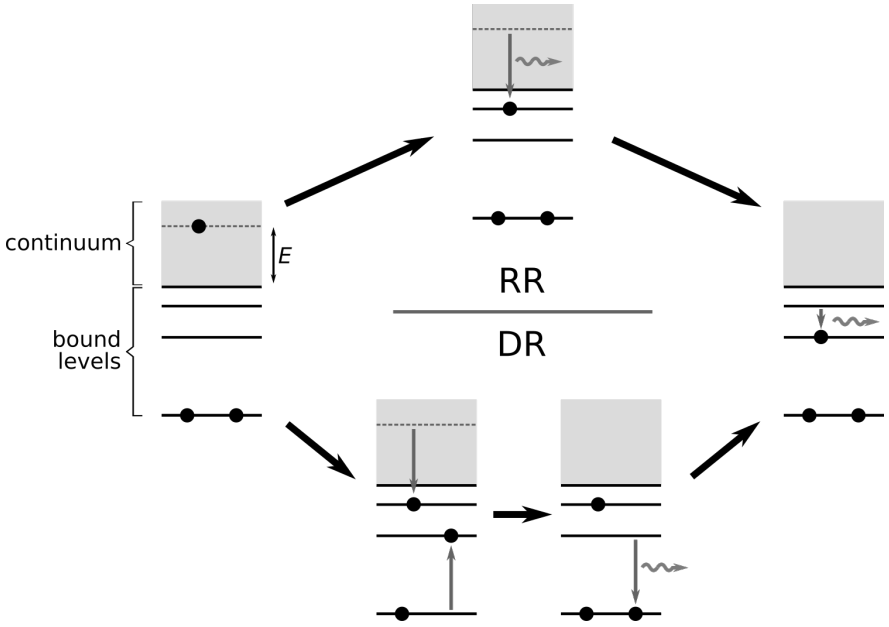

Figure 2.1: Schematic principle of the RR and DR processes. Both processes start with an electron in the continuum of an ion, with collision energy E. The electron is subsequently captured to a bound level of the ion, resulting in a recombined lower charged ion. In contrast to the direct RR (upper pathway in the figure), the indirect DR (lower pathway) is a resonant process involving the excitation of a bound electron. In both processes, the excess energy is taken away by one or more emitted photons.

the semi-classical approximation by Kramers [3], the cross section σ_n^{RR} for electron capture into the n-th shell is given by (compare [51])

$$\sigma_n^{\mathrm{RR}}(E) = \frac{32\pi}{3\sqrt{3}}\,\alpha^3 a_{\mathrm{B}}^2\,\frac{q^4 R^2}{nE\left(q^2 R + n^2 E\right)}, \tag{2.2}$$

with the fine structure constant α, the Bohr radius a_{B}, the ion charge state q, the electron-ion center-of-mass collision energy E and the Rydberg energy R. The total cross section for RR can be obtained by a summation over all possible n into which the electron can be captured,

$$\sigma_{\mathrm{tot}}^{\mathrm{RR}}(E) = \sum_{n=n_{\min}}^{n_{\max}} \sigma_n^{\mathrm{RR}}(E)\, t_n\, G_n(E=0). \tag{2.3}$$

$n_{\min}$ is the lowest shell that is not fully occupied. In experiments, $n_{\max}$ is determined by field ionization, which is explained in section 4.11 on page 69. The weighting factor t_n indicates how much 'space' is still available for electrons in a shell n (or how much it is already filled). The Gaunt factors $G_n(E=0)$ can be applied to scale the semi-classical approximation from equation (2.2) to the quantum-mechanically correct description [52]. As can be seen from equation (2.2), the cross section for RR diverges towards vanishing collision energies and decreases at higher collision energies. It is strongest for electron capture into low-lying shells.

The first dedicated experimental study on RR was performed as a single-pass merged-beams experiment with bare C^{6+} ions by Andersen et al., published in 1990 [53, 52]. While in this experiment an agreement with the theoretical cross section was found, many later experiments (not only on bare ions) observed a higher recombination rate than theoretically predicted (e.g., [54–56], and basically any other storage ring experiment). This increased signal at very low collision energies, also referred to as 'rate enhancement', was found to vary with the presence of magnetic fields [57] and is attributed to additional, field-induced recombination in the merging region of electron and ion beams [58, 59].

RR is the only photorecombination process available in bare ions. All higher-order processes involve the excitation of at least one bound electron. The simplest and in most cases strongest of these is Dielectronic Recombination (DR), which was first proposed by Massey and Bates [4]. As shown in the lower part of figure 2.1, the electron capture coincides with the excitation of one of the bound electrons in the ion. This initial step is called Dielectronic Capture (DC) and is the inverse process to the Auger effect or to autoionization, forming a doubly excited state. Subsequently, both excited electrons can radiatively relax in a multi-step cascade process. As a consequence from the DC, the DR process is resonant and proceeds only at collision energies $E = E^{\mathrm{DR}}$ where the sum of collision energy and binding energy E_{b} of the captured electron corresponds to the excitation energy E_{ex} of the bound core electron, i.e.

$$E_{\mathrm{ex}} = E^{\mathrm{DR}} + E_{\mathrm{b}}. \tag{2.4}$$

In an approximation for hydrogen-like ions with high quantum numbers n and l, the resonance energy E_n^{DR} for DC into the n-th shell can be calculated with the help of the Rydberg formula, yielding

$$E_n^{\mathrm{DR}} \approx E_{\mathrm{ex}} - R\,\frac{q^2}{n^2}. \tag{2.5}$$

Here, E_{ex} denotes the core electron excitation energy, R the Rydberg energy and q the ion charge prior to recombination. Each core excitation is therefore linked to a series of resonance lines, the spacing of which decreases towards the series limit at the excitation energy.

As the doubly excited state formed upon DC has a total energy above the ionization threshold, autoionization competes with the radiative stabilization. This is reflected in the DR cross section. In the 'isolated resonance approximation', where the individual DR resonances are assumed to be sharp and not to overlap, the resonance strength integrated over one resonance is given as [60, 61]

$$\overline{\sigma}_d^{\mathrm{DR}} = \frac{h^3}{8\pi m_{\mathrm{e}}}\,\frac{g_d}{2g_i}\,\frac{1}{E_{\mathrm{r}}}\,\frac{A_{\mathrm{a}}(d \to i)\sum_f A_{\mathrm{r}}(d \to f)}{\sum_{i'} A_{\mathrm{a}}(d \to i') + \sum_{f'} A_{\mathrm{r}}(d \to f')}. \tag{2.6}$$

Here, h is the Planck constant, m_{e} the electron mass and E_{r} the resonance collision energy. The different atomic states involved in the recombination process are denoted i for the initial state prior to recombination, i' for any non-recombined state, d for the intermediate doubly-excited state, and f and f' for the final, radiatively stabilized states.

A_a and A_r are the autoionization and radiative transition rates between the specified states, respectively. The summation accounts for autoionization into any unbound state and radiative relaxation into any stabilized state, respectively. The rate for DC from i to d can be linked to the autoionization rate $A_\mathrm{a}(d \rightarrow i)$ when considering the statistical weights g_d and g_i of the two states.

Theoretically, DR can be addressed by atomic structure codes, e.g., via perturbation theory. Experimentally, DR was first observed in single-pass experiments using merged [6, 7] or crossed electron and ion beams [8]. Later, many experiments were performed at storage rings, as it is outlined in the following section 2.2. Storage ring experiments focus on detecting the recombined ions. In contrast, also the characteristic photons produced in the recombination process can be detected. This approach is followed in Electron Beam Ion Traps (EBITs) (e.g., [62, 63]).

While RR is most prominent at low electron-ion collision energies, DR resonances can in principle occur at low and high collision energies. Therefore, DR can contribute significantly to the recombination signal at low collision energies and usually dominates at higher collision energies. Concerning higher-order recombination, it is apparent from the schematic sketch in figure 2.1 that potentially more than one core electron can be excited in the electron capture process. Out of these processes, trielectronic recombination [64], involving the excitation of two bound electrons, as well as quadruelectronic recombination [65], involving the excitation of three bound electrons, have been observed experimentally. For ions with a complex electronic structure like Au^{25+} or $W^{18...21+}$, which exhibit an open $4f$ shell, the contribution of collective multi-electron excitation has to be considered in the recombination process [16, 66–72].

2.2 Electron-ion recombination experiments in storage rings

Heavy ion storage rings offer unique opportunities for electron-ion recombination studies with molecular and atomic ions by providing controlled conditions [73]. The basic principle of a storage ring is shown in figure 2.2. An ion beam is injected into the ring and subsequently circulates on a closed orbit which is defined by bending elements. These bending elements can be either magnetic or electrostatic deflectors, and therefore two types of storage rings exist: magnetic and electrostatic rings. The storage conditions can be found from the Lorentz force F_L, describing the deflection of the ions in electric and magnetic fields, and the counteracting centrifugal force F_c [74],

$$F_\mathrm{L} \equiv q\,e\,(E_\mathrm{el} + v \times B) = \frac{\gamma\,m\,v^2}{r} \equiv F_\mathrm{c}, \tag{2.7}$$

where q is the charge state, v the velocity and m the mass of the stored ions, e the elementary charge, E_el the electric field strength, B the magnetic flux density, γ the

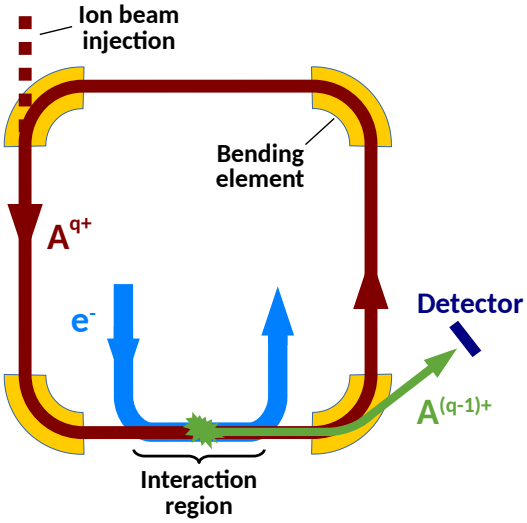

Figure 2.2: Sketch of an electron-ion merged-beams setup in a storage ring. The ion beam (A^{q+}) circulates on a closed orbit defined by the bending elements. In the interaction region, the stored ion beam is overlapped with a beam of electrons (e^-). Recombined ions ($A^{(q-1)+}$) are deflected less strongly in the following bending element and can be collected by a detector.

Lorentz factor and r the bending radius. In the case of pure magnetic deflection, the 'magnetic rigidity' [74]

$$B\,r = \frac{\gamma\,m\,v}{q\,e} \tag{2.8}$$

can be extracted from equation (2.7). In the case of pure electrostatic deflection, the 'electric rigidity' is given as [74]

$$E_{\mathrm{el}}\,r = \frac{\gamma\,m\,v^2}{q\,e}. \tag{2.9}$$

The rigidity of an ion beam therefore describes what deflection strength is needed to bend the beam such that it stays stored in the storage ring. In particular, the magnetic rigidity from equation (2.8) is proportional to the momentum $p = \gamma\,m\,v$ of the stored ion, i.e. $B\,r \propto p$. In contrast, the electric rigidity from equation (2.9) is proportional to the product of momentum and velocity, i.e. $E_{\mathrm{el}}\,r \propto p\,v$, which in the nonrelativistic case yields the proportionality to the ion kinetic energy E_{kin}, i.e. $E_{\mathrm{el}}\,r \propto E_{\mathrm{kin}}$. Therefore, at given (fixed) settings on the magnetic or electrostatic deflectors, corresponding to a specific magnetic or electric rigidity, respectively, a magnetic storage ring can store any ions with the same momentum per charge, while an electrostatic storage ring can store any ions with the same kinetic energy per charge.

Storage rings enable clean recombination experiments, as the ion production in a separate ion source allows for the separation of the various ion species and charge states according to their mass-to-charge ratio m/q prior to the injection into the ring. This permits experiments with a pure, m/q-selected ion beam. Furthermore, storage rings

are characterized by generally good vacuum conditions, allowing for long ion storage times. Therefore, excited atomic ions can relax to their electronic ground states while being stored in the ring, and molecular ions even to their vibrational and rotational ground states (depending on the storage conditions).

The electron beam needed for recombination experiments is usually provided by a so-called 'electron cooler' device and collinearly overlapped with the stored ion beam in the merged-beams technique [75] as depicted in figure 2.2. By variation of the electron beam energy, different electron-ion collision energies can be probed, ranging from the meV range [57] up to several ten keV [76]. Due to the high velocity of the stored ion beam, recombined products also move forward, are deflected less strongly in the next bending element, and can be efficiently collected by single-particle detectors [77].

Prior to the experiments presented in this thesis, electron recombination with atomic ions was studied only in magnetic storage rings (besides single-pass and trap experiments). The first storage ring recombination experiment was performed by Kilgus et al. [78] on H-like O^{7+} in the storage ring TSR in Heidelberg. In the following decades, many such recombination experiments were carried out, and the scope of investigated ions ranged, to give a few examples, from low-charged ions like C^{+} [79] and Si^{3+} [80, 81] to highly-charged ions like W^{18+} [70] and Xe^{25+} [82] to bare ions like Bi^{83+} [56] and U^{92+} [83]. Most of the measurements were performed in the storage rings TSR in Heidelberg, CRYRING in Stockholm, and ESR in Darmstadt. While TSR was put out of operation in 2012, CRYRING was moved to Darmstadt and renamed CRYRING@ESR. It is operational now again, and first recombination experiments have been performed [84, 85, 41]. Nowadays, electron-ion recombination is studied as well in the storage rings CSRm [86, 87] and CSRe [88, 89] in Lanzhou, China.

In this thesis, the first electron recombination experiments with atomic ions at CSR in Heidelberg are reported, which also represent the first recombination experiments with atomic ions in an electrostatic storage ring.

2.3 Limitations in storage ring recombination experiments

Many electron-ion recombination measurements have been carried out in storage rings, but previous experiments were facing limitations especially when investigating ions with a high mass-to-charge ratio. Figure 2.3 shows a histogram of the atomic ion species for which recombination experiments in storage rings have been reported, as a function of their mass-to-charge ratio m/q. It is apparent that the majority of recombination measurements has been carried out with ions of $m/q \leq 4$. In this region, many highly charged ions with relevance for astrophysical plasmas and fusion research are found. Data on ion species with higher m/q are scarce. Although these ion species are potentially present in plasma environments as well, technical limitations prevented their

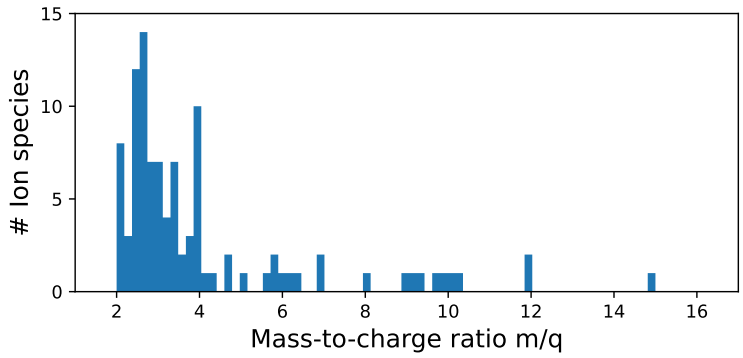

Figure 2.3: Histogram of the atomic ions for which storage ring recombination experiments have been published, itemized by their mass-to-charge ratio m/q. The figure is based on a list of storage ring recombination experiments maintained by Stefan Schippers [61, 9, 90].

investigation so far. The highest m/q in a storage ring experiment with atomic ions was $m/q = 15$ for Sc^{3+} [21, 22]. Statistically challenging single-pass experiments achieved a higher m/q of 24 for Mg^+ [8, 91]. In contrast, storage ring recombination experiments with molecular ions could reach much higher m/q of 41 (with electron cooling) for D_2Cl^+ [92] and ArH^+ [39], and even $m/q = 117$ (without electron cooling) for $OPCl_2^+$ [93].

Compared to typical rate coefficients for dissociative recombination of molecular ions, those for dielectronic recombination in atomic ions are easily several orders of magnitude smaller. Consequently, to enable meaningful studies, much more care has to be taken to suppress the background signal efficiently in recombination experiments with atomic ions.

The main (and almost exclusive) cause of background signal are collisions of the stored ion beam with residual-gas particles in the storage ring. In such collisions, a charge exchange can happen, and an electron is transferred to the ion. These electron-capture collisions hence produce lower-charged ions, which are indistinguishable from ions produced by recombination with free electrons. For the well-defined collision conditions in storage rings, where the ion beam is fast and the residual gas is at rest, the background count rate R_{bg} scales with the residual-gas density n_{rg} and the rate coefficient for electron-capture from residual gas α_{ec}, i.e.

$$R_{\mathrm{bg}} \propto n_{\mathrm{rg}}\, \alpha_{\mathrm{ec}}, \tag{2.10}$$

where α_{ec} refers to the expectation value of the product of electron-capture cross section σ_{ec} and the ion beam velocity v_{i}, i.e. $\alpha_{\mathrm{ec}} = \langle \sigma_{\mathrm{ec}}\, v_{\mathrm{i}} \rangle$. An empirical formula to approximate the expected electron-capture cross section σ_{ec} for various fast ion projectiles and neutral gas targets was reported by Schlachter et al. in 1983 [94] in good agreement with existing data (under specific assumptions about the ion charge state and kinetic ion energy). As an example, the calculation for the electron-capture cross section in

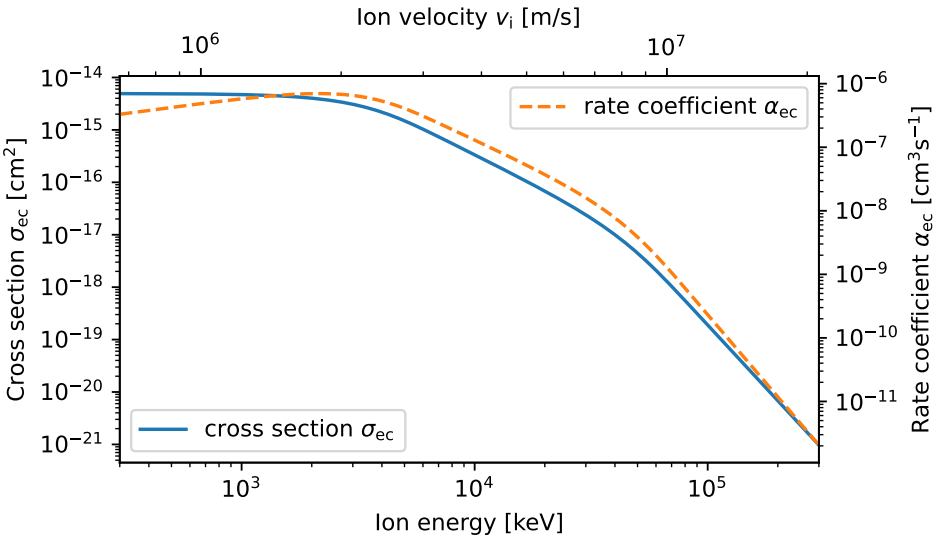

Figure 2.4: Cross section σ_{ec} (blue solid line) for electron capture in collisions of fast Xe^{3+} with neutral He at rest, forming Xe^{2+}, as a function of the kinetic ion energy. The corresponding ion velocity v_i is indicated in the upper part of the figure. The cross section was calculated using the empirical formula by Schlachter et al. [94]. According to the specifications in [94], the calculation is assumed to yield a reasonably reliable cross section above an ion energy of ~ 2.3 MeV. The electron-capture rate coefficient $\alpha_{ec} = \langle \sigma_{ec} v_i \rangle$, to which the background count rate in storage ring experiments is proportional, is shown as dashed orange line.

collisions of fast Xe^{3+} with neutral He at rest, forming Xe^{2+}, is shown in figure 2.4. The general trend of a strongly decreased cross section at increased projectile energies is valid also for all other atomic ions and neutral targets. The electron-capture rate coefficient α_{ec}, to which the background count rate R_{bg} is proportional, is depicted in figure 2.4 as well, and drops at higher ion energies.

To suppress the background signal, earlier recombination experiments in magnetic storage rings were aimed at high kinetic energies (and therefore high velocities v_i) of the stored ion beam, and thus operated in a regime where α_{ec} is small compared to low ion beam energies. However, the lowest reachable α_{ec} is determined by the highest accessible ion velocity $v_{i,max}$, which in turn is given by the magnetic rigidity $B\,r = \frac{\gamma\, m\, v_i}{q\, e}$ (equation (2.8)) of the ion beam, as the bending radius r is defined by the geometry of the storage ring and the magnetic field B is limited by the capability of the deflector magnets. The highest reachable ion velocity in a magnetic storage ring is therefore inversely proportional to the mass-to-charge ratio of the ion,

$$v_{i,max} \propto \left(\frac{m}{q}\right)^{-1}. \tag{2.11}$$

Hence, ions with low m/q can be stored at high velocities, resulting in high collision energies with the residual gas, a low α_{ec}, and ultimately in a low background count

rate R_{bg}. For experiments with ions of high m/q however, the maximum reachable ion velocity $v_{\mathrm{i,max}}$ is lower, and the background signal is not suppressed as efficiently as for ions with low m/q. Consequently, experiments with ions of high m/q are challenging due to a high background count rate R_{bg}. Despite low residual-gas pressures in the order of 10^{-11} mbar in the magnetic storage rings, the highest reported m/q in an electron-recombination experiment with atomic ions is $m/q = 15$ for two measurement campaigns on Sc^{3+} [21, 22] in TSR. These experiments proved extremely challenging as the residual-gas-induced background was up to 100 × higher than the electron-induced signal of interest. Under these conditions, the measurement time required to obtain good statistics exceeds the time frame of such experiments, which is typically about a week. For these reasons, electron-recombination of low-charged heavy ions, which have a high m/q, has not been investigated yet.

2.4 Special conditions in CSR

The Cryogenic Storage Ring (CSR) [33], located at the Max-Planck-Institut für Kernphysik (MPIK) in Heidelberg, offers unique conditions which are promising to enable recombination experiments with low-charged heavy atomic ions of high m/q. CSR and the implemented electron-ion merged-beams setup are presented in more detail in the following chapter 3.

CSR is an electrostatic storage ring capable of storing ions which have been accelerated by up to 300 kV. From the electric rigidity $E_{\mathrm{el}}\, r = \frac{\gamma\, m\, v_{\mathrm{i}}^2}{q\, e}$ (equation (2.9)), the relation

$$v_{\mathrm{i,max}} \propto \left(\frac{m}{q}\right)^{-\frac{1}{2}} \tag{2.12}$$

for the maximum ion velocity is obtained. Thus, the maximum ion velocity decrease with increasing m/q is weaker in electrostatic storage rings than in magnetic storage rings. Nevertheless, only for m/q even larger than ~ 350, an ion beam can be stored at higher velocity in CSR than in comparable magnetic storage rings like TSR or CRYRING. In general, the ion velocities of typical atomic ion beams are considerably lower in CSR than in standard magnetic storage rings, resulting in an unfavorably high rate coefficient α_{ec} for electron-capture from residual gas.

The approach pursued at CSR to suppress the residual-gas-induced background signal and to enable recombination experiments with low-charged heavy ions is to lower the residual-gas density n_{rg} by improving the vacuum conditions. The experimental vacuum chamber of CSR can be cooled down to cryogenic temperatures < 10 K and consequently acts as a large cryopump, where most residual-gas particles (besides hydrogen and helium) freeze out at the chamber walls. Hence, CSR provides a particularly low residual-gas density in the order of $n_{\mathrm{rg}} = 10^3$ to $10^4\,\mathrm{cm}^{-3}$, which corresponds to

a room-temperature-equivalent pressure in the order of 10^{-13} mbar. This is up to two orders of magnitude lower than the pressure in conventional room-temperature storage rings like TSR [95] or CRYRING@ESR [84], which is typically in the low 10^{-11} mbar regime.

The good vacuum conditions are expected to compensate for the low ion beam velocity and allow for recombination studies with ions of high m/q. In this work, it is tested whether this expectation proves true and whether recombination studies with ions of high m/q are indeed feasible in CSR.

In the present setup at CSR, additional limitations arise from typical ion beam sizes, the separation of stored and recombined beams in the electrostatic deflector downstream of the electron-ion interaction region, and the width of the utilized detector. Consequently, it is estimated that recombination studies are restricted to ions with charge states below $q \approx 5$.

Chapter 3

Experimental Setup

Recombination experiments with low-charged heavy ions require special conditions. To enable meaningful experiments with ions of high m/q, the background signal due to collisions of the ions with residual-gas particles has to be suppressed more effectively than it was possible in room-temperature storage rings so far. This was outlined in chapter 2 already. The Cryogenic Storage Ring (CSR), located at the Max-Planck-Institut für Kernphysik (MPIK) in Heidelberg, is the only *cryogenic* storage ring equipped with an in-ring electron target worldwide and therefore provides unique conditions, which are promising for recombination experiments with low-charged heavy ions.

The recombination measurements presented in this thesis were performed in CSR, using the CSR electron cooler and particle detectors. The following sections give an overview of the relevant experimental instrumentation.

3.1 The Cryogenic Storage Ring CSR and its experimental capabilities

CSR is an electrostatic ion storage ring operated at cryogenic temperatures. With an ion orbit of about 35 m, CSR is the largest electrostatic storage ring worldwide. It can store ions that have been accelerated to energies between 20 and 300 keV per ion charge state. CSR was put into operation in 2014, and the first cryogenic beamtime took place in 2015. As a cryogenic storage ring, CSR provides a low residual-gas density and allows for long ion beam storage. Furthermore, stored molecular ions can relax to their lowest vibrational and rotational levels in the low blackbody-radiation field in CSR [96, 97]. CSR is equipped with several experimental stations which enable various kinds of

experiments with the stored ion beam. A detailed overview of CSR was published by von Hahn et al. [33]. Here, the most relevant features are summarized.

Ion beams for the supply of CSR can be generated on two high voltage platforms and accelerated by up to 300 kV and 60 kV, respectively. On these platforms, different types of ion sources can be mounted to produce positive or negative, molecular or atomic ions. Electron-ion recombination experiments rely on fast ion beams from the larger 300 kV-platform. After acceleration, the ions enter the transfer beamline [98] to CSR, where the beam is shaped by quadrupoles and mass-selected by two 45°-magnets. An electrostatic chopper allows to generate pulses from the continuous ion beam produced by the ion source by fast switching of the high voltage on its deflector plates. Like this, the amount of ions injected into CSR can be adjusted. Subsequently, the ions enter the storage ring.

Figure 3.1 shows a schematic overview of CSR. CSR is an electrostatic storage ring, meaning that all its ion beam optics and deflectors work purely electrostatic. The ring has a nominal ion orbit length of 35.12 m. It comprises four straight sections, in which experiments can be performed. Each corner houses four cylindrical deflectors in the configuration of 6° - 39° - 39° - 6°, that sum up to a total deflection of the ion beam of 90°. In every straight section, two quadrupole doublets allow for ion beam shaping and focusing. By adjusting the quadrupole voltages, different operation modes of CSR can be set. Among these operation modes, the 'isochronous mode' [99] enables mass spectrometry in the storage ring. For experiments on electron-ion recombination, the 'achromat mode' is used. It is characterized by zero dispersion in the electron cooler section, which means that the paths of the stored ions in the electron cooler do not depend on their momentum deviation from the nominal momentum. This is helpful, because the beam overlap is maintained even if the ion beam is slightly accelerated or decelerated by interaction with the electron beam.

The injection beamline is aligned with one of the straight sections of CSR. For ion beam injection into CSR, the voltage of the first 6°-deflector (called 'kicker') is switched to zero. Once the ions entered the storage ring, the kicker potential is switched to high voltage on a time scale much shorter than one ion revolution period, so that the ions are stored afterwards.

Three of the four straight sections of CSR are equipped with experimental stations. In the first straight section after the kicker, the stored ion beam can be overlapped with a neutral beam, offering the possibility for the investigation of cold ion-atom collisions [100–102]. Collision products can be analyzed in a dedicated extraction beamline. Furthermore, two cylindrical electrodes for RF bunching of the stored ion beam are installed in this section.

In the electron cooler section, which is the second straight section, merged-beams electron-ion collision experiments can be performed. This setup was used for the experiments presented in this thesis. Detailed information about the electron cooler, which provides the electron beam, is given below in section 3.2. For collecting neutral and

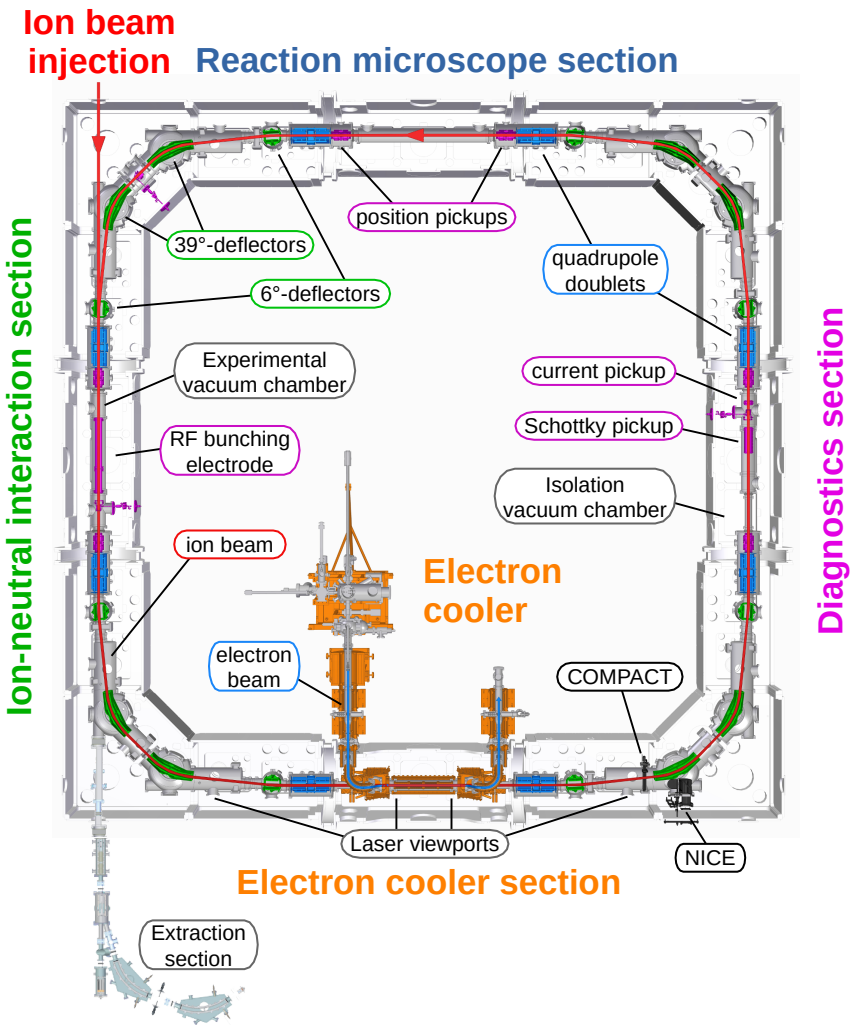

Figure 3.1: Schematic view of the storage ring CSR. The ring is built in a nested structure with two vacuum stages. The ion beam circulates in the inner experimental vacuum chamber, which can be cooled to cryogenic temperatures below 10 K, and which is housed by the outer isolation vacuum chamber. In the corners, the ion beam is deflected by electrostatic deflectors. CSR comprises four straight sections, three of which are equipped with experimental stations to study collision processes. For the experiments presented in this thesis, the electron cooler and the single-particle detectors COMPACT and NICE have been utilized. The ion source platforms are not shown.

charged products from electron interaction, two particle detectors called NICE and COMPACT are mounted in the following corner. Details about these detectors can be found below in section 3.3. Additionally, the electron cooler section is equipped with several viewports that allow for ion-photon interaction studies with lasers perpendicular to the ion beam, or at gracing angle. By applying laser beams, the internal ro-vibrational level population of stored molecular ion beams can be probed in photodetachment [97] and photodissociation studies [96, 103]. The two detectors mentioned above can be used to collect the product particles from laser interaction.

The third section houses two pickups for non-destructive ion beam diagnostics. Both pickups are sensitive to the through-passing ions by detecting the mirror charge induced in cylindrical electrodes. A Schottky noise pickup permits to observe harmonics of the revolution frequency and the momentum spread of a coasting ion beam. It is often used as a diagnostic tool for electron cooling, as explained in section 4.2. A current pickup can be used to determine the total ion number in the ring from a bunched ion beam (see section 4.9.1). For more details on the pickups, see [104, 105].

In 2022 and 2023, a reaction microscope [106] has been implemented in the forth straight section of CSR. Interactions of cold stored ions with a neutral atomic or molecular gas jet, or with lasers, can be studied in full kinematics by collecting all products (electrons, ions, neutrals) on dedicated detectors. The commissioning happened only in fall 2023, and the reaction microscope has not been implemented in the ring yet at the time when the recombination experiments presented in this thesis were conducted.

All straight sections, besides the electron cooler section, are additionally equipped with two pairs of two sliced cylindrical electrodes each. These 'beam position monitors' allow to determine the transverse position of the stored ion beam in the storage ring [104, 105].

The key feature of CSR is its cryogenic environment for the stored ion beam, which is achieved by cool-down of the inner vacuum chamber to temperatures below 10 K. To obtain these cryogenic conditions, CSR is equipped with a closed-cycle liquid helium system. Furthermore, CSR encompasses two vacuum stages as well as two radiation shields. The inner vacuum chamber of CSR provides the 'experimental' vacuum region in which the ion beam is stored, while the outer 'isolation' vacuum prevents convective heat transfer to the inner chamber. The inner chamber comprises cryopumps, which are cooled by a line of liquid helium at a temperature of < 4 K. Three additional, warmer helium lines at ~ 5 K, 40 K and 80 K cool the inner vacuum chamber and two aluminum radiation shields, respectively. Within the outer vacuum chamber, the two radiation shields are mounted in two separate layers to steadily block the 300 K blackbody radiation from the cold experimental vacuum chamber. In addition, the outer 80 K shield is covered with super-insulation from the outside. With this design, wall temperatures at the inner experimental vacuum chamber as low as 4 K can be reached. The detailed cryogenic design is described by von Hahn et al. [33].

As the whole chamber wall acts as a large cryopump, most residual gas (besides hydrogen and helium) freezes out, resulting in extremely low residual-gas densities. In

an early measurement on detachment of OH^-, carried out before the electron cooler was implemented, a ring-averaged residual-gas density of below $140\,cm^{-3}$ was inferred [33]. From a more recent measurement in fall 2021 with an Ar^+ beam at 150 keV, the residual-gas density in the electron cooler section was estimated to 10^3 to $10^4\,cm^{-3}$. Such a residual-gas density corresponds to a room-temperature-equivalent pressure in the order of 10^{-13} mbar, which is up to two orders of magnitude lower than in conventional room-temperature storage rings like TSR [95], ESR [107] and CRYRING@ESR [84].

A strong advantage of low residual-gas densities is the increased lifetime of the stored ion beam. In CSR, beam lifetimes of several hundreds up to thousands of seconds can be reached. This allows molecular ions to radiatively relax to their lowest ro-vibrational ground levels within the blackbody-radiation field of CSR [96, 97] and opens the possibility to perform experiments with cold molecular ions. Experiments with atomic ions benefit from the reduced background signal due to residual-gas collisions, which is especially crucial for recombination experiments with low-charged heavy ions as presented in this thesis.

3.2 The CSR electron cooler

The electron cooler implemented in CSR provides a beam of nearly mono-energetic electrons which is overlapped with the stored ion beam collinearly in the merged-beams technique. The electron cooler serves two purposes. On the one hand, it can be utilized for ion beam phase-space cooling (so-called 'electron cooling' [108], see also section 4.2) when operated with electrons whose velocity matches that of the stored ion beam. Due to the low ion beam velocities in CSR in comparison to other storage rings, the electrons at cooling conditions have to be slow as well. The electron cooler was designed to be able to cool ion beams at electron lab frame energies down to 1 eV [109], corresponding to matched velocities with an ion beam with mass-to-charge ratio of up to $m/q = 160$, accelerated by 300 kV. So far, electron cooling was demonstrated for $m/q = 43$ in the case of 900 keV-Xe^{3+}, corresponding to an electron lab energy of 3.82 eV.

On the other hand, the electron beam provided by the electron cooler serves as a collision target for electron-ion collision experiments. The energy of the electron beam in the interaction section can be precisely controlled, enabling energy-selected electron-ion collisions and allowing, e.g., for recombination experiments.

The electron cooler device comprises two room temperature parts where the electrons are produced and collected, respectively, and a cryogenic part which encompasses the electron-ion interaction region. Along its way, the electron beam is guided by strong magnetic fields. Detailed information on the CSR electron cooler can be found in the work of Shornikov [109], Vogel [105], and Wilhelm [110]. A schematic view of the electron cooler is shown in figure 3.2. Here, the general design is summarized.

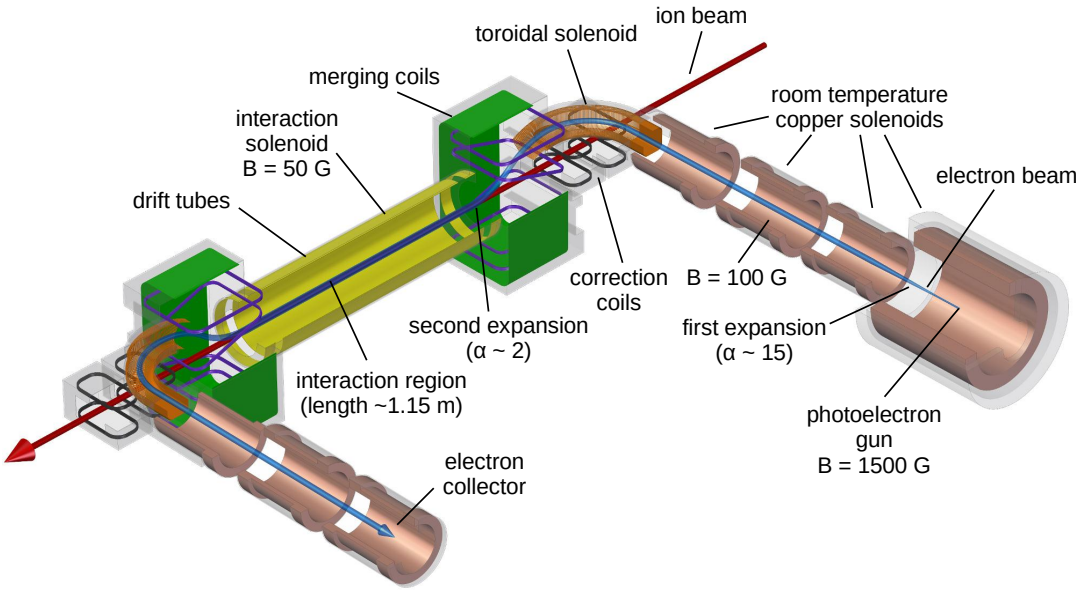

Figure 3.2: Schematic view of the CSR electron cooler, adapted from [110]. The electrons are produced in the room temperature section on the right side by a photoelectron gun consisting of a laser-illuminated photocathode. The electron beam is then expanded and overlapped with the stored ion beam in the cryogenic interaction region, and subsequently guided out and dumped on a collector cup in the left room temperature section.

The electron beam is produced by laser-illumination of a photocathode situated in the room-temperature part of the electron cooler. Multiple photocathodes are available for alternating use. The photocathode setup has been previously in operation at the electron target setup at TSR [111–114], and was transferred to CSR after the decommissioning of TSR. GaAs photocathodes are utilized, which are coated with a thin layer of cesium and oxygen. The Cs/O-layer bends the valence and conduction bands in the semiconductor and shifts the vacuum energy level below the conduction band. This configuration is called 'effective Negative Electron Affinity' (NEA) [115] and increases the yield of free electrons obtained from the photoelectric effect by efficiently allowing electrons in the conduction band to tunnel to the vacuum. The detailed procedure to prepare and handle the photocathodes is described by Weigel [111] and Krantz [113]. For the experiments presented here, the Cs/O coated photocathodes reached quantum efficiencies between 6 % and 12 %. Upon irradiation with a 500 mW, 805 nm laser, enough electrons are extracted to operate the photocathode in a space-charge-limited regime, where the extraction of additional electrons is suppressed due to an electron cloud forming in front of the cathode surface.

The photocathode electron gun is located within a copper solenoid at room tem-

perature, and lifted to a negative potential. By applying a more positive potential (up to several 10 V) on the so-called 'extraction electrodes' close to the cathode surface, electron beams with currents up to 250 µA and higher can be extracted. The electron beam passes three smaller copper solenoids with reduced magnetic guiding field strength while being accelerated towards ground potential at the transition to the toroid region. There, the electron beam enters the cryogenic region of CSR. Within the toroid, the electron beam is bent by 90° sideways and by 30° downwards. Subsequently, the overlapping of the stored ion beam with the electrons is achieved by a dipole field produced by the merging coils, bringing the electron beam in line with the ion beam. In the overlap region, the electron beam is guided by a high-temperature superconducting solenoid with an even reduced magnetic field. The electron energy can be varied here by adjusting the potential on a set of eight drift tubes encompassing the merged beams. In the experiments presented in this thesis, all drift tubes were operated at the same potential. While the total electron-ion overlap length is about ~ 1.15 m, the drift tubes extend over only 87 cm. After passing the drift tubes, the electron beam is demerged from the ion beam, and guided out of CSR towards the electron collector. The demerging proceeds mirrored to the merging. The electron beam is then guided by three room-temperature copper solenoids towards the electron collector cup, where the electrons are dumped and the electron current is measured. A detailed schematic view of the electric and magnetic fields along the electron beam path can be found in the work of Paul [116]. Along the electron beam path, seven pairs of steering coils allow for x- and y-steering of the electron beam. Thereby, the position and angle of the electron beam in the interaction region can be controlled, which is import for obtaining good overlap conditions of electron and ion beams.

Along its way, the electron beam is guided by strong magnetic fields of varying field strengths. By lowering the guiding magnetic field strength B, the electron beam size is increased in a so-called 'adiabatic expansion', with the expansion factor α [117],

$$\alpha = \frac{B_\mathrm{i}}{B_\mathrm{f}} = \frac{r_\mathrm{f}^2}{r_\mathrm{i}^2}, \tag{3.1}$$

where r denotes the electron beam radius and i and f symbolize the initial and final conditions before and after the expansion. At the same time, also the transverse temperature $T_\perp$ of the expanded electron beam is reduced [117],

$$T_{\perp,f} = \frac{T_{\perp,i}}{\alpha}. \tag{3.2}$$

The electron cooler at CSR benefits from the use of photocathodes, where the electrons are produced at a transverse temperature $T_{\perp,i}$ close to room temperature, resulting in a low $T_{\perp,f}$. For the experiments presented in this thesis, magnetic field strengths of 1500 G in the big room-temperature solenoid (where the electrons were produced), 100 G in the smaller room-temperature solenoids and 50 G in the interaction region were chosen, corresponding to an expansion factor in the interaction region of $\alpha = 30$. These

fields are reduced compared to the 'regular' settings used for recombination experiments with molecular ions (compare [116]). Therefore, the heat input on the cryogenic part of the electron cooler and thus the residual-gas pressure in the electron cooler section is reduced, which is of uttermost importance for recombination studies with low-charged heavy atomic ions, as explained in chapter 2.

In previous recombination experiments with molecular ions, electron beam temperatures in the order of $k_{\mathrm{B}}T_{\perp} \approx 1$ to 3 meV transverse and $k_{\mathrm{B}}T_{\parallel} \approx 0.2$ to 0.3 meV longitudinally were assumed [35, 36, 38, 39]. Typical electron densities in the interaction region are 10^5 to $10^6\,\mathrm{cm}^{-3}$.

3.3 Particle detectors

Electron-ion recombination happening in the electron-ion interaction region of the electron cooler produces charged or neutral particles which have to be detected to gain information on the recombination cross section.

The velocity of the product particles is close to that of the parent ion beam, as the energy gain in the collision with the electron is comparatively low. Even the kinetic energy released in the fragmentation of recombined molecular ions does not significantly change the lab frame velocity of the products. Therefore, the product particles fly in the direction of the stored ion beam and are separated from the stored beam in the first 6°-deflector downstream of the electron cooler according to their charge-to-mass ratio. In the corner behind the electron cooler, two particle detectors are installed, which are suitable for collecting product particles produced in electron-ion collision experiments. These detectors fulfill specific criteria arising from the conditions in CSR, like ultra high vacuum compatibility, the operation at cryogenic temperatures, and the sensitivity to particles with energies of only few keV/u. The Cold Movable Particle Counter (COMPACT) [71, 118, 119] was mainly used in the course of the DR measurements presented in this thesis, since it is capable to detect charged product particles. The second detector, called Neutral Imaging in Cold Environment (NICE) [120], is sensitive to neutral fragments and offers imaging capabilities. NICE was partially used for electron-cooling diagnostics (see section 4.2) and for the determination of COMPACT's detection efficiency, which is reported in appendix A. The following sections give an overview of both detectors.

3.3.1 The Cold Movable Particle Counter COMPACT

Electron-ion recombination with multiply charged atomic ions results in lower-charged ions. In CSR, these charged recombination products are separated from the stored main beam in the 6°-deflector downstream of the electron cooler. Behind this deflector, the

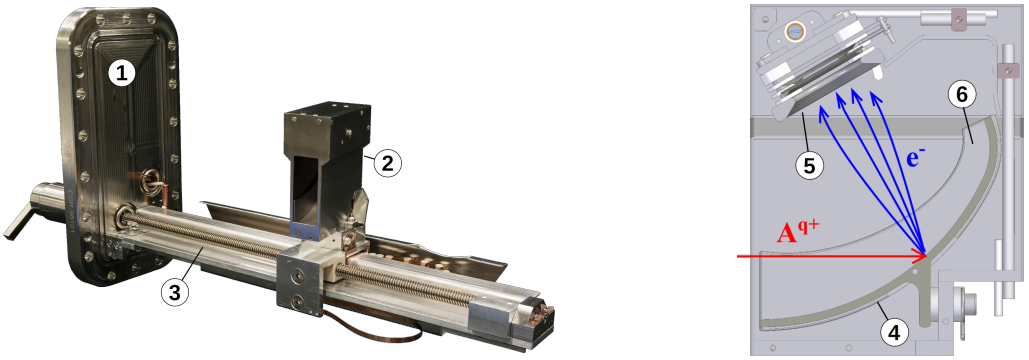

(a) (b)

Figure 3.3: (a) Photograph of the COMPACT detector. COMPACT is mounted on a flange (1) to the experimental vacuum chamber of CSR. The sensor unit (2) is movable on a worm drive (3). (b) Schematic side view of the inside of the sensor unit (2). Incoming particles hit the converter plate (4) and release secondary electrons which are accelerated towards an MCP stack (5). Left and right of the converter plate, side plates (6) are attached which are eventually hit by impinging particles as well. Both figures are adapted from [71].

Cold Movable Particle Counter (COMPACT) is placed. Figure 3.3a shows a picture of COMPACT. The detailed technical design and commissioning of the detector are reported by Spruck et al. [118] and Spruck [71], performance tests are reported by Krantz et al. [119].

To enable the detection of various, differently charged particles, the particle sensor unit of COMPACT is mounted on a translation stage consisting of a worm drive with a threaded rod. Even at cryogenic temperatures, this design allows to move the sensor unit perpendicular to the straight section across the experimental vacuum chamber of CSR. The detector can collect reaction products fulfilling the condition [118]

$$-0.4 \leq \frac{q_\mathrm{d}/m_\mathrm{d}}{q_\mathrm{p}/m_\mathrm{p}} \leq 2.1, \tag{3.3}$$

where q_p, q_d denote the charge states and m_p, m_d the masses of parent (main) and daughter (product) beam particles, respectively. For the most relevant applications, assuming a positively charged atomic ion beam, reaction products ranging from neutrals to ionized products with twice the charge of the stored main beam can be collected. However, there are limitations when the charge-to-mass ratios of parent and daughter particles are close. In this case, the separation of parent and daughter beams behind the 6°-deflector is small and the detector cannot be placed at the desired position to collect the product particles without affecting the main beam. From the detector width and typical ion beam sizes, it is estimated that in the case of atomic recombination the separation is too small for ion beams with $q_\mathrm{p} \gtrsim 6$, limiting the accessible ions for atomic recombination studies to charge states below $q_\mathrm{p} \approx 5$.

In the experiments with stored Ne^{2+} and Xe^{3+} ion beams performed in the course

of this work, the detector was placed at a fixed location where Ne^+ and Xe^{2+} product ions could be detected, respectively.

The particle sensor unit itself is embedded in a movable housing, and works by the principle of detecting secondary electrons produced upon ion impact. A schematic view of the movable sensor unit and its working principle is displayed in figure 3.3b. The front side of the housing is aligned with the main beam after the 6°-deflector, and has an opening of 2 cm horizontally and 5 cm vertically, through which particles can enter. Subsequently, the particles hit a curved aluminum electrode, called 'converter plate', and release secondary electrons. These electrons are accelerated towards an MCP stack in Chevron configuration, and some generate an electron avalanche inside the MCP, which thereafter is detected as an electronic signal on an anode plate. The applied voltages were −400 V on the converter electrode, 800 V on the front of the MCP, 2660 V on the backside of the MCP, and 3000 V on the anode. Two side plates are attached to the converter electrode, and converter and side plates are shaped such that secondary-electron guiding towards the MCP is most efficient. In fact, according to a simulation, basically all secondary electrons reach the MCP upon particle impact across the largest fraction of the converter plate's area [118, 71]. The electronic signal produced in the MCP is decoupled from the high voltage of the anode by a capacitor, amplified by a fast amplifier and subsequently fed to a discriminator [71], where the amplified pulses are converted to a digital signal.

As the resistance across MCPs rises with reduced temperature [121], the MCP stack was heated with a heating wire to $\sim$ 30 to 40 K. Compared to the operation at 6 K, where saturation effects have been observed starting from $1000\,s^{-1}$ [119], much higher count rates above $10\,000\,s^{-1}$ can be achieved without saturation effects by warming up the MCP. For a beam of Ne^+ ions (from recombination of Ne^{2+}), it was verified that saturation effects occurred only at count rates above $\sim 15\,000\,s^{-1}$. At the same time, the dark count rate of COMPACT is well below $1\,s^{-1}$ at all temperatures [119] and assumed to come from β-decay of radioactive nuclei within the MCP material [122]. In the experiments presented in this thesis, the dark count rate of COMPACT was as low as $\sim 0.3\,s^{-1}$.

The design of COMPACT offers various advantages compared to other counting detectors. On one side, the MCP stack is not directly exposed to the heavy product beam but only to light electrons, which prevents possible surface damage due to sputtering. On the other side, the detection efficiency is enhanced because *several* secondary electrons are emitted from the converter plate, thus increasing the chance of hitting the channels of the MCP. The large vertical opening allows impacting particles at a range of heights and makes an additional translation in vertical direction unnecessary.

The detection efficiency of COMPACT can vary for different impacting particle species. For Ne^+ and Xe^{2+} ions, the found efficiencies (neglecting geometric effects) are 0.75 ± 0.25 and 0.76 ± 0.19, respectively. The full procedures applied here to derive the detection efficiencies are reported in appendix A.

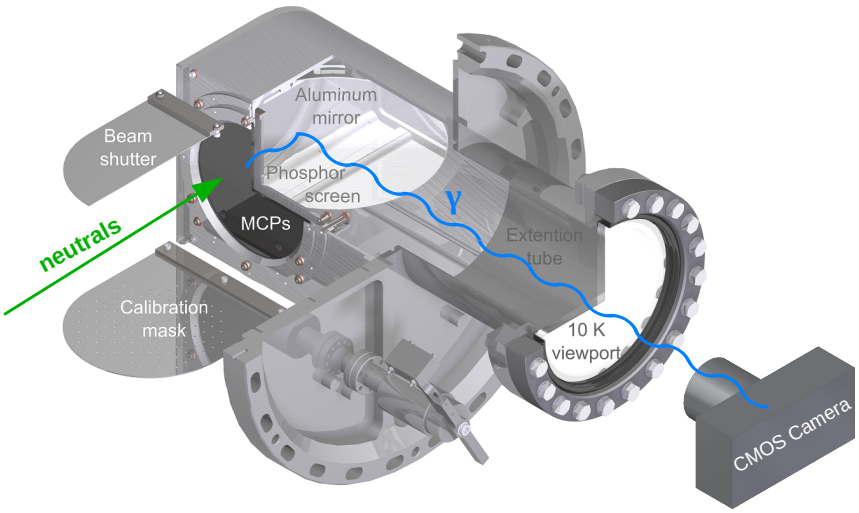

Figure 3.4: Schematic view of the NICE detector. Neutral fragments hitting the MCP stack produce electron avalanches, inducing an electronic signal on the phosphor screen. Subsequently, photons are created at the phosphor screen and recorded by a CMOS camera, which allows to determine the hit positions of the neutral particles. Figure adapted from [116].

3.3.2 The NICE detector - Neutral Imaging in Cold Environment

In dissociative recombination of electrons with molecular ions, the molecules break apart and multiple neutral fragments are produced. To get full information on the process and to be able to derive kinetic energy releases (KER), all fragments have to be collected in a position- and time-sensitive manner. For this purpose, COMPACT can not be used as its aperture opening is too small to collect fragments flying apart with a given KER, and it is not sensitive to impact positions. Thus, the Neutral Imaging in Cold Environment (NICE) detector is installed at neutral position, and has been used for studies of dissociative recombination at CSR [35–40]. Details about NICE can be found in the work of Becker [120].

NICE is installed in the corner downstream of the electron cooler and aligned with the straight electron cooler section of CSR. A schematic drawing of NICE is shown in figure 3.4. Neutral particles impinge on a circular MCP stack in Chevron configuration with a diameter of 12 cm, where they create electron avalanches. These electrons are accelerated towards a phosphor screen which acts as an anode. The induced electronic pulses on the phosphor screen are recorded and give the count rate and precise timing signal of the detector. Upon hitting the phosphor screen, the electrons produce photons, which are reflected by a 90° aluminum mirror through viewports out of the experimental and isolation vacuum chambers, and recorded by a CMOS camera outside of CSR. The light spots on the camera pictures allow for the assignment of the impinging particles' positions.

To decrease the resistance of the MCP, it is heated to $\sim 40\,\mathrm{K}$, permitting count rates of $\sim 5000\,\mathrm{s}^{-1}$ without visible saturation effects on the electronic pulses [116]. In contrast to this, the camera can transfer frames only at rates up to $\sim 1000\,\mathrm{s}^{-1}$, so at high count rates, parts of the imaging data are lost. For camera position calibration purposes, a calibration mask with evenly spaced holes can be moved in front of the MCP. A movable aluminum plate allows to shield the incoming particles and acts as a mechanical shutter, protecting the detector from high count rates. Due to the large MCP, the dark count rate of NICE is around $50\,\mathrm{s}^{-1}$, and evenly distributed across the whole MCP area.

The counting efficiency of NICE for single particles was determined as 0.593 ± 0.015 from the ratio of single-to-double particle hits in a dissociative recombination experiment with CF^+ ions [36]. In this work, NICE has been used mainly to cross-calibrate the counting efficiency of COMPACT, which is extensively described in appendix A.

Chapter 4

Methods, Measurement and Analysis Procedures

In this chapter, general methods and procedures relevant for the storage ring recombination experiments with Ne^{2+} and Xe^{3+} ions are described. First, the concept of the Merged-Beams Rate Coefficient (MBRC), the connection to the underlying cross section and to the experimentally measured count rate of reaction products is introduced in section 4.1. The principle of electron cooling, which has been applied in the experiments to achieve well-defined overlap conditions of electron and ion beams, is presented in section 4.2. Sections 4.3 and 4.4 focus on the properties of the electron beam that are important for the evaluation of the collision conditions. Afterwards, the measurement setup and the data acquisition are explained in sections 4.5 and 4.6, respectively. The extraction of the MBRC from the measured count rates of the recombination products, as well as the absolute scaling are described in sections 4.7 to 4.9. Finally, the level populations in the stored ion beams are addressed in section 4.10, and the influence of field ionization on the recombined ions is presented in section 4.11.

4.1 Merged-beams rate coefficients

The fundamental quantity characterizing a collision process (e.g., between an electron and an ion) is the collision-energy-dependent cross section $\sigma(E)$. Under realistic experimental conditions with many interacting particles, the collision energies of the individual colliding particles have a spread. As a result, only a convolved quantity, the rate coefficient $\alpha = \langle \sigma(E)\, v(E) \rangle$, can be measured, which is the expectation value of the product of cross section and collision velocity $v(E)$. In merged-beams experiments,

a so-called Merged-Beams Rate Coefficient (MBRC) α_{mb} can be derived, which is an experiment-specific quantity as it depends on the experimental collision energy distribution. In the experiments, the nominal collision energy characterizing this distribution is varied and the MBRC can be derived from the measured count rate of the reaction products at the different nominal collision energies.

In the following section 4.1.1, a general relation of cross section, rate coefficient and total reaction rate is derived. In section 4.1.2, the findings are applied to an electron-ion merged-beams collision experiment with an electron-cooled ion beam, representing the conditions in the experiments presented in this thesis.

4.1.1 General relation of rate coefficient and reaction rate

The cross section σ is defined from the probability ω for a reaction to occur in the length slice $\mathrm{d}x$ when one projectile particle, e.g., an electron, propagates through a medium filled with target particles, e.g., ions, of the density n_{i}, i.e.

$$\omega = \sigma \, n_{\mathrm{i}} \, \mathrm{d}x. \tag{4.1}$$

Assuming that several projectile particles N_{e} penetrate the medium as a parallel beam, the number of reactions in the slice $\mathrm{d}x$ can be given as

$$\frac{\mathrm{d}N_{\mathrm{e}}}{\mathrm{d}x} = \sigma \, n_{\mathrm{i}} \, N_{\mathrm{e}}. \tag{4.2}$$

The number of reactions per time is the reaction rate

$$R_r = \frac{\mathrm{d}N_{\mathrm{e}}}{\mathrm{d}t} = \sigma \, v \, n_{\mathrm{i}} \, N_{\mathrm{e}}, \tag{4.3}$$

which depends on the relative velocity v of the colliding projectile and target particles. This can be expressed as a reaction rate per reaction volume, i.e.

$$r_r = \frac{R_r}{V} = n_{\mathrm{e}} \, n_{\mathrm{i}} \, \sigma \, v, \tag{4.4}$$

where the density $n_{\mathrm{e}} = N_{\mathrm{e}}/V$ of projectile particles in the reaction volume V is considered. The reaction cross section is dependent on the center-of-mass collision energy E of the colliding particles, $\sigma = \sigma(E)$. The relative collision velocity $v = v(E)$ is directly linked to the collision energy E via $E = 1/2 \, \mu \, v^2$ with the reduced mass of the colliding particles μ. Therefore, in case the collision energies in many collisions in the volume have not one fixed value but are rather distributed, above equation yields a connection to the expectation value $\langle \sigma v \rangle$,

$$r_r = \frac{R_r}{V} = n_{\mathrm{e}} \, n_{\mathrm{i}} \, \langle \sigma v \rangle = n_{\mathrm{e}} \, n_{\mathrm{i}} \int_E \sigma(E) \, v(E) \, f(E) \, \mathrm{d}E, \tag{4.5}$$

where $f(E)$ is the normalized distribution of center-of-mass collision energies with

$$\int_E f(E) \, \mathrm{d}E = 1. \tag{4.6}$$

The expectation value $\langle \sigma v \rangle$ in equation (4.5) is called 'rate coefficient' α, i.e.

$$\alpha \equiv \langle \sigma v \rangle = \int_0^\infty \sigma(E)\, v(E)\, f(E)\, \mathrm{d}E, \tag{4.7}$$

where the integration covers all possible center-of-mass collision energies E. Equation (4.5) can then be written as

$$r_r = \frac{R_r}{V} = n_\mathrm{e}\, n_\mathrm{i}\, \alpha. \tag{4.8}$$

Accordingly, the reaction rate $\mathrm{d}R_r$ in any infinitesimally small volume $\mathrm{d}V$ can be expressed by

$$\mathrm{d}R_r = n_\mathrm{e}\, n_\mathrm{i}\, \alpha\, \mathrm{d}V. \tag{4.9}$$

Under realistic experimental conditions, the quantities in equation (4.9) depend on the location $\vec{r}$. The rate coefficient depends on the position, because the collision energy distribution is determined by the experimental conditions at location $\vec{r}$. Therefore, the *local* rate coefficient $\alpha_X(\vec{r})$ at location $\vec{r}$ can be given as

$$\alpha_X(\vec{r}) = \int_E \sigma(E)\, v(E)\, f_X(E;\vec{r})\, \mathrm{d}E, \tag{4.10}$$

where $f_X(E;\vec{r})$ is the *local* collision-energy distribution at location $\vec{r}$. In particular, $f_X(E;\vec{r})$ is normalized such that

$$\int_E f_X(E;\vec{r})\, \mathrm{d}E = 1 \qquad \forall\ \vec{r} \tag{4.11}$$

at each individual $\vec{r}$. Furthermore, under realistic experimental conditions, the particle densities are not necessarily homogeneous and vary with position, i.e. $n_\mathrm{e} = n_\mathrm{e}(\vec{r})$ and $n_\mathrm{i} = n_\mathrm{i}(\vec{r})$. Consequently, at any location $\vec{r}$, equation (4.9) yields

$$\mathrm{d}R_r = n_\mathrm{e}(\vec{r})\, n_\mathrm{i}(\vec{r})\, \alpha_X(\vec{r})\, \mathrm{d}V. \tag{4.12}$$

From equation (4.12), the total reaction rate R_r is derived by an integration over all positions, i.e. by covering the complete interaction volume,

$$R_r = \int_V n_\mathrm{e}(\vec{r})\, n_\mathrm{i}(\vec{r}) \int_E \sigma(E)\, v(E)\, f_X(E;\vec{r})\, \mathrm{d}E\, \mathrm{d}V. \tag{4.13}$$

The above equation describes on a fundamental level the total reaction rate in any collision experiment. However, in order to conveniently obtain rate coefficients from an experiment, a representation of R_r is sought that retains the simple dependency $R_r \propto \alpha$, where the rate coefficient α follows the form from equation (4.7), with a global collision energy distribution over all interaction positions $f(E)$. It should be noted that E in equation (4.13) is purely the parameterization of the integration and as such not dependent on $\vec{r}$. Therefore, the integration order can be interchanged and one obtains

$$R_r = \int_E \sigma(E)\, v(E) \int_V n_\mathrm{e}(\vec{r})\, n_\mathrm{i}(\vec{r})\, f_X(E;\vec{r})\, \mathrm{d}V\, \mathrm{d}E. \tag{4.14}$$

From the comparison with the definition of a rate coefficient in equation (4.7), it is found that

$$\int_V n_\mathrm{e}(\vec{r})\, n_\mathrm{i}(\vec{r})\, f_X(E;\vec{r})\,\mathrm{d}V = \varrho\, f(E) \tag{4.15}$$

with the proportionality factor ϱ, which is in particular not a function of the collision energy E. Reordering of the above equation yields

$$f(E) = \frac{1}{\varrho}\int_V n_\mathrm{e}(\vec{r})\, n_\mathrm{i}(\vec{r})\, f_X(E;\vec{r})\,\mathrm{d}V. \tag{4.16}$$

According to equation (4.6), the normalization has to be fulfilled, i.e.

$$\begin{aligned} 1 = \int_E f(E)\,\mathrm{d}E &= \int_E \frac{1}{\varrho}\int_V n_\mathrm{e}(\vec{r})\, n_\mathrm{i}(\vec{r})\, f_X(E;\vec{r})\,\mathrm{d}V\,\mathrm{d}E \\ &= \frac{1}{\varrho}\int_V n_\mathrm{e}(\vec{r})\, n_\mathrm{i}(\vec{r}) \underbrace{\int_E f_X(E;\vec{r})\,\mathrm{d}E}_{1}\,\mathrm{d}V \\ &= \frac{1}{\varrho}\int_V n_\mathrm{e}(\vec{r})\, n_\mathrm{i}(\vec{r})\,\mathrm{d}V. \end{aligned} \tag{4.17}$$

This allows to derive

$$\varrho = \int_V n_\mathrm{e}(\vec{r})\, n_\mathrm{i}(\vec{r})\,\mathrm{d}V. \tag{4.18}$$

Consequently, following equations (4.16) and (4.18), the global center-of-mass collision energy distribution can be expressed as

$$f(E) = \frac{\int_V n_\mathrm{e}(\vec{r})\, n_\mathrm{i}(\vec{r})\, f_X(E;\vec{r})\,\mathrm{d}V}{\int_V n_\mathrm{e}(\vec{r})\, n_\mathrm{i}(\vec{r})\,\mathrm{d}V}, \tag{4.19}$$

with $f_X(E;\vec{r})$ the local collision energy distribution at the location $\vec{r}$.

ϱ from equation (4.18) accounts for the spatial density distribution of the two colliding species and can be seen as a density-overlap. From the combination of equations (4.14) and (4.15), the total reaction rate R_r can be given as

$$R_r = \int_E \sigma(E)\, v(E)\, \varrho\, f(E)\,\mathrm{d}E = \varrho \int_E \sigma(E)\, v(E)\, f(E)\,\mathrm{d}E. \tag{4.20}$$

In particular, with equations (4.7) and (4.18), the general expression for the total reaction rate R_r in a collision experiment is

$$R_r = \alpha\,\varrho = \alpha \int_V n_\mathrm{e}(\vec{r})\, n_\mathrm{i}(\vec{r})\,\mathrm{d}V, \tag{4.21}$$

which is proportional to the rate coefficient α with the density-overlap ϱ as the proportionality factor.

4.1.2 Rate coefficient in an electron-ion merged-beams experiment with an electron-cooled ion beam

The general relation of the total reaction rate and the rate coefficient presented in equation (4.21) is valid for two colliding species of position-variable density distributions and position-variable collision energy distribution. Here, equation (4.21) is utilized to find the connection between the measured count rate R and the rate coefficient in an electron-ion merged-beams setup as it was used for the experiments presented in this thesis.

We define the Merged-Beams Rate Coefficient (MBRC) as

$$\alpha_{\mathrm{mb}} = \int_0^\infty \sigma(E)\, v(E)\, f_{\mathrm{mb}}(E)\, \mathrm{d}E \tag{4.22}$$

where $f_{\mathrm{mb}}(E)$ is the collision energy distribution specific to the merged-beams setup. As not all reaction products (in this case recombined ions) produce a measurable electronic signal on the detector, the experimentally measured count rate R is linked to the total reaction rate R_r via the detection efficiency η, i.e. $R = \eta\, R_r$. Equation (4.21) consequently transforms into an expression for the experimentally measured count rate R, i.e.

$$R = \eta\, \alpha_{\mathrm{mb}}\, \varrho = \eta\, \alpha_{\mathrm{mb}} \int_V n_{\mathrm{e}}(\vec{r})\, n_{\mathrm{i}}(\vec{r})\, \mathrm{d}V. \tag{4.23}$$

For the merged-beams experiments as they were performed in the course of this work, a few assumptions can be made which simplify the calculation of the density-overlap factor ϱ in equation (4.23). The beam overlap has been optimized such that both beams can be assumed to be parallel and centered with respect to each other. Furthermore, the experiments were performed with *electron-cooled* ion beams. The concept of electron cooling is explained in section 4.2. As a result from the electron cooling, the ion beam was fully immersed in the (larger) electron beam and the transverse ion beam area S_{i} can be assumed small in comparison to the transverse electron beam size. It can be assumed that the ions effectively interacted only with electrons in the center of the electron beam. Consequently, the transverse energy and density variation in the electron beam due to the radial dependence of the space charge potential can be neglected. Thus, the volume integral in equation (4.23) can be evaluated in the transverse plane, $\int ...\mathrm{d}V \;\rightarrow\; S_{\mathrm{i}} \int ...\mathrm{d}z$, with the transverse beam interaction cross section area S_{i} and the longitudinal coordinate z. The electron density can be taken as the density in the minimum of the space charge potential along the z-axis, $n_{\mathrm{e}}(\vec{r}) \rightarrow n_{\mathrm{e},0}(z)$. As the ions were homogeneously distributed along the full orbit length in CSR L_{CSR}, the ion density can be specified as $n_{\mathrm{i}}(\vec{r}) \rightarrow n_{\mathrm{i}}(z) = n_{\mathrm{i}} = N_{\mathrm{i}}/(L_{\mathrm{CSR}} \cdot S_{\mathrm{i}})$, with the number of stored ions N_{i}. Under these assumptions, the density-overlap ϱ from equation (4.18) simplifies to

$$\varrho = S_{\mathrm{i}} \int_z n_{\mathrm{e},0}(z)\, \frac{N_{\mathrm{i}}}{L_{\mathrm{CSR}}\, S_{\mathrm{i}}}\, \mathrm{d}z = \frac{N_{\mathrm{i}}}{L_{\mathrm{CSR}}} \int_z n_{\mathrm{e},0}(z)\, \mathrm{d}z. \tag{4.24}$$

The integral over the electron density runs over all possible z-positions and can therefore be expressed as the product $l_{\mathrm{e}}\, \bar{n}_{\mathrm{e},0}$, where l_{e} is the full electron-ion overlap length (from

merging to demerging of the electron beam) and $\bar{n}_{e,0}$ is the mean electron density averaged over the full overlap length. With this,

$$\varrho = \bar{n}_{e,0}\, N_i\, \frac{l_e}{L_{CSR}} \tag{4.25}$$

and equation (4.23) condenses to

$$R = \eta\, \alpha_{mb}\, \bar{n}_{e,0}\, N_i\, \frac{l_e}{L_{CSR}}. \tag{4.26}$$

The MBRC can then be extracted from the measured count rate as

$$\alpha_{mb} = \frac{R}{\eta\, \bar{n}_{e,0}\, N_i\, \frac{l_e}{L_{CSR}}}. \tag{4.27}$$

In the following, 'MBRC' and 'rate coefficient' are often used interchangeably.

4.2 Electron cooling

As shown above in section 4.1.2, the calculation of the MBRC simplifies when the ion beam is small and fully immersed in the larger electron beam, and transverse variations in the electron energy and density can be ignored. One way to achieve these conditions is 'electron cooling', where the electron beam interacts with the ion beam at matching velocities. Detailed information on electron cooling can be found in [108] and the basic concept is explained here in short.

In the storage ring, the ions follow a closed orbit defined by the deflectors and the ion energy. As a result of the ion beam emittance at injection, each individual ion oscillates around this orbit transverse to the beam direction. These oscillations are controlled by the quadrupoles and are called 'betatron oscillations'. The transverse size of the ion beam is directly related to the betatron oscillations. In addition, the ion beam has a longitudinal momentum spread, which leads to a spread in the revolution frequency of the ion beam. Elastic collisions with nearly mono-energetic electrons at very low collision energies can dampen the oscillations of the stored ion beam and reduce its momentum spread, and therefore improve the conditions for electron-ion merged-beams collision experiments. This concept has first been proposed by Budker [123] and is called 'electron cooling'. Since its first experimental implementation for a proton beam [124], electron cooling has been applied in basically all electron-ion recombination experiments carried out at storage rings in order to improve the ion beam quality. To facilitate electron cooling, the stored ion beam is collinearly overlapped with a beam of cold, nearly mono-energetic electrons at matching beam velocities, $v_e = v_i$. In this case, the 'cooling energy' of the electrons can be calculated nonrelativistically as

$$E_{cool} = \frac{m_e}{m_i}\, E_i = \frac{1}{2}\, m_e\, v_i^2 = \frac{1}{2}\, m_e\, L_{CSR}^2\, f_{rev}^2, \tag{4.28}$$

with the electron and ion masses $m_{e/i}$, the ion kinetic energy E_i, the length of the ideal ion orbit in CSR L_{CSR} and the ion revolution frequency f_{rev}. Under the condition of matching beam velocities, the only remaining relative motion in the center-of-mass frame is then caused by the undirected motion of the ions correlated to the betatron oscillations and the momentum spread, and by the temperature of the electron beam, which has to be colder than the temperature of the ion beam. In coulombic collisions, the electrons generate a 'cooling force' and take away undirected kinetic energy from the ions. As the ions pass through a renewed cold electron bath in every revolution, the undirected motions are continuously dampened and the ion beam size and momentum spread shrink, which is referred to as transverse and longitudinal cooling, respectively. As a result, the phase-space of the ion beam is reduced.

Electron cooling is usually applied directly after ion beam injection into the storage ring to achieve well-defined conditions before the actual measurements start. Also in case the electron and ion beam velocities are not entirely matched in the beginning but have a slight detuning, the electron beam can accelerate or decelerate the stored ion beam through the longitudinal cooling force, resulting in matching beam velocities. This effect is called 'dragging'.

In the experiments with Ne^{2+} and Xe^{3+} ions presented in this thesis, electron cooling was applied after each ion beam injection into CSR for several seconds before the actual recombination measurements started. The cooling energies were $E_{cool,Ne^{2+}} = 16.42\,eV$ in the case of Ne^{2+} and $E_{cool,Xe^{3+}} = 3.82\,eV$ in the case of Xe^{3+}.

The effect of longitudinal electron cooling could be observed on the Schottky pickup, which allows to trace the revolution frequencies of the ions and the frequency spread. The longitudinal cooling force acting on Ne^{2+} and Xe^{3+} ions in CSR has been reported in [125].

To trace the transverse cooling, the NICE detector has been used. NICE has imaging capabilities, however it is mounted in neutral position in the corner downstream of the electron cooler and therefore can collect only neutral reaction products. The transverse impact positions of the neutral products on NICE represent a projection of the ion beam shape in the preceding straight section (i.e. the electron cooler section). A shrinking of the projected beam size on NICE indicates a shrinking transverse size of the stored ion beam. In the Ne^{2+} beamtime, the residual-gas pressure in CSR was sufficiently high to produce a detectable amount of neutral neon atoms in double-electron-capture collisions of Ne^{2+} with residual-gas particles. The transverse cooling of the Ne^{2+} beam was observed from the projected beam shape of these neutral neon atoms on NICE. As an example, this is shown in figure 4.1 for the first 2 s in the electron cooling process. In the Xe^{3+} beamtime, the stored Xe^{3+} ion beam contained a slight contamination (on the 1 %-level) of the molecular ion C_2F^+, which was unintentionally produced in the ion source as well and stored in CSR as it had the same mass-to-charge ratio as Xe^{3+}. Upon electron collision, C_2F^+ recombined and dissociated, and the neutral fragments could be used to trace the size of the stored ion beam. However, the fractional abundance of C_2F^+ in the stored ion beam was negligibly small compared to the amount of Xe^{3+}, and

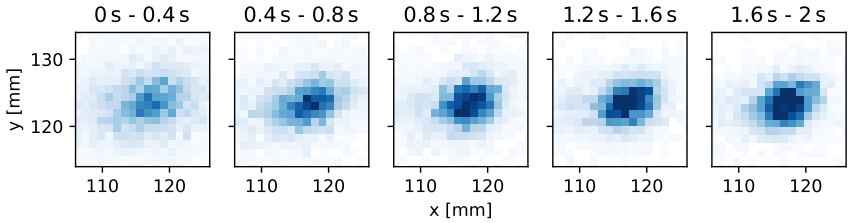

Figure 4.1: Transverse cooling of the Ne^{2+} beam. The individual frames show the impact positions of neutral neon on the NICE detector during the first 2 s of the electron cooling process in time windows of 0.4 s as indicated in the upper part of the figure.

C_2F^+ did not produce any fragments that would end up on the COMPACT detector at the position where Xe^{2+} was collected. Therefore, the contamination by C_2F^+ was irrelevant for the recombination measurements presented in this thesis.

It should be noted that the Xe^{3+} beam was the slowest ion beam to date that has been electron-cooled, with a cooling energy of only 3.82 eV.

4.3 Electron density and electron-ion collision energy

For the evaluation of the MBRC α_{mb} from equation (4.27) on page 32, the average electron density in the electron-ion overlap region is required. Furthermore, the MBRC is linked to the experimental collision energy distribution according to equation (4.22) on page 31. Both the average electron density and the collision energy distribution are related to the properties of the electron beam, which in CSR are influenced by the drift-tubes geometry of the merged-beams setup. In the following section, general properties of the electron beam like the nominal electron energy, the space charge, the electron density and the nominal electron-ion collision energy in the drift tubes are introduced. The derivation of the average electron density in the full overlap region is addressed in section 4.3.1, and the collision energy distribution is presented in section 4.3.2.

In general, the electron energy in the interaction region and all related quantities (like the electron density) should be obtained from a 3D model of the electron cooler, including realistic geometry and the actual shape of the electron beam, by solving the Poisson equation. For some test cases, this was done in the work of Saurabh [126]. In the approach presented in the following, which was used for the data analysis in this work, no 3D simulation was performed. Instead, certain assumptions were made, which in the end allow to calculate the electron energy and density in the interaction region in a simplified procedure.

The experiments presented in this thesis were carried out with electron-cooled ion

beams that were fully immersed in the larger electron beam. It can be assumed that the ion beam was centered in the electron beam and that the transverse size of the ion beam with radius r_{ion} was small compared to the size of the electron beam with radius r_{beam}, i.e. $r_{\mathrm{ion}} \ll r_{\mathrm{beam}}$. Under these conditions, the ions interact exclusively with electrons close to the center of the electron beam, and any radial dependency of electron velocities or densities can be neglected. In the following considerations, only electrons at the center of the electron beam are considered.

The nominal energy of the electron beam E_{e} (neglecting thermal effects) at a given position z along the interaction zone (or overlap length) is defined by the interaction zone potential U_{int} and the space charge potential of the electron beam U_{sc}, i.e.

$$E_{\mathrm{e}}(z) = eU_{\mathrm{int}}(z) - e\left|U_{\mathrm{sc}}(z)\right|, \tag{4.29}$$

with the elementary charge e. The interaction zone potential $U_{\mathrm{int}}(z)$ is a potential with respect to the cathode potential, and it represents the accelerating potential for an electron in absence of the electron beam. The presence of the electron beam introduces the space charge potential $U_{\mathrm{sc}}(z)$, which results from the charge of the electrons in the beam itself. The space charge partially shields the interaction zone potential $U_{\mathrm{int}}(z)$ and consequently lowers the effective electron energy $E_{\mathrm{e}}(z)$.

The interaction zone potential $U_{\mathrm{int}}(z)$ is linked to the voltage applied at the cathode U_{cath} (where the electrons are produced) and to the voltage applied at the drift tubes U_{drift}. In the geometry of the merged-beams setup at CSR, the drift tubes of length $l_{\mathrm{dt}} = 87\,\mathrm{cm}$ cover only a part of the full electron-ion overlap region with a length of $l_{\mathrm{e}} = 115.2\,\mathrm{cm}$ (from merging to full demerging). From the cathode, the electrons are first accelerated towards ground (on the vacuum chamber wall), merged with the ion beam, and subsequently decelerated or further accelerated in the drift tubes (depending on the chosen U_{drift}). Consequently, $U_{\mathrm{int}}(z)$ is varying along the overlap length. Since the interaction region is symmetrical along z, $U_{\mathrm{int}}(z) = U_{\mathrm{int}}(-z)$ and $z = 0$ in the middle of the drift tubes. As an example, the variation of $U_{\mathrm{int}}(z)$ is shown for the cooling conditions in the Xe^{3+} beamtime in figure 4.2.

In general, the interaction zone potential $U_{\mathrm{int}}(z)$ transitions between the two values $U_{\mathrm{int}}^{\mathrm{drift}}$ in the center of the drift tubes at $z = 0$, and $U_{\mathrm{int}}^{\mathrm{out}}$ far outside of the drift tubes. $U_{\mathrm{int}}^{\mathrm{drift}}$ is determined by the experimentally controlled voltage applied to the drift tubes with respect to the cathode voltage, U_{drift}, and the so-called 'contact potential' $U_{\mathrm{cont}}^{\mathrm{drift}}$ [110, 116],

$$U_{\mathrm{int}}^{\mathrm{drift}} = U_{\mathrm{drift}} - U_{\mathrm{cont}}^{\mathrm{drift}}. \tag{4.30}$$

The contact potential at the drift tubes $U_{\mathrm{cont}}^{\mathrm{drift}}$ comprises the difference in the work functions W between drift tubes and cathode, as well as the space charge barrier ΔE_{cath} in front of the cathode [127],

$$U_{\mathrm{cont}}^{\mathrm{drift}} = \frac{1}{e}\left((W_{\mathrm{drift}} - W_{\mathrm{cath}}) + \Delta E_{\mathrm{cath}}\right), \tag{4.31}$$

and is therefore slightly dependent on the extracted electron current and on the cathode properties. $U_{\mathrm{cont}}^{\mathrm{drift}}$ was evaluated in the beamtimes from a comparison of the cooling

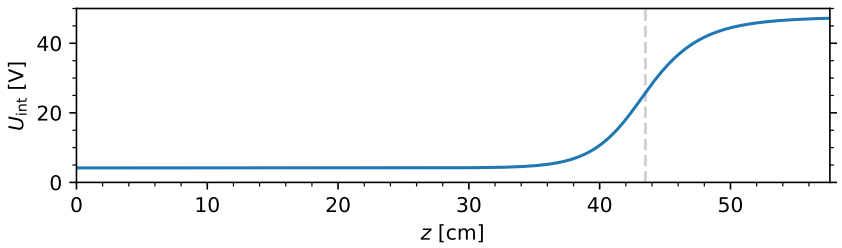

Figure 4.2: Interaction zone potential U_{int} as a function of longitudinal position z along the electron-ion interaction region. The interaction region is symmetrical and only one half of the interaction length (half-length $l_{\mathrm{e}}/2 = 57.6\,\mathrm{cm}$) is shown. $z = 0$ marks the center of the drift tubes, and the dashed vertical line marks the end of the drift tubes (half-length $l_{\mathrm{dt}}/2 = 43.5\,\mathrm{cm}$). The figure represents the cooling conditions for Xe^{3+}, where the cathode voltage was $U_{\mathrm{cath}} = -50\,\mathrm{V}$ and the voltage applied to the drift tubes was $U_{\mathrm{drift}} = 6.66\,\mathrm{V}$ with respect to the cathode.

energy E_{cool} (calculated from equation (4.28)) with the drift tube voltage U_{drift} needed at cooling conditions to fulfill $E_{\mathrm{e}}^{\mathrm{drift}} = E_{\mathrm{cool}}$, with the nominal electron energy inside the drift tubes $E_{\mathrm{e}}^{\mathrm{drift}}$ from equation (4.29), taking into account the space charge in the drift tubes.

Far outside of the drift tubes, the interaction zone potential $U_{\mathrm{int}}^{\mathrm{out}}$ is determined by the potential difference between the vacuum chamber (which is grounded) and the cathode (cathode voltage U_{cath}),

$$U_{\mathrm{int}}^{\mathrm{out}} = -U_{\mathrm{cath}} - U_{\mathrm{cont}}^{\mathrm{out}}. \tag{4.32}$$

Here, the contact potential $U_{\mathrm{cont}}^{\mathrm{out}}$ comprises the work function of the vacuum chamber W_{chamber}, and, similar to equation (4.31), it can be expressed as

$$U_{\mathrm{cont}}^{\mathrm{out}} = \frac{1}{e}\left((W_{\mathrm{chamber}} - W_{\mathrm{cath}}) + \Delta E_{\mathrm{cath}}\right). \tag{4.33}$$

The contact potential $U_{\mathrm{cont}}^{\mathrm{out}}$ to the vacuum chamber wall was not measured, but it is expected to be close to the one at the drift tubes. For simplicity, it is assumed here that the contact potentials of the drift tubes and of the vacuum chamber wall are identical, i.e. $U_{\mathrm{cont}}^{\mathrm{drift}} = U_{\mathrm{cont}}^{\mathrm{out}}$, and the variation in the contact potential with electron current (through a variation in ΔE_{cath}) is ignored. Consequently, a constant contact potential is assumed as $U_{\mathrm{cont}} = U_{\mathrm{cont}}^{\mathrm{drift}}$. For each individual cathode, a fixed $U_{\mathrm{cont}} \approx 2.5\,\mathrm{V}$ was derived at cooling conditions and used throughout the analysis of the recombination data.

With these considerations, the interaction zone potential $U_{\mathrm{int}}(z)$ transitions between the values $U_{\mathrm{int}}^{\mathrm{drift}} = U_{\mathrm{drift}} - U_{\mathrm{cont}}$ in the center of the drift tubes at $z = 0$ and $U_{\mathrm{int}}^{\mathrm{out}} = -U_{\mathrm{cath}} - U_{\mathrm{cont}}$ far outside of the drift tubes. Consequently, the shape of the interaction zone potential $U_{\mathrm{int}}(z)$ is determined by the cathode voltage U_{cath} and the applied drift tube voltage U_{drift}. In the experiments, U_{cath} was usually fixed and U_{drift} was varied to set different collision energies in the drift tubes. For the transition at the edges of the

drift tubes, a function derived from a 3D simulation in the work of Saurabh [126] was assumed. This transition function was employed here to obtain the curve in figure 4.2.

In addition to the interaction zone potential, the electron beam space charge potential $U_{\mathrm{sc}}(z)$ has to be known to calculate the electron energy $E_{\mathrm{e}}(z)$ from equation (4.29). $U_{\mathrm{sc}}(z)$ can be obtained from solving the Poisson equation, taking into account the geometry of the merged-beams setup and the spatial electron distribution within the electron beam. As explained in the following section 4.4, the electron beam current profile can be well approximated by a cylinder of constant radius r_{beam} over the full overlap length. Assuming a cylindrical electron beam with radius r_{beam} and a homogeneous electron density n_{e}, centered in a (larger) tube of radius r_{tube}, the electron beam space charge potential in the beam center (where the electron-cooled ion beam is expected) can be given as

$$U_{\mathrm{sc}} = -\frac{n_{\mathrm{e}}\, e\, r_{\mathrm{beam}}^2}{4\,\epsilon_0}\left(1 + 2\ln\frac{r_{\mathrm{tube}}}{r_{\mathrm{beam}}}\right), \tag{4.34}$$

which represents the minimum of the electron beam space charge potential. For computational reasons, this approximation was used here. The radius of the drift tubes is $r_{\mathrm{tube}}^{\mathrm{drift}} = 5\,\mathrm{cm}$ and the radius of the vacuum chamber $r_{\mathrm{tube}}^{\mathrm{out}} = 10\,\mathrm{cm}$. Still, for simplicity, the space charge at any position z was calculated here with the smaller radius $r_{\mathrm{tube}} = r_{\mathrm{tube}}^{\mathrm{drift}} = 5\,\mathrm{cm}$. The resulting error in the related quantities, however, is expected to be small. Consequently, the z-dependence is accounted for via the variation in the electron density $n_{\mathrm{e}}(z)$,

$$U_{\mathrm{sc}}(z) = -\frac{n_{\mathrm{e}}(z)\, e\, r_{\mathrm{beam}}^2}{4\,\epsilon_0}\left(1 + 2\ln\frac{r_{\mathrm{tube}}}{r_{\mathrm{beam}}}\right). \tag{4.35}$$

For the conditions prevalent in the experiments presented in this thesis, the space charge potential in the drift tubes was up to $U_{\mathrm{sc}}(z=0) \approx 2\,\mathrm{V}$ and is thus not negligible in comparison with the drift tube potential, which was varied between $U_{\mathrm{drift}} \approx 4\,\mathrm{V}$ and $100\,\mathrm{V}$. The electron density

$$n_{\mathrm{e}}(z) = \frac{I_{\mathrm{e}}}{v_{\mathrm{e}}(z)\, e\, \pi\, r_{\mathrm{beam}}^2} \tag{4.36}$$

can be calculated from the measured electron current I_{e}, the radius of the electron beam in the interaction region r_{beam}, and the electron velocity

$$v_{\mathrm{e}}(z) = \sqrt{\frac{2\,E_{\mathrm{e}}(z)}{m_{\mathrm{e}}}}, \tag{4.37}$$

which in turn is linked to the electron lab frame energy $E_{\mathrm{e}}(z)$ from equation (4.29) and to the electron mass m_{e}.

It should be noted that equations (4.29), (4.35), (4.36) and (4.37) are coupled. Especially, all quantities depend on the position z on the overlap axis due to the drift-tubes geometry of the merged-beams setup. For a fixed measured electron current I_{e}, a fixed electron beam radius r_{beam}, a fixed interaction zone potential U_{int} and a fixed position

z along the interaction region, equations (4.29), (4.35), (4.36) and (4.37) have to be solved iteratively.

In the experiments, electron-ion collisions at different energies have been studied by varying the drift tube voltage U_{drift} (and keeping the cathode voltage U_{cath} constant). Thereby, the electron energy in the drift tubes was varied, which in the center of the drift tubes can be given as $E_{\mathrm{e}}(z=0) = E_{\mathrm{e}}^{\mathrm{drift}}$, following equation (4.29). The nominal electron-ion collision energy in the center of the drift tubes is referred to as 'detuning energy' and can be calculated as

$$E_{\mathrm{d}} = \left(\sqrt{E_{\mathrm{e}}^{\mathrm{drift}}} - \sqrt{E_{\mathrm{cool}}}\right)^2, \tag{4.38}$$

with the cooling energy E_{cool} (see equation (4.28)) representing the electron energy at which electron and ion beams have matched velocities. In particular, the detuning energy E_{d} can be used to characterize the experimental collision energy distribution, as described in section 4.3.2.

4.3.1 Average electron density

To derive the MBRC from the measured count rates using equation (4.27) on page 32, the *average* electron density in the interaction region (and in the center of the electron beam) $\bar{n}_{\mathrm{e}}$ has to be known. (The electron density $n_{\mathrm{e},0}$ in the notation from section 4.1.2 is identical to n_{e} in the considerations above.)

To evaluate $\bar{n}_{\mathrm{e}}$, the interaction zone potential $U_{\mathrm{int}}(z)$ has to be considered for a chosen drift tube voltage U_{drift}, corresponding to a detuning energy E_{d}. At any position z in the interaction region, equations (4.29), (4.35), (4.36) and (4.37) have to be solved iteratively so that the position-dependent electron density $n_{\mathrm{e}}(z)$ is obtained. The electron beam radius r_{beam} needed in the calculation of the space charge potential and the electron density (equations (4.35) and (4.36)) is derived in section 4.4. It is constant over the whole overlap region. Figure 4.3 shows the interaction zone potential $U_{\mathrm{int}}(z)$ and the corresponding electron density $n_{\mathrm{e}}(z)$ for three different detuning energies in the Xe^{3+} beamtime. It is clearly visible that a higher U_{int} leads to a lower n_{e}. The average electron density $\bar{n}_{\mathrm{e}}$ that is required for the calculation of the MBRC is then derived from $n_{\mathrm{e}}(z)$ by averaging over the full overlap length l_{e}. The average densities $\bar{n}_{\mathrm{e}}$ are marked as vertical lines for the three detuning energies in figure 4.3b. In particular, depending on the conditions, $\bar{n}_{\mathrm{e}}$ can be higher or lower than the electron density in the center of the drift tube $n_{\mathrm{e}}(z=0)$, which enters the calculation of the detuning energy.

The experimental uncertainty of the electron density amounts to $\Delta n_{\mathrm{e}}(z)/n_{\mathrm{e}}(z) = \Delta\bar{n}_{\mathrm{e}}/\bar{n}_{\mathrm{e}} = 12\,\%$, as derived in section 4.4.

For the sake of simplicity, the average electron density $\bar{n}_{\mathrm{e}}$ will be denoted as n_{e} in the following,

$$n_{\mathrm{e}} \equiv \bar{n}_{\mathrm{e}}, \tag{4.39}$$

and simply referred to as 'electron density'.

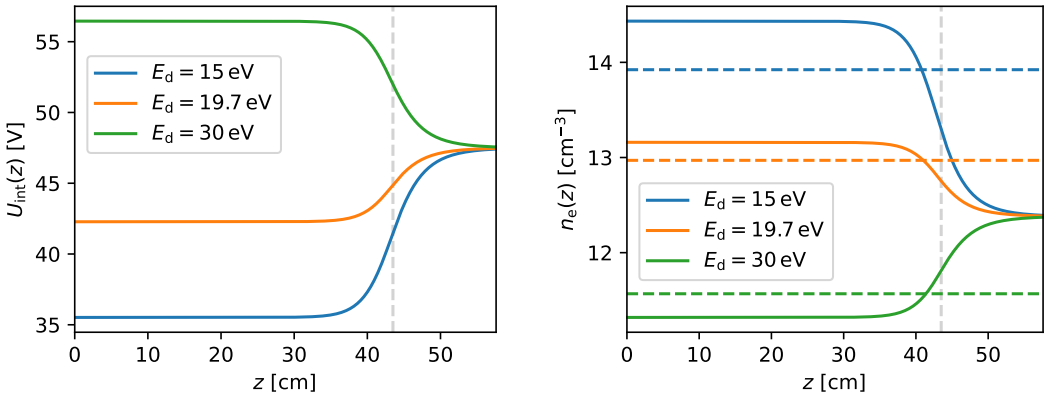

(a) (b)

Figure 4.3: (a) Interaction zone potential $U_{\mathrm{int}}(z)$ as a function of longitudinal position z along the electron-ion overlap length. $z = 0$ marks the center of the drift tube, and only one half of the electron-ion interaction length ($l_e/2 = 57.6\,\mathrm{cm}$) is shown. The dashed vertical line marks the end of the drift tubes (half-length $l_{\mathrm{dt}}/2 = 43.5\,\mathrm{cm}$). The three curves show $U_{\mathrm{int}}(z)$ for three different detuning energies in the Xe^{3+} beamtime at $E_d = 15\,\mathrm{eV}$, $19.7\,\mathrm{eV}$ (at the main DR resonance peak) and $30\,\mathrm{eV}$. The cathode voltage was fixed at $U_{\mathrm{cath}} = -50\,\mathrm{V}$, the drift tube voltage was varied to obtain the different E_d. (b) Electron densities $n_e(z)$ in the center of the electron beam at a total current of $I_e = 120\,\mu\mathrm{A}$. The three solid curves correspond to the potentials shown in (a). The dashed horizontal lines indicate the average electron densities $\bar{n}_e$ over the full overlap length.

4.3.2 Experimental collision energy distribution

The center-of-mass collision energy E in the collision of an electron and an ion is defined by the relative velocity v between the two particles, and the reduced mass μ (which is approximately the electron mass, $\mu \approx m_e$), i.e.

$$E = \frac{1}{2}\,\mu\,v^2. \tag{4.40}$$

In the merged-beams experiments with colliding electron and ion beams, however, both beams have velocity distributions, resulting in a distribution of electron-ion collision energies denoted by $f_{\mathrm{mb}}(E)$ in equation (4.22) on page 31. $f_{\mathrm{mb}}(E)$ is determined on the one side by the thermal velocity spreads in the colliding beams and on the other side by the geometry of the merged-beams setup, which comprises, e.g., the variation of the interaction zone potential U_{int} along the overlap length and the inclination of the beams in the (de-)merging region. As the mass of the electrons is much lower than the mass of the ions, the velocity distribution of the electrons is the main contributor to the electron-ion collision energy spread, despite the fact that the electron beam is colder than the ion beam. As the collision energy distribution $f_{\mathrm{mb}}(E)$ depends on the experimental conditions, also the MBRC α_{mb} from equation (4.22) is experiment-specific.

In the electron-ion merged-beams setup at CSR, the collision energy distribution $f_{\mathrm{mb}}(E)$ is characterized by the chosen detuning energy E_{d} as defined in equation (4.38), by the transverse and longitudinal electron beam temperatures $T_{\perp}$ and $T_{\parallel}$, respectively, by the interaction zone potential $U_{\mathrm{int}}(z)$, by the electron beam space charge U_{sc} and by geometric effects from merging and demerging (accounted for by χ), $f_{\mathrm{mb}}(E) = f_{\mathrm{mb}}(E; E_{\mathrm{d}}, T_{\parallel}, T_{\perp}, U_{\mathrm{int}}, U_{\mathrm{sc}}, \chi)$.

In figure 4.4, two model collision energy distributions are shown for two different detuning energies and for the conditions as in the Xe^{3+} beamtime. The distributions were derived from a Monte-Carlo simulation by Oldřich Novotný. In the two distributions, $k_{\mathrm{B}}T_{\perp} = 2\,\mathrm{meV}$ was assumed for the transverse temperature of the electron beam, and the longitudinal temperature $k_{\mathrm{B}}T_{\parallel}$ varied with electron energy. Effects arising from merging and de-merging and the varying interaction zone potential $U_{\mathrm{int}}(z)$ caused by the drift tubes are taken into account, and the model assumes the space charge at the minimum of the electron beam space charge profile as calculated in equation (4.35). The distributions show two distinct peaks that correspond to the electron-ion collision energies inside and outside of the drift tubes and are directly connected to the interaction zone potential $U_{\mathrm{int}}(z)$ as shown in figures 4.2 and 4.3a. The peaks are broadened due to the longitudinal and transverse temperatures of the electron beam, $T_{\parallel}$ and $T_{\perp}$, respectively. Further details as well as a thorough evaluation of the electron beam temperatures can be found in [116].

For the detuning energies where the observed electron-induced signal was strongest in the Ne^{2+} and Xe^{3+} beamtimes, the full-width at half maximum (FWHM) of the peak corresponding to the respective detuning energy was derived from the simulated collision energy distributions. Assuming reasonable estimates for the electron beam temperatures of $k_{\mathrm{B}}T_{\perp} = 3\,\mathrm{meV}$ and $k_{\mathrm{B}}T_{\parallel} = 0.2\,\mathrm{meV}$ in the simulation of the collision energy distributions, the FWHM energy widths amount to

$$\Delta E_{\mathrm{FWHM,Ne^{2+}}}(E_{\mathrm{d}} = 25.3\,\mathrm{eV}) = 0.25\,\mathrm{eV}, \tag{4.41}$$

$$\Delta E_{\mathrm{FWHM,Xe^{3+}}}(E_{\mathrm{d}} = 19.7\,\mathrm{eV}) = 0.23\,\mathrm{eV}. \tag{4.42}$$

Knowledge of the collision energy distribution $f_{\mathrm{mb}}(E)$ is required for two purposes. Firstly, theoretical cross sections can be convolved with $f_{\mathrm{mb}}(E)$ according to equation (4.22) to obtain theoretical MBRCs. Subsequently, the theoretical MBRCs can be compared with the experimental MBRC. This is how the comparison with theoretical calculations was done in chapters 5 and 6.

Secondly, the underlying cross section $\sigma(E)$ can be numerically deconvolved from the experimental MBRC and thereafter convolved with a different collision energy distribution. For the use in plasma modeling, the so-called 'plasma rate coefficient' can be obtained from the convolution with a Maxwell-Boltzmann distribution, representing

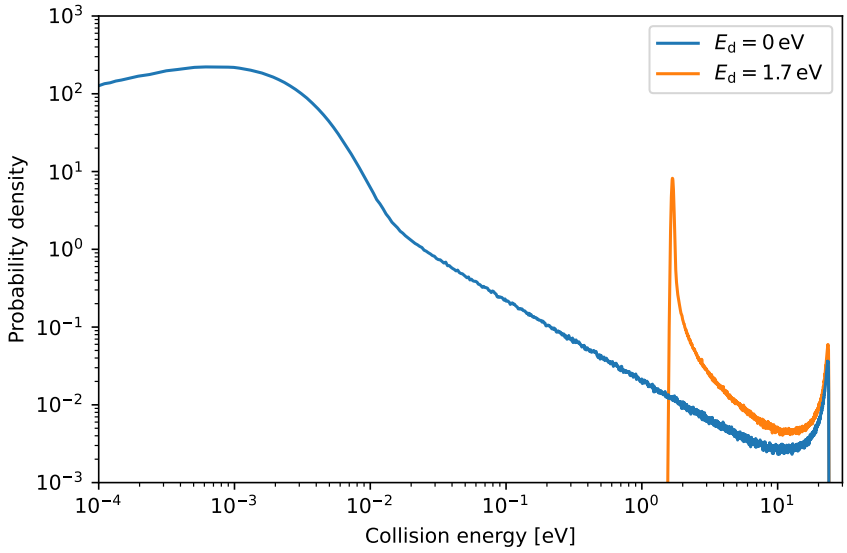

Figure 4.4: Simulated collision energy distributions f_{mb} for detuning energies of $E_{\mathrm{d}} = 0\,\mathrm{eV}$ (blue) and $E_{\mathrm{d}} = 1.7\,\mathrm{eV}$ (orange), respectively, under conditions as present in the Xe^{3+} beamtime. The dominant low-energy peaks correspond to the collision energies inside the drift tubes which are close to the set detuning energies, $E \approx E_{\mathrm{d}} = 0\,\mathrm{eV}$ and 1.7 eV, and the high-energy peaks at a collision energy of $E_{\mathrm{out,d}} \approx 23.6\,\mathrm{eV}$ are caused by the electrons outside of the drift tubes. The distributions were obtained from a Monte-Carlo simulation by Oldřich Novotný.

the collision energy distribution in a plasma. The plasma rate coefficient

$$\alpha_{\mathrm{pl}}(T_{\mathrm{pl}}) = \int_0^\infty \sigma(E)\, v \sqrt{\frac{4E}{\pi}} \left(\frac{1}{k_{\mathrm{B}} T_{\mathrm{pl}}}\right)^{3/2} \exp\left(-\frac{E}{k_{\mathrm{B}} T_{\mathrm{pl}}}\right) \mathrm{d}E \tag{4.43}$$

then allows to calculate the recombination rate at a given plasma temperature T_{pl}. In this thesis, due to uncertainties in the measured MBRCs, no plasma rate coefficients were derived.

4.4 Electron beam profiles and electron beam radius

The calculation of electron densities from equation (4.36) requires the radius of the electron beam in the interaction region r_{beam}. According to equation (3.1) on page 21, the radius r_1 of the electron beam at a given position 1 is linked to the electron beam radius r_2 at another position 2 by the expansion factor $\alpha_{12} = B_1/B_2$ denoting the ratio of the magnetic fields at the respective positions,

$$r_2 = \sqrt{\alpha_{12}}\, r_1. \tag{4.44}$$

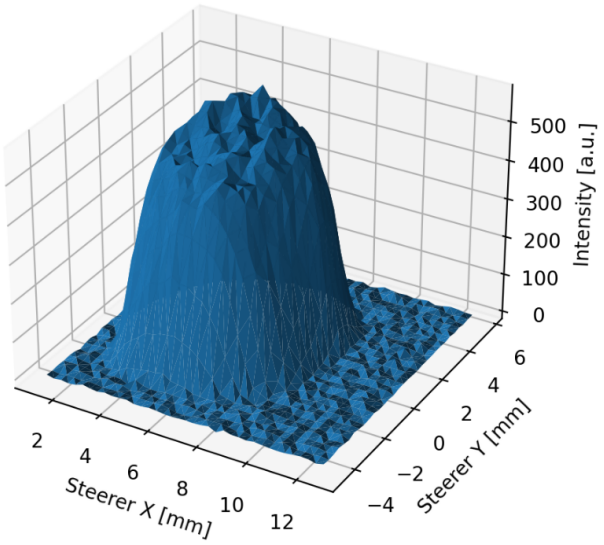

Figure 4.5: Electron beam profile for a total electron current of $I_e = 47\,\mu A$, measured during the Ne^{2+} beamtime. $X-$ and $Y-$coordinates give the beam size at the collector cup. The expansion factor at the cup with respect to the cathode is 6.88.

Consequently, the electron beam radius r_{beam} in the interaction region can be calculated from the effective radius of the photocathode r_{cath},

$$r_{beam} = \sqrt{\alpha}\, r_{cath}, \tag{4.45}$$

with the expansion factor $\alpha = B_{cath}/B_{int}$. During the beamtimes, $\alpha = 30$ was used, and especially the expansion factor α is constant over the full overlap length. The cathode radius r_{cath} is the only radius which does not change with the magnetic field, as it is the radius at the position where the electron beam is produced. r_{cath} can be inferred from the transverse position-dependent current distribution of the electron beam, referred to as 'electron beam profile', which can be recorded at the collector cup at the electron cooler.

For the purpose of measuring such electron beam profiles, the collector cup is equipped with a small pinhole opening of 0.8 mm diameter. A second Faraday cup, the so-called analyzer cup, allows to measure the current that is transmitted through the pinhole. By moving the electron beam across the pinhole with the help of the magnetic steerers in the room-temperature section before the collector, different parts of the electron beam can pass through the pinhole and the electron current distribution can be recorded. The procedure as well as the calibration factors needed to convert the applied steerer current to a position shift of the electron beam are reported in the work of Wilhelm [110]. An example for the profile of an electron beam with a current of $I_e = 47\,\mu A$ is shown in figure 4.5. As the pinhole diameter is small in comparison to the electron beam size, the displayed profile represents the actual electron beam shape fairly well.

The shape of the electron beam profile is influenced by the circular surface of the

photocathode and the potentials on the electrodes close to the cathode surface [116]. Due to imperfections in these potentials and in the surface properties of the cathode, the electron beam profile is not completely cylindrical. As it is visible in figure 4.5, the profile is not entirely flat on the top and drops smoothly on the edges. It has been observed that the profiles become flatter with increased electron current. For computational reasons, the shape of the profile is approximated here by a cylinder. Therefore, the height of the (almost) flat top of the profile is averaged and a cylinder of the same length is modeled with a radius r_{cup}, such that the total currents integrated over the profile and the cylinder are identical (this is explained in detail in [110]). With the known magnetic fields at the collector cup and at the cathode (resulting in an expansion factor of 6.88), the radius r_{cup} can then be translated to the effective cathode radius r_{cath} following equation (4.44).

To some extent, the effective cathode radius r_{cath} depends on the extracted electron current and can vary slightly when the cathode is operated for extended periods. Additionally, the electron beam profile depends on the cathode surface, and thus different photocathodes or activations exhibit slightly different radii for the same electron current. During the two beamtimes presented in this thesis, several electron beam profiles have been taken for different currents and cathodes. The derived effective cathode radii ranged from $r_{\mathrm{cath}} = 1.08\,\mathrm{mm}$ for $I_{\mathrm{e}} = 8.5\,\mu\mathrm{A}$ to 1.27 mm for 161 µA. However, electron beam profiles have not been measured for all currents used in the DR experiments.

In the Ne^{2+} beamtime, electron currents of $I_{\mathrm{e}} = 47\,\mu\mathrm{A}$, 130 µA, 190 µA and 246 µA were applied. Several profiles for currents between 46 µA and 192 µA were taken, but not necessarily for the same cathode as used in the DR experiment. Based upon these measurements, the effective cathode radii for the given electron currents thus were estimated to $r_{\mathrm{cath}} = 1.20\,\mathrm{mm}$, 1.24 mm, 1.26 mm and 1.29 mm.

The electron currents used in the Xe^{2+} beamtime ranged from $I_{\mathrm{e}} = 8.5\,\mu\mathrm{A}$ to 180 µA. Electron beam profiles have been recorded for the same cathode as used in the DR experiment at currents of 8.5 µA, 50 µA, 86 µA and 161 µA, yielding cathode radii of $r_{\mathrm{cath}} = 1.08\,\mathrm{mm}$, 1.23 mm, 1.26 mm and 1.27 mm. To estimate the radii for the currents where no profile was measured, the four measured cathode radii were fitted with good agreement by an exponential function, and the according r_{cath} were extracted from the fit. The fit function was

$$r_{\mathrm{cath}}(I_{\mathrm{e}}) = a - b\,\exp(-c\,I_{\mathrm{e}}) \tag{4.46}$$

with $a = 1.268\,248\,53\,\mathrm{mm}$, $b = 0.264\,060\,15\,\mathrm{mm}$ and $c = 0.039\,237\,54\,\mu\mathrm{A}^{-1}$. Figure 4.6 shows the cathode radii derived from the profile measurements, as well as the fit. Additionally, in the figure also the resulting electron beam radii in the interaction region r_{beam} are given (as calculated from equation (4.45) with $\alpha = 30$), that are needed for the calculation of electron densities.

The uncertainty in the effective cathode radius is the main contributor to the uncertainty in the electron density (see equation (4.36) and section 4.3.1). In the work of Paul [116], $\Delta r_{\mathrm{cath}} = 0.05\,\mathrm{mm}$ was found from a comparison of electron beam profiles measured at the collector cup and at a second, similar cup at the gun side. This abso-

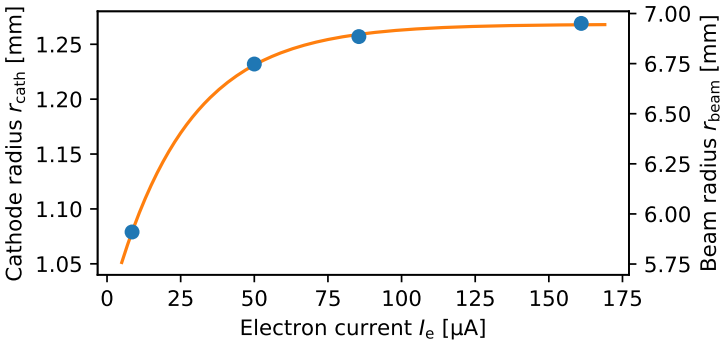

Figure 4.6: The blue circles indicate the effective cathode radii r_{cath} as derived from electron beam profile measurements during the Xe^{3+} beamtime for four different electron currents of $I_{\mathrm{e}} = 8.5\,\mu\mathrm{A}$, $50\,\mu\mathrm{A}$, $86\,\mu\mathrm{A}$ and $161\,\mu\mathrm{A}$. The orange line represents the fit according to equation (4.46), which was used to estimate the cathode radius at other electron currents. The axis on the right specifies the resulting electron beam radius in the interaction region r_{beam} (expansion factor $\alpha = 30$).

lute uncertainty would correspond to relative uncertainty between 3.8 % and 4.6 % on r_{cath} for the different electron currents used throughout the beamtimes. To account for the additional uncertainty due to the estimation of the cathode radius without having measured profiles for all of the electron currents, the uncertainty of the cathode radius is generously estimated as $\Delta r_{\mathrm{cath}}/r_{\mathrm{cath}} = 8\,\%$ for all cathode radii used in the analysis of both beamtimes presented in this thesis. As the uncertainty in the measured electron current is small, the uncertainty of the electron density n_{e} from equation (4.36), following error propagation, can subsequently be approximated as

$$\frac{\Delta n_{\mathrm{e}}}{n_{\mathrm{e}}} \approx \sqrt{2\left(\frac{\Delta r_{\mathrm{cath}}}{r_{\mathrm{cath}}}\right)^2} = 11.3\,\% \approx 12\,\%. \tag{4.47}$$

This uncertainty enters the total uncertainty of the absolute MBRC, as shown in section 4.9.

4.5 Measurement layout

In the experiments, ions were injected into CSR, stored, and collisions with electrons were probed. After storing the ions for a fixed amount of time, the stored ions were dumped and fresh ions were injected. Here, the whole cycle from ion injection until they are dumped and the next ions are injected is referred to as one ‘injection cycle’. Each injection cycle was subdivided into three phases, so-called ‘schemes’: pre-cooling scheme, measurement scheme, and off scheme. The layout of the whole injection cycle

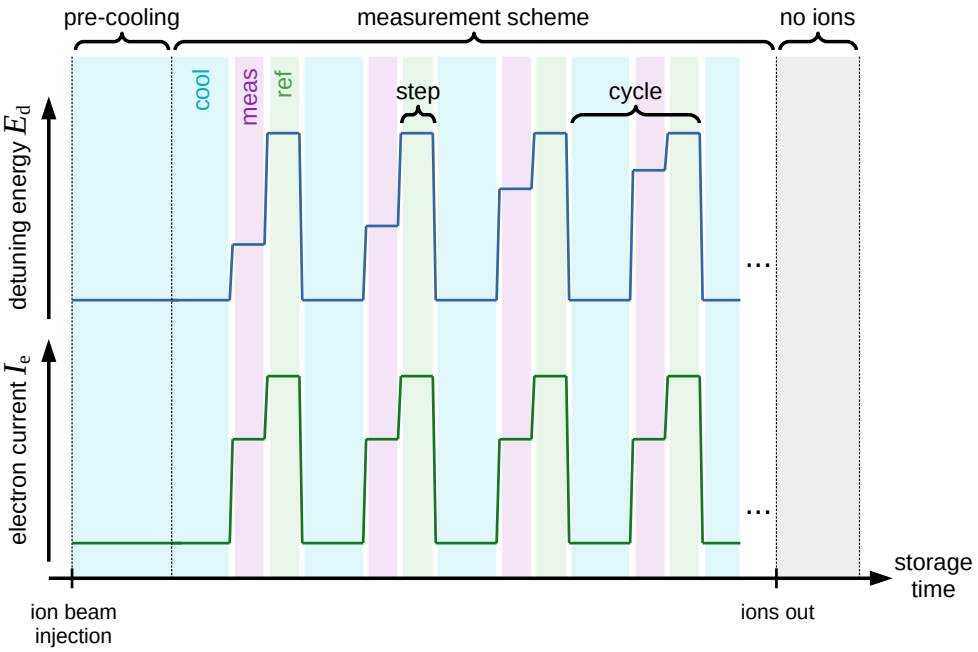

Figure 4.7: Sketch of the injection cycle layout in the Xe^{3+} beamtime. Each injection cycle was split into three phases, called 'schemes': pre-cooling, measurement and off scheme (without ions). The measurement scheme was separated into multiple 'cycles' consisting of several 'steps'. In this case, one cycle consisted of a cooling step, a measurement step at a variable detuning energy in the drift tubes, and a reference step. An individual electron current was applied in each step type. The steps were separated by short waiting periods during which the voltages were adjusted, guaranteeing a stable electron current and energy in each step. The storage time axis in the figure is not to scale. The injection cycle setup in the Ne^{2+} beamtime was similar, but all reference steps were omitted.

(for the setup as in the Xe^{3+} beamtime) is displayed in figure 4.7.

Electron cooling was applied permanently during the pre-cooling scheme. Within this phase, the phase-space of the stored ion beams was reduced to achieve a good beam overlap, as explained in section 4.2. During the measurements with Ne^{2+}, the pre-cooling scheme had a duration of 5 s, and the duration in the Xe^{3+} beamtime ranged between 10 s and 21 s. The pre-cooling times were chosen as a trade-off between reasonably defined conditions concerning beam overlap and ion momentum spread, and the duty cycle for the measurement scheme in order to accelerate the accumulation of statistics.

In the measurement scheme, multiple detuning energies were sampled. This phase was segmented into 'cycles'. Each cycle in the Ne^{2+} beamtime incorporated subsequent 'steps' at cooling energy (cooling step) and a non-zero detuning energy (measurement step). In the Xe^{3+} beamtime, each cycle consisted of a cooling step, a measurement step,

Table 4.1: Overview of the injection cycle timing in the Ne^{2+} and Xe^{3+} beamtimes. The durations of the individual phases (or schemes) t_{sch} and of the different steps t_{st} are given, as well as the detuning energies E_d sampled in the respective step.

Ion	Scheme	t_{sch} [s]	Step	t_{st} [ms]	E_d [eV]
Ne^{2+}	pre-cooling	5	cool		0
	measurement	18 - 51	cool	50	0
			meas	40	0 - 33
	off	2	no ions		
Xe^{3+}	pre-cooling	10 - 21	cool		0
	measurement	18 - 37	cool	100	0
			meas	25	0 - 61.6
			ref	25	24
	off	2	no ions		

and a reference step. These cycles were repeated over the measurement scheme, and the fast alternation between multiple steps at different detuning energies is referred to as 'wobbling'. The measurement detuning energy was varied in subsequent cycles by varying the potential on the drift tubes, thus allowing to scan a given detuning energy range within one injection cycle. The cooling steps ensured good ion beam conditions throughout the measurement scheme, preventing a blow-up of the beam due to intra-beam scattering. For the reference step, a fixed detuning energy was chosen where hardly any electron-induced recombination signal was detected. The reference detuning energy in the Xe^{3+} beamtime was $\sim 24\,\mathrm{eV}$. While the reference step simplifies the background subtraction in the data analysis process, it was omitted in the Ne^{2+} beamtime to gather statistics as fast as possible because the background count rate was high. To increase the electron-induced signal in the measurement and reference steps, the electron current was boosted for these steps by increasing the potential on the extraction electrode. The electron currents applied in the Ne^{2+} beamtime ranged from 47 µA to 246 µA, and in the Xe^{3+} beamtime from 8.5 µA to 180 µA. More details on the electron currents used in different detuning energy ranges can be found in chapters 5 and 6. To ensure stable voltages at the extraction and drift tube electrodes, a 5 ms waiting period was implemented in between the consecutive steps. The lengths of the individual steps were chosen as 50 ms cooling and 40 ms measurement in the Ne^{2+} beamtime, and 100 ms cooling, 25 ms measurement and 25 ms reference in the Xe^{3+} beamtime.

For the off scheme, the ion beam was kicked out of CSR and the dark count rate of the COMPACT detector was measured for roughly 2 s. The detailed timing is noted in table 4.1.

Within the measurement scheme, a chosen number of detuning energies was scanned

multiple times. The ion beam intensity decayed significantly over the time needed for one energy scan, resulting in higher statistics accumulated at energies at the beginning of the energy scan. Therefore, sets of two injection cycles were defined, where the detuning energies were scanned from low to high in the first injection cycle and from high to low in the second. Thereby, a more evenly distributed count rate was ensured across all of the detuning energies, reducing the scatter in the statistical uncertainties. An example for the recorded count rates can be found in figure 4.8 on page 49.

The maximum detuning energy was limited to 33 eV in the Ne^{2+} beamtime and 61.6 eV in the Xe^{3+} beamtime by the maximum drift tube voltage of $U_{\mathrm{drift}} = 100\,\mathrm{V}$. The accessible detuning energy range was split into several subranges (see tables 5.1 and 6.1 on page 72 and on page 96) that were probed in separate measurements, called 'runs'. A run consisted of multiple subsequent injection cycles scanning the same energy range. Within a run, the parameters of the measurement scheme were fixed besides non-avoidable fluctuations in the ion current and in the residual-gas density in the ring.

4.6 Data acquisition

As explained in section 4.5, the measurement consisted of various steps at different detuning energies. Most of the data acquisition worked on the level of steps, and for each step, a separate record was made in the the stored data structure.

In each individual step, the number of counts on COMPACT was recorded. Therefore, the electronic signal from the MCP was decoupled from the high voltage by a capacitor, amplified by a fast amplifier and subsequently fed to a discriminator [71]. Within the discriminator, a discrimination threshold was set and the amplified pulses were converted to a digital signal. The number of digital pulses in each individual step (excluding the 5 ms waiting step) was read out by a PC-attached FPGA card. Additionally, the precise durations of the individual steps were measured and stored, which allowed for the calculation of count rates. The control voltage sent to the power supply attached to the drift tubes was recorded as well as the actual voltage on the drift tube, which was measured with sub-step time resolution. Previous tests have shown that the actual drift tube voltage is proportional to the control voltage and can be reliably and precisely inferred from it. Therefore, and for the sake of simplicity and a noise-free signal, the control voltage was used in the analysis to derive the drift tube voltage.

Furthermore, the electron current was measured in each step with sub-step time resolution. The electron current was set by the voltage on the extraction electrode, and previous tests have demonstrated that the same electron currents were obtained when repeatedly setting the same extraction voltages. As the cathode degradation was not significant within one run, the electron currents were measured for the relevant extraction voltages before the runs, and used in the analysis instead of the currents

measured in the individual steps.

4.7 Count rates and relative rate coefficients

As derived in section 4.1.2, especially equation (4.27) on page 32, the MBRC is linked to the measured count rate, the electron density and the ion number in the ring. The evaluation of the ion number is challenging, and especially the ion number evolution with storage time can hardly be measured directly. Therefore, the ion number was not measured in each run and instead, a proxy signal proportional to the ion number was used to derive *relative* rate coefficients. These relative rate coefficients were later absolutely scaled via dedicated measurements where the ion number was recorded, as is explained in section 4.9. In this section, the procedure to extract relative rate coefficients from the measured count rates is presented.

In each step during a measurement run, the number of pulses C on COMPACT was counted and the integration time t spent in the respective step was measured. By summing up counts and integration times over several steps of the same type (i.e. cooling, measurement, or reference steps), average count rates

$$R = \frac{\sum C}{\sum t} \tag{4.48}$$

could be calculated. Therefore, counts and integration times from multiple injection cycles were combined. In principle, count rates can be evaluated for the whole run (including all storage times) or in specific storage time windows.

Count rates measured at the electron-ion merged-beams setup at CSR consist of contributions from different processes. The overall rate R comprises an electron induced rate R_e, a rate R_rg induced by collisions of the stored ions with residual-gas particles, and a detector-specific dark count rate R_dark, i.e.

$$R = R_\mathrm{e} + R_\mathrm{rg} + R_\mathrm{dark}. \tag{4.49}$$

As an example, the measured count rates from one run in the Xe^{3+} beamtime are displayed in figure 4.8. The blue points show the count rates measured in the measurement steps, the orange area marks the count rates measured in the reference steps that were chosen at a detuning energy where the electron-induced rate R_e was basically 0. Most of the signal, also in the measurement steps, is coming from R_rg, and only the blue area is the electron-induced count rate R_e.

R_dark, which depends on the discriminator settings, was inferred from the off scheme when the ion beam was kicked out of CSR at the end of each injection. In the measurements presented in this thesis, $R_\mathrm{dark} \approx 0.3\,\mathrm{s}^{-1}$ was found, in agreement with previous findings [119]. Compared to the total count rates of $\sim 10^4\,\mathrm{s}^{-1}$, the dark count rate is negligibly small.

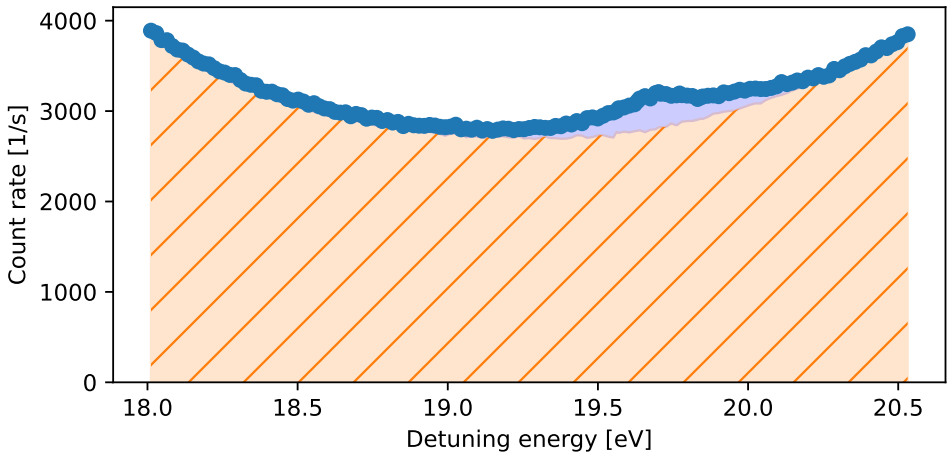

Figure 4.8: Measured average count rates in one run from the Xe^{3+} beamtime, scanning detuning energies between 18 eV and 20.5 eV. The bulk of the signal, indicated by the hatched orange area, is background signal produced by electron-capture collisions with residual-gas particles. Only the blue area corresponds to actual electron-induced signal. The bent shape of the count rate over the energy range reflects the ion beam lifetime and the fact that subsequent injection cycles were scanning in opposite directions, starting either from the lowest or the highest detuning energy, as explained in section 4.5. In the Ne^{2+} beamtime, due to the smaller recombination rate coefficient, the electron-induced signal was even weaker compared to the background signal.

The ion-induced rates R_e and R_rg are linked to merged-beams rate coefficients α for the underlying processes,

$$R_\mathrm{k} = \alpha_\mathrm{k} \cdot \eta_\mathrm{k} \cdot n_\mathrm{k} \cdot N_\mathrm{i} \cdot \frac{l_\mathrm{k}}{L_\mathrm{CSR}}, \tag{4.50}$$

with $k \in \{\mathrm{e}, \mathrm{rg}\}$ for electron- and residual-gas-induced signals, respectively. Assuming an effective rate coefficient α_rg which reflects the residual-gas composition (in CSR this is mainly hydrogen and helium), and assuming that the residual-gas composition in CSR does not change, the rate coefficient α_rg for electron-capture from residual gas is constant over the whole measurement as it is determined by the constant ion energy. The rate coefficient for recombination with free electrons α_e is the quantity to be extracted from the measured count rates. It depends on the detuning energy E_d, $\alpha_\mathrm{e} = \alpha_\mathrm{e}(E_\mathrm{d})$, as explained in section 4.1. η_e and η_rg denote the detection efficiencies of COMPACT for events involving electrons and residual-gas particles, respectively. n_e and n_rg denote the densities of electrons and residual-gas particles in the respective overlap regions. For the representation given above in equation (4.50), it has to be assumed that the ion beam is fully immersed in the electron beam and in the residual gas, respectively. N_i is the total ion number in the ring, L_CSR the nominal ion orbit in CSR of 35.12 m and l_e the full electron-ion overlap length. l_rg is defined by the length between the two

6°-deflectors in the straight section in which recombined products from collisions with residual gas are collected on COMPACT.

The measurement schemes in the recombination experiments included multiple steps at cooling energy, measurement energies, and reference energy, which in the following are indicated by the indices c, m, r for the respective steps. Combining equations (4.49) and (4.50) then gives the composition of the measured count rate in the step j = c, m, r:

$$R_\mathrm{j} = \alpha_\mathrm{e,j}\,\eta_\mathrm{e,j}\,n_\mathrm{e,j}\,N_\mathrm{i}\,\frac{l_\mathrm{e}}{L_\mathrm{CSR}} + \alpha_\mathrm{rg}\,\eta_\mathrm{rg,j}\,n_\mathrm{rg}\,N_\mathrm{i}\,\frac{l_\mathrm{rg}}{L_\mathrm{CSR}} + R_\mathrm{dark}. \tag{4.51}$$

The relevant information to be extracted from the measured rates is the energy-dependent electron-ion recombination rate coefficient $\alpha_\mathrm{e,m}$, which is possible with some considerations. The dark count rate R_dark is a property of the detector and thus remains the same for all steps. Also L_CSR, l_rg and l_e are constant, as well as α_rg as long as the residual-gas composition is not changed. The pressure in CSR is fluctuating only slowly on the timescale of several seconds, and subsequent steps follow fast after each other (each cycle is much shorter than a second). Thus it can be safely assumed that the residual-gas density n_rg does not change between the neighboring steps. The same argument holds for the ion number N_i, as the cycle duration is short in comparison to the beam lifetime. Due to different electron-ion detuning energies, the rate coefficient α_e is varying between the different steps. Consequently, $\alpha_\mathrm{e,m}(E_\mathrm{d})$ at a specific detuning energy E_d can be extracted from the (average) count rate in the measurement steps at E_d by subtraction of the dark count rate and subsequent normalization to the (average) dark-count-subtracted count rate in the cooling or reference steps from the same cycles. As cooling and reference steps are always at a fixed detuning energy, the respective count rates can serve as a proxy for the ion number.

The electron density n_e is influenced by the different electron velocities (and thus detuning energies) and electron currents used in different steps. In the experiments, hints of ion beam focusing effects due to the electron density in the interaction region have been observed, which affect the ion beam size and therefore (potentially) the geometric detection efficiencies. For this reason, the detection efficiencies for electron- and residual-gas-induced events $\eta_\mathrm{e/rg}$ depend on the chosen step. The focusing effects are discussed in sections 5.2.5 and 6.2.3.

In the following two subsections, the procedures how to derive relative rate coefficients from the Ne^{2+} and Xe^{3+} data are presented.

4.7.1 Relative rate coefficient determination for Ne^{2+}

In the Ne^{2+} beamtime, the whole collision-energy spectrum was split into several ranges in E_d with each covering a different energy range, as it is shown in table 5.1 on page 72. The measurement scheme consisted of alternating cooling and measurement steps. A reference step, which would have made data analysis more solid (see the procedure for Xe^{3+} in section 4.7.2 below), was not included due to the high background rate from residual gas and in order to increase the time spent in the measurement steps. The

extraction of the detuning-energy dependent rate coefficient for electron-induced signal is possible based on the rate ratio

$$\frac{R_\mathrm{m} - R_\mathrm{dark}}{R_\mathrm{c} - R_\mathrm{dark}}$$

with R_m and R_c being the count rates in measurement and cooling steps, respectively. Here, the cooling signal serves as a normalization. By employing equation (4.51) for the count rates in the measurement and cooling steps and reordering, electron-induced rate coefficients can be extracted as

$$\alpha_\mathrm{e,m} = \frac{A}{n_\mathrm{e,m}} \left[\left(\frac{R_\mathrm{m} - R_\mathrm{dark}}{R_\mathrm{c} - R_\mathrm{dark}} \right) - B \right], \tag{4.52}$$

with the scaling parameter

$$A = \frac{R_\mathrm{c} - R_\mathrm{dark}}{\eta_\mathrm{e,m}\, N_\mathrm{i}\, \frac{l_\mathrm{e}}{L_\mathrm{CSR}}} = \frac{R_\mathrm{e,c} + R_\mathrm{rg,c}}{\eta_\mathrm{e,m}\, N_\mathrm{i}\, \frac{l_\mathrm{e}}{L_\mathrm{CSR}}} = \frac{\alpha_\mathrm{e,c}\, n_\mathrm{e,c}\, \eta_\mathrm{e,c}\, l_\mathrm{e} + \alpha_\mathrm{rg}\, n_\mathrm{rg}\, \eta_\mathrm{rg,c}\, l_\mathrm{rg}}{\eta_\mathrm{e,m}\, l_\mathrm{e}} \tag{4.53}$$

and the offset parameter

$$B = \frac{R_\mathrm{rg,m}}{R_\mathrm{c} - R_\mathrm{dark}} = \frac{R_\mathrm{rg,m}}{R_\mathrm{e,c} + R_\mathrm{rg,c}} = \frac{\alpha_\mathrm{rg}\, n_\mathrm{rg}\, \eta_\mathrm{rg,m}\, l_\mathrm{rg}}{\alpha_\mathrm{e,c}\, n_\mathrm{e,c}\, \eta_\mathrm{e,c}\, l_\mathrm{e} + \alpha_\mathrm{rg}\, n_\mathrm{rg}\, \eta_\mathrm{rg,c}\, l_\mathrm{rg}}. \tag{4.54}$$

Both parameters A and B depend on the detection efficiencies η for electron- and residual-gas-induced events, respectively, in the cooling and measurement steps. As mentioned earlier, the detection efficiencies are potentially affected by the electron density in the specific step, which in the measurement steps is changing with the detuning energy, and therefore $\eta_\mathrm{e,m} = \eta_\mathrm{e,m}(E_\mathrm{d})$ and $\eta_\mathrm{rg,m} = \eta_\mathrm{rg,m}(E_\mathrm{d})$. Nevertheless, here the detection efficiencies are assumed constant, which makes both A and B constant for all detuning energies within one run (as long as the residual-gas density n_rg is not changing strongly on the timescale needed for one energy scan). However, the assumption of constant detection efficiencies and resulting constant A and B for all detuning energies is not necessarily valid, and especially a small variation in B can have a significant effect. This is discussed further in sections 5.2.5 and 6.2.3.

With the assumption of energy-independent detection efficiencies, the offset parameter B can be chosen such that the electron-induced rate coefficient from equation (4.52) is set to zero at detuning energies where no electron-induced events are expected. This procedure is described further in section 5.1.

The evaluation of the scaling parameter A is not directly possible, as the ion number N_i was not measured in the regular runs and most of the quantities in equation (4.53), especially the rate coefficients $\alpha_\mathrm{e,c}$ and α_rg, but also the residual-gas density n_rg, are not known precisely. Therefore, equation (4.52) cannot be evaluated. Instead, 'relative rate coefficients' were derived, which are normalized to the rate coefficient at a specific detuning energy and therefore don't require the evaluation of A.

From equation (4.52), unscaled rate coefficients $\alpha'_{\mathrm{e,m}}$ can be derived as

$$\alpha'_{\mathrm{e,m}} = \frac{\alpha_{\mathrm{e,m}}}{A} = \frac{1}{n_{\mathrm{e,m}}} \left[\left(\frac{R_{\mathrm{m}} - R_{\mathrm{dark}}}{R_{\mathrm{c}} - R_{\mathrm{dark}}} \right) - B \right]. \tag{4.55}$$

All of the runs included measurement steps at three detuning energies around $E_{\mathrm{d}} = 25.3\,\mathrm{eV}$, where the electron-induced signal was strongest (referred to as 'DR peak', compare the spectrum in figure 5.1 on page 74). The average of the unscaled rate coefficients at the three detuning energies around 25.3 eV is referred to as α'_{peak}. Assuming A as constant for all detuning energies, relative rate coefficients α_{rel} can be obtained by normalization of $\alpha'_{\mathrm{e,m}}$ to α'_{peak}, i.e.

$$\alpha_{\mathrm{rel}} = \frac{\alpha'_{\mathrm{e,m}}}{\alpha'_{\mathrm{peak}}} = \frac{\alpha_{\mathrm{e,m}}}{\alpha_{\mathrm{peak}}} = \frac{1}{n_{\mathrm{e,m}}\,\alpha'_{\mathrm{peak}}} \left[\left(\frac{R_{\mathrm{m}} - R_{\mathrm{dark}}}{R_{\mathrm{c}} - R_{\mathrm{dark}}} \right) - B \right]. \tag{4.56}$$

As measurement steps at the same three detuning energies entering α'_{peak} were included in all runs from all detuning energy ranges, data from all detuning energy ranges can be put on the same relative scale. These combined relative rate coefficients can subsequently be absolutely scaled by evaluation of the absolute rate coefficient for one detuning energy in a dedicated measurement where the ion number is recorded, which is described in section 4.9.

4.7.2 Relative rate coefficient determination for Xe^{3+}

In contrast to the recombination measurements with Ne^{2+}, the Xe^{3+} measurements included an additional wobbling step at a fixed reference energy. This allows to use an improved data analysis procedure with less assumptions, based on the rate ratio

$$\frac{R_{\mathrm{m}} - R_{\mathrm{dark}}}{R_{\mathrm{r}} - R_{\mathrm{dark}}}$$

with R_{m} and R_{r} the count rates in measurement and reference steps. By applying equation (4.51) to the count rates in the rate ratio above and reordering, the electron-induced rate coefficient in the measurement step can be extracted as

$$\alpha_{\mathrm{e,m}} = \frac{A}{n_{\mathrm{e,m}}} \left[\left(\frac{R_{\mathrm{m}} - R_{\mathrm{dark}}}{R_{\mathrm{r}} - R_{\mathrm{dark}}} \right) - B \right], \tag{4.57}$$

with the scaling parameter

$$A = \frac{R_{\mathrm{r}} - R_{\mathrm{dark}}}{\eta_{\mathrm{e,m}}\, N_{\mathrm{i}}\, \frac{l_{\mathrm{e}}}{L_{\mathrm{CSR}}}} = \frac{R_{\mathrm{e,r}} + R_{\mathrm{rg,r}}}{\eta_{\mathrm{e,m}}\, N_{\mathrm{i}}\, \frac{l_{\mathrm{e}}}{L_{\mathrm{CSR}}}} = \frac{\alpha_{\mathrm{e,r}}\, n_{\mathrm{e,r}}\, \eta_{\mathrm{e,r}}\, l_{\mathrm{e}} + \alpha_{\mathrm{rg}}\, n_{\mathrm{rg}}\, \eta_{\mathrm{rg,r}}\, l_{\mathrm{rg}}}{\eta_{\mathrm{e,m}}\, l_{\mathrm{e}}} \tag{4.58}$$

and the offset parameter

$$B = \frac{R_{\mathrm{rg,m}}}{R_{\mathrm{r}} - R_{\mathrm{dark}}} = \frac{R_{\mathrm{rg,m}}}{R_{\mathrm{e,r}} + R_{\mathrm{rg,r}}} = \frac{\alpha_{\mathrm{rg}}\, n_{\mathrm{rg}}\, \eta_{\mathrm{rg,m}}\, l_{\mathrm{rg}}}{\alpha_{\mathrm{e,r}}\, n_{\mathrm{e,r}}\, \eta_{\mathrm{e,r}}\, l_{\mathrm{e}} + \alpha_{\mathrm{rg}}\, n_{\mathrm{rg}}\, \eta_{\mathrm{rg,r}}\, l_{\mathrm{rg}}}. \tag{4.59}$$

On purpose, the reference step was chosen at a detuning energy of $E_\mathrm{d} \approx 24\,\mathrm{eV}$ where no DR signal was expected (or observed in the experiment). The calculated RR rate coefficient at this reference energy is on the order of $\sim 10^{-13}\,\mathrm{cm^3\,s^{-1}}$. As such a small signal could not be resolved in the experiment, it is safe to assume that $\alpha_\mathrm{e,r} \approx 0$. With this, the parameters A and B simplify to

$$A = \frac{\alpha_\mathrm{rg}\, n_\mathrm{rg}\, \eta_\mathrm{rg,r}\, l_\mathrm{rg}}{\eta_\mathrm{e,m}\, l_\mathrm{e}} \tag{4.60}$$

and

$$B = \frac{\eta_\mathrm{rg,m}}{\eta_\mathrm{rg,r}}. \tag{4.61}$$

Still, due to ion beam focusing by the electrons in the interaction region, the detection efficiencies η for electron- and residual-gas-induced events, respectively, in the reference and measurement step are potentially dependent on the chosen detuning energy. While the detuning energy in the reference step was fixed, it was varied in the measurement steps and therefore $\eta_\mathrm{e,m} = \eta_\mathrm{e,m}(E_\mathrm{d})$ and $\eta_\mathrm{rg,m} = \eta_\mathrm{rg,m}(E_\mathrm{d})$. Nonetheless, here the detection efficiencies $\eta_\mathrm{e,m}$ and $\eta_\mathrm{rg,m}$ are assumed constant for all detuning energies within one run, which makes A and B constants.

The accessible detuning energy range was split into multiple sub-ranges, which were measured in individual runs (see table 6.1 on page 96). For the largest part of the measurement runs, especially when scanning high detuning energies and when similar electron densities were used for reference and measurement steps, it can be assumed that the detection efficiencies $\eta_\mathrm{rg,m}$ and $\eta_\mathrm{rg,r}$ are similar, so $B = 1$. The validity of the assumption of constant A and B and $B = 1$ is discussed in section 6.2.3 on page 102.

The direct evaluation of the rate coefficient $\alpha_\mathrm{e,m}$ from equation (4.57) would require the precise value of the scaling parameter A. However, A cannot be directly calculated from equation (4.58) since the ion number N_i was not measured in the regular runs, and also the calculation of A from equation (4.60) is not feasible as the rate coefficient for electron-capture from residual gas α_rg, the residual-gas density n_rg, and the detection efficiencies η are not known precisely. Instead, relative rate coefficients were derived similar to the procedure in the Ne^{2+} beamtime described above in section 4.7.1.

First, following equation (4.57), unscaled rate coefficients

$$\alpha'_\mathrm{e,m} = \frac{\alpha_\mathrm{e,m}}{A} = \frac{1}{n_\mathrm{e,m}} \left[\left(\frac{R_\mathrm{m} - R_\mathrm{dark}}{R_\mathrm{r} - R_\mathrm{dark}} \right) - B \right] \tag{4.62}$$

were derived. Each run in the Xe^{3+} beamtime included five measurement energies around $E_\mathrm{d} = 19.7\,\mathrm{eV}$, where the electron-induced signal was strongest (referred to as 'DR peak', compare the spectrum in figure 6.1 on page 98). The average of the unscaled rate coefficients at these five detuning energies is referred to as α'_peak. Assuming A as constant for all detuning energies within one run (or energy range), relative rate

coefficients α_{rel} can be obtained by normalization of $\alpha'_{\mathrm{e,m}}$ to α'_{peak}, i.e.

$$\alpha_{\mathrm{rel}} = \frac{\alpha'_{\mathrm{e,m}}}{\alpha'_{\mathrm{peak}}} = \frac{\alpha_{\mathrm{e,m}}}{\alpha_{\mathrm{peak}}} = \frac{1}{n_{\mathrm{e,m}}\,\alpha'_{\mathrm{peak}}} \left[\left(\frac{R_{\mathrm{m}} - R_{\mathrm{dark}}}{R_{\mathrm{r}} - R_{\mathrm{dark}}} \right) - B \right]. \tag{4.63}$$

Since measurement steps at the same five detuning energies that contribute to α'_{peak} were included in all runs from all detuning energy ranges, data from all detuning energy ranges can be put on the same relative scale. These combined relative rate coefficients can subsequently be absolutely scaled by evaluation of the absolute rate coefficient for only a few detuning energies in a dedicated measurement where the ion number is recorded, which is described in section 4.9.

4.8 Detection efficiency of the COMPACT detector

To bring the relative rate coefficient on an absolute scale, information on the detection efficiency is essential. For the recombination measurements presented in this thesis, the COMPACT detector was used, which is described in section 3.3.1 on page 22. The detection efficiency of COMPACT, η, consists of the geometric detection efficiency η_{g} and the intrinsic detection efficiency η_{i}, i.e.

$$\eta = \eta_{\mathrm{g}} \cdot \eta_{\mathrm{i}}. \tag{4.64}$$

The geometric detection efficiency η_{g} accounts for the fraction of the recombined product particles that reach the converter plate of the COMPACT detector. The intrinsic counting efficiency η_{i} reflects the probability of a product particle hitting the converter plate to generate an electronic signal in the detector and to be counted.

η_{g} can be determined by a position scan where COMPACT is moved to several positions around the recombined product beam location. In this work, η_{i} was obtained from a comparison to the NICE detector, which is situated in neutral position in the corner behind the electron cooler and has a known detection efficiency. Therefore, neutrals were detected on NICE and COMPACT in alternation. The full procedures applied to obtain the detection efficiency of the COMPACT detector for Ne^{2+} and Xe^{3+} are described in detail in A. As a result, the total detection efficiencies

$$\eta_{\mathrm{Ne^{2+}}} = 0.74 \pm 0.25 \tag{4.65}$$

for Ne^{+} ions produced by recombination of Ne^{2+}, and

$$\eta_{\mathrm{Xe^{3+}}} = 0.75 \pm 0.19 \tag{4.66}$$

for Xe^{2+} ions produced by recombination of Xe^{3+}, were derived.

In the experiments performed in the course of this work, hints were found that a changing electron density in the electron-ion interaction region can lead to a changed focusing of the ion beam in the interaction region, subsequently to a differently focused product beam, and finally to a changed (geometric) detection efficiency. These hypothesized 'focusing effects' were observed in between different steps (e.g. cooling and measurement steps, or measurement steps at different detuning energies) with different electron densities and could be explained with a $\sim 1\,\%$-variation in the detection efficiencies of the respective steps. These effects are discussed further in sections 5.2.5 and 6.2.3.

4.9 Absolute scaling

In sections 4.7.1 and 4.7.2, the energy-dependent recombination rate coefficients $\alpha_{\mathrm{rel}}(E_{\mathrm{d}})$ were derived on a *relative* scale for the recombination of Ne^{2+} and Xe^{3+}, respectively. These relative rate coefficients can be put on an absolute scale by the scaling parameter A from equations (4.52) and (4.57). As A includes many factors like the rate coefficient for electron-capture from residual gas α_{rg} or the residual-gas density n_{rg}, which are insufficiently known, A cannot be derived directly. Instead, dedicated measurements were conducted in order to experimentally determine the absolute scale. For the calculation of absolute MBRCs, the measured count rates have to be correlated to the stored ion number. The procedure is explained in this section.

In the dedicated absolute scaling runs, the ion number N_{i} in the ring was measured at a chosen storage time simultaneously with the count rates. The ion number measurement is explained in section 4.9.1 below. The runs were set up similar to the regular DR measurement runs as described in section 4.5, and included schemes for pre-cooling, measurement, and dark count rate determination. Reference steps were included in the measurement schemes for both ions, Ne^{2+} and Xe^{3+}. The electron-induced rate coefficients therefore can be obtained similar to equation (4.57) by normalizing on the reference rate. To achieve reasonable statistics fast, only a few measurement energies around the DR series limits were included in the dedicated absolute scaling runs. Care was taken to apply the same electron current in the measurement and reference steps, as well as to choose the reference energies close to the measurement energies so that the electron density did not vary too much in between the steps.

From the individual runs, proportionality factors

$$S = \frac{R_{\mathrm{r}} - R_{\mathrm{dark}}}{N_{\mathrm{i}}} \tag{4.67}$$

were derived, correlating the count rate in the reference step R_{r} at the time of the ion number measurement to the measured ion number N_{i}. It should be noted that S

depends strongly on the residual-gas density in the storage ring and thus can be used only for scaling of the data obtained within the same run. With increasing residual-gas density, S would grow. Nevertheless, no indication was found for severe variation in the residual gas density during the individual absolute scaling runs, and consequently S is assumed independent of the storage time and constant within one run.

Usually it is beneficial to choose the reference at an energy where the electron-induced signal is negligibly small. This was the case in the Xe^{3+} absolute scaling runs. However, in the Ne^{2+} runs, the electron-induced signal at the reference energy was approximately 4 % of the signal at the DR peak, and this has to be accounted for in the absolute scaling. Based on S from equation (4.67) and the relative rates $(R_\mathrm{m} - R_\mathrm{r})/(R_\mathrm{r} - R_\mathrm{dark})$, and by application of equation (4.51) on page 50, the following equation can be written:

$$\frac{S}{n_{\mathrm{e,m}}\eta_{\mathrm{e,m}}\frac{l_\mathrm{e}}{L_\mathrm{CSR}}}\left(\frac{R_\mathrm{m}-R_\mathrm{r}}{R_\mathrm{r}-R_\mathrm{dark}}\right) = \alpha_{\mathrm{e,m}}\left(1-\frac{\alpha_{\mathrm{e,r}}}{\alpha_{\mathrm{e,m}}}\frac{n_{\mathrm{e,r}}}{n_{\mathrm{e,m}}}\frac{\eta_{\mathrm{e,r}}}{\eta_{\mathrm{e,m}}}\right) + \frac{\left(\eta_{\mathrm{rg,m}}-\eta_{\mathrm{rg,r}}\right)\alpha_\mathrm{rg}n_\mathrm{rg}l_\mathrm{rg}}{n_{\mathrm{e,m}}\eta_{\mathrm{e,m}}l_\mathrm{e}}. \tag{4.68}$$

Above equation yields an expression for the electron-induced rate coefficient at the measurement step, $\alpha_{\mathrm{e,m}}$, if the detection efficiencies η as well as the ratio $\tilde{\alpha} = \alpha_{\mathrm{e,r}}/\alpha_{\mathrm{e,m}}$ of electron-induced rate coefficients in measurement and reference steps are known,

$$\alpha_\mathrm{mb} = \alpha_{\mathrm{e,m}} = \frac{\dfrac{S}{n_{\mathrm{e,m}}\eta_{\mathrm{e,m}}\frac{l_\mathrm{e}}{L_\mathrm{CSR}}}\left(\dfrac{R_\mathrm{m}-R_\mathrm{r}}{R_\mathrm{r}-R_\mathrm{dark}}\right) - \left(\eta_{\mathrm{rg,m}}-\eta_{\mathrm{rg,r}}\right)\dfrac{\alpha_\mathrm{rg}n_\mathrm{rg}l_\mathrm{rg}}{n_{\mathrm{e,m}}\eta_{\mathrm{e,m}}l_\mathrm{e}}}{\left(1-\tilde{\alpha}\,\dfrac{n_{\mathrm{e,r}}}{n_{\mathrm{e,m}}}\dfrac{\eta_{\mathrm{e,r}}}{\eta_{\mathrm{e,m}}}\right)}. \tag{4.69}$$

As measurement and reference energies were chosen close-by and sampled with the same electron current, focusing effects on the stored ion beam due to varying electron densities are expected to be weak. Therefore, the detection efficiencies in measurement and reference steps are equal for residual-gas-induced events, $\eta_{\mathrm{rg,m}} \approx \eta_{\mathrm{rg,r}}$, as well as for electron-induced events, $\eta_{\mathrm{e,m}} \approx \eta_{\mathrm{e,r}}$. Accordingly, equation (4.69) simplifies to

$$\alpha_\mathrm{mb} = \frac{S}{\left(n_{\mathrm{e,m}} - \tilde{\alpha}\,n_{\mathrm{e,r}}\right)\eta_{\mathrm{e,m}}\frac{l_\mathrm{e}}{L_\mathrm{CSR}}}\left(\frac{R_\mathrm{m}-R_\mathrm{r}}{R_\mathrm{r}-R_\mathrm{dark}}\right). \tag{4.70}$$

In case the reference electron-induced signal is marginal as in the Xe^{3+} measurements, S represents purely the residual-gas-induced rate per ion, $\tilde{\alpha} = 0$ and

$$\alpha_\mathrm{mb} = \frac{S}{n_{\mathrm{e,m}}\eta_{\mathrm{e,m}}\frac{l_\mathrm{e}}{L_\mathrm{CSR}}}\left(\frac{R_\mathrm{m}-R_\mathrm{r}}{R_\mathrm{r}-R_\mathrm{dark}}\right). \tag{4.71}$$

Equations (4.70) and (4.71) were used to absolutely scale the electron-induced signal at the DR series limits of Ne^{2+} and Xe^{3+}, respectively, as it is described below in sections 4.9.2 and 4.9.3. Due to the observed ion beam focusing effects, the rate coefficient at the RR peak at $E_\mathrm{d} = 0\,\mathrm{eV}$ could not be reliably brought to the same relative

scale as the rate coefficients at higher detuning energies, and consequently could not be scaled by the absolute rate coefficient value at the DR series limit. Nonetheless, as the RR peak was sampled in the absolute scaling runs as well via the cooling step, it can be absolutely scaled separately. Therefore, the indices in equation (4.69) have to be converted, i.e. m → c. The cooling steps were sampled at considerably lower electron density than the reference steps, consequently the assumption $\eta_\mathrm{c} \approx \eta_\mathrm{r}$ is not necessarily valid and the term $(\eta_\mathrm{rg,c} - \eta_\mathrm{rg,r})\, \alpha_\mathrm{rg} n_\mathrm{rg} l_\mathrm{rg} / (n_\mathrm{e,c} \eta_\mathrm{e,c} l_\mathrm{e})$ in equation (4.69) does not cancel out. As the count rate in the reference steps R_r was almost exclusively produced by collisions of the stored ions with residual-gas particles, $R_\mathrm{r} \approx \alpha_\mathrm{rg}\, n_\mathrm{rg}\, \eta_\mathrm{rg,r}\, N_\mathrm{i}\, \frac{l_\mathrm{rg}}{L_\mathrm{CSR}}$ (only a few events per second out of a few $1000\,\mathrm{s}^{-1}$ were electron-induced or dark counts), the assumption

$$S = \frac{R_\mathrm{r} - R_\mathrm{dark}}{N_\mathrm{i}} \approx \alpha_\mathrm{rg}\, n_\mathrm{rg}\, \eta_\mathrm{rg,r}\, \frac{l_\mathrm{rg}}{L_\mathrm{CSR}} \tag{4.72}$$

can be made with S from equation (4.67). Subsequently, equation (4.69) can be converted into

$$\alpha_\mathrm{mb,c} = \frac{S}{\left(n_\mathrm{e,c} - n_\mathrm{e,r}\, \tilde{\alpha}_\mathrm{c}\, \tilde{\eta}_\mathrm{e}\right) \eta_\mathrm{e,c}\, \frac{l_\mathrm{e}}{L_\mathrm{CSR}}} \left[\left(\frac{R_\mathrm{c} - R_\mathrm{r}}{R_\mathrm{r} - R_\mathrm{dark}} \right) + 1 - \tilde{\eta}_\mathrm{rg}^{-1} \right], \tag{4.73}$$

where $\tilde{\alpha}_\mathrm{c} = \alpha_\mathrm{e,r}/\alpha_\mathrm{e,c}$, $\tilde{\eta}_\mathrm{e} = \eta_\mathrm{e,r}/\eta_\mathrm{e,c}$ and $\tilde{\eta}_\mathrm{rg} = \eta_\mathrm{rg,r}/\eta_\mathrm{rg,c}$. With some assumptions on the various detection efficiencies, equation (4.73) allows to derive the absolute MBRC in the cooling step at $E_\mathrm{d} \approx 0\,\mathrm{eV}$. In case the electron-induced signal in the reference step is negligible as in the Xe^{3+} beamtime, $\tilde{\alpha}_\mathrm{c} = 0$ and equation (4.73) simplifies to

$$\alpha_\mathrm{mb,c} = \frac{S}{n_\mathrm{e,c}\, \eta_\mathrm{e,c}\, \frac{l_\mathrm{e}}{L_\mathrm{CSR}}} \left[\left(\frac{R_\mathrm{c} - R_\mathrm{r}}{R_\mathrm{r} - R_\mathrm{dark}} \right) + 1 - \tilde{\eta}_\mathrm{rg}^{-1} \right]. \tag{4.74}$$

In the sections 4.9.2 and 4.9.3 below, equations (4.73) and (4.74) are used to absolutely scale the recombination signal at $E_\mathrm{d} = 0\,\mathrm{eV}$.

4.9.1 Ion number determination

For the calculation of absolute MBRCs, the stored ion number has to be correlated to an ion-induced count rate as described above. The ion number in the ring was identified with the help of the capacitative current pickup [104, 105].

The current pickup is capable of detecting the mirror charge induced by ion bunches flying through the pickup, thus requiring a bunched beam. The ion number N_i in CSR can be inferred from the integral of the induced voltage $U_\mathrm{p}(t)$ over one ion beam revolution period,

$$N_\mathrm{i} = \frac{P}{Z\, e\, T_0\, G} \int_0^{T_0} U_\mathrm{p}(t) \mathrm{d}t, \tag{4.75}$$

with the charge state Z of the stored ions, the elementary charge e, the ion beam revolution time T_0, the gain of the pickup amplifier G, and a proportionality factor P.

The revolution times in CSR were $T_0 \approx 14.6\,\mu s$ for the 600 keV-Ne^{2+} beam and $T_0 \approx 30.3\,\mu s$ for the 900 keV-Xe^{3+} beam. The pickup amplifier gain was $G = 2138$. In [105], the proportionality is given as

$$P = \frac{C_p\, L_{CSR}}{L_p}, \tag{4.76}$$

where C_p is the capacity and L_p the length of the current pickup, and L_{CSR} the length of the ion orbit in CSR. Since the calculation of P from these parameters has proven to be error-prone in the past, the current pickup was calibrated against a Faraday cup instead during this beamtime campaign. The calibration procedure is reported in [36]. In separate measurements several weeks apart, pulses of Kr^+, Ne^{2+}, and CH^+ beams were injected into CSR, and the voltage $U_p(t)$ induced in the current pickup was recorded during the first revolution and averaged over several injections. Subsequently, but in a separate measurement, the ion pulses were dumped on a Faraday cup in front of CSR, and the ion current within the pulses was measured. Here as well, multiple pulses were averaged. The ion beam intensity was stable between the measurements. Such calibration measurements were performed for different ion beam intensities, and a linear behavior between the Faraday cup current and the current pickup voltage was observed. All three beams (Kr^+, Ne^{2+}, CH^+) gave similar results. From the comparison of the current measured on the cup and the voltage induced in the current pickup, $P = 8.79 \times 10^{-11}\,F$ was found with an uncertainty of 10 %, mainly related to the stability of the ion sources [36].

For the actual ion number measurements used for absolute scaling in the Ne^{2+} and Xe^{3+} beamtimes, RF-bunched beams were used. To bunch the initially coasting ion beams, the voltage on the RF-bunching electrode was ramped up to its nominal value. The RF frequency, with which the applied voltage was alternated, was chosen as a higher (n-th) harmonic of the ion beam revolution frequency, resulting in n ion bunches in the storage ring. It was verified by the time structure of the particle hits on the COMPACT detector that the bunches were well-separated and basically no signal was produced between the bunches. Basically all ion were inside the bunches. Once the ion beam was bunched, the time-dependent voltage on the current pickup was recorded for a few thousand revolutions. Afterwards, the voltage on the bunching electrode was ramped down and the beam debunched.

The data from the current pickup were analyzed using an analysis code by Ábel Kálosi. As the induced voltage in the current pickup was weak, and to cancel out random noise fluctuations, the recorded signal $U_p(t)$ was averaged. For this, the data was cut into time slices of single revolutions and the average of all recorded revolutions was taken, yielding a much cleaner signal. An example for such an averaged waveform of a bunched Xe^{3+} beam is displayed in figure 4.9. The individual bunches show a clean shape and are well separated. The quality of the recorded induced voltage for bunched Ne^{2+} beams was similar.

As the current pickup is working capacitatively, the zero-baseline in the recorded signals is not directly identifiable. To derive the ‘full’ integral over the induced volt-

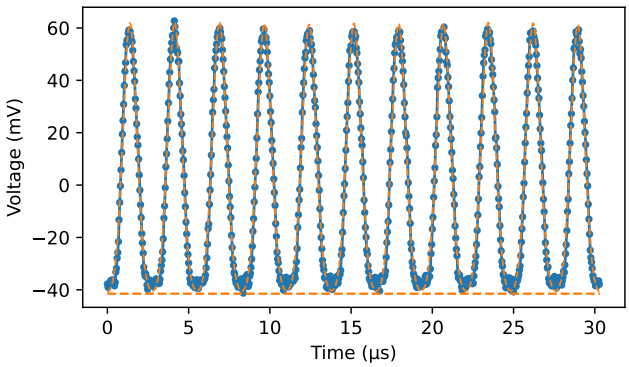

Figure 4.9: Voltage $U_\mathrm{p}(t)$ measured on the current pickup within one revolution period of a bunched Xe^{3+} beam, averaged over 100 ms (blue circles). The ion beam was RF-bunched with the eleventh harmonic of the ion revolution frequency, and the resulting eleven bunches are clearly visible and well separated. The orange dashed line represents a fit of Gaussians to the bunches, the horizontal line indicates the baseline derived from the Gaussian fit.

age nonetheless, the recorded data was evaluated in two ways. In the first approach, the baseline was adjusted to the lowest signal in between the bunches, and the integral over the bunches was calculated by the trapezoidal rule. In the second approach, Gaussian functions were fitted to the bunches. Here, the fitted baseline laid below the lowest measured signal, thus revealing an ion current that was potentially missed in the other approach. A Gaussian fit together with the derived baseline is displayed in figure 4.9 as well. The two models did not differ much. Ion numbers were evaluated from both models and averaged over all injection cycles in the respective run. Subsequently, the mean value of the run-averaged ion numbers from the two models was taken for the further analysis with an uncertainty of 5 %, which well covers the results of both methods. The overall uncertainty in the ion number measurements includes the uncertainties in the calibration procedure as well as in the model and sums up to 11.2 %.

It was observed that the ion beam lifetime was significantly reduced for bunched beams in comparison to coasting beams. Therefore, the ion number was not measured in all runs, but only in a few runs which were dedicated to derive the absolute scale. The regular DR measurements were conducted with a coasting ion beam. Within the runs foreseen for absolute scaling, the ion beam was pre-cooled first in coasting mode and rebunched only later in the measurement scheme for the duration of the ion number measurement.

4.9.2 Absolute scale for the Ne^{2+} recombination rate coefficient

In the Ne^{2+} beamtime, the absolute scaling runs were set up similar to the regular runs, containing a 5 s pre-cooling scheme. The measurement scheme included wobbling

Table 4.2: Ion numbers N_i and proportionality factors S (from equation (4.67)) for the dedicated absolute scaling runs in the Ne^{2+} beamtime. $t_\mathrm{i,meas}$ indicates the start of the ion number measurement, which had a duration of 0.4 s. $(R_\mathrm{m} - R_\mathrm{r}) / (R_\mathrm{r} - R_\mathrm{dark})$ and $(R_\mathrm{c} - R_\mathrm{r}) / (R_\mathrm{r} - R_\mathrm{dark})$ are calculated from the average count rates in the measurement schemes over the whole run with a statistical uncertainty of $\sim 4\,\%$ and $\sim 10\,\%$, respectively. Uncertainties for N_i and S are 11.2 % and 11.6 %, respectively.

Run	$t_\mathrm{i,meas}$ [s]	N_i [10^7 ions]	S [$\mathrm{s}^{-1}/10^5$ ions]	$\left(\frac{R_\mathrm{m}-R_\mathrm{r}}{R_\mathrm{r}-R_\mathrm{dark}}\right)$	$\left(\frac{R_\mathrm{c}-R_\mathrm{r}}{R_\mathrm{r}-R_\mathrm{dark}}\right)$
148	12.1	5.98	7.70	0.0508	0.0191
149	22.1	5.41	7.83	0.0472	0.0152
151	22.1	3.98	8.35	0.0501	0.0182
152	12.1	4.38	7.99	0.0492	0.0151

between cooling, measurement, and reference energies in the sequence cooling - measurement - cooling - reference. The step durations were 50 - 40 - 50 - 40 ms with 5 ms waiting steps in between. Electron currents were chosen as 47.5 µA for the cooling step and 190.5 µA for measurement and reference steps. In the measurement steps, only one single detuning energy at the main recombination feature (referred to as 'DR peak') was sampled at 25.28 eV. The reference was chosen at 26.55 eV beyond the DR peak. In four individual runs, the stored Ne^{2+} beam was re-bunched after 10 s and 20 s, respectively, and the ion numbers were measured 2.1 s later for a duration of 0.4 s. The total time in which bunching was applied was 3 s. The count rates at the reference energy were fitted by a linear function in a window of 2 s around the time of the ion number measurement, and the average reference rates during the ion number measurement period were extracted. Subsequently, scaling parameters $S = (R_\mathrm{r} - R_\mathrm{dark}) / N_\mathrm{i}$ could be obtained, which are shown in table 4.2. The relative uncertainty of each individual S is composed of the relative uncertainty in the ion number measurement of 11.2 % and the relative uncertainty in the fitted reference rate, which is approximated as 5 % in agreement with the statistical uncertainty at each individual reference step. The total uncertainty for S thus is 12.3 %. The count rates in the measurement, cooling and reference steps were averaged over the whole measurement scheme, allowing to calculate the average relative rates $(R_\mathrm{m} - R_\mathrm{r}) / (R_\mathrm{r} - R_\mathrm{dark})$ and $(R_\mathrm{c} - R_\mathrm{r}) / (R_\mathrm{r} - R_\mathrm{dark})$ which are given in table 4.2 as well.

4.9.2.1 Scaling of the DR peak

Following equation (4.70) on page 56, the product $\tilde{S} = S \times \left(\frac{R_\mathrm{m}-R_\mathrm{r}}{R_\mathrm{r}-R_\mathrm{dark}}\right)$ was evaluated for the four individual runs in table 4.2, and an average value of $\tilde{S} = 39.29\,\mathrm{s}^{-1}/10^7$ ions was obtained with an uncertainty margin of 15 % accounting for the uncertainties in S, the relative rates, as well as the scatter in $\tilde{S}$ from the different runs. It was found out only later in the analysis of the relative rate coefficient that the chosen reference energy

Table 4.3: Parameters used for the calculation of the absolute merged-beams rate coefficient α_{mb} at a collision energy of $E_{\mathrm{d}} = 25.28\,\mathrm{eV}$ in the Ne^{2+} beamtime.

Variable	Value	Relative uncertainty [%]
$\tilde{S}$	$39.29\,\mathrm{s}^{-1}/10^7$ ions	15
$n_{\mathrm{e,m}}$	$15.8 \times 10^5\,\mathrm{cm}^{-3}$	12
$n_{\mathrm{e,r}}$	$15.6 \times 10^5\,\mathrm{cm}^{-3}$	12
$\eta_{\mathrm{e,m}}$	0.74	33.3
$\tilde{\alpha}$	0.04	50
l_{e}	115.2 cm	2
L_{CSR}	35.12 m	0.3

exhibited an electron-induced signal of $\sim 4\,\%$ of the signal at the measurement energy at the DR peak. Therefore, equation (4.70) had to be applied to derive the absolute scale for the measurement energy. From the quantities listed in table 4.3, the absolute value of the MBRC α_{mb} at the detuning energy of $E_{\mathrm{d}} = 25.28\,\mathrm{eV}$ is obtained as

$$\alpha_{\mathrm{mb}}(E_{\mathrm{d}} = 25.28\,\mathrm{eV}) = 10.6 \times 10^{-11}\,\mathrm{cm}^3\,\mathrm{s}^{-1}. \tag{4.77}$$

As the main source of uncertainty, the detection efficiency $\eta_{\mathrm{e,m}}$ can be identified. Using error propagation assuming independent, normally distributed variables, the relative uncertainty of the merged-beams rate coefficient α_{mb} from equation (4.70) can be expressed as

$$\begin{aligned}\frac{\Delta\alpha_{\mathrm{e,m}}}{\alpha_{\mathrm{e,m}}} = \Bigg[&\left(\frac{\Delta\tilde{S}}{\tilde{S}}\right)^2 + \left(\frac{\Delta\eta_{\mathrm{e,m}}}{\eta_{\mathrm{e,m}}}\right)^2 + \left(\frac{\Delta l_{\mathrm{e}}}{l_{\mathrm{e}}}\right)^2 + \left(\frac{\Delta L_{\mathrm{CSR}}}{L_{\mathrm{CSR}}}\right)^2 \\ &+ \left(\frac{n_{\mathrm{e,r}}\Delta\tilde{\alpha}}{n_{\mathrm{e,m}} - \tilde{\alpha}n_{\mathrm{e,r}}}\right)^2 + \left(\frac{\tilde{\alpha}\Delta n_{\mathrm{e,r}}}{n_{\mathrm{e,m}} - \tilde{\alpha}n_{\mathrm{e,r}}}\right)^2 + \left(\frac{\Delta n_{\mathrm{e,m}}}{n_{\mathrm{e,m}} - \tilde{\alpha}n_{\mathrm{e,r}}}\right)^2 \Bigg]^{1/2}.\end{aligned} \tag{4.78}$$

With the uncertainties listed in table 4.3, the estimated uncertainty budget for $\alpha_{\mathrm{mb}}(E_{\mathrm{d}} = 25.28\,\mathrm{eV})$ adds up to $38.7\,\%$, which is approximated here as

$$\frac{\Delta\alpha_{\mathrm{mb}}(E_{\mathrm{d}} = 25.28\,\mathrm{eV})}{\alpha_{\mathrm{mb}}(E_{\mathrm{d}} = 25.28\,\mathrm{eV})} \approx 40\,\%. \tag{4.79}$$

4.9.2.2 Scaling of the RR peak

For the absolute scaling of the RR peak at 0 eV, equation (4.73) on page 57 was utilized. As the detection efficiencies $\eta_{\mathrm{e,c}}$, $\eta_{\mathrm{e,r}}$, $\eta_{\mathrm{rg,c}}$, and $\eta_{\mathrm{rg,r}}$ for electron- and residual-gas-induced events in the cooling and reference steps, respectively, and in particular

Table 4.4: Parameters used for the calculation of the absolute merged-beams rate coefficient $\alpha_{\mathrm{mb,c}}$ at a collision energy of $E_\mathrm{d} = 0\,\mathrm{eV}$ in the Ne^{2+} beamtime. The values for S and $(R_\mathrm{c} - R_\mathrm{r})/(R_\mathrm{r} - R_\mathrm{dark})$ were averaged from the values in table 4.2.

Variable	Value	Relative uncertainty [%]
S	$7.97\,\mathrm{s}^{-1}/10^5$ ions	12.3
$\frac{R_\mathrm{c}-R_\mathrm{r}}{R_\mathrm{r}-R_\mathrm{dark}}$	0.0169	10
$n_\mathrm{e,c}$	$8.5 \times 10^5\,\mathrm{cm}^{-3}$	12
$n_\mathrm{e,r}$	$15.6 \times 10^5\,\mathrm{cm}^{-3}$	12
$\eta_\mathrm{e,c}$	0.74	33.3
$\tilde{\eta}_\mathrm{e}$	1.01	1.5
$\tilde{\eta}_\mathrm{rg}$	1.01	1.5
$\tilde{\alpha}_\mathrm{c}$	0.04	70
l_e	115.2 cm	2
L_CSR	35.12 m	0.3

their differences are not known precisely, assumptions have to be made here. Since the electron density in the reference step was almost twice as high as in the cooling step, the focusing of the ion beam due to the electron beam space charge is assumed to be stronger in the reference step, potentially resulting in a slightly higher detection efficiency in the reference step. Therefore, $\tilde{\eta}_\mathrm{e} = \eta_\mathrm{e,r}/\eta_\mathrm{e,c} > 1$ and $\tilde{\eta}_\mathrm{rg} = \eta_\mathrm{rg,r}/\eta_\mathrm{rg,c} > 1$. In agreement with the findings that are presented in section 5.2.5 on page 82, a 1 %-deviation was assumed here, i.e. $\tilde{\eta}_\mathrm{e} = 1.01$ and $\tilde{\eta}_\mathrm{rg} = 1.01$, with a generous uncertainty of 1.5 %, which allows for values between 0.995 and 1.025. With the quantities listed in table 4.4, the absolute MBRC at cooling is obtained as

$$\alpha_\mathrm{mb}(E_\mathrm{d} = 0\,\mathrm{eV}) = 11.2 \times 10^{-11}\,\mathrm{cm}^3\,\mathrm{s}^{-1}. \tag{4.80}$$

It should be noted that the absolute value for $\alpha_\mathrm{mb}(E_\mathrm{d} = 0\,\mathrm{eV})$ was obtained here for conditions where the cathode potential was at $U_\mathrm{cath} = -50\,\mathrm{V}$. As it is shown in section 6.3 on page 109, the cooling signal varied with different settings of the electron cooler, and especially with different cathode potentials which affected the electron-ion collision energy outside of the drift tubes.

The result for $\alpha_\mathrm{mb}(E_\mathrm{d} = 0\,\mathrm{eV})$ is very sensitive on the actual value of $\tilde{\eta}_\mathrm{rg}$, which also accounts for the largest fraction of the uncertainty budget. The relative uncertainty of $\alpha_\mathrm{mb,c}$ from equation (4.73), as obtained using error propagation assuming independent,

Table 4.5: Ion numbers N_i and proportionality factors S (from equation (4.67)) for the dedicated absolute scaling runs in the Xe^{3+} beamtime. $t_\mathrm{i,meas}$ indicates the start of the ion number measurement, which had a duration of 0.1 s. $(R_\mathrm{m} - R_\mathrm{r}) / (R_\mathrm{r} - R_\mathrm{dark})$ and $(R_\mathrm{c} - R_\mathrm{r}) / (R_\mathrm{r} - R_\mathrm{dark})$ are calculated from the average count rates in the measurement schemes over the whole run with a statistical uncertainty of $< 3\,\%$ and $< 7\,\%$, respectively. All measurement energies were averaged to obtain R_m. Uncertainties for N_i and S are 11.2 % and 12.3 %, respectively.

Run	$t_\mathrm{i,meas}$ [s]	N_i [10^6 ions]	S [$\mathrm{s}^{-1}/10^5$ ions]	$\left(\frac{R_\mathrm{m}-R_\mathrm{r}}{R_\mathrm{r}-R_\mathrm{dark}}\right)$	$\left(\frac{R_\mathrm{c}-R_\mathrm{r}}{R_\mathrm{r}-R_\mathrm{dark}}\right)$
58	44.0	3.52	25.91	0.1092	0.0357
	45.5	3.28	25.33		
60	44.0	8.27	24.66	0.1111	0.0334
	45.5	7.10	24.57		

normally distributed variables, can be given as

$$\begin{aligned}\frac{\Delta\alpha_\mathrm{mb,c}}{\alpha_\mathrm{mb,c}} = \Bigg[&\left(\frac{\Delta S}{S}\right)^2 + \left(\frac{\Delta\eta_\mathrm{e,c}}{\eta_\mathrm{e,c}}\right)^2 + \left(\frac{\Delta l_\mathrm{e}}{l_\mathrm{e}}\right)^2 + \left(\frac{\Delta L_\mathrm{CSR}}{L_\mathrm{CSR}}\right)^2 \\ &+ \left(\frac{\Delta n_\mathrm{e,c}}{n_\mathrm{e,c}} \frac{n_\mathrm{e,c}}{(n_\mathrm{e,c} - n_\mathrm{e,r}\,\tilde{\alpha}_\mathrm{c}\,\tilde{\eta}_\mathrm{e})}\right)^2 + \left(\frac{\Delta n_\mathrm{e,r}}{n_\mathrm{e,r}} \frac{n_\mathrm{e,r}\,\tilde{\alpha}_\mathrm{c}\,\tilde{\eta}_\mathrm{e}}{(n_\mathrm{e,c} - n_\mathrm{e,r}\,\tilde{\alpha}_\mathrm{c}\,\tilde{\eta}_\mathrm{e})}\right)^2 \\ &+ \left(\frac{\Delta\tilde{\alpha}_\mathrm{c}}{\tilde{\alpha}_\mathrm{c}} \frac{n_\mathrm{e,r}\,\tilde{\alpha}_\mathrm{c}\,\tilde{\eta}_\mathrm{e}}{(n_\mathrm{e,c} - n_\mathrm{e,r}\,\tilde{\alpha}_\mathrm{c}\,\tilde{\eta}_\mathrm{e})}\right)^2 + \left(\frac{\Delta\tilde{\eta}_\mathrm{e}}{\tilde{\eta}_\mathrm{e}} \frac{n_\mathrm{e,r}\,\tilde{\alpha}_\mathrm{c}\,\tilde{\eta}_\mathrm{e}}{(n_\mathrm{e,c} - n_\mathrm{e,r}\,\tilde{\alpha}_\mathrm{c}\,\tilde{\eta}_\mathrm{e})}\right)^2 \\ &+ \left(\frac{\Delta\tilde{R}_\mathrm{c}}{\tilde{R}_\mathrm{c}} \frac{\tilde{R}_\mathrm{c}}{(\tilde{R}_\mathrm{c} + 1 - \tilde{\eta}_\mathrm{rg}^{-1})}\right)^2 + \left(\frac{\Delta\tilde{\eta}_\mathrm{rg}}{\tilde{\eta}_\mathrm{rg}} \frac{1}{\tilde{\eta}_\mathrm{rg}\,(\tilde{R}_\mathrm{c} + 1) - 1}\right)^2 \Bigg]^{1/2},\end{aligned} \tag{4.81}$$

where $\tilde{R}_\mathrm{c} = (R_\mathrm{c} - R_\mathrm{r}) / (R_\mathrm{r} - R_\mathrm{dark})$. Consequently, the uncertainties from table 4.4 result in a large uncertainty of $\alpha_\mathrm{mb}(E_\mathrm{d} = 0\,\mathrm{eV})$ of

$$\frac{\Delta\alpha_\mathrm{mb}(E_\mathrm{d} = 0\,\mathrm{eV})}{\alpha_\mathrm{mb}(E_\mathrm{d} = 0\,\mathrm{eV})} = 68\,\%. \tag{4.82}$$

4.9.3 Absolute scale for the Xe^{3+} recombination rate coefficient

In the Xe^{3+} beamtime, a long pre-cooling scheme of 42 s was chosen for the absolute scaling runs. The subsequent measurement scheme included wobbling between cooling, measurement, and reference steps with step lengths of 100 ms, 25 ms and 25 ms, respectively, separated by 5 ms waiting steps. The electron current in the cooling step was 8.5 µA, while in the measurement and reference steps a considerably higher current of 100 µA was applied. For the reference detuning energy, 24 eV was selected which

Table 4.6: Parameters used for the calculation of the absolute merged-beams rate coefficient $\alpha_{\mathrm{mb,avg}}$ at the DR peak in the Xe^{3+} beamtime.

Variable	Value	Relative uncertainty [%]
$\tilde{S}$	$27.67\,\mathrm{s}^{-1}/10^6$ ions	15
$\eta_{\mathrm{e,m}}$	0.75	25
$n_{\mathrm{e,m}}$	$10.9 \times 10^5\,\mathrm{cm}^{-3}$	12
l_{e}	115.2 cm	2
L_{CSR}	35.12 m	0.2

was above the main recombination feature at $E_{\mathrm{d}} \approx 19.7\,\mathrm{eV}$ (referred to as 'DR peak', see also the spectrum in figure 6.2 on page 100). Five detuning energies at 19.56 eV, 19.63 eV, 19.70 eV, 19.77 eV and 19.84 eV around the DR peak were scanned in the measurement steps. At storage times between 43 s and 46 s, the ion beam was bunched, and two ion number measurements were conducted at 44 s and 45.5 s for a duration of 0.1 s.

The count rates in the reference steps were fitted by a linear function during the bunching period, and the average reference rates during the ion number measurement period were extracted. With this, scaling parameters $S = (R_{\mathrm{r}} - R_{\mathrm{dark}})\,/N_{\mathrm{i}}$ were calculated. The results are shown in table 4.5. The relative uncertainty of S is composed of the relative uncertainty in the ion number measurement of 11.2 % and the relative uncertainty in the fitted reference rate, which is approximated as 3 % in agreement with the statistical uncertainty at each individual reference step. The total uncertainty for S thus is 11.6 %.

The count rates at all five measurement energies were averaged to one effective rate over the whole measurement scheme, and the reference and cooling count rates as well. Relative rates $(R_{\mathrm{m}} - R_{\mathrm{r}})\,/\,(R_{\mathrm{r}} - R_{\mathrm{dark}})$ and $(R_{\mathrm{c}} - R_{\mathrm{r}})\,/\,(R_{\mathrm{r}} - R_{\mathrm{dark}})$ were evaluated and are given in table 4.5.

4.9.3.1 Scaling of the DR peak

The product $\tilde{S} = S \times \left(\frac{R_{\mathrm{m}} - R_{\mathrm{r}}}{R_{\mathrm{r}} - R_{\mathrm{dark}}}\right)$ was evaluated for the four measurements in table 4.5, and an average value of $\tilde{S} = 27.67\,\mathrm{s}^{-1}/10^6$ ions was obtained with an uncertainty margin of 15 % accounting for the uncertainties in S, the relative rates, as well as the scatter in $\tilde{S}$ from the different measurements. At the reference detuning energy of 24 eV, basically no electron-induced signal was observed, and the expected signal from RR at this energy is calculated to $\sim 1 \times 10^{-13}\,\mathrm{cm}^3\,\mathrm{s}^{-1}$, which is negligibly small in comparison to the other experimental uncertainties. For this reason, $\alpha_{\mathrm{e,r}} \approx 0$ was assumed and equation (4.71) on page 56 could be utilized to absolutely scale the recombination signal at the measurement energies at the DR peak. From the quantities listed in table 4.6, the absolute value of the averaged rate coefficient $\alpha_{\mathrm{mb,avg}}$ at collision energies of $E_{\mathrm{d}} =$

Table 4.7: Parameters used for the calculation of the absolute merged-beams rate coefficient $\alpha_{\mathrm{mb,c}}$ at a collision energy of $E_\mathrm{d} = 0\,\mathrm{eV}$ in the Xe^{3+} beamtime. The values for S and $(R_\mathrm{c} - R_\mathrm{r})/(R_\mathrm{r} - R_\mathrm{dark})$ were averaged from the values in table 4.5.

Variable	Value	Relative uncertainty [%]
S	$25.12\,\mathrm{s}^{-1}/10^5$ ions	11.6
$\frac{R_\mathrm{c}-R_\mathrm{r}}{R_\mathrm{r}-R_\mathrm{dark}}$	0.0345	7
$n_\mathrm{e,c}$	$3.2 \times 10^5\,\mathrm{cm}^{-3}$	12
$\eta_\mathrm{e,c}$	0.75	25
$\tilde{\eta}_\mathrm{rg}$	1.015	2
l_e	115.2 cm	2
L_CSR	35.12 m	0.3

19.56 eV, 19.63 eV, 19.70 eV, 19.77 eV and 19.84 eV can be derived as

$$\alpha_\mathrm{mb,avg} = 10.4 \times 10^{-10}\,\mathrm{cm}^3\,\mathrm{s}^{-1}. \tag{4.83}$$

The main source of uncertainty is the detection efficiency $\eta_\mathrm{e,m}$. The relative uncertainty of the merged-beams rate coefficient α_mb from equation (4.71) can be expressed as

$$\frac{\Delta\alpha_\mathrm{e,m}}{\alpha_\mathrm{e,m}} = \sqrt{\left(\frac{\Delta\tilde{S}}{\tilde{S}}\right)^2 + \left(\frac{\Delta\eta_\mathrm{e,m}}{\eta_\mathrm{e,m}}\right)^2 + \left(\frac{\Delta l_\mathrm{e}}{l_\mathrm{e}}\right)^2 + \left(\frac{\Delta L_\mathrm{CSR}}{L_\mathrm{CSR}}\right)^2 + \left(\frac{\Delta n_\mathrm{e,m}}{n_\mathrm{e,m}}\right)^2}. \tag{4.84}$$

The estimated uncertainty budget sums up to 31.6 %, which is approximated here as

$$\frac{\Delta\alpha_\mathrm{mb,avg}}{\alpha_\mathrm{mb,avg}} = 32\,\%. \tag{4.85}$$

The five energies at the DR peak, for which $\alpha_\mathrm{mb,avg}$ was derived, were included in all regular DR measurement runs.

4.9.3.2 Scaling of the RR peak

For the absolute scaling of the RR peak at $E_\mathrm{d} = 0\,\mathrm{eV}$, equation (4.74) on page 57 was used as the electron-induced signal in the reference step was negligibly small. The ratio $\tilde{\eta}_\mathrm{rg} = \eta_\mathrm{rg,r}/\eta_\mathrm{rg,c}$ of the detection efficiencies for residual-gas-induced events in the cooling and reference step is not known precisely. The electron density in the reference step was $10.3 \times 10^5\,\mathrm{cm}^{-3}$ and thus roughly three times as high as in the cooling step ($3.2 \times 10^5\,\mathrm{cm}^{-3}$). Consequently, the focusing of the ion beam due to the electron beam space charge is assumed to be stronger in the reference step, potentially resulting in a slightly higher detection efficiency in the reference step. Therefore, $\tilde{\eta}_\mathrm{rg} = \eta_\mathrm{rg,r}/\eta_\mathrm{rg,c} > 1$.

Similar to the case in the evaluation of the absolute scale for the RR peak in Ne^{2+} (see section 4.9.2.2), $\tilde{\eta}_{\mathrm{rg}} = 1.015$ was assumed here with an uncertainty of 2 % which allows for a variation between 0.995 and 1.035. From the quantities listed in table 4.7, the absolute MBRC at cooling is obtained as

$$\alpha_{\mathrm{mb}}(E_{\mathrm{d}} = 0\,\mathrm{eV}) = 15.5 \times 10^{-10}\,\mathrm{cm}^3\,\mathrm{s}^{-1} \tag{4.86}$$

In the absolute scaling runs, the cathode potential was at $U_{\mathrm{cath}} = -50\,\mathrm{V}$.

The result for the absolute value of the MBRC at cooling is very sensitive to $\tilde{\eta}_{\mathrm{rg}}$. The relative uncertainty of $\alpha_{\mathrm{mb}}(E_{\mathrm{d}} = 0\,\mathrm{eV})$ can be evaluated by error propagation from equation (4.74) as

$$\begin{aligned}\frac{\Delta\alpha_{\mathrm{mb,c}}}{\alpha_{\mathrm{mb,c}}} = \Bigg[&\left(\frac{\Delta S}{S}\right)^2 + \left(\frac{\Delta\eta_{\mathrm{e,c}}}{\eta_{\mathrm{e,c}}}\right)^2 + \left(\frac{\Delta l_{\mathrm{e}}}{l_{\mathrm{e}}}\right)^2 + \left(\frac{\Delta L_{\mathrm{CSR}}}{L_{\mathrm{CSR}}}\right)^2 + \left(\frac{\Delta n_{\mathrm{e,c}}}{n_{\mathrm{e,c}}}\right)^2 \\ &+ \left(\frac{\Delta\tilde{R}_{\mathrm{c}}}{\tilde{R}_{\mathrm{c}}}\,\frac{\tilde{R}_{\mathrm{c}}}{(\tilde{R}_{\mathrm{c}} + 1 - \tilde{\eta}_{\mathrm{rg}}^{-1})}\right)^2 + \left(\frac{\Delta\tilde{\eta}_{\mathrm{rg}}}{\tilde{\eta}_{\mathrm{rg}}}\,\frac{1}{\tilde{\eta}_{\mathrm{rg}}\,(\tilde{R}_{\mathrm{c}} + 1) - 1}\right)^2 \Bigg]^{1/2},\end{aligned} \tag{4.87}$$

where $\tilde{R}_{\mathrm{c}} = (R_{\mathrm{c}} - R_{\mathrm{r}})\,/\,(R_{\mathrm{r}} - R_{\mathrm{dark}})$. The uncertainty of $\alpha_{\mathrm{mb}}(E_{\mathrm{d}} = 0\,\mathrm{eV})$ resulting from the uncertainties listed in table 4.7 amounts to

$$\frac{\Delta\alpha_{\mathrm{mb}}(E_{\mathrm{d}} = 0\,\mathrm{eV})}{\alpha_{\mathrm{mb}}(E_{\mathrm{d}} = 0\,\mathrm{eV})} = 50\,\%. \tag{4.88}$$

4.10 Level populations

In recombination experiments, ions in all excited levels present in the stored beam contribute to the observed rate coefficient and potentially exhibit different recombination signatures. Therefore, knowledge about the level populations is important for the interpretation of the recorded data.

The conditions present in ion sources, such as the ECR source [128] used to produce the Ne^{2+} and Xe^{3+} ions, are usually characterized by high temperatures, which are necessary for the violent process of electron-impact ionization. Consequently, the ions extracted from the source possibly populate not only the ground level but also several excited levels, which potentially decay to the ground level while being stored in a storage ring.

Here, the fine structure levels of the ground configuration have been taken into account to estimate the level population contributing to the recombination signal in the storage ring measurements presented in this thesis. The fine structure levels are listed in table 4.8. Radiative transition rates for Ne^{2+} levels within the $[He]2s^2 2p^4$ configuration

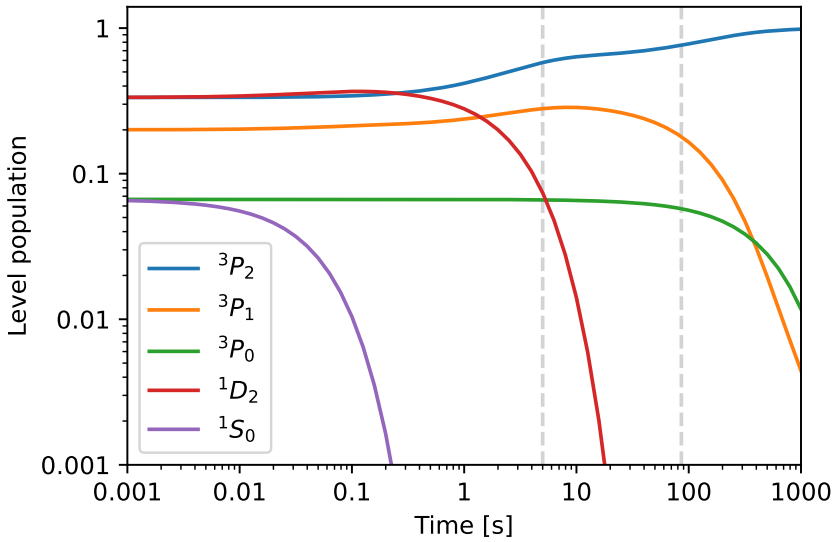

(a) Populations of the fine structure levels of the Ne^{2+} ground configuration as a function of storage time.

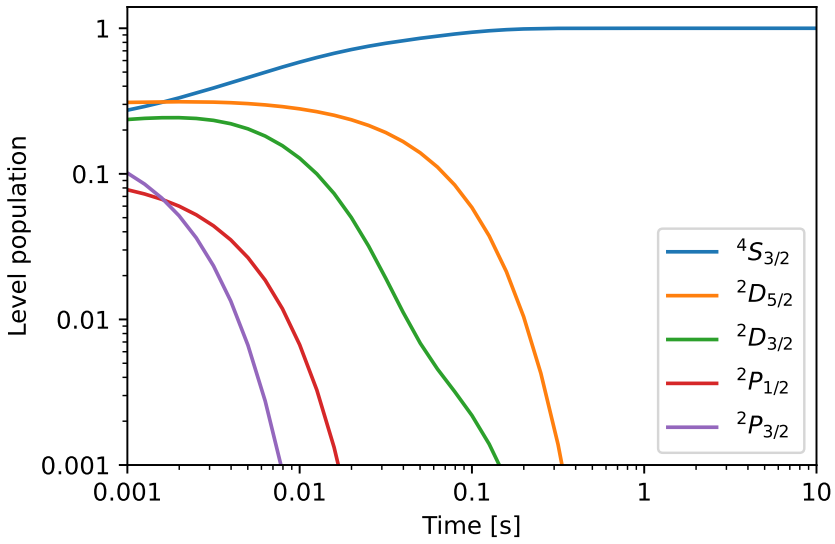

(b) Populations of the fine structure levels of the Xe^{3+} ground configuration as a function of storage time.

Figure 4.10: Calculated fractional populations for the fine structure levels of the (a) Ne^{2+} and (b) Xe^{3+} ground configurations as functions of storage time in CSR. Initially, a statistical distribution was assumed. Note the different time scales in the two plots. In the case of Ne^{2+}, even after 100 s three states are still populated by more than 5 %. The dashed vertical lines indicate the storage times at which the recombination measurement scheme started ($t_{\mathrm{stor}}^{\mathrm{start}} = 5\,\mathrm{s}$) and at which it ended at the latest ($t_{\mathrm{stor}}^{\mathrm{end,max}} = 86\,\mathrm{s}$). The Xe^{3+} beam is purely in the $^4S_{3/2}$ ground state after less than 1 s. In the Xe^{3+} beamtime, the measurement scheme started earliest after 10 s of storage.

Table 4.8: Fine structure levels for the ground configuration of Ne^{2+} and Xe^{3+}, according to the NIST Atomic Spectra Database [129].

Ion	Configuration	Level	Energy [eV]
Ne^{2+}	$[He]2s^2 2p^4$	$^3P_2$	0.000
		$^3P_1$	0.080
		$^3P_0$	0.114
		$^1D_2$	3.204
		$^1S_0$	6.912
Xe^{3+}	$[Kr]5s^2 5p^3$	$^4S_{3/2}$	0.000
		$^2D_{3/2}$	1.645
		$^2D_{5/2}$	2.171
		$^2P_{1/2}$	3.476
		$^2P_{3/2}$	4.420

and Xe^{3+} levels within the $[Kr]4d^{10}5s^2 5p^3$ configuration are insufficiently known experimentally. Therefore, the radiative rates including E1, E2, E3, M1 and M2 transitions have been calculated using the *AUTOSTRUCTURE* (AS) atomic code [130, 131]. For the case of Ne^{2+}, Einstein coefficients reported in the NIST Atomic Spectra Database [129] for some M1 transitions agree within a factor of < 2 with the calculated rates. Subsequently, the level populations at a given time after ion extraction from the source were computed using the code reported by Spruck [71], assuming a statistical initial population of the different fine structure levels. Figure 4.10 shows the fractional level populations for both systems as a function of time after ion extraction from the source, which is practically identical with the storage time in CSR.

The calculated transition rates between the fine structure levels of the Ne^{2+} ground configuration are low, therefore a considerable fraction stays in excited metastable levels even after long storage times. The measurement scheme in the recombination experiment started after a storage time of 5 s and had a duration of typically 40 s to 50 s. Within this time, the population of the $^1D_2$ level drops from 7 % to basically 0, and the fractional populations in $^3P_2$, $^3P_1$ and $^3P_0$ range around 68 %, 26 % and 6 %, respectively.

For Xe^{3+}, the excited fine structure levels decay fast to the $^4S_{3/2}$ ground level. The calculations indicate a pure beam at the beginning of the measurement scheme, which started after a storage time of 10 s or 21 s.

4.11 Field ionization

The product ions from recombination in the electron-ion interaction region inside the CSR electron cooler are counted by the COMPACT detector in the corner downstream of the electron cooler (see figure 3.1 on page 17). On their way to the detector, the product ions pass the demerging and correction coils, a quadrupole, and the 6°-deflector, all of which exhibit electric or magnetic fields. Ions in high Rydberg levels therefore are prone to field ionization and have a reduced probability to reach the detector in case they don't relax to lower-lying levels before they arrive at the respective fields. The principle quantum number n_c, from which on a Rydberg level is field ionized, can be calculated as [132]

$$n_c = \sqrt[4]{\frac{q^3}{9\,F}}, \tag{4.89}$$

where q denotes the charge state of the ion prior to recombination, and F denotes the electric field in atomic units ($1\,\mathrm{au} = 5.142 \times 10^9\,\mathrm{V\,cm^{-1}}$). In the simplest approach, all ions that capture a free electron into $n < n_c(F_{\max})$, with $F_{\max}$ the maximum field strength along the ion path, withstand the field ionization and reach the detector. In CSR, the maximum relevant field strength is $F_{\max} \approx 3\,\mathrm{kV\,cm^{-1}}$ in the 6°-deflector. The corresponding 'cut-off' quantum numbers n_c for Ne^{2+} and Xe^{3+} are

$$n_{c,\mathrm{Ne}^{2+}} = 36$$

for recombined Ne^+, and

$$n_{c,\mathrm{Xe}^{3+}} = 48$$

for recombined Xe^{2+}.

In reality, high-lying Rydberg levels decay at least partially to levels with n below the critical quantum number n_c, and the different field strengths along the ion path to the detector have to be taken into account. A model to calculate the survival probabilities is published by Schippers et al. [133]. Using the *hydrocal* code by Stefan Schippers [90], survival probabilities for the initial electron capture into specific Rydberg levels were determined for the conditions in CSR. To this end, hydrogenic radiative decay rates of the Rydberg levels were calculated and the cut-off was derived by assuming realistic ion flight times through the electric and magnetic fields in CSR. Figure 4.11 shows the survival probabilities for recombined Ne^+ and Xe^{2+} ions, respectively. Due to relaxation during the flight time, Rydberg states with $n \geq n_c$ can have a considerable likelihood to reach the detector. Especially p-states with angular quantum number $l = 1$ have high survival probabilities even for high n. However, they are not necessarily populated to a large extent in the recombination process.

Ions that capture a free electron to a Rydberg level $n\,l$ in the recombination process contribute to the measured recombination rate coefficient according to the above stated survival probabilities. For an accurate interpretation of the experimental data and for a comparison with theory, also the states with $n \geq n_c$ would have to be considered.

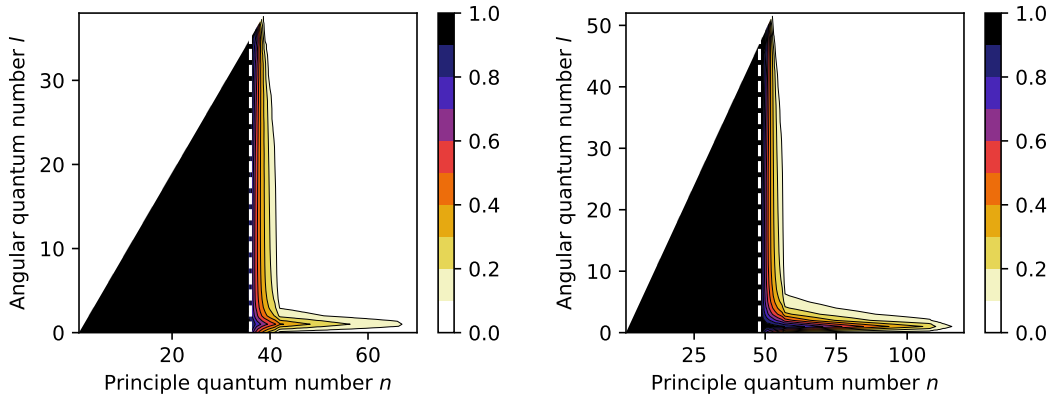

(a) Ne^{+} (b) Xe^{2+}

Figure 4.11: Survival probabilities for Rydberg levels $n\,l$ of (a) Ne^{+} (recombined Ne^{2+}) and (b) Xe^{2+} (recombined Xe^{3+}) to reach the COMPACT detector. The recombined ions produced in the electron cooler are exposed to electric and magnetic fields along their path to the detector, and are potentially field-ionized. The probabilities were calculated using the *hydrocal* code [90] and are plotted for values above 0.1. The dashed white lines symbolize the 'cut-off' quantum numbers $n_c = 36, 48$ as derived from equation (4.89).

Chapter 5

Results on Electron Recombination of Ne^{2+}

The beamtime on electron-ion recombination of O-like Ne^{2+} was the first recombination experiment with atomic ions at CSR. It was planned as a proof-of-principle experiment to demonstrate the feasibility of such recombination measurements at CSR. A suitable candidate ion for such a first test was desired to fulfill certain requirements:

- Easy producibility to guarantee a stable and intense ion beam.
- Low charged, ideally with $q \leq 5$. The separation between the stored parent beam and recombined ions had to be sufficiently large behind the 6°-deflector, otherwise the COMPACT detector used in the experiment would not be able to capture the recombined ions without affecting the stored beam.
- Occurrence of DR resonances in the accessible electron-ion collision energy range and with sufficient strengths that guarantee measurable signal-to-background ratios.
- Ideally, experimental data are already available from the literature for eventual comparison.

The choice of Ne^{2+} was strongly motivated by another experiment at CRYRING@ESR at GSI in Darmstadt, investigating the recombination of Ne^{2+} with free electrons [41]. The CRYRING@ESR experiment was performed shortly before the beamtime at CSR and found recombination rate coefficients in the order of several $10^{-11}\,\mathrm{cm^3\,s^{-1}}$ at collision energies below 30 eV, and therefore Ne^{2+} met the requirements. For the experiments, the most abundant isotope ^{20}Ne was selected, which has a natural abundance of $> 90\,\%$ and a mass of 19.9924 u [134]. With $m/q \approx 10$, Ne^{2+} has a moderately high mass-to-charge ratio.

Table 5.1: Overview of the measurement ranges for Ne^{2+}. The electron current in the measurement step I_e and the corresponding electron densities n_e are displayed. All ranges were measured with an electron current at cooling of $\sim 47\,\mu A$, resulting in a density of $8.0 \times 10^5\,cm^{-3}$. The pre-cooling time was 5.3 s in all ranges. $t_{stor,max}$ denotes the maximum storage time at which the ions were kicked out of CSR. Most detuning energy ranges were covered by more than one run.

Range [eV]	I_e [uA]	n_e [$10^5\,cm^{-3}$]	$t_{stor,max}$ [s]
0 - 1	47	8.5 - 6.5	47 - 86
1 - 10	130	17.3 - 13.2	46.8
10 - 20	190	18.7 - 16.5	46.8
20 - 27	190	16.5 - 15.5	56.4
21 - 26.5	192	16.5 - 15.8	25.2
21 - 26.5	246	19.8 - 18.9	25.2
27 - 33	190	15.5 - 14.9	43.0

In this chapter, the results from the recombination measurements at CSR are presented. The general measurement layout is described in chapter 4 above, especially in section 4.5 on page 44. Section 5.1 explains how the recorded data were combined and how the rate coefficients were derived. The actual results are presented in sections 5.2 and 5.3. Section 5.2 focuses on the 'high energy' part of the measured spectrum with detuning energies ranging from 1 eV to 33 eV. In this region, DR resonances were observed, which are discussed and compared with theoretical calculations and with the earlier CRYRING@ESR experiment. Artifacts from the measurement procedure enhance the derived rate coefficients at detuning energies below ~ 17 eV. This effect is attributed to focusing of the ion beam by the space charge of the electrons and is discussed as well. Section 5.3 focuses on the RR peak in the 'low energy' part of the spectrum with detuning energies up to 1 eV. Here, the influence of the electron cooler settings on the RR peak are reviewed, and a comparison with a theoretical calculation is made. The main findings are again summarized in section 5.4.

5.1 Combining data from different runs and ranges

During the Ne^{2+} beamtime, multiple runs have been recorded scanning different detuning energy ranges between 0 eV and 33 eV. The ranges are shown in table 5.1 with the applied electron current I_e in the measurement step, the corresponding electron densities n_e and the maximum storage time $t_{stor,max}$. Most ranges were covered by more

than one run. To stitch together the energy-dependent MBRC, data from different runs and ranges had to be combined. The runs within the individual ranges were merged by adding up all counts and step lengths, and subsequently calculating the relative rates $(R_\mathrm{m} - R_\mathrm{dark})/(R_\mathrm{c} - R_\mathrm{dark})$ for each measurement energy independently. To bring the different ranges together, relative rate coefficients were evaluated utilizing equation (4.56) on page 52. The offset parameter B was chosen for each range separately. First, B was adjusted for the 27 eV to 33 eV range, where no DR signal was expected (also the CRYRING@ESR experiment [41] did not observe any resonance peaks there). B was chosen such that the relative rate coefficient was practically zero across the whole range. Subsequently, the offset parameters for the other energy ranges were adjusted such that the relative rate coefficients transition smoothly and such that no jumps occur in between the different ranges after scaling. Each range was normalized individually to the average rate coefficient α'_peak at the three reference energies 25.25 eV, 25.27 eV and 25.30 eV on the strongest recombination feature (referred to as 'DR peak'), which were included in each run. Thereafter, the data were binned in E_d to combine data points at the same detuning energy but from different ranges, and to lower the statistical uncertainty. Therefore, an uncertainty-weighted mean was calculated for the average rate coefficient $\alpha_\mathrm{rel}(E_{\mathrm{d},n})$ in each bin n from the individual data points $\alpha_{\mathrm{rel},j}(E_{\mathrm{d},n})$ in the corresponding bin and from the corresponding statistical uncertainty $\sigma_j(E_{\mathrm{d},n})$, i.e.

$$\alpha_\mathrm{rel}(E_{\mathrm{d},n}) = \frac{\sum_j \alpha_{\mathrm{rel},j}(E_{\mathrm{d},n})\, \sigma_j^{-2}(E_{\mathrm{d},n})}{\sum_j \sigma_j^{-2}(E_{\mathrm{d},n})}, \tag{5.1}$$

with j running over all data points in the bin n. The statistical uncertainty of the binned relative rate coefficient then corresponds to

$$\sigma(E_{\mathrm{d},n}) = \sqrt{\frac{1}{\sum_j \sigma_j^{-2}(E_{\mathrm{d},n})}}. \tag{5.2}$$

The derived relative rate coefficients were then absolutely scaled with the value obtained in section 4.9.2.

In this procedure, the lowest range between 0 eV and 1 eV covering the peak of the RR signal was treated separately from the remainder of the spectrum. The reason for this separation is a distortion of the derived rate coefficients towards lower detuning energies as a result of nonuniform ion beam focusing by the electron beam space charge, which is discussed in section 5.2.5.

5.2 Recombination at higher energies between 1 eV and 33 eV

The relative rate coefficients of the different ranges from 1 eV to 33 eV as listed in table 5.1, excluding the RR peak, are shown in figure 5.1, as well as the binned spectrum.

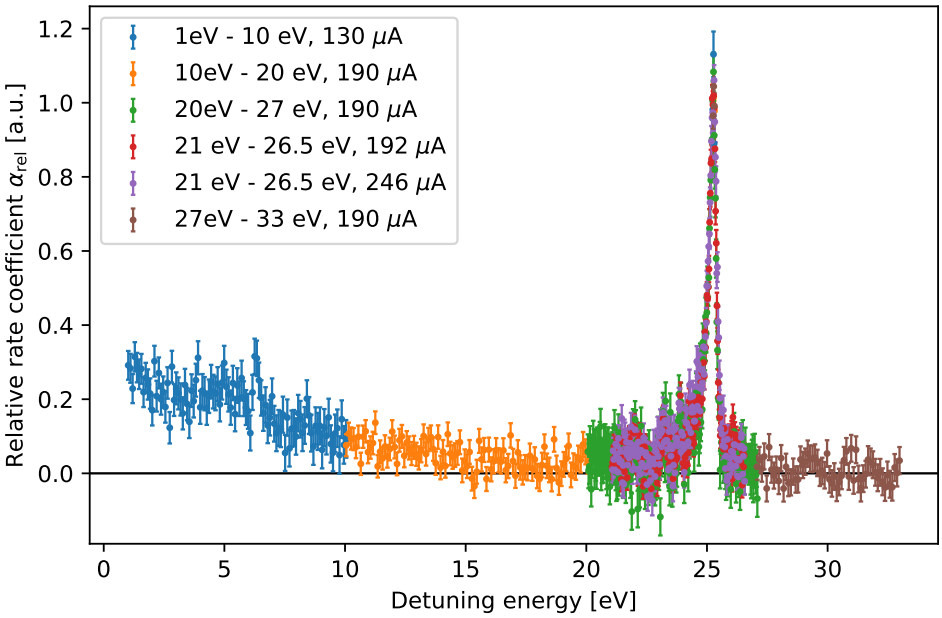

(a) Rate coefficients from individual energy ranges on a relative scale.

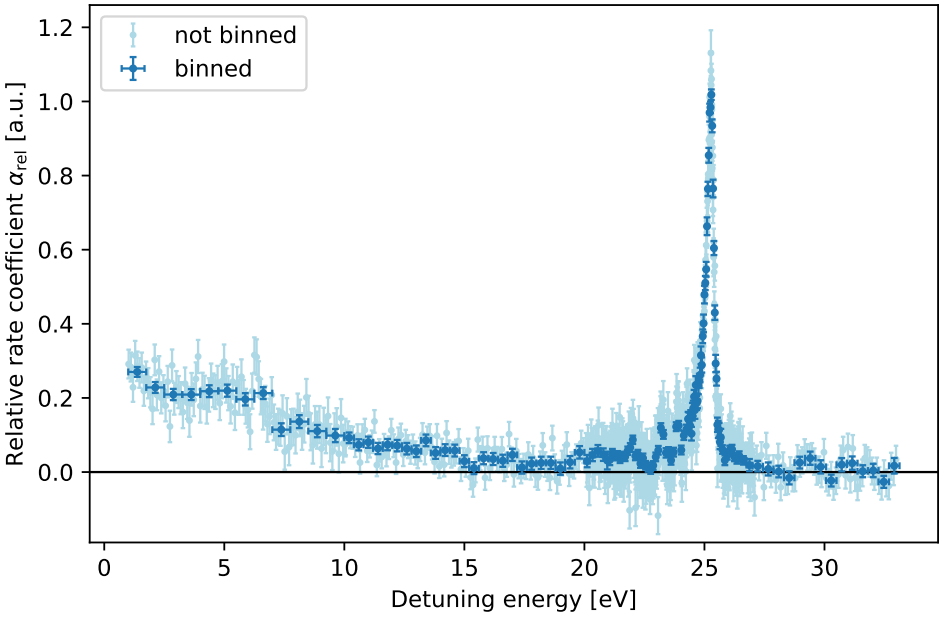

(b) Relative rate coefficients from above, binned.

Figure 5.1: Relative merged-beams rate coefficients at detuning energies between 1 eV and 33 eV, (a) combined from different runs and ranges, and (b) binned. The error bars indicate the statistical uncertainties. The signal rise towards lower energies is assumed to be an artifact from the measurement setup.

Table 5.2: Level energies of the first eight excited levels of Ne^{2+} in the configurations [He]$2s^2 2p^4$ and [He]$2s2p^5$, according to the NIST Atomic Spectra Database [129].

Configuration	Level	Energy [eV]
$2s^2 2p^4$	$^3P_2$	0.000
	$^3P_1$	0.080
	$^3P_0$	0.114
	$^1D_2$	3.204
	$^1S_0$	6.912
$2s2p^5$	$^3P_2$	25.329
	$^3P_1$	25.401
	$^3P_0$	25.441
	$^1P_1$	35.891

The most prominent feature in the spectrum is the peak around $E_\mathrm{d} = 25\,\mathrm{eV}$. It is caused by the series limit of DR resonances involving the excitation of a $2s$ electron to the $2p$ orbital. The DR features are discussed below in section 5.2.1. The increase of the rate coefficient from $E_\mathrm{d} \approx 17\,\mathrm{eV}$ towards lower energies is an artifact most likely caused by ion beam focusing due to the electron beam. It is discussed in section 5.2.5. The structure at $E_\mathrm{d} \approx 7\,\mathrm{eV}$ probably arises from a combination of focusing effects and a transition in the collision energy distribution. At this detuning energy, the potentials inside and outside of the drift tubes match and the electrons inside and outside of the drift tubes have the same average velocity and density. Finally, at high collision energies around 30 eV, a structure is visible which fairly resembles peaks. No resonances are expected there, and especially the resonance energies for a potential excitation into the $2s2p^5\,{}^1P_1$ level (compare table 5.2 and equation (2.5)) do not coincide with the structure. As the CRYRING@ESR experiment [41] did not observe such a structure either, it is assumed to be a statistical fluctuation.

From the relative rate coefficients in figure 5.1, absolute rate coefficients can be obtained with the scaling parameter found in section 4.9.2. However, due to the artifact at lower energies, which could not be easily corrected in the analysis process, not the complete spectrum is shown on an absolute scale. Only the region around the DR resonances, where the relative rate coefficients could be reliably derived, is given on an absolute scale in the following section.

5.2.1 DR resonance features associated with a $2s \rightarrow 2p$ core excitation

Figure 5.2 shows the absolutely scaled rate coefficient for detuning energies between 21.5 eV and 26.4 eV. Around $E_\mathrm{d} = 25\,\mathrm{eV}$, a prominent recombination feature is clearly visible with a maximum rate coefficient of $1.06 \times 10^{-10}\,\mathrm{cm^3\,s^{-1}}$. At detuning energies

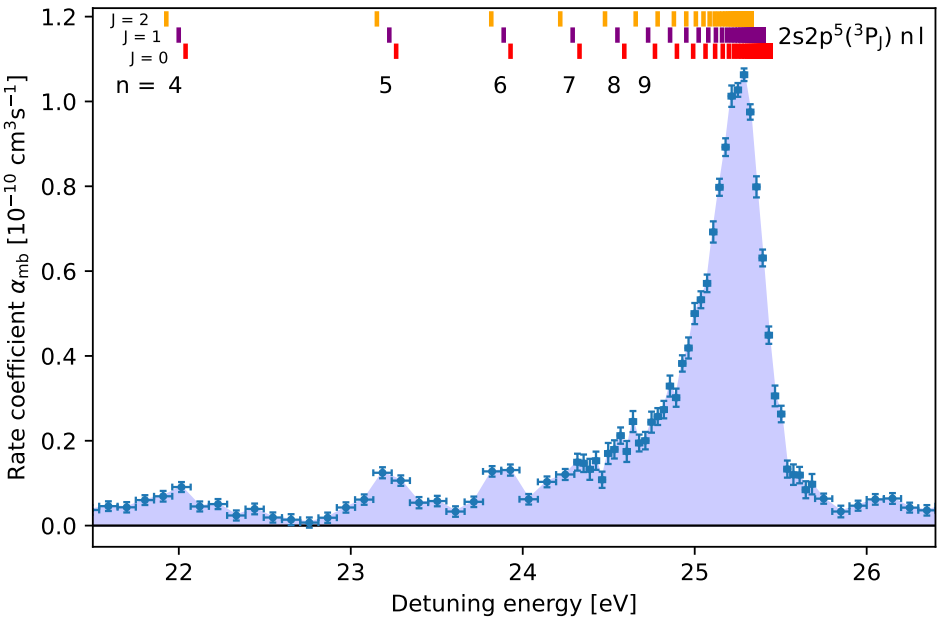

Figure 5.2: Measured merged-beams rate coefficient α_{mb} for detuning energies between 21.5 eV and 26.4 eV where DR resonances for the core excitation $2s^2 2p^4 \rightarrow 2s2p^5$ are observed. The error bars indicate the statistical uncertainty. The additional uncertainty due to the absolute scaling procedure amounts to 40 %. The lines in the upper part of the figure mark the DR resonance energies for a core excitation from the $2s^2 2p^4\,{}^3P_2$ ground state into the $2s2p^5\,{}^3P_J$ triplett.

of $E_{\mathrm{d}} \approx 22.0\,\mathrm{eV}$, 23.2 eV and 23.9 eV, three smaller peaks are resolvable in the MBRC with $\alpha_{\mathrm{mb}} \approx 0.9 \times 10^{-11}\,\mathrm{cm^3\,s^{-1}}$, $1.2 \times 10^{-11}\,\mathrm{cm^3\,s^{-1}}$ and $1.3 \times 10^{-11}\,\mathrm{cm^3\,s^{-1}}$. All of these resonance features can be assigned to DR involving a $2s \rightarrow 2p$ core excitation of the Ne^{2+} ion, more specifically involving an excitation into the $2s2p^5\,{}^3P$ triplett.

According to the NIST Atomic Spectra Database [129], there are three excited levels in the $2s2p^5\,{}^3P$ triplett with excitation energies around $E_{\mathrm{ex}} \approx 25.4\,\mathrm{eV}$ (see table 5.2). The resonance energies E_n^{DR} for the DR process can be calculated by equation (2.5) on page 7. The lines in figure 5.2 indicate the calculated resonance energies for the excitation from the $2s^2 2p^4\,{}^3P_2$ ground level of Ne^{2+} into the $2s2p^5\,{}^3P$ triplett. The three measured peaks in the MBRC at detuning energies of $E_{\mathrm{d}} \approx 22.0\,\mathrm{eV}$, 23.2 eV and 23.9 eV match the expected resonance energies for capture of the free electron into level with $n = 4, 5, 6$, respectively. The resonance energies are increasingly closely spaced as the series limit is approached. Therefore, the peaks for capture into $n = 7, 8, 9$ are only vaguely separable before the resonances overlap strongly and accumulate in the prominent peak at the series limit at $E_{\mathrm{d}} \approx 25.3\,\mathrm{eV}$.

With the given collision energy resolution and statistics achieved in the experiment, resonances correlated to excitations into individual levels within the $2s2p^5\,{}^3P$ triplett are not separable. Their spacing is below 0.1 eV (compare table 5.2), which is smaller

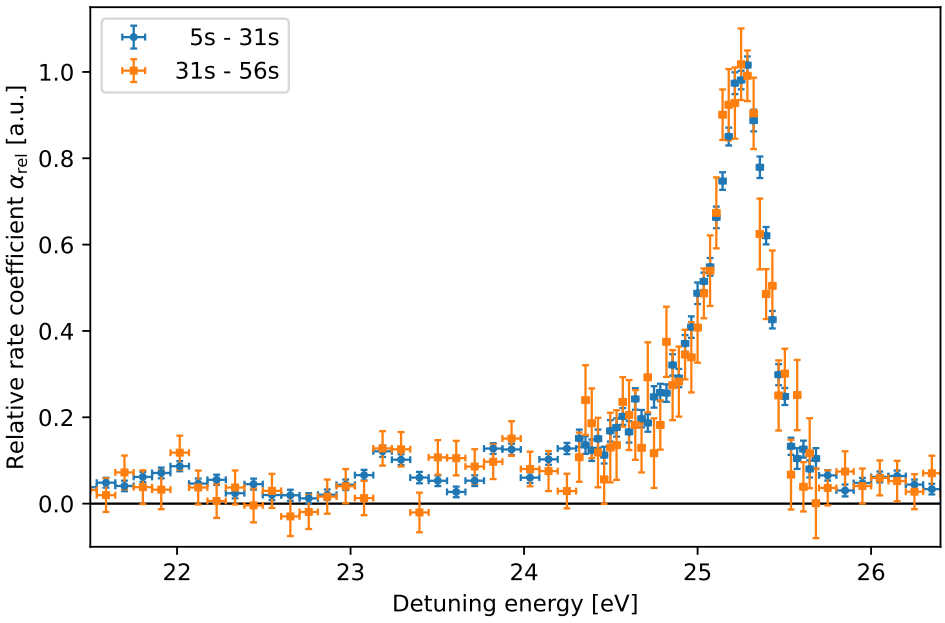

Figure 5.3: Relative recombination rate coefficients of Ne^{2+} for two storage time windows of 5 s to 31 s and 31 s to 56 s.

than the expected energy resolution due to the electron beam temperatures of about 0.26 eV, as derived in section 4.3. With the same argument, it can also not be discriminated between resonances correlated to ions in different metastable levels that are potentially present in the stored ion beam (which are, according to section 4.10, mostly $2s^2 2p^4\, ^3P_J$ with $J = 2, 1, 0$). No clear resonance features were found for capture into $n = 2$ and $n = 3$, which were expected at $E_\mathrm{d} \approx 11.8$ eV and $E_\mathrm{d} \approx 19.3$ eV, respectively.

The experimentally investigated detuning energy range covers also the expected resonance energies for electron capture into low n states linked to a core excitation into the $2s2p^5\, ^1P_1$ level or the $2s^2 2p^3 3s$ and $2s^2 2p^3 3p$ configurations. No distinct features corresponding to these excitations were found. In any case, the experimental merged-beams rate coefficient gives clear evidence for DR resonances associated with a $2s^2 2p^4 \rightarrow 2s2p^5\, ^3P_J$ core excitation.

5.2.2 Storage time dependency

As found in section 4.10 on page 66, the stored Ne^{2+} ion beam might consist of different fine structure levels of the $2s^2 2p^4$ ground configuration. All of these potentially populated levels can, in principle, contribute to the measured MBRC. To estimate the effect of a potential change of the level population with storage time, the measured rate coefficient around the $2s \rightarrow 2p$ series limit was evaluated for two different storage time windows. The lengths of these windows correspond to the duration of a single energy scan. The resulting relative rate coefficients for storage times of 5 s to 31 s and 31 s to

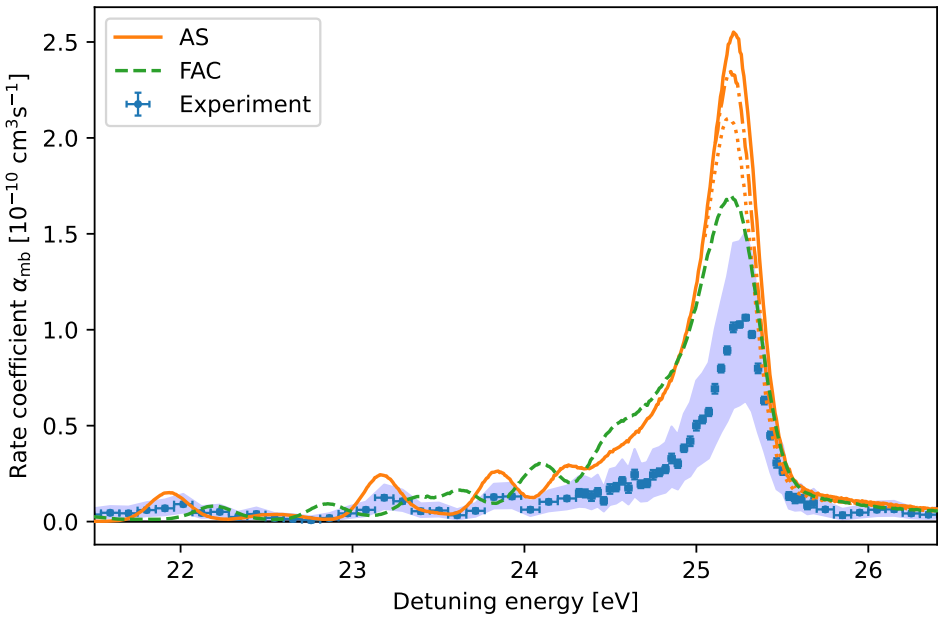

Figure 5.4: Comparison of the experimental merged-beams recombination rate coefficient of Ne^{2+} with theoretical calculations making use of *AUTOSTRUCTURE* (AS) and the *Flexible Atomic Code* (FAC). The shaded blue area indicates the systematic uncertainty of 40 % on the experimental rate coefficient. The solid orange line corresponds to the AS calculation including electron capture into levels with $n \leq 35$ in agreement with the expected experimental cut-off quantum number. The dash-dotted and dotted orange lines mark AS calculations with $n \leq 30$ and $n \leq 27$, respectively. The FAC calculation (green dashed line), which was performed by Singh, Harman, and Keitel [135], accounts for electron capture into $n \leq 30$.

56 s are presented in figure 5.3. The strongly different statistical error bars reflect the fact that more runs were available for short storage times, and the limited ion beam lifetime in CSR. With the given statistics, no indication of a storage time dependence is discernible.

5.2.3 Comparison with theoretical calculations

The experimentally obtained MBRC of DR of Ne^{2+} is compared to two theoretical calculations here. In a first approach, autoionization and radiative transition rates, and subsequently DR cross sections were calculated for a $2s \rightarrow 2p$ core excitation out of the $2s^2 2p^4\, {}^3P_2$ ground level, using the *AUTOSTRUCTURE* (AS) code [130, 131]. In the AS calculation, the core excitation energies from the NIST Atomic Spectra Database (see table 5.2) were employed. In agreement with the expected cut-off due to field ionization, electron capture into levels up to $n \leq 35$ (with $l \leq 20$) was considered. In addition, two AS calculations with lower $n \leq 30$ and $n \leq 27$ were performed. The collision-energy-dependent cross sections were subsequently convolved with the experimental

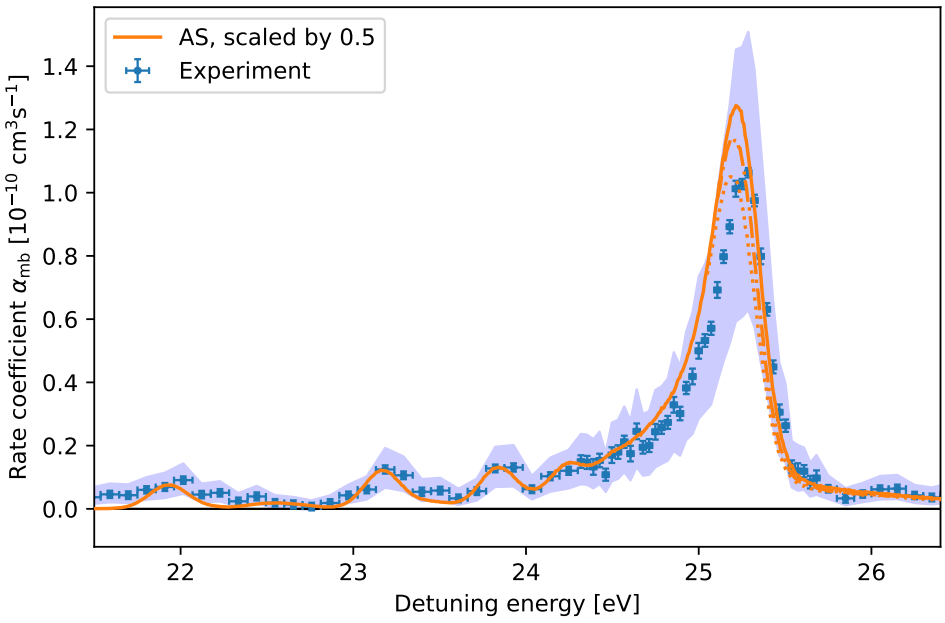

Figure 5.5: Comparison of the experimental merged-beams recombination rate coefficient of Ne^{2+} with the theoretical AS calculations including electron capture into levels with $n \leq 35$ (solid line), $n \leq 30$ (dash-dotted line), and $n \leq 27$ (dotted line). The theoretical rate coefficients were scaled by a factor of 0.5. The shaded blue area indicates the systematic uncertainty of 40 % on the experimental rate coefficient.

collision energy distribution (compare section 4.3.2 on page 39) to obtain the theoretical MBRCs. Therefore, a Monte-Carlo simulation implemented in the *hydrocal* code by Stefan Schippers [90] was utilized, assuming electron beam temperatures of $kT_{\parallel} = 0.2\,\text{meV}$ and $kT_{\perp} = 3\,\text{meV}$. In a second approach, Singh, Harman, and Keitel [135] calculated DR cross sections utilizing the *Flexible Atomic Code* (FAC) [136, 137] for a $2s \rightarrow 2p$ core excitation out of the $2s^2 2p^4\,{}^3P_2$ ground level and electron capture into levels up to $n \leq 30$ with $l \leq n - 1$. Here as well, the core excitation energies were adjusted to the values from the NIST Atomic Spectra Database. The cross sections were convolved into MBRCs in the same manner as the AS cross sections. Both AS and FAC calculations made use of the 'distorted wave' approach and employed self-consistent potentials. While the AS calculations were performed within several minutes of computation time, the FAC calculations were much more extensive, including the calculation of about 11 000 configuration state functions and a computation time of approximately 12 hours on a single core for electron capture into $n = 30$ [135].

The theoretical calculations are shown together with the experimental results in figure 5.4. It should be noted that the experimental cut-off quantum number for high Rydberg levels is expected to be $n_c = 36$, with $n < n_c$ contributing to the measured signal (see section 4.11). Only the AS calculation accounts for the expected cut-off correctly. For technical reasons, the FAC calculation was limited to $n \leq 30$. From the

additional AS calculation up to $n \leq 30$ (dash-dotted line in figure 5.4) the difference in the MBRC between the two cut-off quantum numbers can be estimated as $\sim 10\,\%$ on the main peak, and a similar deviation is expected for the FAC calculation.

All theoretical calculations yield larger rate coefficients than measured experimentally. Averaged over the detuning energy range between 21.5 eV and 26.4 eV shown in figure 5.4, the MBRCs from the AS calculations with $n \leq 35$, $n \leq 30$, $n \leq 27$, and from the FAC calculation with $n \leq 30$ are higher than the experimental MBRC roughly by a factor of ~ 2.1, 2.0, 1.9 and 1.9, respectively. However, the large uncertainties have to be considered, which are 40 % for the systematic experimental uncertainty and $\sim 20\,\%$ for the FAC calculation [135, 138].

Figure 5.5 shows the experimental MBRC together with the AS calculations, scaled by 0.5. Taking into account this scaling factor, the individual positions and shapes of the resonances for electron capture into $n = 4, 5, 6$ at $E_\mathrm{d} \approx 22.0\,\mathrm{eV}$, 23.2 eV and 23.9 eV are well reproduced, and the calculation with $n \leq 27$ also reproduces the shape of the main peak at the series limit, although the energy scales seem to be shifted by $\sim 0.07\,\mathrm{eV}$.

In contrast, the FAC calculation does not reproduce the resonance peaks below 24 eV correctly, but at the series limit, it yields a lower rate coefficient than the AS calculations. At the series limit, the FAC calculation exceeds the experimental data by roughly a factor of ~ 1.8.

5.2.4 Comparison with the CRYRING@ESR experiment

The motivation for choosing Ne^{2+} for the proof-of-principle experiment in CSR arose from an earlier experiment at GSI, where Ne^{2+} was investigated in one of the first electron-ion recombination experiments at CRYRING@ESR after its move to Darmstadt [41]. Esther Menz kindly provided their experimental data for a comparison of the two storage ring experiments.

Figure 5.6 shows both experimentally obtained MBRCs in the energy region where the DR resonances were found. Due to the different experimental conditions, the rate coefficients are not directly comparable. The underlying experimental electron-ion collision energy distributions are strongly different in CRYRING@ESR and CSR. While in the CSR experiment the drift tubes were used and the collision energy distribution therefore is characterized by two peaks (see section 4.3.2 on page 39), the detuning energies in the CRYRING@ESR experiment were set by varying the cathode potential and the collision energy distribution contains only one prominent peak. Additionally, different geometries when merging and demerging the electron beam into and out of the ion beam influence the collision energy distribution, as well as the electron beam temperatures. In essence, the largest part of the discrepancy can be explained by the fact that in the CRYRING@ESR experiment a larger fraction of all interacting electrons were at (or close to) the nominal detuning energy, while in CSR, due to the finite length of the drift tubes, only a smaller fraction of the interacting electrons provided

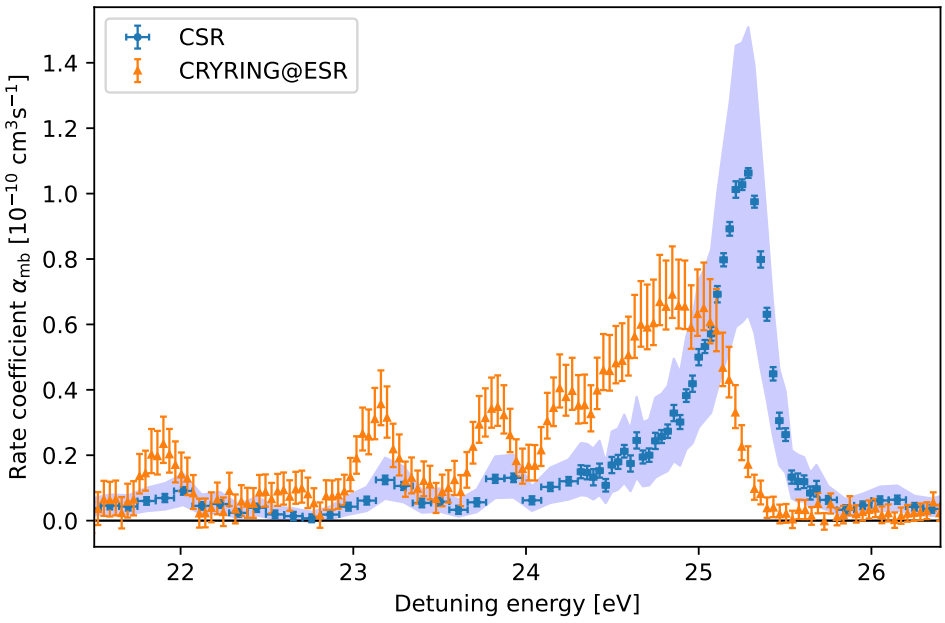

Figure 5.6: Comparison of the experimental merged-beams recombination rate coefficient of Ne^{2+} as obtained in CSR (blue) and CRYRING@ESR [41] (orange). The systematic uncertainty of 40 % in the CSR measurement is marked by the shaded area. The error bars on the CRYRING@ESR data include all uncertainties. The rate coefficients are not directly comparable due to the different experimental conditions, which influence the total signal strength and slightly distort the resonance shapes.

the desired energy. Therefore, the MBRC measured in CRYRING@ESR is larger.

For the conditions in CSR and a detuning energy of $E_d = 25.1\,\text{eV}$, the fraction ξ of electrons in the interaction region with velocities corresponding to electron-ion collision energies close to the detuning energy was estimated. In a sense, this is the fraction of electrons inside the drift tubes, but the potential and electron density transitions similar to those shown in figure 4.3 on page 39 have to be taken into account. Therefore, a flattened Maxwellian (see, e.g., [117]), representing a purely thermal distribution, was fitted to the main peak close to E_d in the collision energy distribution. From this rough estimate it was found that at $E_d = 25.1\,\text{eV}$ approximately $\xi \approx 55\,\%$ of the electrons provided energies close to the desired collision energy. When scaling the MBRC accordingly, both experiments agree within error bars as shown in figure 5.7, but the MBRC from CSR is still tentatively smaller. It should be noted once again that this comparison method is approximate. Due to the changing drift tube potential with E_d, the fraction $\xi = \xi(E_d)$ depends on the detuning energy. In the detuning energy range shown in figure 5.7, ξ is not varying too much but only by a few percent.

Both experimental MBRCs show the three distinct peaks at $E_d \approx 22.0\,\text{eV}$, 23.2 eV and 23.9 eV, corresponding to electron capture into $n = 4, 5, 6$. The peak at $E_d \approx 24.2\,\text{eV}$, linked to electron capture into $n = 7$, is resolved slightly better in the CRYRING@ESR

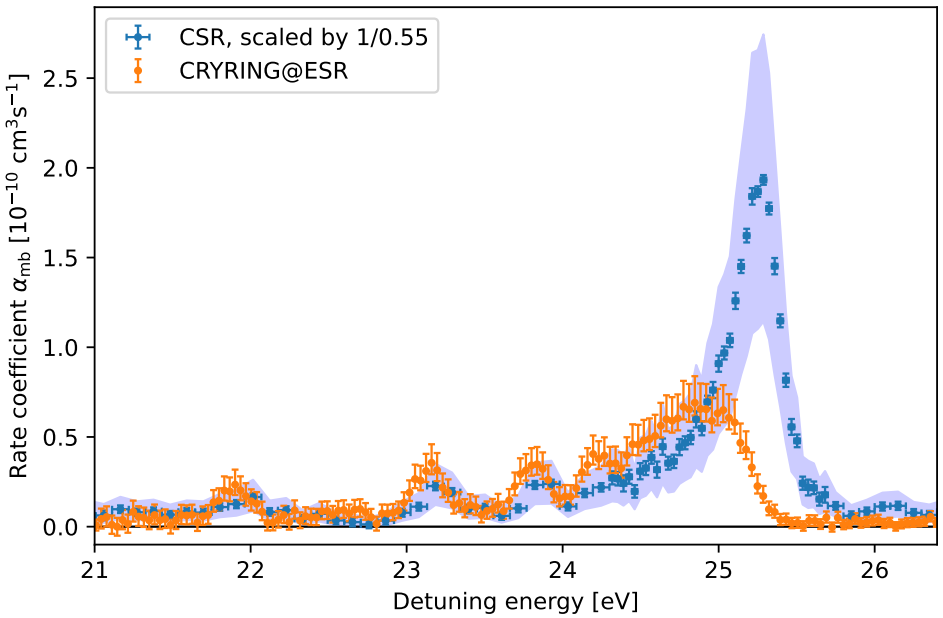

Figure 5.7: Comparison of the experimental merged-beams recombination rate coefficient of Ne^{2+} as obtained in CSR (blue) and CRYRING@ESR (orange). The systematic uncertainty of 40 % in the CSR measurement is marked by the shaded area. The CSR data was scaled by a factor $1/\xi = 1/0.55 = 1.82$ in order to roughly account for the different collision energy distributions. With this simplified scaling factor, both experiments agree within error bars. The much stronger signal near the series limit in the CSR experiment arises from the higher cut-off due to field ionization in the weaker electromagnetic fields in CSR.

data. The overall energy scale is slightly shifted in the two data sets by less than 0.1 eV. The most striking discrepancy in the two curves is the significantly higher signal in the CSR data around the series limit at 25.3 eV. It is caused by the different field ionization. While the expected cut-off quantum number in CSR is $n_c = 36$ (as derived in section 4.11 on page 69), the expected cut-off in the CRYRING@ESR experiment is only around $n_c = 13$ [41] due to the much higher field strengths in the CRYRING@ESR deflector magnets. This reflects an advantage of recombination measurements in CSR, which allow for the detection of electron capture into higher Rydberg states than is possible in magnetic storage rings.

Overall, the comparison of the two measurements in the detuning energy range around the DR series limit demonstrates that electron-ion recombination experiments with atomic ions in CSR can yield reasonable results.

5.2.5 Rising signal towards lower energies: Ion beam focusing effects

Whereas the MBRC obtained from the CSR experiment is reasonable in the region where the DR resonances occur, the MBRC at detuning energies below $E_d \approx 17$ eV is

conspicuously increased, as can be seen in figure 5.1. Although radiative recombination peaks at 0 eV and has a long tail at higher energies, the expected signal strength at an energy of 1 eV is already in the order of $10^{-13}\,\mathrm{cm^3\,s^{-1}}$, which is well below the sensitivity in this experiment. The CRYRING@ESR experiment yielded an MBRC of basically zero in the corresponding energy range [41]. Thus the enhanced signal found in CSR is not correlated to any underlying recombination rate coefficient, but it is an artifact from the measurement procedure, which is explained in the following.

The most likely reason for this strange observation is ion beam focusing due to the electron beam space charge, and a related change in the detection efficiency of the recombined ions. The electrons in the interaction region act as a focusing lens for the ion beam. The more electrons are present in the interaction region, the stronger the focusing effect. For a constant electron current, the electron density and thus the total charge in the interaction region rises towards lower collision energies, where the electrons are slower. Assuming a decreased size of the stored ion beam in this case, also the size of the recombined ion beam decreases. Due to the small effective horizontal width of the COMPACT detector in the Ne^+ position of only $\sim 18\,\mathrm{mm}$ (see appendix A.1.1), which is roughly the size of the recombined ion beam, such a focusing might lead to an increased detection efficiency for electron-induced as well as residual-gas-induced events in the measurement step at lower detuning energies. The relative rate coefficients as shown in figure 5.1 were derived from (identical to equation (4.56))

$$\alpha_{\mathrm{rel}} = \frac{1}{n_{\mathrm{e,m}}\,\alpha'_{\mathrm{peak}}}\left[\left(\frac{R_{\mathrm{m}} - R_{\mathrm{dark}}}{R_{\mathrm{c}} - R_{\mathrm{dark}}}\right) - B\right], \tag{5.3}$$

with the offset parameter B from equation (4.54),

$$B = \frac{\alpha_{\mathrm{rg}}\,n_{\mathrm{rg}}\,\eta_{\mathrm{rg,m}}\,l_{\mathrm{rg}}}{\alpha_{\mathrm{e,c}}\,n_{\mathrm{e,c}}\,\eta_{\mathrm{e,c}}\,l_{\mathrm{e}} + \alpha_{\mathrm{rg}}\,n_{\mathrm{rg}}\,\eta_{\mathrm{rg,c}}\,l_{\mathrm{rg}}} \propto \eta_{\mathrm{rg,m}}. \tag{5.4}$$

In principle, B can be energy dependent via the changing detection efficiency for residual-gas-induced events in the measurement step $\eta_{\mathrm{rg,m}}$. This effect might also be non-linear. In the analysis, as the individual constituents could not be quantified directly, B was not calculated but adjusted manually. Only one constant B was assumed for each detuning energy range when stitching together the spectrum, and B was chosen to fit the respective range to the next higher range. Therefore, B can well be underestimated for lower detuning energies, leading to an artificial increase of α_{rel}.

The sensitivity of the obtained MBRC on the choice of B can be demonstrated from a dedicated measurement which is presented here.

During the regular runs, a varying cooling signal was observed, depending on the electron cooler settings, as shown below in section 5.3. It was speculated that a varying cooling signal (which was used for normalization) might as well distort the signal below $E_{\mathrm{d}} \approx 17\,\mathrm{eV}$. To investigate the observed increased signal at lower detuning energies and the influence of a potentially corrupted normalization on the cooling step, a dedicated

Table 5.3: Offset parameter B for normalization procedures based on different relative rates $\tilde{R}$ as in equation (5.5). The given value for B was used in figure 5.8.

$\tilde{R}$	B	value
$\frac{R_\mathrm{m}-R_\mathrm{dark}}{R_\mathrm{c}-R_\mathrm{dark}}$	$\frac{\alpha_\mathrm{rg}\, n_\mathrm{rg}\, \eta_\mathrm{rg,m}\, l_\mathrm{rg}}{\alpha_\mathrm{e,c}\, n_\mathrm{e,c}\, \eta_\mathrm{e,c}\, l_\mathrm{e} + \alpha_\mathrm{rg}\, n_\mathrm{rg}\, \eta_\mathrm{rg,c}\, l_\mathrm{rg}}$	0.986
$\frac{R_\mathrm{m}-R_\mathrm{dark}}{R_\mathrm{r}-R_\mathrm{dark}}$	$\frac{\alpha_\mathrm{rg}\, n_\mathrm{rg}\, \eta_\mathrm{rg,m}\, l_\mathrm{rg}}{\alpha_\mathrm{e,r}\, n_\mathrm{e,r}\, \eta_\mathrm{e,r}\, l_\mathrm{e} + \alpha_\mathrm{rg}\, n_\mathrm{rg}\, \eta_\mathrm{rg,r}\, l_\mathrm{rg}} \approx \frac{\eta_\mathrm{rg,m}}{\eta_\mathrm{rg,r}}$	1
$\frac{R_\mathrm{m}-R_\mathrm{dark}}{R_\mathrm{o}-R_\mathrm{dark}}$	$\frac{\eta_\mathrm{rg,m}}{\eta_\mathrm{rg,o}}$	1.014

measurement was set up to test different normalization procedures. In this dedicated measurement, six measurement energies were scanned at $E_\mathrm{d} \approx 1\,\mathrm{eV}$, 5 eV, 10 eV, 20 eV, 25.3 eV and 33 eV, spanning almost across the full accessible detuning energy range. The wobbling scheme included a reference step at 28 eV and an off step without electrons. The electron current in measurement and reference steps was 130 µA and therefore lower than in most of the regular runs.

The additional steps allow for testing of different normalization procedures. A general expression to derive the electron-induced rate coefficient in the measurement step from a relative rate $\tilde{R} = \frac{R_\mathrm{m}-R_\mathrm{dark}}{R_j-R_\mathrm{dark}}$ with $j \in$ c,r,o noting the respective step is

$$\alpha_\mathrm{e,m} = \frac{A}{n_\mathrm{e,m}} \left(\tilde{R} - B\right). \tag{5.5}$$

As an example, three different normalization procedures are compared here. The relative rates $\tilde{R}$ as well as the corresponding offset parameters B are given in table 5.3. The results obtained from the different normalization procedures are shown in figure 5.8.

When normalizing on an electron-induced signal, e.g., on the cooling step with $\tilde{R} = \frac{R_\mathrm{m}-R_\mathrm{dark}}{R_\mathrm{c}-R_\mathrm{dark}}$ as done for the regular runs, the offset B can only be calculated with accurate knowledge of the rate coefficients α_e and α_rg for recombination with free electrons and for electron-capture from residual-gas particles, respectively. As this is not feasible, B has to be estimated such that the obtained rate coefficient becomes 0 where expected, which partially failed in the analysis above. For the representation in figure 5.8, $B = 0.986$ was assumed. Here, a rise of the relative rate coefficient towards lower energies is noticeable.

A normalization on the reference step, $\tilde{R} = \frac{R_\mathrm{m}-R_\mathrm{dark}}{R_\mathrm{r}-R_\mathrm{dark}}$, simplifies the interpretation significantly, given the fact that the reference is chosen at an energy with negligible electron-induced recombination rate coefficient. In this case, $B \approx \frac{\eta_\mathrm{rg,m}}{\eta_\mathrm{rg,r}}$ is close to unity in case measurement and reference energy are close and in case the same electron current is used in both steps. This procedure was used in the Xe^{3+} beamtime. It gives similar results as the normalization on the cooling signal, but does not require a manual

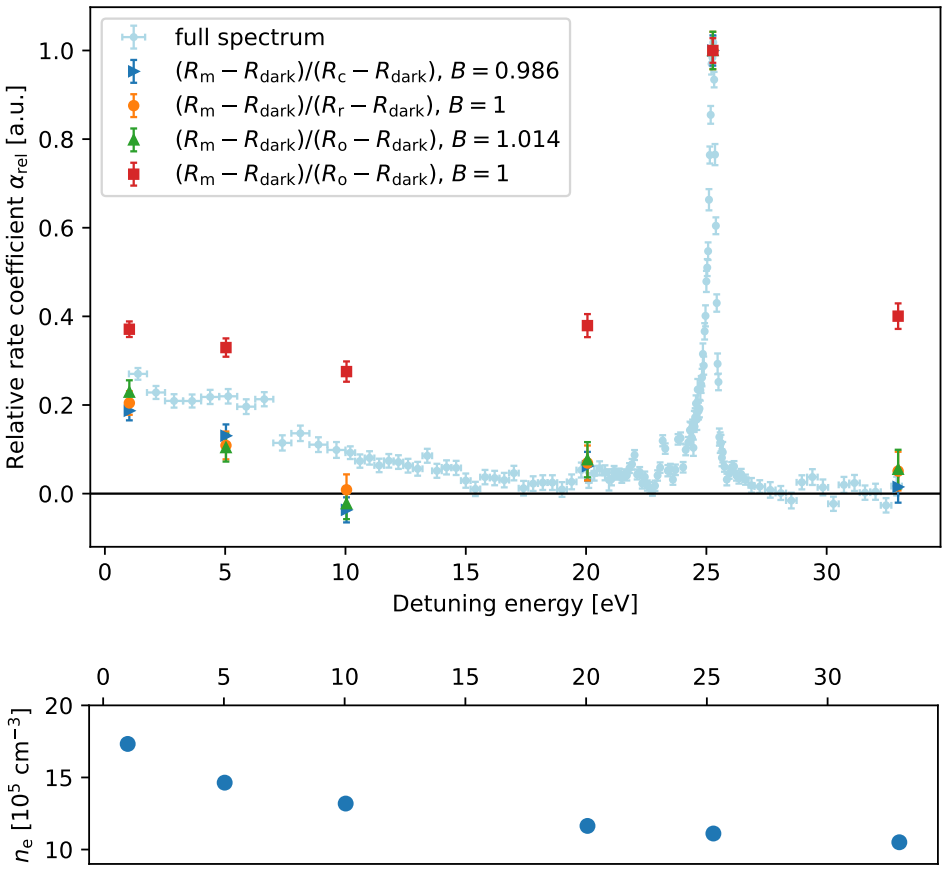

Figure 5.8: Relative rate coefficients as obtained from different normalization procedures from the dedicated scan in the Ne^{2+}beamtime (upper figure). R_i symbolize the measured count rates in the various steps: R_m is the count rate in the measurement step, R_c the count rate in the cooling step, R_o the count rate in the off step, and R_{dark} the dark count rate. All curves were obtained from equation (5.5) and normalized to the value at $E_d = 25.3\,eV$. The used offset parameters B are indicated. The spectrum from figure 5.1 is shown for comparison in light blue. The electron densities n_e in the measurement step at the respective detuning energies are shown in the lower figure.

adjustment of B. However, the relative rate coefficient is rising here as well for low energies which are far from the reference energy of 28 eV.

When normalizing on the off step, $\tilde{R} = \frac{R_m - R_{dark}}{R_o - R_{dark}}$, the offset B is the ratio between detection efficiencies for residual-gas-induced signal in the measurement and in the off step, i.e. $B = \frac{\eta_{rg,m}}{\eta_{rg,o}}$. Here, the effect of focusing is directly visible when comparing relative rate coefficients evaluated with $B = 1$ and $B = 1.014$, as shown figure 5.8. A small variation of B on the 1 %-level distorts the spectrum significantly. With an assumed difference in $\eta_{rg,m}$ and $\eta_{rg,o}$ of only 1.4 %, the obtained relative rate coefficient fits the other normalization procedures, as shown in figure 5.8.

All compared normalization procedures give approximately the same result when an appropriate B is assumed. The normalization procedure itself therefore does not cause the rise towards lower energies, which is still apparent. The effect of the electron beam on the detection efficiency is clearly observable from the behavior of the off-normalized signal. A small change in the assumed B, which is in this case the ratio of detection efficiencies in measurement and off steps, influences the result substantially. This finding indicates that a sub-% variation in the detection efficiency at different detuning energies might indeed be the cause for the observed signal increase towards lower detuning energies.

The electron densities in the measurement steps are indicated in the lower part of figure 5.8. Below $E_\mathrm{d} = 10\,\mathrm{eV}$, the electron densities drop from $17.3 \times 10^5\,\mathrm{cm}^{-3}$ to $13.2 \times 10^5\,\mathrm{cm}^{-3}$, above 10 eV, the densities do not vary too strongly anymore and range down to $10.5 \times 10^5\,\mathrm{cm}^{-3}$ at 33 eV. This aligns with the observed increase in the MBRC at low detuning energies, which is potentially produced by a stronger focusing of the ion beam at higher electron densities and a subsequently larger detection efficiency. The discrepancy between the MBRC from the dedicated measurement here and the overall spectrum from the regular runs, which is shown in light blue in figure 5.8, can be explained by the different electron currents used. Especially in the region below 10 eV, a higher electron current I_e was used here (150 µA) than in the regular runs (130 µA), explaining the even stronger increase of the MBRC here. At higher detuning energies, a lower I_e was applied here than in the regular runs (130 µA), resulting in potentially reduced focusing effects here.

In order to get a rough estimate on the ion beam focusing effect due to the electron beam space charge, Manfred Grieser calculated the betatron functions in CSR for different electron densities. His calculations indicate a variation in the horizontal betatron function β_x in the electron cooler section for varying electron densities n_e. The comparison of $n'_\mathrm{e} = 17.3 \times 10^5\,\mathrm{cm}^{-3}$ and $n''_\mathrm{e} = 13.2 \times 10^5\,\mathrm{cm}^{-3}$ (roughly corresponding to the conditions at $E_\mathrm{d} = 1\,\mathrm{eV}$ and 10 eV, respectively, in the measurement runs; see table 5.1) yields $\beta_\mathrm{x}(n'_\mathrm{e}) \approx 0.934\,\beta_\mathrm{x}(n''_\mathrm{e})$ [139]. A variation in the horizontal betatron function β_x translates to the horizontal ion beam size x via the emittance ϵ,

$$x = \sqrt{\epsilon\,\beta_\mathrm{x}}. \tag{5.6}$$

The calculated shift in the betatron function therefore leads to a $\sim 3\,\%$ reduced ion beam size in the electron cooler for the higher density, $x(n'_\mathrm{e}) \approx 0.966\,x(n''_\mathrm{e})$. The quantitative relation between this beam shrinking and the resulting detection efficiency is not trivial. For the latter, the overall beam size matters (whether the product beam is fully captured by the COMPACT detector or not) and the contribution of the detector side plates (see appendix A). The offset parameters B that would be needed to bring the signal at 1 eV and 10 eV to zero differ by roughly $\sim 1\,\%$, which directly translates to a $\sim 1\,\%$ decrease in the detection efficiency at 10 eV compared to 1 eV. This value is in the same order of magnitude as the calculated ion beam shrinking.

While such a 1 %-variation in the detection efficiency is almost negligible concerning the *absolute* scaling of the rate coefficient, it leads to strong distortions in the *relative* rate coefficients. Although ion beam focusing by the electron beam space charge can be assumed as a likely explanation for the signal increase towards lower energies, unfortunately this effect cannot be easily quantified or corrected in the measured data. Luckily, the most interesting part of the recorded spectrum, where the DR resonances were observed, was not severely affected by these focusing effects due to the smaller variation in the electron density in this region.

In section 5.4, it is described how the effect of varying ion beam focusing on the obtained rate coefficients can be mitigated in future experiments.

5.3 Recombination close to 0 eV

In the discussion above, detuning energies close to zero were excluded so far. The signal from RR is strongest at these low energies, and the recorded data in this region is reviewed here.

During the regular 'high energy' runs, it was found that the electron-induced rate at cooling energy ($E_{\mathrm{d,cool}} = 0\,\mathrm{eV}$) changed with respect to the electron-induced rate at the DR peak when varying the electron cooler settings. To investigate this behavior, dedicated measurements around the RR peak at 0 eV were conducted for four different cooler settings. In the individual measurements, the magnetic guiding fields in the electron cooler as well as the cathode potential U_{cath} were varied, influencing the electron energy outside of the drift tubes. The four settings were:

- low B fields, $U_{\mathrm{cath}} = -50\,\mathrm{V}$ (standard settings for runs at higher energies)
- low B fields, $U_{\mathrm{cath}} = -30\,\mathrm{V}$
- low B fields, $U_{\mathrm{cath}} = -60\,\mathrm{V}$
- high B fields, $U_{\mathrm{cath}} = -50\,\mathrm{V}$

In the low fields configuration, the magnetic guiding fields were set to 1500 G, 100 G and 50 G in the big and small room temperature solenoids and in the interaction region, respectively. The magnetic fields in the high fields configuration were 3000 G, 200 G and 100 G. In both configurations, an expansion of $\alpha = 30$ was kept. The high field configuration consisted of the fields that are usually applied for recombination experiments with molecular ions to guarantee an adiabatic transport of the electron beam (see [109]). However, recombination experiments with atomic ions are much more sensitive to the residual-gas pressure than experiments with molecular ions, and it has

Table 5.4: Cathode potentials U_{cath} together with the corresponding nominal collision energies $E_{\mathrm{out,d}}$ outside of the drift tubes. The electron densities $n_{\mathrm{e,c}}$ at cooling and at detuning energies of $E_{\mathrm{d}} \approx 0.13\,\mathrm{eV}$ for the electrons faster ($n_{\mathrm{e}}^{\mathrm{fast}}$) and slower ($n_{\mathrm{e}}^{\mathrm{slow}}$) than the ion beam are given in $10^5\,\mathrm{cm}^{-3}$.

U_{cath} [V]	$E_{\mathrm{out,d}}$ [eV]	$n_{\mathrm{e,c}}$	$n_{\mathrm{e}}^{\mathrm{fast}}(0.13\,\mathrm{eV})$	$n_{\mathrm{e}}^{\mathrm{slow}}(0.13\,\mathrm{eV})$
−30	1.3	8.5	8.0	9.1
−50	7.8	8.0	7.5	8.6
−60	12.2	7.8	7.3	8.5

been found that the background signal from electron-capture collisions with residual gas can be severely reduced when lowering the magnetic fields. Lower magnetic fields reduce the heat influx to the interaction region, and a colder interaction region directly translates to a lower residual-gas density as more residual-gas particles freeze out at the chamber wall. Therefore, the low fields configuration was the standard setting for the runs at higher detuning energies.

Besides varying the magnetic guiding fields, also the voltage at the photocathode U_{cath} was varied. Therefore, the electron lab frame energy in the interaction region outside of the drift tubes varied, and consequently also the collision energy outside the drift tubes, which is characterized here by the nominal out-of-drift-tube detuning energy $E_{\mathrm{out,d}}$. In table 5.4, the different $E_{\mathrm{out,d}}$ corresponding to the different U_{cath} are noted.

The measurement schemes in the 0 eV to 1 eV scans consisted of cooling and measurement steps only. In contrast to the runs at higher energies, no measurement steps at the DR peak at $E_{\mathrm{d}} \approx 25.3\,\mathrm{eV}$ were inculded in most of the runs here. To avoid dragging effects, the scans were set symmetrically around 0 eV, sampling alternatingly collisions with electrons faster and slower than the ion beam. The electron current in cooling and measurement steps was 47 µA, and the corresponding electron densities at cooling and at a detuning energy of 0.13 eV (which was the highest E_{d} included in the measurement at $U_{\mathrm{cath}} = -50\,\mathrm{V}$) with the electron beam faster and slower than the ion beam, respectively, are listed in table 5.4.

Figure 5.9 displays the recorded relative rates $\frac{R_{\mathrm{m}}-R_{\mathrm{dark}}}{R_{\mathrm{c}}-R_{\mathrm{dark}}}$ for collisions with faster and slower electrons for low guiding fields and $U_{\mathrm{cath}} = -50\,\mathrm{V}$. Both branches are not expected to overlap perfectly, as the relative rates in figure 5.9 are neither corrected for the changing electron densities (which are slightly higher for the slow branch and therefore increase the count rates there, compare table 5.4) nor for the fact that the electrons in the slow branch sampled over the RR peak in the transition region at the end of the drift tubes (which also increases the count rates there). Nonetheless, the still rather good agreement of the faster and the slower branch in figure 5.9 suggests that these effects are weak and especially that ion beam focusing effects as described in section 5.2.5 do not distort the shape of the RR peak.

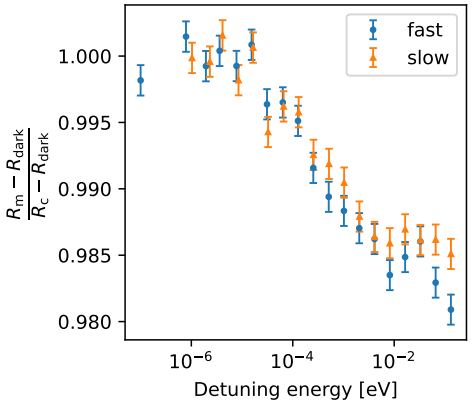

Figure 5.9: Comparison of the relative rates $\frac{R_m - R_{dark}}{R_c - R_{dark}}$ for ion collisions with faster and slower electrons at low magnetic guiding fields and a cathode voltage $U_{cath} = -50\,V$ (resulting in a nominal out-of-drift-tube detuning energy of $E_{out,d} \approx 7.8\,eV$).

Absolute scaling of the RR peak was only possible for the conditions with low magnetic fields and a cathode voltage of $U_{cath} = -50\,V$ (see section 4.9.2.2 on page 61). Due to missing reference points at the DR peak, the low-energy measurements can also not be put on a reliable relative scale. Therefore, the RR peak is discussed mostly qualitatively in the following, focusing on the differences in the various settings.

5.3.1 Influence of the out-of-drift-tube energy

The three measurements with low fields were carried out right after each other and took approximately 6 h, 7.5 h and 2 h for $U_{cath} = -50\,V$, $-30\,V$ and $-60\,V$, respectively. Figure 5.10a shows the relative count rates normalized to the cooling signal, $\frac{R_m - R_{dark}}{R_c - R_{dark}}$, for these three measurements. The signals for the measurements at $-50\,eV$ and $-60\,eV$ look fairly similar, but the curve obtained with the lower cathode voltage ($U_{cath} = -30\,V$) differs. Assuming an electron-induced signal of almost 0 at a detuning energy of 1 eV, the rates suggest that in the runs with higher cathode voltages approximately 98.2 % of the signal is caused by residual gas (corresponding to the offset parameter B from equation (4.52)), while it is only 96.5 % at the lower cathode potential. This observation can have two reasons:

1. The residual-gas pressure in CSR was lower for the measurement at $U_{cath} = -30\,V$ than for the other two measurements at $-50\,V$ and $-60\,V$.

2. The electron-induced signal is stronger for the measurement at $U_{cath} = -30\,V$ than for the other two measurements at $-50\,V$ and $-60\,V$.

The first reason cannot be excluded completely as the ion numbers were not measured in these runs and the recorded count rate is proportional to both, ion number and residual-gas density. However, the measurements were conducted right after each other in the

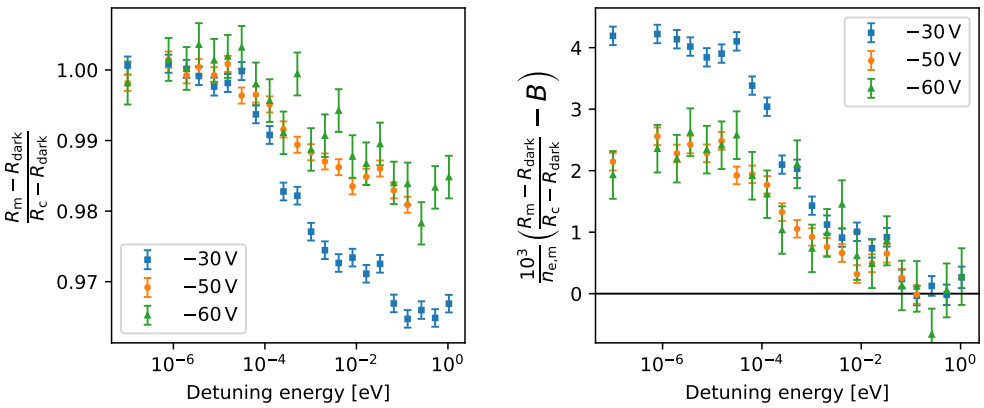

(a) (b)

Figure 5.10: Comparison of the measurements at different cathode voltages $U_{\text{cath}} = -30\,\text{V}$, $-50\,\text{V}$ and $-60\,\text{V}$, corresponding to nominal out-of-drift-tube detuning energies of $E_{\text{out,d}} = 1.3\,\text{eV}$, $7.8\,\text{eV}$ and $12.2\,\text{eV}$, respectively. The displayed data come from collisions where the electrons were faster than the ions. The relative rates in (a) suggest offset parameters B of 0.965, 0.981 and 0.983, respectively, denoting the fraction of the residual-gas-induced signal on the total count rate. In (b), the relative rates were offset by B and corrected for the effect of varying electron density.

order $U_{\text{cath}} = -50\,\text{V}$, $-30\,\text{V}$, $-60\,\text{V}$, and no indication was found that the residual-gas pressure went strongly down and up again over that time. The trend is visible even when filtering on injections that are close in time to the switch in the cathode voltages. A pure effect of residual-gas pressure therefore seems unlikely to explain the discrepancy. In figure 5.10b, the offset B due to residual-gas-induced events was subtracted and the influence of the varying electron density was corrected. The difference between low and high cathode voltages is roughly a factor of 2. The variation in the collision energy distributions at the different cathode potentials cannot explain the discrepancy. The reason for the changing signal at 0 eV remains not understood.

For the conditions at high magnetic fields, only one measurement was taken at a cathode voltage of $U_{\text{cath}} = -50\,\text{V}$. This measurement was carried out several days after the measurements at low magnetic fields, and the residual-gas density at that time (due to the higher heat influx to the interaction region at higher magnetic fields) was strongly different. For this reason, the measurement at high magnetic fields was not considered in the comparison of different out-of-drift-tube energies above.

5.3.2 Shape of the RR peak

Regardless of the cathode woltage and the strength of the magnetic guiding fields, a comparison of the shape of the RR peak can be made. The relative rate coefficients were derived for each of the cooler settings using appropriate offset parameters B, and were

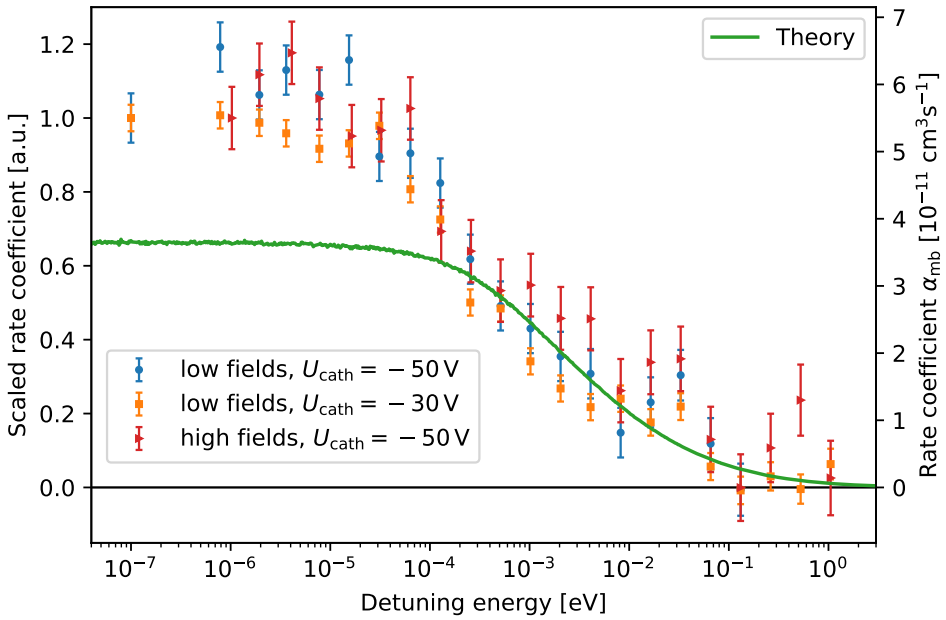

Figure 5.11: Comparison of the shape of the RR peak for different cooler settings (low and high magnetic guiding fields, different cathode voltages U_{cath}). Each of the runs was scaled to the signal at 0 eV and plotted on a relative scale (left side). The absolute MBRCs are not necessarily identical for all measurements. For comparison, a theoretical calculation of the MBRC due to RR is shown (solid green line, axis on the right). The *hydrocal* code [90] was used for the calculation, assuming electron beam temperatures of $kT_{\parallel} = 0.25\,\mathrm{meV}$ and $kT_{\perp} = 2.5\,\mathrm{meV}$, and capture into $n \leq 35$. The representation is chosen such that the theoretical and experimental curves overlap at energies $\gtrsim 2 \times 10^{-4}\,\mathrm{eV}$.

scaled to the signal at 0 eV collision energy. These scaled rate coefficients are shown for low fields at cathode potentials of $U_{\mathrm{cath}} = -50\,\mathrm{V}$ and $-30\,\mathrm{V}$ (the measurement at $-60\,\mathrm{V}$ was excluded here due to bad statistics) and for high fields at $U_{\mathrm{cath}} = -50\,\mathrm{V}$ in figure 5.11. With given statistics, it is difficult to find any differences in the shape of the peak. For comparison, the expected MBRC for RR was calculated, using the *hydrocal* code [90], for electron capture into states with $n \leq 35$, and electron beam temperatures of $kT_{\parallel} = 0.25\,\mathrm{meV}$ and $kT_{\perp} = 2.5\,\mathrm{meV}$ were assumed. Below 0.1 meV, the calculated MBRC is $\sim 3.6 \times 10^{-11}\,\mathrm{cm^3\,s^{-1}}$, which is just inside of the assumed uncertainty margin of the experimentally obtained value of $(11.2 \pm 7.6) \times 10^{-11}\,\mathrm{cm^3\,s^{-1}}$ at 0 eV, which was derived in section 4.9.2.2 on page 61. The representation in figure 5.11 is chosen such that the theoretical calculation overlaps with the experimentally obtained data for detuning energies above 0.2 meV. The overshooting experimental signal below 0.2 meV might be a hint for rate enhancement as observed at very low collision energies in many storage ring experiments (e.g. [56, 57]), attributed to the collision dynamics in the fields of the electron coolers [58, 59].

However, due to poor statistics and an imprecise absolute scaling, any final statement about the experimentally derived rate coefficient for RR remains speculative.

5.4 Summary and conclusion

In this chapter, the results from the recombination experiment of O-like Ne^{2+} with free electrons at CSR have been presented. The experiment was planned as a proof-of-principle to verify that electron-ion recombination with atomic ions can be measured at CSR.

Recombination at detuning energies between 0 eV and 33 eV has been measured. In the region between 21.5 eV and 26.4 eV, DR resonances correlated to the excitation of a $2s$ electron to the $2p$ orbital were found, and the MBRC could be absolutely scaled with an uncertainty of 40 %. At the DR series limit at $E_\mathrm{d} \approx 25.3\,\mathrm{eV}$, the MBRC is $\alpha_\mathrm{mb} \approx 10.6 \times 10^{-11}\,\mathrm{cm^3\,s^{-1}}$. The lowest resolvable MBRC is below $1 \times 10^{-11}\,\mathrm{cm^3\,s^{-1}}$. The results are in qualitative agreement with an earlier recombination measurement performed at CRYRING@ESR [41], demonstrating the feasibility of such measurements at CSR. Due to the lower field strengths in CSR compared to magnetic storage rings operating at higher ion energies, like CRYRING@ESR, the cut-off due to field ionization is reduced, thus allowing for the study of recombination into higher Rydberg levels.

MBRCs obtained from theoretical calculations reproduce the overall structure of the experimentally observed DR features, but exceed the measured MBRC by a factor of approximately 2.

At lower detuning energies, the derived rate coefficients are artificially increased, most likely because of focusing of the ion beam by the electron beam space charge, and a subsequent change in the detection efficiency. These effects mostly occur when the variation of the electron density within one run is large. These effects could not be corrected for in the analysis. However, focusing effects were small in the most interesting region around the DR resonances. As the rate coefficients are distorted at energies below $E_\mathrm{d} \approx 17\,\mathrm{eV}$ for this reason, no plasma rate coefficients were derived in this thesis.

At very low detuning energies below 1 eV, the RR peak has been recorded. Although absolute scaling only possible with a large uncertainty, hints for a varying MBRC close to 0 eV were found for different electron cooler settings. A comparison of the shape of the RR peak with a theoretical calculation suggests rate enhancement, which was also observed in earlier storage ring experiments. In future experiments, the suspected rate enhancement, and especially the effect of the out-of-drift-tube energy, can potentially be studied in more detail.

The hardest challenge in the present experiment was the extremely high background from ion collisions with the residual gas. Charge exchange collisions of the stored ion

beam with the residual gas produced approximately 98 % of the total count rate at cooling and approximately 95 % of the total count rate at the DR series limit. In other words, only approximately 2 % and 5 %, respectively, of the total signal were actually electron-induced at the strongest features in the recombination spectrum. A reduced residual-gas density in the ring, and therefore a reduced background signal, would be the most important improvement for atomic recombination experiments at CSR in general. Not only would the time needed to acquire good statistics be shortened, but also the effects of ion beam focusing due to the electron density in the interaction region would be mitigated.

In the Ne^{2+} experiment, the ratio $(R_m - R_{dark})/(R_c - R_{dark})$ was close to unity across the whole spectrum. In this situation, already a small, sub-% variation of the offset parameter B (compare equation (5.3) on page 83), which depends on the detection efficiency, causes severe distortions. Thus, small variations in the detection efficiency, potentially caused by varying ion beam focusing, had a strong effect. Besides the low electron-induced signal, two additional reasons made the result of this focusing so severe:

1. The electron density varied substantially in certain detuning energy ranges.
2. The horizontal extent of the product-particle beam of Ne^+ ions was roughly the same as the width of the COMPACT detector.

These points need to be improved for future experiments.

The first point is easy to address by splitting the accessible detuning energy range in more sub-ranges and sampling each of these with reasonably similar and moderate electron densities.

Concerning the second point, if the recombined ion beam had been sufficiently smaller than the width of COMPACT, the ion beam focusing would not have resulted in a varying detection efficiency. In future experiments, these conditions could be achieved by reducing the number of ions injected into the ring, which would result in a smaller transverse size of the stored (and cooled) ion beam, and consequently, a smaller size of the product ion beam. However, reducing the ion number directly results in less recombination signal, and data-taking would take longer. Alternatively, a larger detector could be potentially used. A wider version of COMPACT exists with a width of 4 cm (instead of 2 cm). Nevertheless, a wider detector carries the risk of cutting into the stored ion beam, depending on the charge state of the ion beam, and the risk of collecting a mix of product particles with different m/q. Still, a wider detector might be helpful for recombination studies with ions in charge states $q \lesssim 3$, but there are competing interests from other experiments at CSR that rely on a narrow detector.

Furthermore, the experiment would benefit from an additional reference step at a detuning energy with basically zero electron-induced signal and the same detection efficiency (so the same electron density) as in the measurement step. This would allow for a normalization procedure which is independent of a potentially changing cooling signal and would permit to reliably infer the baseline in the rate coefficient.

Some of the above mentioned improvements were already implemented for the second recombination experiment with Xe^{3+}, which is presented in the next chapter.

Chapter 6

Results on Electron Recombination of Xe^{3+}

After the general feasibility of electron-ion recombination measurements with atomic ions at CSR was demonstrated in the proof-of-principle measurement with Ne^{2+}, a second beamtime was scheduled to investigate the recombination of a system with considerably higher mass-to-charge ratio.

Sb-like Xe^{3+} was chosen as it can be easily produced from an ECR ion source, granting a stable and intense ion beam for injection into CSR. The experiments were performed with the isotope $^{129}Xe^{3+}$, which is the second most abundant isotope of xenon with a fractional abundance of 26.4 % [140]. $^{129}Xe^{3+}$ has a mass-to-charge ratio of $m/q \approx 43$, which is by far the highest m/q in a storage ring recombination experiment with atomic ions. Up to now, $^{129}Xe^{3+}$ is the slowest electron-cooled ion beam in CSR with a cooling energy of only 3.82 eV.

In the photoionization of Xe^{2+}, which is the inverse process to electron recombination of Xe^{3+}, a 'giant resonance' has been found [46, 47], and it was a question whether such a collective many-electron effect can also be observed in the electron recombination.

The Xe^{3+} beamtime was scheduled shortly after the Ne^{2+} beamtime. By the time the experiment was performed, the findings from the Ne^{2+} beamtime, especially the suspected ion beam focusing effects, were not fully understood yet. Therefore, the Xe^{3+} recombination experiment incorporated some improvements compared to the Ne^{2+} experiment, but not all findings from this thesis could be implemented.

The obtained results from the recombination experiment with Xe^{3+} are presented in this chapter. The general measurement layout is described in chapter 4 above, especially in section 4.5 on page 44. Section 6.1 explains how the recorded data were combined and how the rate coefficients were derived. The actual results from the recombination measurements are presented in sections 6.2 and 6.3. Section 6.2 focuses on the 'high energy' part of the measured spectrum with detuning energies ranging from 0.5 eV to 61.6 eV. In this region, DR resonance features were found. The experimental results are compared to theoretical calculations. Section 6.3 focuses on the RR peak in the 'low

Table 6.1: Overview of the measurement ranges for Xe^{3+}. The electron current in the measurement step I_e and the corresponding electron densities n_e are displayed. $n_{e,r}$ denotes the electron densities in the reference step at 24 eV. When multiple densities are given, there are runs with different electron current at reference. $n_{e,peak}$ is the average density at the five measurement energies close to the DR peak at 19.7 eV that were included in all runs. ($n_{e,peak}$ was excluded from the range given for n_e.) All ranges were measured with a cooling electron current of 8.5 µA, resulting in a density of $3.2 \times 10^5\,cm^{-3}$. The pre-cooling time was either 10 s or 21 s. t_{stor}^{max} denotes the maximum storage time at which the ions were kicked out of CSR. Most ranges were covered by more than one run.

Range [eV]	I_e [uA]	n_e [$10^5\,cm^{-3}$]	$n_{e,r}$ [$10^5\,cm^{-3}$]	$n_{e,peak}$ [$10^5\,cm^{-3}$]	t_{stor}^{max} [s]
0 - 0.7	8.5	3.2 - 2.4	3.5	1.3	54.0
0.5 - 2	50	11.3 - 9.4	8.3/10.3	5.7	56.6
2 - 5	60	11.1 - 9.3	8.3/10.3	6.7	53.7
5 - 10	80	12.1 - 10.4	8.3/10.3	8.7	56.0
10 - 15	100	12.9 - 11.7	10.3	10.9	56.0
15 - 18.5	100	11.7 - 11.0	10.3	10.9	46.5
15 - 22	86	10.0 - 9.1	10.8	9.3	54.3
15 - 22	120	13.9 - 12.6	12.3	13.0	54.3
15 - 22	180	20.7 - 18.7	18.2	19.2	54.3
18 - 20.5	120	13.3 - 12.8	12.3	13.0	36.5
20 - 25	120	12.9 - 12.2	12.3	13.0	35.6
22 - 30	120	12.6 - 11.6	12.3	13.0	58.9
30 - 40	140	13.4 - 12.4	14.2	15.0	58.0
40 - 61.6	160	14.1 - 12.4	16.2	17.1	58.6

energy' part of the spectrum with detuning energies up to 0.7 eV. Here, the RR peak shape is compared for different cooler settings and a comparison with a theoretical calculation is made. The main findings are again summarized in section 6.4.

6.1 Combining data from different runs and ranges

In the Xe^{3+} beamtime, the experimentally accessible detuning energy range between 0 eV and 61.6 eV was split into several sub-ranges that were scanned in independent runs. Table 6.1 shows these (sub-)ranges together with the applied electron current I_e

in the measurement step and the corresponding electron densities n_e. Care was taken to ensure that the electron density did not vary too much within one range and that the electron densities in different ranges stayed comparable in order to reduce ion beam focusing effects as observed in the Ne^{2+} beamtime. Therefore, the accessible range was divided in a lot more subranges than in the Ne^{2+} beamtime and the electron current was adjusted for each range individually. Each run included reference steps at a detuning energy of $E_d = 24\,\text{eV}$. The electron current for these steps was usually chosen such that the current was not too different from the one applied in the measurement steps, ensuring that the electron density $n_{e,r}$ remained comparable to the one in the measurement steps. The corresponding densities $n_{e,r}$ are given in table 6.1. Additionally, the electron density $n_{e,peak}$ is given. It is the average density at the five 'reference' measurement energies at $E_d = 19.56\,\text{eV}$, $19.63\,\text{eV}$, $19.70\,\text{eV}$, $19.77\,\text{eV}$ and $19.84\,\text{eV}$ around the main resonance feature (referred to as 'DR peak'), which were included in all runs and used for scaling. The maximum storage time t_{stor}^{max} after which the ions were kicked out of CSR is displayed in table 6.1 as well. Most ranges were covered by more than one run.

To combine the data from different runs within one range, all counts and step lengths from the different runs were summed up and the relative rates $(R_m - R_{dark})/(R_r - R_{dark})$ were calculated for each measurement detuning energy independently. In contrast to the analysis of the Ne^{2+} data, the normalization was done on the reference count rate R_r. Subsequently, relative rate coefficients α_{rel} were calculated following equation (4.63) on page 54 with the assumed offset parameter $B = 1$ for all runs. Each run included five measurement energies around the DR peak that were used to normalize the relative rate coefficients in the individual ranges by α'_{peak}. Hereafter, the data were binned in E_d in order to combine data points at the same detuning energy from different ranges and to lower the statistical uncertainty. In the same way as for the Ne^{2+} data described in section 5.1, an uncertainty-weighted mean for each bin was calculated with equation (5.1) on page 73. The relative rate coefficients were then absolutely scaled using the scaling factor obtained in section 4.9.3 on page 63.

The low energy region with detuning energies close to 0 eV was treated separately from the rest of the spectrum, as again potential ion beam focusing effects were observed that affect the derived MBRC at lower energies.

6.2 Recombination at energies between 0.5 eV and 61.6 eV

The binned recombination spectrum for Xe^{3+} is shown in figure 6.1 on an absolute scale for detuning energies between 0.5 eV and 61.6 eV, excluding the RR peak at 0 eV. The most prominent feature in the spectrum is the peak at a detuning energy of $E_d = 19.7\,\text{eV}$ with a height of $\alpha_{mb} \approx 13.1 \times 10^{-10}\,\text{cm}^3\,\text{s}^{-1}$. The signal is produced mostly

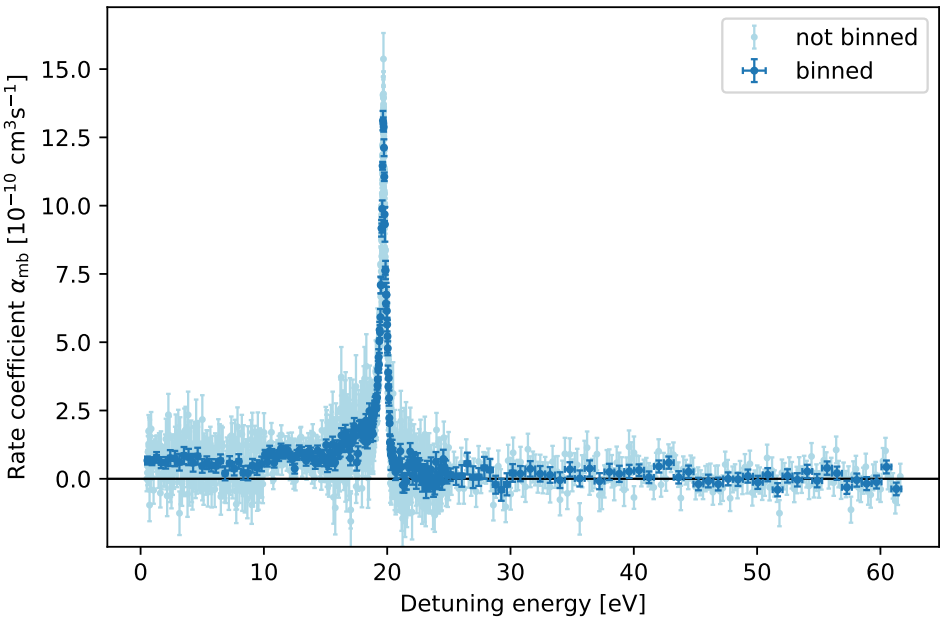

Figure 6.1: Absolute merged-beams rate coefficient for electron recombination of Xe^{3+} at detuning energies between 0.5 eV and 61.6 eV. The light blue symbols correspond to the data from the individual ranges, the dark blue symbols represent the binned spectrum. The error bars indicate the statistical uncertainty. The additional uncertainty due to the absolute scaling procedure amounts to 32 %. At low detuning energies, the rate coefficient might be overestimated due to an artifact from the measurement setup which is not accounted for in the systematic uncertainty.

by DR resonances comprising a $5p \rightarrow 5d$ core excitation, and are discussed below in section 6.2.1. Detuning energies even above the ionization energy of Xe^{3+} of 42.2 eV [141] were scanned. At energies above $E_d \approx 23$ eV, the rate coefficient is basically flat and consistent with zero. No resonances could be found here, and especially no trace of a giant resonance is detectable at these detuning energies. At detuning energies below the main peak, the recombination signal is constantly above zero, ranging around $\alpha_{mb} \approx 0.7 \times 10^{-10}\,cm^3\,s^{-1}$. This non-zero signal is caused partly by the transition from the out-of-drift-tube region to the drift tubes. Due to the chosen cathode voltage of $U_{cath} = -50$ V, the electrons in the interaction region outside of the drift tubes had an energy corresponding to an electron-ion detuning energy of $E_{out,d} \approx 22$ eV, which is above the main DR peak at $E_d = 19.7$ eV. To reach low detuning energies, the electrons had to be slowed down in the drift tubes and subsequently sampled over the DR peak in the transition region at the end of the drift tubes (compare also figure 4.3a on page 39). Nonetheless, the low-energy signal might to some extent be artificially enhanced due to potential ion beam focusing effects similar to those observed during the Ne^{2+} beamtime. Further details are given below in section 6.2.3.

6.2.1 DR resonance features

Figure 6.2 shows parts of the measured recombination spectrum, focusing on the main resonance peak around $E_\mathrm{d} = 19.7\,\mathrm{eV}$. The displayed error bars are of statistical nature and the additional systematic uncertainty due to the absolute scaling procedure amounts to 32 % (see section 4.9.3 on page 63). The observed peak has a FWHM of about 0.5 eV and a height of about $\alpha_\mathrm{mb} \approx 13.1 \times 10^{-10}\,\mathrm{cm^3\,s^{-1}}$. At the peak, the expected energy resolution due to the electron beam temperatures is about 0.23 eV, as derived in section 4.3. In contrast to the findings in the Ne^{2+} beamtime presented in chapter 5, no resonance series could be resolved here. The reason for this is the rich level structure of Xe^{3+}, and the peak certainly incorporates a multitude of individual resonances. Of the 94 singly excited levels reported in the NIST Atomic Spectra Database [129], all have excitation energies below 30 eV, and 29 lie in the range between 12 eV and 21 eV and therefore potentially contribute to the observed MBRC. The level energies are displayed in table 6.2. The expected DR resonance energies correlated to $5s \rightarrow 5p$, $5p \rightarrow 5d$ and $5p \rightarrow 6s$ core excitations were calculated with the Rydberg formula (2.5) on page 7, and are indicated as small lines in figure 6.2. Resonance energies are plotted for electron capture in Rydberg states with $n < 48$, corresponding to the expected cut-off quantum number due to field ionization in the 6°-deflector (see section 4.11 on page 69), and for core excitations out of the $5s^2 5p^3\ {}^4S_{3/2}$ ground level, as this is the only populated level contributing to the measured rate coefficient according to the calculation in section 4.10 on page 66. For the sake of clarity, resonance energies originating from $5p \rightarrow 6p$ and $5p \rightarrow 4f$ are not plotted as no strong features could be assigned to these core excitations.

Judging from figure 6.2, the prominent peak consists mainly of resonances correlated to a $5p \rightarrow 5d$ core excitation. Especially the Rydberg series connected to the core excitation to the $5s^2 5p^2 5d\ {}^4P_{5/2}$ level at an energy of 19.793 eV seems to exhibit a large recombination cross section. It is not clear whether the dent at $E_\mathrm{d} \approx 19.9\,\mathrm{eV}$ is just a statistical fluctuation, but it coincides with the expected series limit for excitation into the $5s^2 5p^2 5d\ {}^4P_{3/2}$ level at an energy of 20.015 eV. The same holds for the weakly indicated dent at $E_\mathrm{d} \approx 20.1\,\mathrm{eV}$, which coincides with the series limit for excitation into the $5s^2 5p^2 5d\ {}^4P_{1/2}$ level at an energy of 20.193 eV. These three excited levels belong to the same multiplet, and the Rydberg series linked to these three levels are particularly highlighted in figure 6.2b. Given the large number of potential resonances and the broad recombination feature observed in the experiment, it is not possible to unambiguously identify any other contributing core excitations.

6.2.2 Storage time dependency

The level population present in the stored Xe^{3+} beam is calculated in section 4.10 on page 66. A pure beam in the $5s^2 5p^3\ {}^4S_{3/2}$ ground level is predicted for the relevant storage times. Nonetheless, a potential storage time evolution was investigated by evaluating the MBRC in the detuning energy range from 18 eV to 20.5 eV for three storage

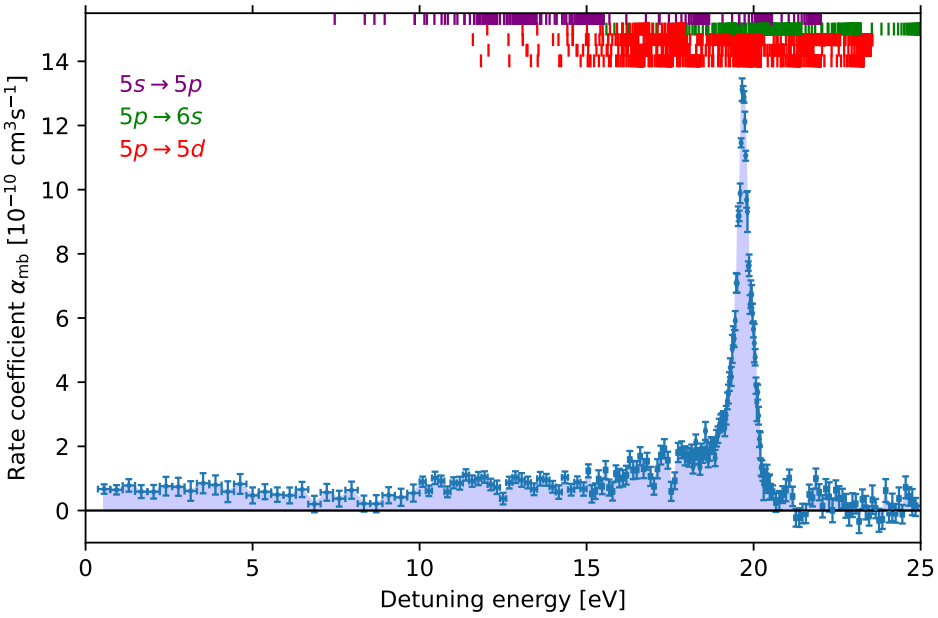

(a)

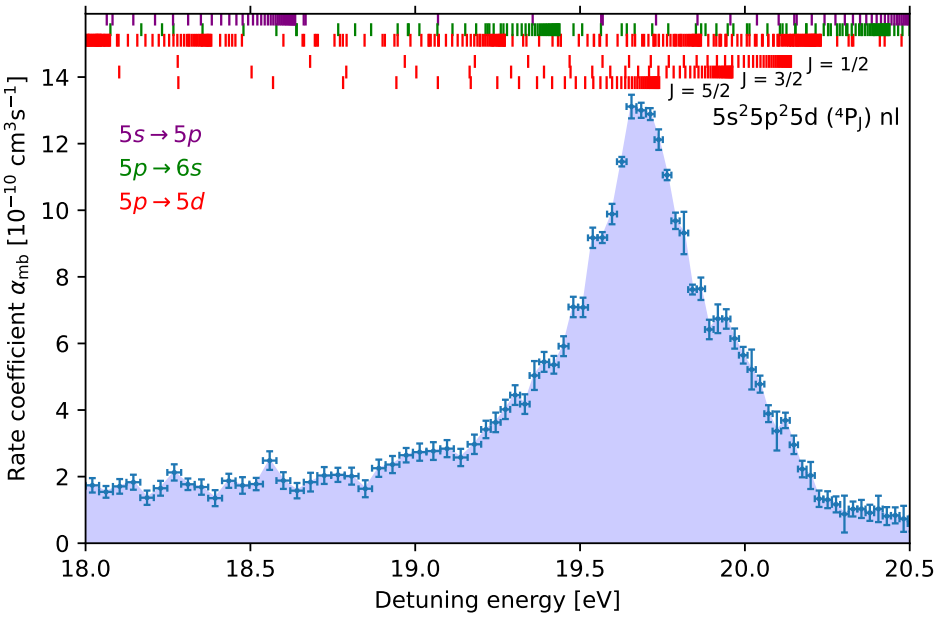

(b)

Figure 6.2: Absolute MBRC for electron recombination of Xe^{3+} in the detuning energy ranges between (a) 0.5 eV and 25 eV and (b) 18 eV and 20.5 eV around the main resonance. The additional systematic uncertainty on the experimental rate coefficient is 32 %, but the signal at low energies might be additionally artificially increased. The lines in the upper part of the plots indicate the expected resonance energies as calculated with the Rydberg formula (2.5) for various core excitations and $n < 48$. Purple lines indicate an excitation of a $5s$ electron to a $5p$ level, green lines correspond to a core excitation $5p \rightarrow 6s$ and red lines denote $5p \rightarrow 5d$. In (b), three Rydberg series linked to excitations into the $5s^25p^25d\ ^4P_J$ multiplet are highlighted.

Table 6.2: Energies for excited levels of Xe^{3+} according to the NIST Atomic Spectra Database [129] for configurations [Kr]$4d^{10}$.... The columns indicate the levels and the corresponding energy in eV.

$5s^25p^3$	
Level	E [eV]
$^4S_{3/2}$	0.000
$^2D_{3/2}$	1.645
$^2D_{5/2}$	2.171
$^2P_{1/2}$	3.476
$^2P_{3/2}$	4.420

$5s5p^4$	
Level	E [eV]
$^4P_{5/2}$	12.357
$^4P_{3/2}$	13.257
$^4P_{1/2}$	13.546
$^2D_{3/2}$	15.117
$^2D_{5/2}$	15.557
$^2S_{1/2}$	18.689
$^2P_{3/2}$	20.581
$^2P_{1/2}$	22.063

$5s^25p^26s$	
Level	E [eV]
$^4P_{1/2}$	19.491
$^4P_{3/2}$	20.492
$^2P_{1/2}$	20.731
$^4P_{5/2}$	21.138
$^2P_{3/2}$	21.477
$^2D_{5/2}$	23.067
$^2D_{3/2}$	23.253
$^2S_{1/2}$	25.052

$5s^25p^25d$	
Level	E [eV]
$^2P_{3/2}$	16.493
$^4F_{3/2}$	16.735
$^4F_{5/2}$	16.923
$^2P_{1/2}$	16.961
$^4F_{7/2}$	17.559
$^2F_{5/2}$	17.584
$^2F_{7/2}$	17.979
$^4D_{1/2}$	17.991
$^4F_{9/2}$	18.101
$^4D_{3/2}$	18.127
$^4D_{5/2}$	18.435
$^4D_{7/2}$	19.325
$^4P_{5/2}$	19.793
$^2G_{7/2}$	19.920
$^4P_{3/2}$	20.015
$^4P_{1/2}$	20.193
$^2G_{9/2}$	20.267
$^2D_{3/2}$	20.283
$^2D_{5/2}$	20.954
$^2P_{1/2}$	21.436
$^2F_{5/2}$	21.826
$^2D_{3/2}$	21.836
$^2F_{7/2}$	22.060
$^2D_{5/2}$	22.193
$^2P_{3/2}$	22.636
$^2S_{1/2}$	23.343
$^2D_{5/2}$	23.561
$^2D_{3/2}$	23.603

$5s^25p^24f$	
Level	E [eV]
$^4G_{5/2}$	22.336
$^4G_{7/2}$	22.592
$^4D_{7/2}$	23.251
$^4G_{9/2}$	23.340
$^2D_{5/2}$	23.398
$^2G_{7/2}$	23.537
$^4F_{3/2}$	23.787
$^4D_{5/2}$	23.802
$^4D_{3/2}$	24.274
$^4F_{7/2}$	24.341
$^4F_{5/2}$	24.364
$^4D_{1/2}$	24.382
$^2D_{3/2}$	24.722
$^2G_{9/2}$	25.054
$^2F_{5/2}$	25.442
$^2F_{7/2}$	25.444
$^2G_{9/2}$	25.568
$^2G_{7/2}$	25.629
$^2F_{5/2}$	25.866
$^2D_{3/2}$	26.500
$^2D_{5/2}$	27.153
$^2F_{7/2}$	27.241
$^2P_{1/2}$	27.374
$^2F_{7/2}$	28.389

$5s^25p^26p$	
Level	E [eV]
$^4D_{1/2}$	23.075
$^4D_{3/2}$	23.655
$^2S_{1/2}$	24.036
$^2D_{3/2}$	24.391
$^4D_{5/2}$	24.666
$^2D_{5/2}$	24.857
$^4P_{1/2}$	24.908
$^4S_{3/2}$	24.924
$^4D_{7/2}$	25.163
$^4P_{3/2}$	25.310
$^2P_{3/2}$	25.548
$^4P_{5/2}$	25.672
$^2P_{1/2}$	25.955
$^2F_{5/2}$	26.734
$^2D_{3/2}$	26.798
$^2D_{5/2}$	26.894
$^2F_{7/2}$	26.934
$^2P_{1/2}$	27.287
$^2P_{3/2}$	27.834
$^2P_{1/2}$	28.865
$^2P_{3/2}$	29.206

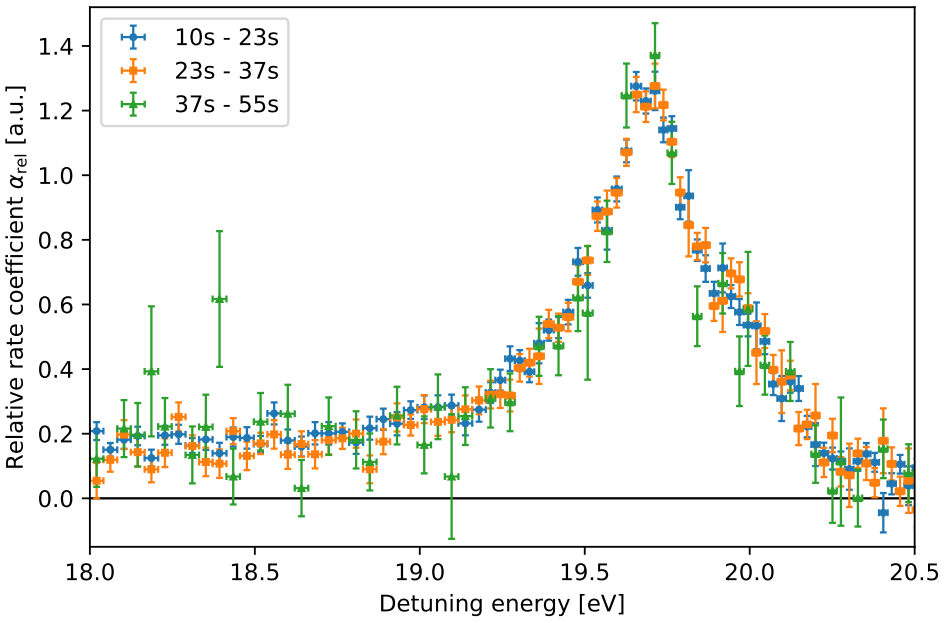

Figure 6.3: Recombination rate coefficients of Xe^{3+} in the energy range 18 eV to 20.5 eV for three storage time windows of 10 s to 23 s, 23 s to 37 s and 37 s to 55 s.

time windows. The obtained rate coefficients for the time windows 10 s to 23 s, 23 s to 37 s, and 37 s to 55 s are shown in figure 6.3. Only a few runs included long storage times in this energy range, therefore the statistical uncertainty is much larger for the latest time window. Still, the rate coefficients from all time windows, and especially from the two earlier, agree within the given statistical uncertainties. No time evolution is detectable.

6.2.3 Enhanced signal at lower energies: Ion beam focusing effects

In the Ne^{2+} beamtime, a distortion of the measured rate coefficient spectrum at lower energies was observed. This behavior was attributed to focusing of the stored ion beam due to lensing by the electron beam space charge in the interaction region (see section 5.2.5 on page 82), which subsequently changes the detection efficiencies. The observed effect was dependent on the detuning energy and led to a rising signal towards lower energies.

During the Xe^{3+} beamtime, care was taken to attenuate such focusing effects and to enable a more reliable data analysis. Therefore, the electron densities in the measurement steps were reduced and more homogeneous compared to the Ne^{2+} beamtime, and a reference step was introduced at an electron density close to the one in the measurement steps. Indeed these measures seem to have worked at least partially. Within the individual energy ranges, no slope is visible as it was the case in the Ne^{2+} beamtime. In the spectrum presented in figure 6.1, no increase towards lower energies is apparent.

However, the MBRC at detuning energies below the main resonance is constantly above zero and it cannot be completely excluded that the reason for this is partially again ion beam focusing.

The electron-recombination rate coefficient can be derived from the measured rates by equation (4.57),

$$\alpha_{\mathrm{e,m}} = \frac{A}{n_{\mathrm{e,m}}} \left[\left(\frac{R_{\mathrm{m}} - R_{\mathrm{dark}}}{R_{\mathrm{r}} - R_{\mathrm{dark}}} \right) - B \right], \tag{6.1}$$

where the scaling parameter A and the offset parameter B are

$$A = \frac{\alpha_{\mathrm{rg}}\, n_{\mathrm{rg}}\, \eta_{\mathrm{rg,r}}\, l_{\mathrm{rg}}}{\eta_{\mathrm{e,m}}\, l_{\mathrm{e}}} \quad \text{and} \quad B = \frac{\eta_{\mathrm{rg,m}}}{\eta_{\mathrm{rg,r}}}, \tag{6.2}$$

according to equations (4.60) and (4.61). As can be seen in table 6.1, the electron densities in reference and measurement steps were chosen close to each other. The expected variation in the detection efficiencies in these steps thus is small (besides for the RR peak which is discussed below in section 6.3), and the offset parameter seems well under control with $B = 1$. The individual detuning energy ranges were scaled relatively to each other with the help of five additional measurement energies around $E_{\mathrm{d}} = 19.7\,\mathrm{eV}$ on the DR peak. These energies were sampled with the same current as all other measurement steps. Especially for the low energy ranges $E_{\mathrm{d}} = 0.5\,\mathrm{eV}$ to $2\,\mathrm{eV}$, $2\,\mathrm{eV}$ to $5\,\mathrm{eV}$ and $5\,\mathrm{eV}$ to $10\,\mathrm{eV}$, the resulting electron densities at the DR peak were significantly lower than for the rest of the measurement energies (see $n_{\mathrm{e,peak}}$ in table 6.1). This gives rise to a potential reduction in the detection efficiency for electron-induced signal at the DR peak $\eta_{\mathrm{e,m,peak}}$ due to weaker ion beam focusing, i.e. $\eta_{\mathrm{e,m,peak}} < \eta_{\mathrm{e,m,low}}$, with $\eta_{\mathrm{e,m,low}}$ the detection efficiency at the lower detuning energies. As $\eta_{\mathrm{e,m}}$ enters the scaling parameter A, the low energy part of the measured energy range would then require a scaling by

$$A_{\mathrm{low}} = \frac{\alpha_{\mathrm{rg}}\, n_{\mathrm{rg}}\, \eta_{\mathrm{rg,r}}\, l_{\mathrm{rg}}}{\eta_{\mathrm{e,m,low}}\, l_{\mathrm{e}}}, \tag{6.3}$$

whereas the points at the DR peak require

$$A_{\mathrm{peak}} = \frac{\alpha_{\mathrm{rg}}\, n_{\mathrm{rg}}\, \eta_{\mathrm{rg,r}}\, l_{\mathrm{rg}}}{\eta_{\mathrm{e,m,peak}}\, l_{\mathrm{e}}}. \tag{6.4}$$

In the data analysis procedure, relative rate coefficients α_{rel} were obtained for the full detuning energy range first and subsequently absolutely scaled at the DR peak. For the derivation of relative rate coefficients α_{rel} (compare equation (4.63) on page 54), it was assumed that A is constant for all detuning energies. This is here no longer valid since $A_{\mathrm{low}} < A_{\mathrm{peak}}$. Consequently, following the first part of equation (4.63),

$$\alpha_{\mathrm{rel}} = \frac{\alpha_{\mathrm{e,m,low}}/A_{\mathrm{low}}}{\alpha_{\mathrm{peak}}/A_{\mathrm{peak}}} = \frac{A_{\mathrm{peak}}}{A_{\mathrm{low}}} \frac{\alpha_{\mathrm{e,m,low}}}{\alpha_{\mathrm{peak}}} > \frac{\alpha_{\mathrm{e,m,low}}}{\alpha_{\mathrm{peak}}}, \tag{6.5}$$

it is found that the relative rate coefficient as obtained under the assumption of constant A is potentially overestimated for low detuning energies. Therefore, also the given

absolute MBRC at low energies is potentially overestimated. Additionally, also the detection efficiency for residual-gas-induced signal $\eta_{\mathrm{rg,m,peak}}$ at the DR peak would be reduced in comparison to the one in the reference step, $\eta_{\mathrm{rg,r}}$, due to the reduced electron density. The offset parameter B_{peak} at the peak would then actually be smaller than 1. Throughout the data analysis, $B = 1$ was used also at the DR peak, which would even augment the signal at lower energies due to the scaling to the DR peak.

For these reasons, the signal at low detuning energies might be artificially increased. As can be seen in figures 6.1 and 6.2, the MBRC has a minimum at $E_{\mathrm{d}} \approx 8\,\mathrm{eV}$, and it is likely that the increase towards lower detuning energies is related to the focusing effects.

For the high energy runs, the different focusing at the measurement energies and at the DR peak would compress the signal a little, but it is mostly compatible with zero. It might also be that the high energy runs are not affected as all densities are above a 'critical' density, where more focusing does not relate to a varying detection efficiency.

Around the main DR resonance, such ion beam focusing effects are assumed to be negligible as all electron densities are similar. The derived absolute MBRC in this energy region thus seems trustworthy.

6.2.4 Comparison with theoretical calculations

Due to the many electrons, Xe^{3+} is a complex system and the theoretical calculation of DR becomes challenging. The experimentally obtained MBRC for dielectronic recombination of Xe^{3+} is compared to two theoretical calculations here. In the calculations, the core excitations $5p \rightarrow 5d$, $5s \rightarrow 5p$, and $5p \rightarrow 6s$ out of the $[\mathrm{Kr}]4d^{10}5s^2 5p^3\,{}^4S_{3/2}$ ground level are considered. An *AUTOSTRUCTURE* (AS) calculation was performed including electron capture into Rydberg levels with $n \leq 47$ (and $l \leq 20$) in agreement with the expected cut-off quantum number as derived in section 4.11 on page 69 for a hard cut-off. In the calculation, the excitation energies were adjusted according to the values from the NIST Atomic Spectra Database [129]. The calculated cross sections were convolved with the experimental collision energy distribution generated from a Monte-Carlo simulation implemented in the *hydrocal* code by Stefan Schippers [90]. In the simulation, electron beam temperatures of $kT_{\parallel} = 0.2\,\mathrm{meV}$ and $kT_{\perp} = 3\,\mathrm{meV}$ were assumed. Like this, theoretical MBRCs for the three considered core excitations were obtained. The three MBRCs as well as their sum are displayed in figure 6.4.

At the main resonance around $E_{\mathrm{d}} = 19.7\,\mathrm{eV}$, which is mostly caused by DR involving a $5p \rightarrow 5d$ excitation, the MBRC obtained from the AS calculation exceeds the experimental MBRC roughly by a factor of 2. A scaling by a factor of 0.55, as shown in figure 6.5a, leads to a better agreement, but the peak shapes deviate slightly. Around $E_{\mathrm{d}} \approx 13\,\mathrm{eV}$, the AS calculation predicts recombination features attributed to a $5s \rightarrow 5p$ core excitation, as shown in figure 6.5b. Experimentally, there are only weak hints for these resonances. The experimental MBRC rises slightly in the energy range $E_{\mathrm{d}} \approx 8\,\mathrm{eV}$ to 12 eV, tentatively drops at $E_{\mathrm{d}} = 12.5\,\mathrm{eV}$ and rises again a little towards 13 eV.

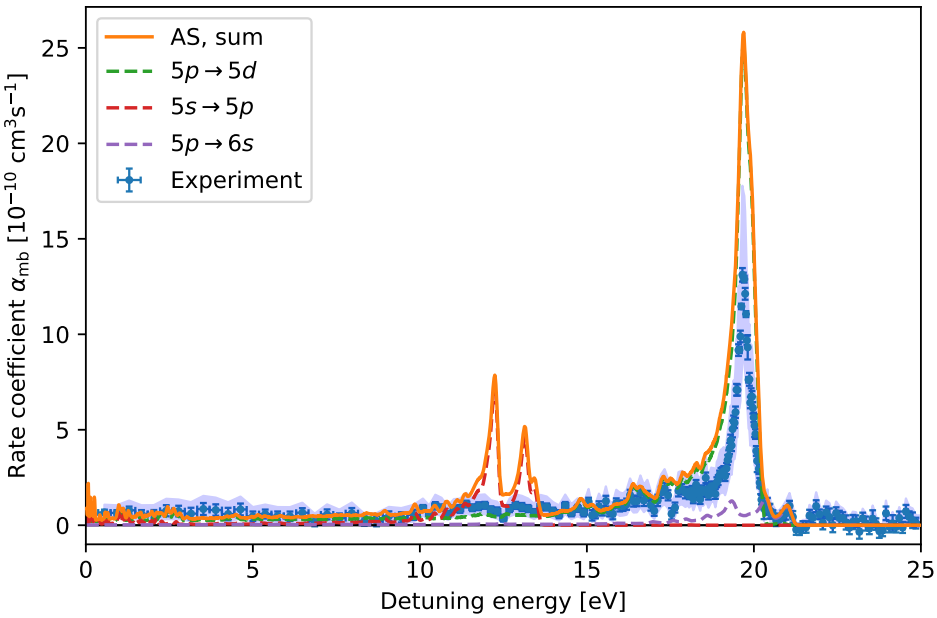

Figure 6.4: Comparison of the experimental merged-beams recombination rate coefficient of Xe^{3+} with a theoretical AS calculation. The calculation includes the core excitations $5p \rightarrow 5d$, $5s \rightarrow 5p$, and $5p \rightarrow 6s$, and electron capture into levels with $n \leq 47$ in agreement with the expected experimental cut-off. The shaded area around the experimental rate coefficient marks the systematic uncertainty of 32 % due to the absolute scaling procedure.

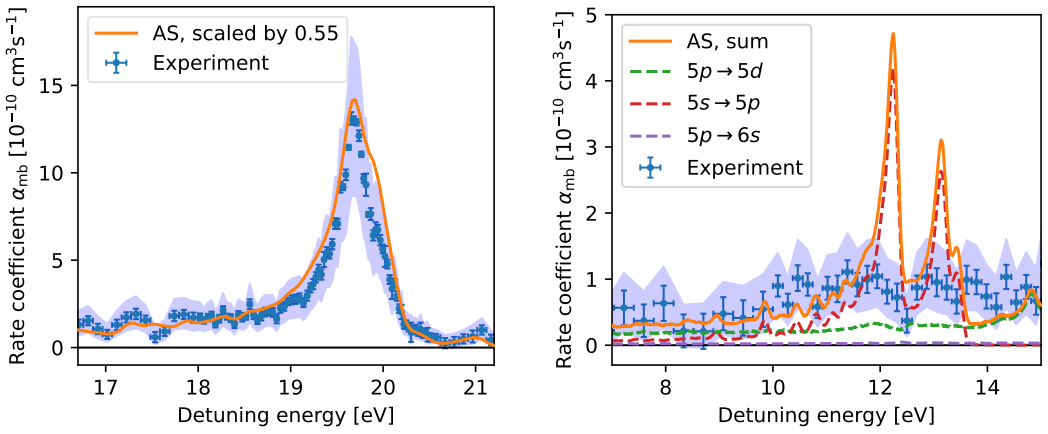

(a) AS scaled

(b) $5s \rightarrow 5p$ features

Figure 6.5: (a) Comparison of the experimental MBRC with the AS calculation, scaled by a factor 0.55. The orange line represents the sum of the rate coefficients from the three considered core excitations. (b) In the energy region between 10 eV and 14 eV, the AS calculation predicts recombination features associated with a $5s \rightarrow 5p$ core excitation.

However, the statistical uncertainties are large, and it is not clear whether this is just a statistical fluctuation. In any case, the experimentally observed MBRC is certainly lower than the theoretically predicted MBRC in this detuning energy range. At higher detuning energies $E_\mathrm{d} \gtrsim 23\,\mathrm{eV}$, the theoretical calculation yields zero in agreement with the experiment. In contrast to the overshooting at the main DR peak, the calculation yields a tentatively lower rate coefficient than measured at detuning energies $E_\mathrm{d} \lesssim 8\,\mathrm{eV}$, but it is likely that the experimental MBRC is overestimated in this energy region due to ion beam focusing effects, as explained in section 6.2.3.

While the AS calculations could be performed rather fast with a total computation time of below one hour, Singh, Harman, and Keitel [135] conducted more sophisticated calculations with the *Flexible Atomic Code* (FAC). Their calculations involve the excitations $5p \to 5d$, $5s \to 5p$, and $5p \to 6s$ (the same excitations that are taken into account in the AS calculation presented above), and electron capture into $n \leq 46$ with $l \leq n-1$. Cross sections for the electron capture into $n = 47$, which is still expected to be seen in the experiment, were not be calculated for technical reasons, but the additional signal is assumed to be small. The computational effort put into these calculations was immense. As an example, the calculations for electron capture into $n = 46$ involved the calculation of $\sim 320\,000$ configuration state functions for $5p \to 5d$, $\sim 110\,000$ for $5s \to 5p$, and $\sim 95\,000$ for $5p \to 6s$. In total, about one billion radiative transitions have been considered. The computation time was about 30 to 50 days on up to 64 cores for each n between 5 and 46 [135]. The level energies calculated by FAC are not very accurate. Instead of shifting the energies to the values from the NIST Atomic Spectra Database, as it was done for the AS calculations for Ne^{2+} and Xe^{3+} and in the FAC calculation for Ne^{2+}, the level energies were calculated with the more accurate GRASP code [142]. The theoretical calculation of the collision-energy-dependent cross sections therefore does not rely on any experimental input.

Similar to the procedure for the AS calculation, the cross sections were convolved to rate coefficients using a realistic collision energy distribution assuming electron beam temperatures of $kT_\parallel = 0.2\,\mathrm{meV}$ and $kT_\perp = 3\,\mathrm{meV}$. The theoretical MBRCs for DR involving the aforementioned excitations are shown in figure 6.6 in comparison with the experimental MBRC.

The calculated resonance energies agree reasonably with the experimentally observed resonance energies, especially when considering the uncertainty in the order of $\sim 1\,\%$ on the energies calculated with GRASP [135]. The overall strength of the rate coefficient calculated by FAC agrees better with the experiment than the rate coefficients obtained from the AS calculation (compare figure 6.4). At higher energies not shown in the figure, the predicted rate coefficient is zero in agreement with the experiment.

A detail figure focusing on the DR peak is shown in figure 6.7a. The peak is mostly produced by DR involving a $5p \to 5d$ excitation. The theoretical calculation yields a mostly higher rate coefficient than the experiment. In the detuning energy range between 18 eV and 20.5 eV, which is shown in figure 6.7a, the MBRC from the FAC calculation is on average larger than the experimental MBRC by a factor of ~ 1.65.

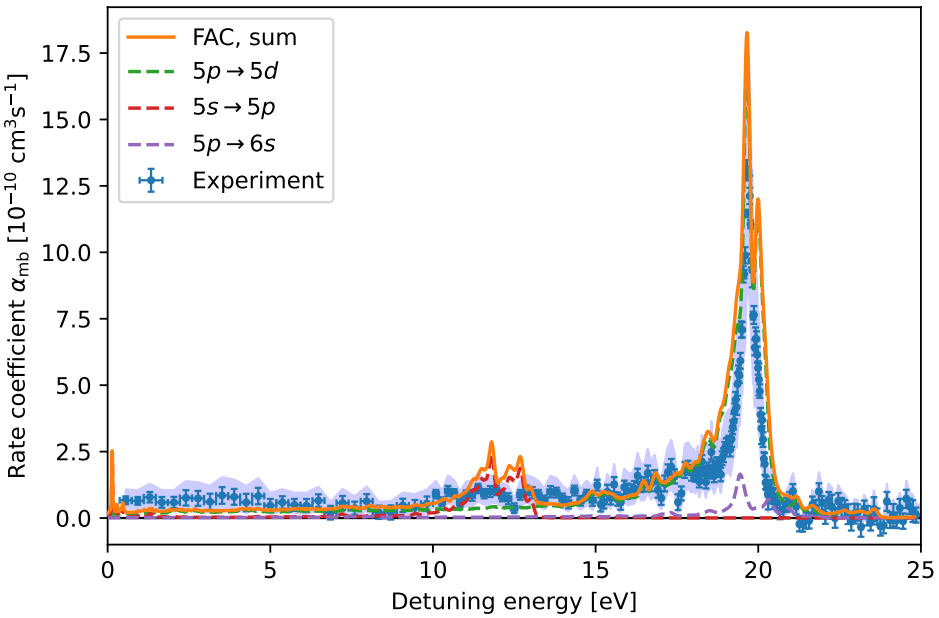

Figure 6.6: Comparison of the experimental merged-beams recombination rate coefficient of Xe^{3+} with a theoretical calculation performed by Singh, Harman, and Keitel [135], using the *Flexible Atomic Code* (FAC). The calculation includes the core excitations $5p \rightarrow 5d$, $5s \rightarrow 5p$, and $5p \rightarrow 6s$, and electron capture into levels with $n \leq 46$. The expected experimental cut-off was $n_c = 48$. The shaded area around the experimental rate coefficient marks the uncertainty of 32 % due to the absolute scaling.

(In contrast, in this energy range, the AS calculation is on average larger than the experiment by a factor of 2.19.) Taking into account the uncertainty for the theoretical FAC cross section of $\sim$ 20 % [135, 138] as well as the systematic experimental uncertainty of 32 %, the averaged rate coefficients in the detuning energy range between 18 eV and 20.5 eV just agree within the uncertainties. Figure 6.7b shows the FAC calculation scaled by a factor of $1/1.65 = 0.61$. It seems that the second calculated peak at 20 eV corresponds to the shoulder at 19.9 eV on the experimental peak. This discrepancy is in line with the estimated uncertainty on the calculated energies in the order of $\sim$ 1 % [135], which corresponds to $\sim$ 0.2 eV at an energy of 20 eV. It was verified that the most significant contributions to the DR peak in the theoretical calculation are linked to excitations from the $5s^2 5p^3\ {}^4S_{3/2}$ ground level of Xe^{3+} to the excited $5s^2 5p^2 5d\ {}^4P_J$ multiplet [135], as was already concluded from the experimental data in section 6.2.

At detuning energies around 12 eV, the FAC calculation predicts resonance features attributed to a $5s \rightarrow 5p$ excitation, for which there are only tentative hints in the experiment, as can be seen in figure 6.7c. At even lower detuning energies, the calculation yields an almost constant signal of $\alpha_{\mathrm{mb}} \approx 0.25 \times 10^{-10}\,\mathrm{cm^3\,s^{-1}}$. The experimental rate coefficient in this region is above zero and featureless as well, but potentially overestimated due to ion beam focusing effects, as discussed in section 6.2.3.

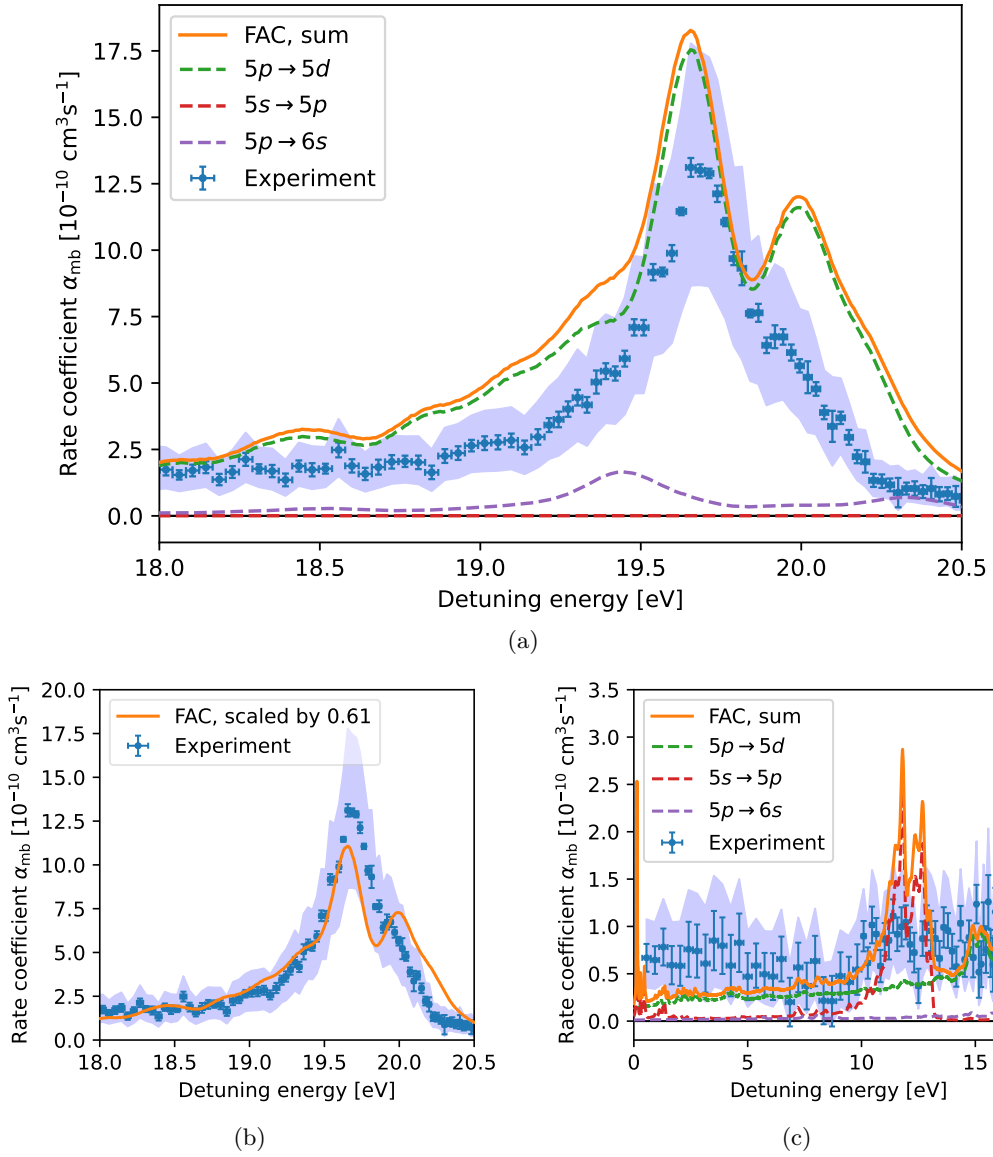

Figure 6.7: Comparison of the experimental merged-beams recombination rate coefficient of Xe^{3+} with the theoretical FAC calculation of DR performed by Singh, Harman, and Keitel [135]. The rate coefficients for the three considered core excitations as well as their sum are shown in (a) for the energy range 18 eV to 20.5 eV. In (b), the sum of the three is scaled by a factor of $1/1.65 = 0.61$. In (c), the low detuning energies below 18 eV are shown for the unscaled theory. The shaded area around the experimental rate coefficient in all figures marks the uncertainty of 32 % due to the absolute scaling. It should be noted that at low energies, i.e. in (c), the experimental rate coefficient may be overestimated, especially at $E_d \lesssim 8$ eV.

6.3 Recombination close to 0 eV

In the sections above, only detuning energies $> 0.5\,\mathrm{eV}$ were discussed so far. The recorded data at detuning energies close to zero, where the signal from RR is strongest, are reviewed here. Two measurements at low and high magnetic guiding fields were carried out.

The dedicated runs to measure the RR peak close to $E_\mathrm{d} = 0\,\mathrm{eV}$ were set up similar to the regular runs at higher detuning energies, including alternating cooling, measurement and reference steps. Five points at the DR peak were sampled as well. Separate measurements were carried out with two different magnetic guiding fields for the electron beam. The 'low fields configuration' were the standard settings throughout the beamtime, with magnetic fields of 1500 G, 100 G and 50 G in the big and small room temperature solenoids and in the interaction region, respectively. The magnetic fields in the 'high fields configuration' were 3000 G, 200 G and 100 G, as usually applied in recombination experiments with molecular ions. These two configurations were identical to those tested in the Ne^{2+} beamtime (see section 5.3). Here, the cathode voltage was kept constant at $U_\mathrm{cath} = -50\,\mathrm{V}$ for all measurements, corresponding to a nominal collision energy outside the drift tubes of $E_\mathrm{out,d} \approx 24.3\,\mathrm{eV}$. To avoid dragging effects, the detuning energies were alternately sampled with electrons faster and slower than the ion beam. The electron current in cooling and measurement steps was 8.5 µA, corresponding to electron densities between $n_\mathrm{e,cool} = 3.2 \times 10^5\,\mathrm{cm}^{-3}$ at cooling and $n_\mathrm{e}^\mathrm{fast} = 2.4 \times 10^5\,\mathrm{cm}^{-3}$ at a detuning energy of 0.7 eV with faster electrons, or $n_\mathrm{e}^\mathrm{slow} = 5.1 \times 10^5\,\mathrm{cm}^{-3}$ at 0.7 eV for collisions with slower electrons. Due to the significant difference in electron velocities, the five energies at the DR peak around $E_\mathrm{d} = 19.7\,\mathrm{eV}$ were sampled with a lower electron density of only $n_\mathrm{e,peak} = 1.3 \times 10^5\,\mathrm{cm}^{-3}$. The electron density in the reference step was $n_\mathrm{e,r} = 3.5 \times 10^5\,\mathrm{cm}^{-3}$ (see also table 6.1).

Figure 6.8 shows the relative rates $(R_\mathrm{m} - R_\mathrm{dark})/(R_\mathrm{r} - R_\mathrm{dark})$ for collisions with faster and slower electrons at the different electron cooler settings. The faster and slower branches are not expected to overlap perfectly, as the relative rates in figure 6.8 are neither corrected for the changing electron densities (which are higher for the slow branch and therefore increase the count rates there), nor for the fact that the electrons in the slow branch sampled over the RR peak in the transition region at the end of the drift tubes (which also increases the count rates there). Nonetheless, the still rather good agreement of faster and slower branches in figure 6.8 suggests that these effects are not too strong and especially that ion beam focusing effects as described in sections 5.2.5 and 6.2.3 do not strongly distort the shape of the RR peak.

As derived in section 4.7.2 on page 52, the baseline in the relative rate is determined by the offset parameter $B = \eta_\mathrm{rg,m}/\eta_\mathrm{rg,r}$, which gives the ratio of detection efficiencies for residual-gas-induced signal in the measurement and reference steps, respectively. The signal slightly below 1 for the low fields configuration and $E_\mathrm{d} \gtrsim 0.1\,\mathrm{eV}$ indicates $\eta_\mathrm{rg,m} < \eta_\mathrm{rg,r}$, although the reference electron density $n_\mathrm{e,r} = 3.5 \times 10^5\,\mathrm{cm}^{-3}$ was close

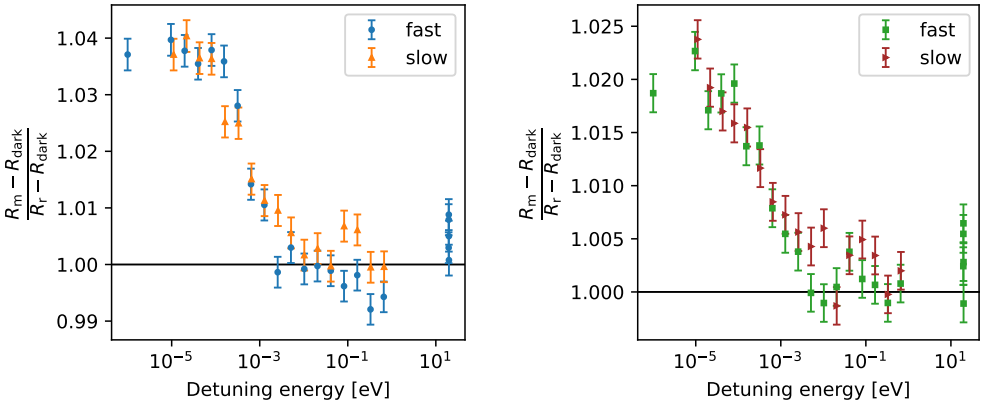

(a) low fields

(b) high fields

Figure 6.8: Comparison of the relative count rates $(R_m - R_{dark})/(R_r - R_{dark})$ for ion collisions with faster and slower electrons (a) with low magnetic guiding fields and (b) with high magnetic guiding fields.

to the one in the measurement step, which did not go below $2.4 \times 10^5\,\mathrm{cm}^{-3}$. For the measurement at high magnetic guiding fields, such focusing effects at low energies are statistically not resolvable.

What can be concluded nonetheless is that focusing effects occur at the five energies that were sampled around the DR peak at $E_d = 19.7\,\mathrm{eV}$ in both field configurations (see figure 6.8). $B \approx 0.99$ is needed to achieve the same peak shape as obtained in the regular runs at higher energies (compare figure 6.2 on page 100). The energy points on the DR peak can therefore not be directly employed to scale the RR peak absolutely. However, in the dedicated absolute scaling runs at low magnetic guiding fields, a rate coefficient at cooling of $\alpha_{mb}(E_d = 0\,\mathrm{eV}) = 15.5 \times 10^{-10}\,\mathrm{cm}^3\,\mathrm{s}^{-1}$ was estimated with an uncertainty of 50 % (see section 4.9.3.2 on page 65). It should be noted that $\alpha_{mb}(E_d = 0\,\mathrm{eV})$ includes not only the RR signal but also the non-zero baseline caused by electrons sampling over the DR resonance energies in the transition region at the end of the drift tubes. Still, this baseline signal contributes less than $1 \times 10^{-10}\,\mathrm{cm}^3\,\mathrm{s}^{-1}$ at low detuning energies, as can be seen, e.g., in figure 6.7c.

6.3.1 Shape of the RR peak

Although the RR signal could be absolutely scaled only under the conditions with low magnetic guiding fields, and although both measurements at low and high magnetic fields could not be put on the same relative scale due to the unreliable signal at the detuning energies close to the DR peak (where the electron density was very low and focusing effects played a role), still the shape of the RR peak can be compared for the two electron cooler settings with low and high magnetic guiding fields. Relative rate coefficients were obtained by applying a suitable offset parameter $B = 0.994$ for low and $B = 1$ for high guiding fields. Thereby, the non-zero baseline, which is mostly not

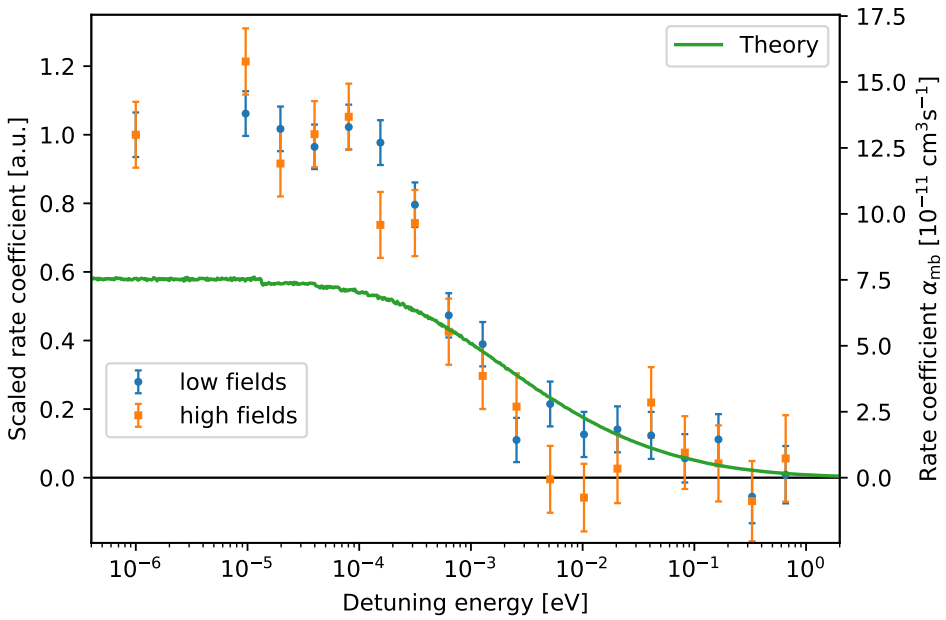

Figure 6.9: Comparison of the shape of the RR peak for low and high magnetic guiding fields. Only collisions with electrons faster than the ion beam are shown. Each of the runs was scaled to the signal at 1×10^{-6} eV and plotted on a relative scale (left side). The absolute MBRCs are not necessarily identical for the two cooler settings. For comparison, a theory calculation of the MBRC due to RR is shown (solid green line, axis on the right). *hydrocal* was used for the calculation, assuming electron beam temperatures of $kT_{\parallel} = 0.25\,\text{meV}$ and $kT_{\perp} = 2.5\,\text{meV}$ and capture into $n \leq 47$.

correlated to RR but to the sampling over the DR resonance energies, is subtracted. After offset-subtraction, the data were corrected for the electron density variation, and scaled independently to the signal at the lowest detuning energy. Figure 6.9 shows the relative rate coefficients for collisions with faster electrons. There is a slight indication that the recombination signal decreases faster towards higher detuning energies in the high fields configuration, but this trend cannot be definitively confirmed with given statistics. It should be noted that the absolute MBRC is not necessarily the same under both conditions.

For comparison, a theory calculation of the RR rate coefficient with assumed electron beam temperatures of $kT_{\parallel} = 0.25\,\text{meV}$ and $kT_{\perp} = 2.5\,\text{meV}$ and capture into $n < 48$ is shown as a green line in figure 6.9. The representation was chosen such that the theoretical calculation overlaps with the experimentally obtained data points for the low fields configuration at detuning energies $\gtrsim 1\,\text{meV}$. Figure 6.9 suggests an overshooting experimental signal below 1 meV, which might indicate rate enhancement, as observed at very low detuning energies in many storage ring experiments (e.g. [56, 57]), attributed to the collision dynamics in the fields of the electron coolers [58, 59]. These findings agree with the observations from the Ne^{2+} beamtime in section 5.3.

The calculated rate coefficient is $\alpha_{\mathrm{mb,th}} \approx 7.5 \times 10^{-11}\,\mathrm{cm^3\,s^{-1}}$ at detuning energies below $2 \times 10^{-5}\,\mathrm{eV}$ and therefore roughly (or even more than) one order of magnitude smaller than the experimentally obtained value of $\alpha_{\mathrm{mb}}(E_{\mathrm{d}} = 0\,\mathrm{eV}) = (15.5 \pm 7.8) \times 10^{-10}\,\mathrm{cm^3\,s^{-1}}$ (see section 4.9.3 on page 63), also when subtracting a generous value of $1 \times 10^{-10}\,\mathrm{cm^3\,s^{-1}}$ to account for the non-RR baseline. The discrepancy is not covered by the experimental uncertainty.

However, it cannot be excluded that a potential low-lying DR resonance very close to zero, potentially below the experimental energy resolution, contributes to the observed signal.

6.4 Summary and conclusion

In this chapter, the results from the recombination experiment of Sb-like Xe^{3+} with free electrons have been presented. It was the second electron-ion recombination experiment with atomic ions performed at CSR, and the first storage-ring recombination experiment at all with atomic ions with a mass-to-charge ratio as high as $m/q = 43$. The previously highest m/q was only 15 [21, 22]. The experiment with Xe^{3+} demonstrates the feasibility of recombination experiments with low-charged heavy atomic ions at CSR.

Recombination at detuning energies between 0 eV and 61.6 eV was measured. A prominent resonance feature around $E_{\mathrm{d}} = 19.7\,\mathrm{eV}$ was found, mostly produced by DR involving the excitation of a $5p$ electron to the $5d$ orbital. The experimental data were absolutely scaled with a systematic uncertainty of 32 %, and the MBRC at the peak of the DR resonance feature is as high as $\alpha_{\mathrm{mb}} = 13.1 \times 10^{-10}\,\mathrm{cm^3\,s^{-1}}$. The lowest resolvable rate coefficient was below $1 \times 10^{-10}\,\mathrm{cm^3\,s^{-1}}$. At detuning energies $\gtrsim 23\,\mathrm{eV}$, the obtained rate coefficient is mostly compatible with zero, and especially no recombination feature like a giant resonance correlated to the excitation of $4d$ electrons, which had been observed in photoionization of Xe^{2+}, was found in the accessible detuning energy range. A constantly non-zero rate coefficient was observed at detuning energies below the main resonance feature, attributed mostly to electrons in the transition region at the end of the drift tubes, where the electrons were decelerated (or accelerated, respectively) and provided electron-ion collision energies close to the main DR resonance. Due to effects correlated to ion beam focusing by the electron beam space charge and subsequently changing detection efficiencies, the low-energy signal at detuning energies $E_{\mathrm{d}} \lesssim 8\,\mathrm{eV}$ is likely overestimated. This effect could not be corrected for in the data analysis.

The experimental MBRC was compared with two theoretical calculations of DR. The calculations approximately reproduce the overall structure of the experimentally

observed recombination spectrum. Around the main DR peak, both theoretical calculations predict rate coefficients larger by a factor of approximately 2.2 and 1.7, respectively, than those that have been measured experimentally. Both calculations predict recombination features associated to a $5s \rightarrow 5p$ excitation, for which only tentative hints could be found experimentally.

Recombination at very low detuning energies close to 0 eV, where RR is expected to be strongest, was measured for two different electron cooler settings at low and high magnetic guiding fields. The shape of the recorded peak does not strongly differ between the two settings, but suggests rate enhancement as observed in earlier storage ring experiments and tentatively in the Ne^{2+} experiment as well. Approximate absolute scaling was only possible for the 0 eV peak at low guiding fields, exhibiting a signal strength more than one order of magnitude higher than the expected RR signal.

The derived MBRC was not transformed into a plasma rate coefficient due to the uncertainty in the rate coefficient in the low energy region and the not completely understood signal at 0 eV.

As in the Ne^{2+} beamtime, ion beam focusing effects, correlated to the electron density in the interaction region and resulting in slightly varying detection efficiencies, distorted the experimental data at low detuning energies at least to some extent. The Xe^{3+} beamtime was scheduled shortly after the Ne^{2+} beamtime, and the suspected focusing effects were not completely understood at that time. Still, some improvements were made in comparison to the Ne^{2+} experiment:

- The variation in electron density within each individual detuning energy range was reduced.
- A reference step was included, simplifying the analysis procedure.
- The electron density in the reference step was chosen close to the one in the measurement step.

These measures mitigated the effect of ion beam focusing in comparison to the Ne^{2+} experiment, and made the data analysis more solid as the offset parameter B from equation (6.1) on page 103 no longer had to be guessed. However, introducing a reference step reduces the fractional time spent in the measurement steps, and thus a longer measurement time is required to achieve the same statistics.

The fact that the scaling of the individual ranges to each other relied on five points at the DR peak that were sampled in the measurement steps in each run introduced additional uncertainties. These five energies at the DR peak were measured with the same electron current as all other measurement energies in the runs, resulting in

- a (much) lower density at the DR peak than at all other energies when sampling lower energies,

- a (much) higher density at the DR peak than at all other energies when sampling higher energies.

Accordingly, the detection efficiencies are potentially no longer identical, leading to

- an artificially enhanced signal at low energies,
- an artificially compressed signal at high energies.

Therefore, in future experiments, care should be taken to measure the data points needed for scaling (i.e. those that enter α'_{peak} in equation (4.63) on page 54) at the same electron density as all other energies in the run.

As already mentioned for Ne^{2+} in section 5.4, a smaller ion beam might reduce the distortion of the signal. This could be achieved by injecting less ions into the ring, however a weaker ion beam would lead to less electron-induced signal and require longer measurement times to reach similar statistics. A wider detector might help as well, but care would have to be taken not to disturb the stored main beam. Already now, COMPACT was close to the stored beam.

The overall situation would be improved by a lower residual-gas density in CSR. In the Xe^{3+} beamtime, the residual-gas density was fluctuating substantially due to unstable settings of the cryo-machine providing the cooling power for CSR. On average, the electron-induced rate at the DR peak was about $\sim 12\,\%$ of the total rate, and therefore the relative rate $(R_{\mathrm{m}} - R_{\mathrm{dark}})/(R_{\mathrm{r}} - R_{\mathrm{dark}})$ was not much larger than 1 across the whole measured detuning energy range. A reduction of the residual-gas density would reduce the background rate such that $(R_{\mathrm{m}} - R_{\mathrm{dark}})/(R_{\mathrm{r}} - R_{\mathrm{dark}})$ becomes sufficiently larger than unity. In this case, a small, sub-% variation of B from equation (6.1), due to varying detection efficiencies as a result of varying ion beam focusing, would not affect the obtained rate coefficients so severely.

Chapter 7

Summary and Outlook

In this work, the first electron-ion recombination measurements with atomic ions have been performed at the Cryogenic Storage Ring (CSR). Two experiments on the recombination of O-like Ne^{2+} and Sb-like Xe^{3+} demonstrate the feasibility of such measurements at CSR in general, as well as the feasibility of such measurements with *low-charged heavy ions* of high mass-to-charge ratio m/q in particular. The mass-to-charge limit in recombination measurements with atomic ions was significantly pushed in the experiment with Xe^{3+} ($m/q = 43$). Previous storage ring experiments did not investigate recombination in atomic ions with a mass-to-charge ratio higher than 15 due to technical limitations. Experiments with low-charged heavy ions, which have not been demonstrated in other experiments, are now feasible at CSR.

The reported experiments represent the first recombination measurements with atomic ions in an *electrostatic* storage ring, and the experiments were carried out at much lower ion and electron energies than in any previous storage ring experiment on the recombination of atomic ions.

The first experiment on the recombination of Ne^{2+} with free electrons was planned as a proof-of-principle. Detuning energies between 0 eV and 33 eV were scanned, and recombination features from Dielectronic Recombination (DR) and Radiative Recombination (RR) were observed. In the detuning energy region between 21.5 eV and 26.4 eV, resonances were found from DR involving the excitation of one of the bound $2s$ electrons in Ne^{2+} to the $2p$ orbital. The Merged-Beams Rate Coefficient (MBRC) was obtained on an absolute scale for detuning energies between 21.5 eV and 26.4 eV with a systematic uncertainty of 40 %. The observed resonance energies are in agreement with results from an earlier recombination experiment with Ne^{2+} performed at the storage ring CRYRING@ESR [41]. The overall lower electromagnetic fields in CSR, compared to standard magnetic storage rings like CRYRING@ESR, enable the study of recombination involving electron capture into much higher Rydberg levels, as field ionization

effects are reduced. Theoretical calculations reproduce the overall structure of the experimentally observed DR features, but exceed the measured MBRC by a factor of ~ 2. For recombination close to 0 eV, where RR is strongest, tentative indications were found for rate enhancement and for varying signal strength depending on the electron cooler settings, particularly the out-of-drift-tube energy.

The experimental data at detuning energies below ~ 17 eV are partially compromised, likely because of ion beam focusing effects correlated to the space charge of the electron beam. Due to a strong variation of the electron density in the interaction region with the detuning energy, the ion beam was focused differently throughout the detuning energy range and accordingly the geometrical detection efficiency for the recombined ions was changing in the order of 1 %. This suspected small variation still had a large effect on the obtained electron-ion recombination rate coefficient.

In the second recombination experiment, Xe^{3+} has been studied, which has a mass-to-charge ratio as high as 43. Detuning energies between 0 eV and 61.6 eV were scanned, and a broad resonance feature around 19.7 eV was found, mostly attributed to DR involving a $5p \rightarrow 5d$ excitation. The MBRC could be obtained on an absolute scale with a systematic uncertainty of 32 %. Two theoretical calculations approximately reproduce the overall structure of the experimentally observed DR feature, but exceed the measured MBRC by a factor of ~ 2.2 and ~ 1.7, respectively. Close to 0 eV detuning energy, a high recombination rate coefficient was observed, which is considerably stronger than the expected signal due to RR.

Although the ion beam focusing effects as suspected in the Ne^{2+} beamtime were much better under control, they may still have led to an artificial enhancement of the experimentally obtained MBRC at lower detuning energies.

With a cooling energy of only 3.82 eV, which was the lowest cooling energy in any storage ring experiment to date, Xe^{3+} paves the way for experiments with very slow but electron-cooled ion beams.

The two experiments presented in this thesis show that the good vacuum conditions inside CSR indeed enable recombination measurements with atomic ions, despite the extremely low kinetic ion energies in CSR compared to other storage rings. When carried out carefully, reliable MBRCs can be obtained.

The observed rate enhancement at very low detuning energies may motivate the further investigation of this effect in the special geometry of the CSR electron-ion merged-beams setup in future experiments.

A major difficulty in the experiments was the suspected ion beam focusing effects caused by varying electron densities in the interaction region, leading to changing detection efficiencies. The uncertainties in the MBRC resulting from these focusing effects prevented the derivation of reliable plasma rate coefficients for the use in plasma modeling. In future experiments, these focusing effects can potentially be reduced by using

similar electron densities in all relevant measurement steps.

The most thorough improvement for recombination measurements with atomic ions would be a further reduction of the residual-gas density in CSR, and especially in the electron cooler section. This would decrease the background signal produced by charge-transfer collisions of the stored ions with residual-gas particles and shorten the measurement time needed to achieve reasonable statistics. Therefore, the limit for the lowest resolvable MBRC in the experiment would be lowered. Additionally, a larger fraction of the electron-induced signal on the total count rates would mitigate the effect of ion beam focusing on the MBRC as well.

In order to reduce the residual-gas density, it is planned to implement two additional cold heads as an upgrade to the electron cooler. These cold heads will provide more cooling power in the vicinity of the electron-ion interaction region, which will supposedly result in a reduced residual-gas density in the electron cooler section as more residual-gas particles freeze out on the then even colder vacuum chamber walls. In the course of the author's doctoral work, such an upgrade was designed and extensive cryogenic tests were carried out. The implementation into CSR is planned for the near future.

In conclusion, the experiments presented in this thesis and the foreseen improvements lay the ground for further recombination studies with low-charged heavy ions of astrophysical relevance, e.g., with ions found in kilonovae, and with low-charged heavy ions of complex electronic structure as a benchmark for theoretical calculations.

On the way to investigating increasingly heavy and complex systems, an electron-ion collision experiment with molecular C_{60}^{+} ions ($m/q = 720$) has already been carried out at CSR.

Appendix A

Detection Efficiency of the COMPACT Detector for Ne^+ and Xe^{2+} Ions

In the recombination experiments with Ne^{2+} and Xe^{3+} ions performed in the course of this work, recombined Ne^+ and Xe^{2+} ions have been detected with the COMPACT detector which is presented in section 3.3.1 on page 22. By counting the electronic pulses from the detector generated upon a hit by a recombined ion, count rates were derived. In order to link these count rates to the MBRC, and in particular in order to obtain *absolute* MBRCs, it is crucial to know the detection efficiency for the recombined particles.

The overall detection efficiency η of the COMPACT detector is determined by two partial efficiencies, the geometric detection efficiency η_g and the intrinsic detection efficiency η_i, i.e.

$$\eta = \eta_g \cdot \eta_i. \tag{A.1}$$

While the geometric efficiency η_g accounts for the probability for a recombined ion to reach the converter plate of COMPACT, the intrinsic (or counting) efficiency η_i reflects the likelihood for a recombined ion hitting the converter plate to produce an electronic signal and to be counted.

In earlier work [71, 118, 119], the intrinsic counting efficiency was investigated for different ionic and neutral particles, and in [119], a method to determine the geometric efficiency is presented. However, the detection efficiency of the COMPACT detector is influenced by the temperature of the MCP stack, by the mass and energy of the impinging particles, by the discriminator settings in the read-out chain of the electronic signal, and by the shape of the impinging particle beam. To obtain a reliable value for the detection efficiency under the conditions as in the recombination experiments presented in this thesis, dedicated measurements were performed. In contrast to the previously applied method, where the pulse height distribution of the recorded pulses was modeled [71, 118, 119], a cross-calibration against the NICE detector is performed

here. In this chapter, both partial efficiencies of COMPACT are addressed for the case of detecting Ne^+ and Xe^{2+} at 600 keV and 900 keV, respectively.

A.1 Geometric detection efficiency

The size of the recombined product beam at the position of the COMPACT detector depends on the size of the stored parent ion beam in the electron-ion interaction region, as well as on the focusing by the quadrupoles between the interaction region and the detector. The entrance window of the COMPACT housing has a height of 5 cm and a width of only 2 cm. The 'active' area of the detector, which is the area of the converter electrode that is 'visible' for the incoming particle beam, is determined by the bent shape of the converter electrode and by the angle between the detector and the incoming beam. Therefore, the width of the active area is effectively even smaller than the opening of the housing, as explained below in section A.1.1. Consequently, not necessarily the whole product beam can be captured by the detector.

COMPACT is movable in the experimental vacuum chamber by a worm drive connected to a hand wheel where the detector position can be read out in arbitrary units of 'tics'. Tics can be converted to a detector displacement in mm by the convention 10 tics = 4 mm. To derive the horizontal beam size of the Ne^+ and Xe^{2+} product beams, and to estimate how much of it is collected by COMPACT at its respective positions during the recombination measurements at 240 tics and 280 tics (96 mm and 112 mm), COMPACT was moved horizontally across the product beam locations and count rates were recorded at different positions every 5 tics (every 2 mm). This procedure of position-scanning was already demonstrated in [119].

Mathematically, the sampling of the beams by COMPACT can be described as the convolution of the active area of the detector and the beam shapes. The entrance window of COMPACT has a height of 5 cm and is expected to be much larger than the vertical elongation of the product beams. From cross-checks with neutral particles on the NICE imaging detector, it was found that both Ne^{2+} and Xe^{3+} beams were reasonably centered, and it is therefore assumed that in vertical direction basically the whole beams were captured by COMPACT. This simplifies the description of the position scan measurements to a 1D convolution of the effective width of COMPACT and the horizontal beam projection. The active area of COMPACT is approximated by a box function with the effective width w_{eff},

$$f_{\mathrm{det}}(x; w_{\mathrm{eff}}) = \Theta\left(x - \frac{w_{\mathrm{eff}}}{2}\right) - \Theta\left(x + \frac{w_{\mathrm{eff}}}{2}\right), \tag{A.2}$$

where x denotes the horizontal coordinate. This representation doesn't consider different widths for different vertical positions of the impacting particles, but w_{eff} is in-

terpreted as the average of all these vertical positions (see section A.1.1 for further explanation).

For the product ion beam, a Gaussian beam profile is assumed with the intensity distribution

$$I_{\mathrm{beam}}(x; A, \mu, \sigma) = \frac{A}{\sqrt{2\pi\sigma^2}} \exp\left(-\frac{(x-\mu)^2}{2\sigma^2}\right) \tag{A.3}$$

along the horizontal axis. A is the integral of the beam intensity, σ the standard deviation, and μ the center of the distribution. The convolution of f_{det} and I_{beam},

$$\begin{aligned}\Gamma(x; A, \mu, \sigma, w_{\mathrm{eff}}) &= (f_{\mathrm{det}} * I_{\mathrm{beam}})\,(x; A, \mu, \sigma, w_{\mathrm{eff}}) \\ &= \frac{A}{2}\left(\mathrm{erf}\left(\frac{x-\mu+w_{\mathrm{eff}}/2}{\sqrt{2}\sigma}\right) - \mathrm{erf}\left(\frac{x-\mu-w_{\mathrm{eff}}/2}{\sqrt{2}\sigma}\right)\right),\end{aligned} \tag{A.4}$$

describes the signal captured by COMPACT at a given detector position x, and can be used to model the position scan measurements presented in the following sections. It should be noted that also within the scan range the effective width changes due to different angles, so $w_{\mathrm{eff}} = w_{\mathrm{eff}}(x)$. Given the fact that the effective width is already imprecisely known resulting from the uncertain effect of the side plates (see section A.1.1 for further explanation), the additional effect of position-dependent w_{eff} is not considered.

From the fit of equation (A.4) to the measured count rates at different detector positions, the (Gaussian) shape of the product beam I_{beam} can be reconstructed, and the fraction of the beam captured by COMPACT defines the geometric detection efficiency,

$$\eta_{\mathrm{g}} = \frac{\int_{x_1}^{x_2} I_{\mathrm{beam}}(x; A_{\mathrm{fit}}, \mu_{\mathrm{fit}}, \sigma_{\mathrm{fit}})\,\mathrm{d}x}{\int I_{\mathrm{beam}}(x; A_{\mathrm{fit}}, \mu_{\mathrm{fit}}, \sigma_{\mathrm{fit}})\,\mathrm{d}x}, \tag{A.5}$$

with $x_1 = x_{\mathrm{det}} - \frac{w_{\mathrm{eff}}}{2}$ and $x_2 = x_{\mathrm{det}} + \frac{w_{\mathrm{eff}}}{2}$, and COMPACT at measurement position x_{det}.

A.1.1 Effective width of COMPACT

The COMPACT detector is mounted with an inclination of 6° towards the straight section of CSR, resulting in an alignment with the stored beam behind the 6°-deflector. When moving the detector to a different position, e.g., where recombined ions are expected, the area of the converter electrode that is exposed to a product beam is reduced due to the bent shape of the converter electrode and partial shadowing by the housing (compare figure 3.3 on page 23). The effective width of the detector is an important parameter in the derivation of the detection efficiency, as explained above. Thus, the effective width of COMPACT for different angles of the impinging beam is estimated in this section.

When an ion beam enters COMPACT at an angle, only parts of the converter electrode are hit, but possibly also parts of the side plates. Although the detection probability for an ion hitting the side plate is not calculated here, it is likely that at least

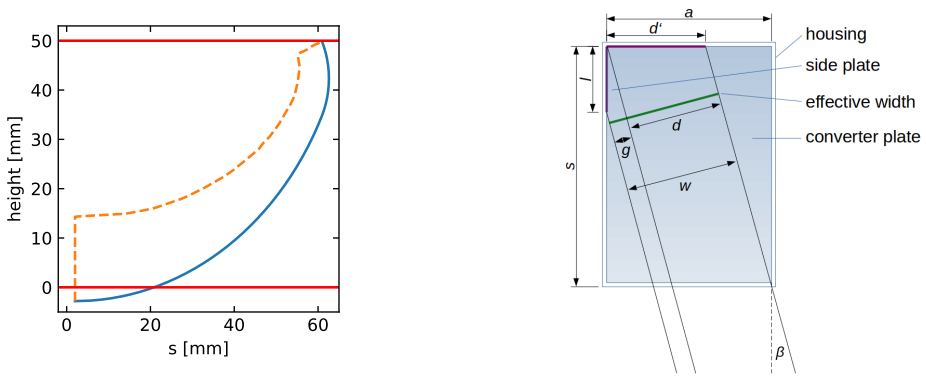

(a) (b)

Figure A.1: (a) Side view of the shapes of converter plate (solid blue line) and side plate (dashed orange line). s indicates the distance from the front of the detector, which is at $s = 0\,\text{mm}$. The red lines mark the vertical opening of the housing. (b) Schematic drawing of the top view on the converter plate. A broad ion beam hitting COMPACT with an angle β illuminates the fraction d' of the whole converter plate width a, as well as the side plate with width l. The exposed parts of the converter and side plates are marked in purple. This results in an exposed width w (marked in green) and an effective width w_{eff} between d and w when considering the counting probabilities.

some of these events create secondary electrons that reach the MCP. Accordingly, the side plates add effective width to the detector. A schematic drawing can be found in figure A.1. Furthermore, the effective width is dependent on the height h at which the particle enters, due to the curved shape of the converter electrode (compare figure A.1a and figure 3.3b on page 23). A possible tilt of COMPACT in vertical direction is not considered here.

The 'depth' $s(h)$ of COMPACT, so the distance between the front of the detector housing and the converter electrode, was derived from the existing drawings of the detector. For the following geometrical considerations, the variables as displayed in figure A.1b are used. The geometric width $d(h)$ of the converter plate that is exposed to the ion beam can be given as

$$d(h) = d'(h)\cos\beta = (a - s(h)\tan\beta)\cos\beta, \tag{A.6}$$

with the total width of the converter plate $a = 20\,\text{mm}$ and the angle β between detector and beam. Adding to this is the geometrical width of the side plate,

$$g(h) = l(h)\sin\beta, \tag{A.7}$$

depending on the depth $l(h)$ of the side plate (which is the horizontal distance between the orange and blue curves in figure A.1a). The overall exposed width $w(h)$ thus is the sum of both,

$$w(h) = d(h) + g(h). \tag{A.8}$$

The counting efficiency is potentially reduced for an ion hitting the side plate compared

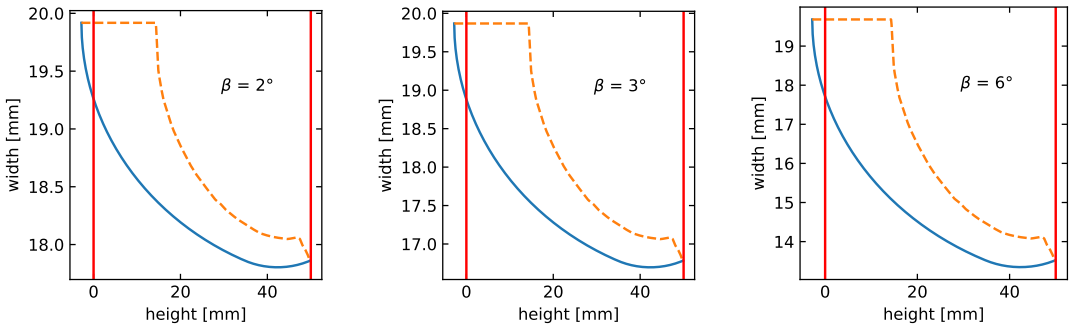

(a) Xe^{2+} position, $\beta = 2°$. (b) Ne^{+} position, $\beta = 3°$. (c) Neutral position, $\beta = 6°$.

Figure A.2: Geometric width of the COMPACT detector for different inclination angles β towards the beam, corresponding to the positions to detect (a) Xe^{2+}, (b) Ne^{+} and (c) neutral particles. The blue solid line marks the width $d(h)$ of the converter plate at different heights, the orange dashed line represents the combined width of converter and side plate $w(h)$. The red lines mark the vertical opening of the detector housing.

to an ion hitting the converter plate. Instead of evaluating the differences in the counting efficiency, this is accounted for in an 'effective width' of COMPACT $w_{\text{eff}}(h)$, which is expected to lie in between $d(h)$ and $w(h)$, i.e. $d(h) \leq w_{\text{eff}}(h) \leq w(h)$. Figure A.2 shows the effective widths for angles between detector and product beam of $\beta = 2°$, 3° and 6°, corresponding to the angles when detecting Xe^{2+}, Ne^{+} and neutral particles, respectively. The red lines in figure A.2 indicate the vertical opening of the detector housing. Even for these small angles, the active width is considerably reduced compared to the full width of the converter plate and depends strongly on the height at which the product beam is impinging. A broad beam hitting COMPACT will sample different heights of the detector. Averaged over all accessible heights h, the mean values $\bar{d}$ of $d(h)$ and $\bar{w}$ and $w(h)$ corresponding to the geometric widths for angles of 2°, 3° and 6° are given in table A.1. Here, the effective width w_{eff} is calculated as arithmetic mean $(\bar{d} + \bar{w})/2$, and the uncertainties include the largest and smallest possible $w(h)$ and $d(h)$. Due to the unknown efficiency for production and detection of secondary electrons coming from the side plates, the given w_{eff} should be taken as an estimate only.

A.1.2 Geometric detection efficiency for Ne^{+}

In the Ne^{2+} beamtime, the position scan across the Ne^{+} product beam was performed for an injection scheme similar to the one used for the recombination measurements as presented in section 4.5 on page 44, comprising 5.3 s of pre-cooling, 25.6 s of wobbling between cooling energy and measurement energies, and 2.1 s without ions. In the measurement scheme, detuning energies between 20 eV and 27 eV were scanned. The applied electron currents were $I_{\text{e,cool}} = 45\,\mu\text{A}$ and $I_{\text{e,meas}} = 160\,\mu\text{A}$, resulting in electron

Table A.1: Widths of the COMPACT detector for different beam angles. $\bar{d}$ and $\bar{w}$ denote the mean over $d(h)$ and $w(h)$, respectively, in the height range where particles can enter the detector (red lines in figure A.2). The effective width w_{eff} given here is calculated as the mean of $\bar{d}$ and $\bar{w}$. The errors are chosen to cover the largest w as well as the lowest d over the height range.

	β	$\bar{d}$ [mm]	$\bar{w}$ [mm]	w_{eff} [mm]
Xe^{2+}	2°	18.2	18.8	$18.5^{+1.4}_{-0.7}$
Ne^+	3°	17.3	18.3	$17.8^{+2.1}_{-1.1}$
neutrals	6°	14.5	16.5	$15.5^{+4.2}_{-2.1}$

densities of $n_{\text{e,cool}} = 7.7 \times 10^5\,\text{cm}^{-3}$ and $n_{\text{e,meas}} = 14.2 \times 10^5\,\text{cm}^{-3}$ to $13.4 \times 10^5\,\text{cm}^{-3}$, respectively. The ion number was measured in the beginning of each injection when the injected ion beam was still in one bunch. Figure A.3a shows the ion-number-normalized count rates measured in the different wobbling steps at different detector positions. The signals are almost identical in cooling and measurement steps, and are to a large extend resulting from collisions with residual-gas particles. In several fits with w_{eff} as a free fit parameter or fixed at the maximum/mean/minimum values from table A.1, the convolution function (A.4) was fitted to the position scan data in figure A.3a. The fit results are reported in table A.2. Compared to the expected effective widths shown in table A.1, the fitted values in cooling and measurement steps are rather small with $w_{\text{eff}} \approx 17\,\text{mm}$, but within the expected range, indicating a small contribution of the side plates. However, σ and w_{eff} are partially anti-correlated, and fixing w_{eff} at the mean value of 17.8 mm still results in good agreement of the fit with the measured data. As an example, figure A.3b shows the measurement signal together with the fits. Although the agreement between the data and the fits varies for the different assumed effective widths, in all cases, more than 99 % of the recombined Ne^+ beam is expected to be collected by COMPACT at the recombination measurement position $x_{\text{rec,Ne}^+} = 96\,\text{mm}$, where the detector was placed throughout the regular recombination measurement runs. The geometric efficiencies derived from the individual fits are listed in table A.2. To account for the uncertainties in the fitting process and in the model itself, the overall geometric detection efficiency for the detection of Ne^+ is estimated as

$$\eta_{\text{g,Ne}^+} = 0.99 \pm 0.01. \tag{A.9}$$

A.1.2.1 Ion beam focusing effects

In the measured recombination data presented in chapter 5, distortions of the obtained MBRC were found (compare section 5.2.5 on page 82) which could be explained by a change of the geometric detection efficiency with the detuning energy. This is attributed to ion beam focusing effects. Due to its space charge, the electron beam acts as a lens

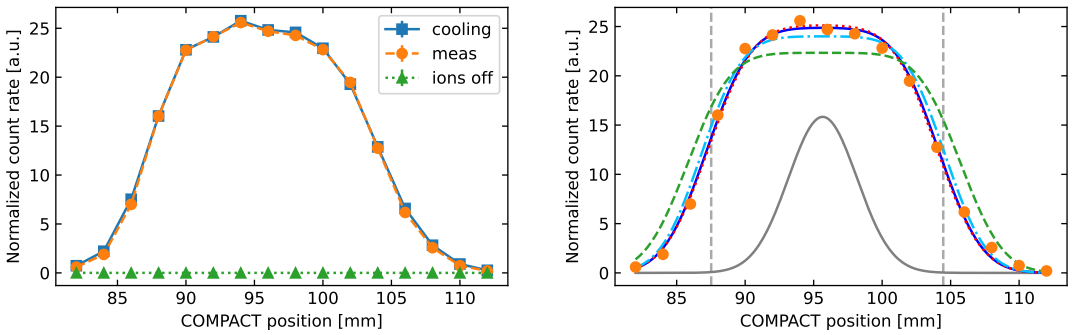

(a) (b)

Figure A.3: (a) Ion-number-normalized count rates at different COMPACT positions across the Ne^+ product beam position. The cooling step is depicted in blue squares, the measurement step in orange circles, and the dark count rate in green triangles. (b) Count rates in the measurement step (orange circles) together with fits of the convolution function (A.4) for w_{eff} as a free fit parameter (solid dark blue line), and fixed at the minimum (dotted red line), mean (dash-dotted light blue line) and maximum (dashed green line) values for w_{eff} according to table A.2. The solid gray line gives the shape of the Ne^+ product beam according to the free fit (arbitrarily normalized), and the dashed gray lines mark the width w_{eff} in that case, assuming COMPACT at the recombination measurement position $x_{\mathrm{rec,Ne^+}} = 96\,\mathrm{mm}$.

and leads to focusing of the stored ion beam. This effect is dependent on the electron density in the electron-ion interaction region, and a higher electron density is expected to focus the stored beam stronger, resulting in a reduced size of the product beam and thus in a higher geometric detection efficiency. In each scanned detuning energy range, the electron current was kept constant and consequently, the electron density increased towards lower detuning energies where the electrons were slower. The observed distortions in the data could be explained by a small variation in the geometric detection efficiency on the 1 %-level.

The statistics in the COMPACT position scan presented above are not good enough to evaluate the position scan data from the measurement steps for selected detuning energies. Also, the variation in the electron densities for the different measurement detuning energies included in the position scan is expected too small to result in a measurable variation in the geometric detection efficiency. Nonetheless, the electron density was changing considerably between the cooling and the measurement step by almost a factor of 2.

When comparing the fitted Ne^+ product beam widths σ for cooling and measurement steps in table A.2, the width is systematically slightly larger in the cooling step than in the measurement step, although the error bars overlap. This fact is also reflected in the change in the fitted geometric detection efficiency $\eta_{\mathrm{g,fit}}$ in table A.2. It can be concluded that a changing electron density indeed might result in varying product beam sizes and slightly varying geometrical detection efficiencies η_{g}. However, the observed variation

Table A.2: Fitting results according to the fit of the convolution function (A.4) to the COMPACT scan over the Ne^+ beam in the cooling and measurement steps, as shown in figure A.3a. Fits with different fixed effective widths w_{eff} at the maximum, mean, and minimum values according to table A.1 were performed, as well as a fit taking w_{eff} as a free parameter. The error bars indicate the fitting uncertainties. $\eta_{\text{g,fit}}$ gives the amount of the Ne^+ beam captured by COMPACT at the recombination measurement position $x_{\text{rec,Ne}^+} = 96\,\text{mm}$, according to equation (A.5).

		w_{eff} [mm]	μ [mm]	σ [mm]	$\eta_{\text{g,fit}}$ [%]
w_{eff} free	cool	17.0 ± 0.2	95.7 ± 0.1	2.7 ± 0.2	99.84
	meas	16.9 ± 0.2	95.7 ± 0.1	2.5 ± 0.1	99.92
w_{eff} max	cool	19.9	95.8 ± 0.4	2.6 ± 0.6	99.99
	meas	19.9	95.8 ± 0.4	2.5 ± 0.6	99.99
w_{eff} mean	cool	17.8	95.7 ± 0.1	2.5 ± 0.2	99.95
	meas	17.8	95.7 ± 0.1	2.4 ± 0.2	99.98
w_{eff} min	cool	16.7	95.6 ± 0.1	2.7 ± 0.1	99.75
	meas	16.7	95.7 ± 0.1	2.6 ± 0.1	99.87

of η_{g} is on the limit of the sensitivity achievable in the position scan. Still, it is assumed that these effects are well covered within the uncertainty given for the overall geometric detection efficiency for Ne^+ in equation (A.9).

A.1.3 Geometric detection efficiency for Xe^{2+}

For the position scan across the Xe^{2+} product beam, a scheme of 20 s pre-cooling, 34 s of wobbling and 2.1 s without ion beam was chosen. The wobbling scheme consisted of varying collision energies between cooling, 19.6 eV (at the main DR resonance peak), and an off step without electrons. This scheme is different from the one used for the regular recombination experiments explained in section 4.5, where the pre-cooling scheme was varied between 10 s and 20 s and the wobbling scheme included a step at a reference detuning energy instead of the step without electrons. The electron current in the cooling step was $I_{\text{e,cool}} = 8.5\,\mu\text{A}$, resulting in an electron density of $n_{\text{e,cool}} = 3.2 \times 10^5\,\text{cm}^{-3}$. In the measurement step at the DR peak, the electron current was $I_{\text{e,meas}} = 85.5\,\mu\text{A}$, resulting in an electron density of $n_{\text{e,meas}} = 9.3 \times 10^5\,\text{cm}^{-3}$.

The count rates at different COMPACT positions in the different wobbling steps are shown in figure A.4a. While the count rates around 112 mm arise from the impinging Xe^{2+} product ions, the strong increase in the count rate at higher (more ring-inward) positions is attributed to scraping the edge of the stored Xe^{3+} parent beam. The count rates in the different steps basically follow the same trend, but differ at high positions.

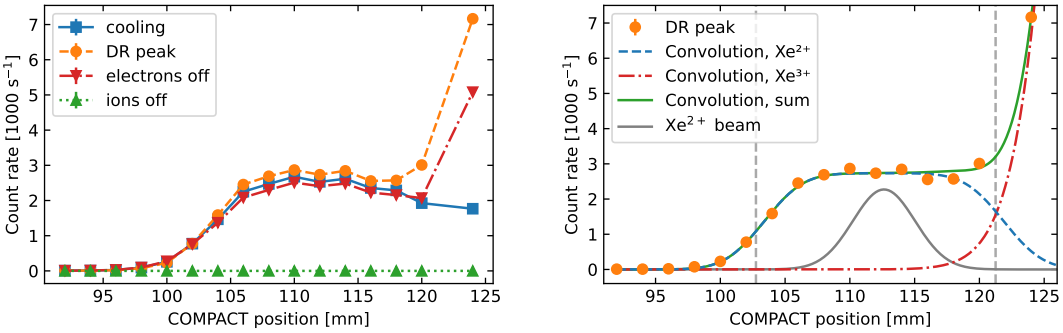

(a) (b)

Figure A.4: (a) Count rates at different COMPACT positions across the Xe^{2+} product beam position. The cooling step is depicted in blue squares, the measurement step (at the DR peak around 19.6 eV) in orange circles, the off step in red triangles and the dark count rate in green triangles. The rise at higher positions comes from scraping of the stored Xe^{3+} beam. (b) Count rates in the measurement step (orange circles) together with a fit of the convolution function (A.10) for $w_{\text{eff}} = 18.5\,\text{mm}$ (solid green line), as well as the contributions of the Xe^{2+} (dashed blue line) and Xe^{3+} (dash-dotted red line) beams. The solid gray line gives the Gaussian shape of the Xe^{2+} product beam according to the fit, and the dashed gray lines mark the effective width w_{eff}, assuming COMPACT at the recombination measurement position $x_{\text{rec,Xe}^{2+}} = 112\,\text{mm}$.

This behavior potentially reflects the ion beam expansion when not actively cooling it with electrons at matched velocities, and is discussed together with the ion beam focusing effects due to the electron beam space charge in section A.1.3.1.

In contrast to the COMPACT scan in the neon beamtime shown in section A.1.2, here the ion number was not recorded simultaneously, but the ion source was stable enough to provide the same amount of ions for each injection within a few percent.

To account for both the signals produced by the product and the main beam, the sum of two convolution functions as in equation (A.4), i.e.

$$G(x; A_1, \mu_1, \sigma_1, A_2, \mu_2, \sigma_2, w_{\text{eff}}) = \Gamma(x; A_1, \mu_1, \sigma_1, w_{\text{eff}}) + \Gamma(x; A_2, \mu_2, \sigma_2, w_{\text{eff}}), \quad \text{(A.10)}$$

was used for fitting of the count rates in figure A.4a. Here, A_1, μ_1, σ_1 are parameters for the beam of recombined Xe^{2+} ions and A_2, μ_2, σ_2 for the main Xe^{3+} beam. Similar to the procedure for Ne^{+}, the width w_{eff} of COMPACT is assumed constant over the whole scan region.

Due to the strongly rising count rate when moving COMPACT further into the main beam, only positions up to 124 mm could be scanned without overwhelming the detector. The superposition of the two beams and the insufficient sampling of the main beam restrict the fit accuracy. To improve the fit results, the position of the main beam was fixed to the expected closed-orbit position of $\mu_2 = 146\,\text{mm}$, and multiple fits were performed with w_{eff} as a free fit parameter or fixed at the maximum/mean/minimum

values from table A.1. The fit parameters for the fit of G from equation (A.10) to the different wobbling steps in figure A.4a are shown in table A.3 together with the corresponding geometric detection efficiency $\eta_{\mathrm{g,fit}}$ for the Xe^{2+} beam with COMPACT at position $x_{\mathrm{rec,Xe^{2+}}} = 112\,\mathrm{mm}$ where the DR measurements were taken. In addition, also the count rate $R_{\mathrm{Xe^{3+}}}$ produced by the flank of the main Xe^{3+} beam with COMPACT at position 112 mm is noted in table A.3. All fits match the data well, but the free-fitted w_{eff} are smaller than the lowest effective width assumed in section A.1.1, where w_{eff} ranges from 17.8 mm to 19.9 mm. As an example, figure A.4b shows the fit with a fixed $w_{\mathrm{eff}} = 18.5\,\mathrm{mm}$ to the measurement signal.

From the fit results, COMPACT captures more than 99 % of the product beam at position 112 mm in all steps shown in figure A.4a, and the count rate induced by the flank of the main beam at the given position is negligible compared to the count rate produced by Xe^{2+}, which was several $1000\,\mathrm{s^{-1}}$. Accounting for the uncertainties in the model and the fitting procedure, the overall geometric detection efficiency of COMPACT at the measurement position at 112 mm is estimated as

$$\eta_{\mathrm{g,Xe^{2+}}} = 0.99 \pm 0.01. \tag{A.11}$$

A.1.3.1 Ion beam focusing effects

As explained in section A.1.2.1 for the case of neon, the geometrical detection efficiency η_{g} is dependent on the electron density in the interaction region. Varying electron densities can lead to a changing focusing of the stored ion beam and consequently to a varying size of the product beam. In the position scan presented above, the electron density in the cooling step ($n_{\mathrm{e,cool}} = 3.2 \times 10^5\,\mathrm{cm^{-3}}$) was roughly one third of the electron density in the measurement step ($n_{\mathrm{e,meas}} = 9.3 \times 10^5\,\mathrm{cm^{-3}}$). Therefore, a stronger focusing is expected in the measurement step in comparison to cooling and off steps. This is tentatively confirmed from the fitted widths σ_1 of the Xe^{2+} product beam, which are listed in table A.3. However, this is in contradiction to the prominent finding in figure A.4, where at high positions (where the stored Xe^{3+} beam is scraped) the count rate in the cooling step is considerably lower than in measurement and off steps. This indicates a smaller beam in the cooling step. Most likely, when comparing cooling and measurement steps, the geometric detection efficiency is governed by the interplay of the ion beam focusing by the electron beam space charge on the one side and on the other side by the ion beam blow-up due to intrabeam scattering when the ion beam is not actively electron-cooled. In the Ne^+ position scan, the ion beam focusing seemed to be dominant as the product beam width was tentatively smaller in the measurement steps than in the cooling steps (see section A.1.2.1). For Xe^{2+}, the sensitivity of the position scan method (and especially the fitting model) is not sufficient to find a clear conclusion. As only one detuning energy was probed in the measurement steps, the variation of η_{g} with the detuning energy could not be investigated here.

Still, it is assumed that potential focusing effects are well covered within the uncertainty given for the overall geometric detection efficiency for Xe^{3+} in equation (A.11).

Table A.3: Fitting results according to the fit of the convolution function (A.10) to the COMPACT scan over the Xe^{2+} beam in the cooling (c), measurement (m) (at the DR peak at 19.6 eV), and off (o) steps, as shown in figure A.4a. Fits with different fixed effective widths w_{eff} at the maximum, mean, and minimum values according to table A.1 were performed, as well as a fit taking w_{eff} as a free parameter (from top to bottom in the table). The error bars indicate the fitting errors. $\eta_{\text{g,fit}}$ gives the fraction of the Xe^{2+} beam captured by COMPACT at the recombination measurement position $x_{\text{rec,Xe}^{2+}} = 112\,\text{mm}$, according to equation (A.5). $R_{\text{Xe}^{3+}}$ is the rate produced by the stored Xe^{3+} beam on COMPACT at 112 mm.

	w_{eff} [mm]	μ_1 [mm]	σ_1 [mm]	σ_2 [mm]	$\eta_{\text{g,fit}}$ [%]	$R_{\text{Xe}^{3+}}$ [s^{-1}]
c	19.9	113.0 ± 0.2	2.8 ± 0.4	2.5 ± 207.8	99.92	0
m	19.9	113.3 ± 0.2	2.3 ± 0.2	4.8 ± 0.3	99.99	0
o	19.9	113.2 ± 0.2	2.8 ± 0.3	2.5 ± 1758.9	99.91	0
c	18.5	112.5 ± 0.1	2.7 ± 0.2	3.3 ± 6.9	99.94	0
m	18.5	112.6 ± 0.2	2.4 ± 0.3	5.5 ± 0.3	99.98	2
o	18.5	112.6 ± 0.2	2.8 ± 0.2	4.7 ± 0.3	99.86	0
c	17.8	112.3 ± 0.1	2.7 ± 0.2	5.6 ± 0.9	99.92	1
m	17.8	112.3 ± 0.2	2.5 ± 0.3	5.9 ± 0.3	99.95	6
o	17.8	112.3 ± 0.1	2.9 ± 0.2	5.3 ± 0.2	99.79	1
c	17.7 ± 3.2	112.2 ± 1.7	2.7 ± 0.2	5.9 ± 9.4	99.91	1
m	13.6 ± 0.3	110.1 ± 0.2	2.5 ± 0.2	9.2 ± 0.3	97.51	237
o	15.6 ± 0.7	111.3 ± 0.4	2.9 ± 0.2	7.1 ± 0.7	99.20	26

A.2 Intrinsic detection efficiency

The intrinsic detection efficiency η_i of the COMPACT detector represents the probability for a particle hitting the converter electrode to be counted as an event. In previous experiments, η_i was derived from an analysis of the distribution of amplitudes of the electronic pulses (referred to as Pulse Height Distribution (PHD)) produced by the impinging product particles in comparison to the pulses generated by UV photons [119]. The model to theoretically describe the PHD of COMPACT is reported in [118], [71], and [119], and is based on a model for electron emission in photomultipliers [143]. It allows to derive η_i by taking into account the number of secondary electrons released from the converter electrode upon a particle impact, the likelihood for these secondary electrons to reach the MCP, the probability to generate an electron avalanche within the MCP, and the discrimination threshold of the used read-out electronics.

In this thesis, η_i was derived in a different procedure from a cross-check against the NICE detector, which has a known detection efficiency. Partially, the procedure still relied on the modeling of PHDs, so the above mentioned model to describe the PHD is presented here, following [71, 118, 119].

The likelihood for n secondary electrons released from the converter electrode to reach the MCP can be modeled by a Pólya distribution

$$W_n(\tilde{\gamma}, b) = \frac{\tilde{\gamma}^n}{n!}\,(1 + b\,\tilde{\gamma})^{-n-1/b} \prod_{j=0}^{n-1}(1 + j\,b), \tag{A.12}$$

where $\tilde{\gamma}$ is the average number of electrons reaching the MCP and b the relative variance of $\tilde{\gamma}$. $\tilde{\gamma} = \langle\gamma\epsilon_c\rangle$ is determined by the number of secondary electrons γ released from the converter electrode, weighted by the probability ϵ_c to reach the MCP. Therefore, $\tilde{\gamma}$ can in principle vary spatially across the converter plate area. Once reaching the MCP, each electron has the probability $\epsilon = 0.6$ to generate an avalanche, accounting for the open area ratio of the MCP channels [119]. The probability of inducing k avalanches when multiple secondary electrons hit the MCP surface follows a binomial distribution, and in combination with the Pólya distribution above leads to the probability

$$P_k(\tilde{\gamma}, b) = \sum_{n=k}^{\infty} \binom{n}{k} \epsilon^k\,(1-\epsilon)^{n-k}\,W_n(\tilde{\gamma}, b) \tag{A.13}$$

for producing k MCP avalanches after a particle impinged on the converter electrode, assuming that the secondary electrons enter different MCP channels. Especially, P_0 is the probability that no avalanche is generated. While $(1 - P_0)$ gives the probability to produce at least one avalanche within the MCP, the intrinsic detection efficiency is smaller than $(1 - P_0)$ due to the discrimination threshold of the MCP read-out electronics. With the help of the pulse height distribution of the electronic signal recorded at the MCP, this effect can be estimated.

In case multiple secondary electrons hit different MCP channels, the electronic signals of the avalanches pile up. If f_1 denotes the PHD for exactly one electron hitting the MCP, the pile-up of k avalanches can be expressed by the convolution

$$f_k = f_{k-1} * f_1. \tag{A.14}$$

The whole pulse height spectrum F, produced by the impact of particles releasing several secondary electrons, can then be modeled by the sum of individual f_k and their corresponding probabilities P_k, i.e.

$$F(h;\tilde{\gamma},b) = \frac{1}{1-P_0}\sum_{k=1}^{\infty} P_k(\tilde{\gamma},b)\, f_k(h). \tag{A.15}$$

The underlying f_1 can be derived by illuminating the converter plate of the COMPACT detector with UV photons that release at maximum one secondary electron. The obtained distribution is reported to follow a decreasing exponential [119] or the sum of a Gaussian and a decreasing exponential [71, 118], respectively.

The fit of equation (A.15) to the experimentally recorded PHDs for heavy-particle impact yields $\tilde{\gamma}$ and b, and therefore allows to calculate P_0. Taking into account the fraction of the fitted PHD below the discrimination threshold, the intrinsic detection efficiency of COMPACT can be determined, as demonstrated in [119] for a number of different detected particles. The obtained efficiencies range from $\eta_\mathrm{i} = 56(4)\,\%$ for Ag_2 at 60 keV and 6 K detector temperature to $\eta_\mathrm{i} = 84(2)\,\%$ for N at 30 keV and 83 K. Especially, detection efficiencies can vary between ionic and neutral particles of the same species. This was shown for N^+ and N at the same conditions, where $\eta_\mathrm{i} = 72(4)\,\%$ and $84(2)\,\%$ were found, respectively, corresponding to a relative difference of $\sim 15\,\%$ [119].

The intrinsic detection efficiencies η_i can vary considerably for different impacting particles and depend on multiple factors like the particle energy and the discrimination threshold. In the Ne^{2+} and Xe^{3+} beamtimes, f_1 (i.e. the PHD from UV photons) was not measured and the detection efficiencies for Ne^+ and Xe^{2+} were not derived from the model presented above, but partially relied on it. Instead, a different approach is followed here, comparing the detection efficiency of COMPACT to the known efficiency of the NICE detector. In the neon beamtime, the calibration was performed on neutral Ne produced from double-electron capture of Ne^{2+} from residual-gas particles. In the xenon beamtime, a similar calibration was done on fragments from dissociative recombination of C_2F^+ that was unintentionally present in the stored Xe^{3+} beam to a small extent. The derived detection efficiency for C_2F fragments was linked to the intrinsic detection efficiency for Xe^{2+} with the help of the recorded PHDs. The detailed procedures are explained in the following subsections.

A.2.1 Intrinsic detection efficiency for Ne^+

Similar to the procedure in section A.1, the count rate on COMPACT produced by neutral neon atoms was recorded at several detector positions around the neutral po-

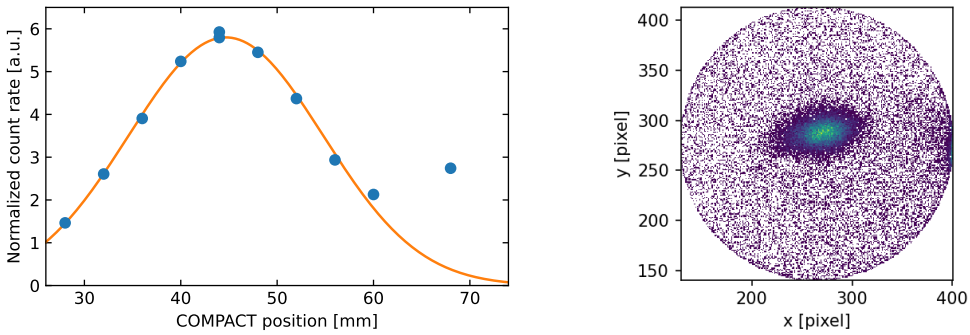

(a) (b)

Figure A.5: (a) Ion-number-normalized count rates at various COMPACT positions across the neutral product beam position (blue circles). The central peak around 45 mm is produced by neutral neon after double-electron-capture by Ne^{2+} from the residual gas. The increase at higher positions is caused by Ne^+. The orange line represents a fit of the convolution function to the neutral signal. (b) Spot distribution on the NICE detector. The central spot is caused by neutral neon, and a trace of Ne^+ is visible at higher x.

sition, as shown in figure A.5a. At more ring-inward positions, COMPACT captured parts of the Ne^+ beam produced by capture of only one electron from residual gas. For comparison, figure A.5b shows the spot distribution on NICE. Here as well, the central part is produced by neutral neon, and at higher x, a trace of Ne^+ is visible.

To compare the signal on the two detectors, a scan with a box function over the count rate distribution on NICE was simulated to mimic the COMPACT position scan. Both the COMPACT scan and the mimicked scan from the NICE data were compared subsequently to obtain the detection efficiency of COMPACT. The individual steps are explained in the following.

A.2.1.1 Evaluation of the COMPACT scan

A double-peak convolution function according to equation (A.10) was fitted to the ion-number-normalized count rate recorded by COMPACT around the neutral position, and the Gaussian width σ_1, center μ_1, and integral A_1 were extracted. Three different fits were performed using the effective widths $w_{\text{eff}} = 13.4\,\text{mm}$, $15.5\,\text{mm}$ and $19.7\,\text{mm}$, corresponding to the smallest, mean, and largest width found in section A.1.1 (compare table A.1 on page 124). All fits match the recorded data reasonably well. Figure A.5a shows the convolution of the neutral beam following equation (A.4), using the fit parameters obtained in the fit by equation (A.10). Visually, all three fits for the different w_{eff} are almost identical, but the fitted Gaussian widths of the neutral beam σ_1 vary between $9.2\,\text{mm}$, $8.9\,\text{mm}$ and $7.9\,\text{mm}$ for the widths given above, with fitting uncertainties below 7 %.

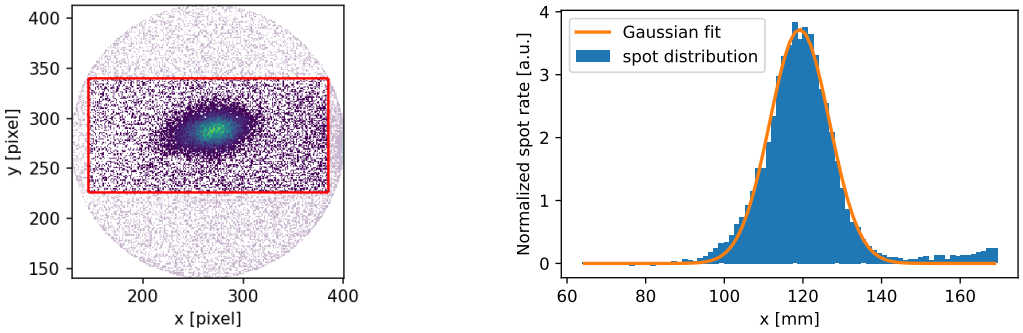

(a) (b)

Figure A.6: (a) The red window marks the region of the NICE image taken into account for the simulation of the COMPACT scan (see text). (b) Ion-number-normalized spot distribution on NICE obtained when projecting the red area in (a) to the x-axis, corrected for dark spots and transformed to mm according to the pixel-to-mm calibration factor for NICE. The orange line is a Gaussian fit to the spot distribution.

A.2.1.2 Count rate distribution on NICE

Figure A.5b shows the spot distribution on the NICE detector. To mimic the COMPACT position scan, a rectangular window was selected from the NICE projection, representing the fraction of the spot distribution covered in the COMPACT scan. The height of the window was chosen as the height of the opening in the COMPACT housing of 5 cm, using the pixel-to-mm conversion factor 1/0.44, which had been derived with the help of the calibration mask from an OH^+ beam. The selection is marked in figure A.6a, and the procedure below is not sensitive to the exact vertical position of the selection window as long as the central spot is not cut. The spot distribution within the selection was projected to the horizontal axis and corrected for dark spots. Subsequently, a Gaussian was fitted to the projection with good agreement, as shown in figure A.6b. The Gaussian width of the neutral beam obtained from the fit is 7.6(1) mm on NICE.

For a drifting neutral beam produced in the electron cooler section, it is expected that the projection of the parent beam size increases the farther the distance from the center of the straight section. Therefore, a lager neutral beam width is expected on NICE in comparison to COMPACT. However, all neutral beam widths obtained from the evaluation of the COMPACT position scan in section A.2.1.1 are larger than the value derived from the NICE image. Only for the largest assumed effective width of COMPACT of $w_{\mathrm{eff}} = 19.7\,\mathrm{cm}$ (compare section A.2.1.1), the fitted Gaussian width of $\sigma_1 = 7.9(4)\,\mathrm{mm}$ agrees within the error bars with the beam width obtained from NICE. The reason for this mismatch is unclear. An additional focusing effect due to the quadrupole settings is unlikely, as the neutrals are produced in collisions with residual gas along the whole straight section. Here, the x-axis of the spot distribution projection in figure A.6b was scaled and shifted such that width and center agree with

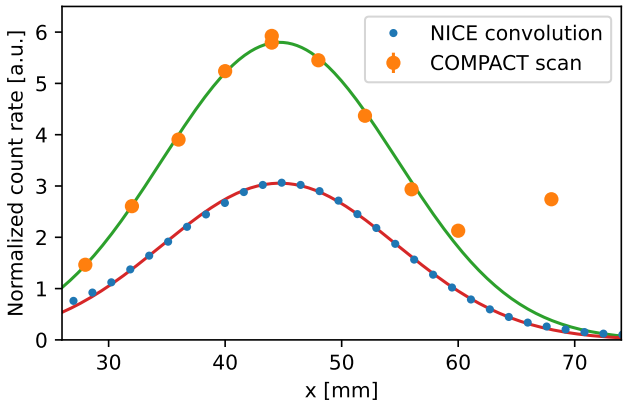

Figure A.7: Ion-number-normalized count rate on COMPACT (orange circles) at various positions around the neutral position, and the result of the convolution of the ion-number-normalized count rate distribution from NICE and a box function (width 19.7 cm), mimicking the COMPACT scan. The solid lines show fits of the convolution function (A.4) to the signal produced by neutral neon.

the fit results from the COMPACT scan.

Due to saturation effects of the camera (see [116]), the rate of spots on NICE is reduced in comparison to the rate of electronic pulses or triggers. The data acquisition on NICE was triggered by a silicon-photomultiplier, and subsequently electronic pulses as well as light spots were recorded. In approximately a quarter of all triggering events, no pulse or spot were detected, possibly due to non-optimal detector settings. However, the rates for triggers and electronic pulses were approximately equal after subtraction of dark counts. Therefore, in the following analysis, the dark-count-corrected trigger rate was taken as the detector count rate. The spot distribution (similar to figure A.6b, but with the x-axis scaled and shifted as explained above) was normalized and used as a weight to obtain the x-dependent count rate distribution. The count rate distribution was then normalized to the measured ion number.

A.2.1.3 Comparison of COMPACT and NICE count rates and detection efficiencies

A scan of a box function (representing COMPACT) across the x-dependent count rate distribution derived from NICE in section A.2.1.2 was simulated by integrating the count rate in a window with width $w_{\text{eff}} = 13.4\,\text{mm}$, 15.5 mm and 19.7 mm, respectively. Figure A.7 shows both the normalized count rate from the COMPACT scan and the simulated convolution of the count rate on NICE with a box function of width $w_{\text{eff}} = 19.7\,\text{cm}$, together with fits of the convolution function (A.4). While the count rate on COMPACT increases towards higher positions due to collection of Ne^+, this effect is not seen in the data from NICE. The reason for the strongly suppressed Ne^+ signal on NICE is not understood, but may be related to the beam trajectory.

The detection efficiency of COMPACT can be extracted when comparing the count rate integrals A_1 of the Gaussians after fitting the convolution function (A.10) to the data in figure A.7. The ratio $A_{1,\mathrm{COMPACT}}/A_{1,\mathrm{NICE}}$ directly relates to the intrinsic detection efficiencies of the two detectors, i.e.

$$\frac{A_{1,\mathrm{COMPACT}}}{A_{1,\mathrm{NICE}}} = \frac{\eta_{\mathrm{i,COMPACT}}}{\eta_{\mathrm{i,NICE}}}. \tag{A.16}$$

With the known intrinsic efficiency of NICE of $\eta_{\mathrm{i,NICE}} = 0.593(15)$ [36], the intrinsic detection efficiency of COMPACT can be extracted. The obtained efficiencies for detection of neutral neon are $\eta_{\mathrm{i,COMPACT}} = 1.2$, 1.0 and 0.8 for assumed widths of $w_{\mathrm{eff}} =$ 13.4 mm, 15.5 mm and 19.7 mm, respectively. The derived values vary substantially, and detection efficiencies above unity are not physical.

The detector calibration presented above was performed on neutral neon, whereas in the recombination experiments Ne^+ ions were detected. γ-factors, describing how many secondary electrons are released from a surface upon particle impact, can vary by $\sim 40\,\%$ for neutral and ionic particles of the same species and at the same energy, as shown by a comparison of N and N^+ detection in [119]. Such a variation for neutral neon and Ne^+ might affect the detection efficiency of COMPACT, as the detector design is based on the detection of secondary electrons. As multiple secondary electrons are produced after a particle hit, the influence of a varying γ-factor for neutral neon and Ne^+ on the overall detection efficiency is assumed to be not too strong. In the example of N and N^+ detection reported in [119], the detection efficiencies varied by $\sim 15\,\%$. In the Ne^{2+} beamtime, no PHDs for impacting Ne and Ne^+ were recorded from which a variation in the detection efficiency could have been calculated. Instead, the intrinsic detection efficiency of COMPACT is roughly estimated here. Taking into account the uncertainties in the whole procedure (mismatch between beam projections on COMPACT and NICE, uncertainty in the COMPACT width w_{eff}, fitting uncertainties, γ-factor), the intrinsic detection efficiency of COMPACT for Ne^+ is estimated as

$$\eta_{\mathrm{i,COMPACT,Ne^+}} = 0.75 \pm 0.25. \tag{A.17}$$

This estimate is in line with the values reported in [119] for other systems at much lower particle energies.

A.2.2 Intrinsic detection efficiency for Xe^{2+}

Unlike Ne^{2+}, Xe^{3+} does not neutralize in collisions with the residual gas in CSR. A direct calibration of COMPACT to NICE on neutral xenon therefore was not possible. Instead, it was made use of a small molecular contamination of C_2F^+ present in the stored Xe^{3+} beam. Upon recombination with electrons, C_2F^+ dissociates into neutral fragments. Although the fraction of the molecular contaminant on the total number of stored ions was very low, the electron-induced count rate was high enough to perform

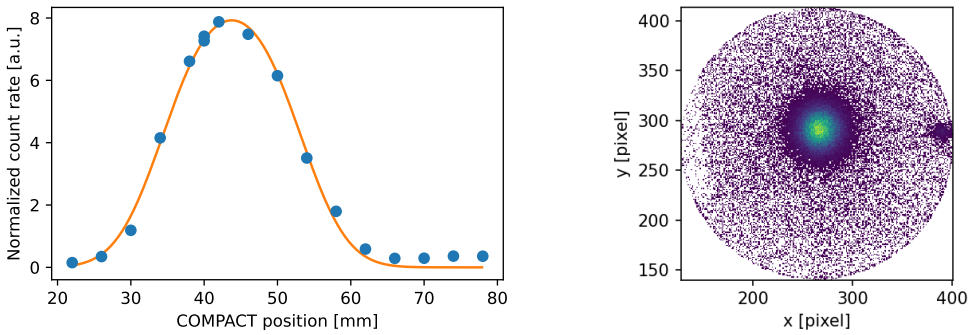

(a) (b)

Figure A.8: (a) Ion-number-normalized count rates at various COMPACT positions across the neutral position (blue circles), where fragments from dissociative recombination of C_2F^+ with free electrons were collected. The orange line represents a fit of the convolution function (A.4) to the neutral signal ($w_{\text{eff}} = 19.7\,\text{mm}$). (b) Spot distribution on the NICE detector. The central spot is caused by C_2F fragments, while the low-intensity spot at higher x is produced by Xe^+ after double-electron-capture from residual gas.

a detector cross-calibration of COMPACT and NICE. Like this, the intrinsic detection efficiency for neutral C_2F fragments was derived and thereafter linked to the detection efficiency of Xe^{2+} by a comparison of the PHDs.

A.2.2.1 Detection efficiency for C_2F fragments

The procedure to derive the intrinsic detection efficiency $\eta_{\text{i,COMPACT,C}_2\text{F}}$ for C_2F fragments is similar to the one presented for Ne^+ in section A.2.1, comparing the count rate distributions on COMPACT and NICE shown in figure A.8a and figure A.8b, respectively. Here, the signal was produced from collisions of the molecular ions with electrons at cooling energy.

COMPACT scan evaluation

COMPACT was moved to several positions around the neutral position and the count rate was recorded, collecting neutral fragments produced by dissociative recombination of C_2F^+. Although practically all of the injected ions were Xe^{3+}, the signal of the current pickup is a proxy for the number of C_2F^+ ions. Figure A.8a shows the recorded count rates normalized by the ion number. The convolution function (A.4) was fitted to the count rate scan, assuming three different effective widths of COMPACT of $w_{\text{eff}} = 13.4\,\text{mm}$, $15.5\,\text{mm}$ and $19.7\,\text{mm}$, representing the span of possible widths as derived in section A.1.1. The resulting Gaussian widths are $\sigma = 6.8\,\text{mm}$, $6.3\,\text{mm}$ and $4.7\,\text{mm}$, respectively, with fitting errors below 7 %.

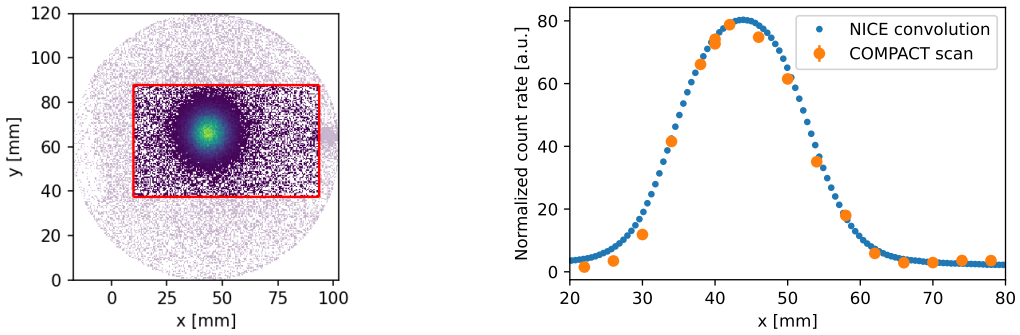

(a) (b)

Figure A.9: (a) Spot distribution of C_2F fragments on NICE, transformed to mm. The red frame indicates the window in which the COMPACT scan was simulated (see blue circles in (b)). (b) Ion-number-normalized count rates at different x positions across the neutral position. Small blue circles indicate the simulated scan from the count rate distribution on NICE as a convolution with a box of width $w_{\text{eff}} = 15.5\,\text{mm}$. The larger orange circles give the signal from the COMPACT detector recorded at the given positions, as shown in figure A.8a.

Count rate distribution on NICE and position scan mimicking

The method to mimic the COMPACT position scan from the NICE data used here is similar to the one described in section A.2.1.2, but it is complicated by the fact that C_2F^+ produces *multiple* neutral fragments upon recombination.

Using the pixel-to-mm calibration factor of 1/0.44, the NICE image was transformed to mm. A rectangular window was chosen in which the COMPACT scan was reconstructed, as shown in figure A.9a. The window had a height of 5 cm, corresponding to the height of the COMPACT detector.

Special care had to be taken when simulating the COMPACT scan from the spot distribution on NICE, as C_2F^+ dissociates into multiple fragments. From an estimate based on the detected single, double, and triple spot events on NICE, neglecting potential losses due to the finite size of the detector, but taking into account the single-particle counting efficiency, it was found that the dissociation leads to two and three fragments roughly in equal parts. The electronic count rate obtained from NICE is the rate for dissociation *events*, but not for individual fragment hits. COMPACT can trigger if at least one particle impinges on the converter plate (or side plate). In case multiple fragments from the same dissociation event hit COMPACT, the time separation is too short to produce multiple triggers, but the electron avalanches within the MCP pile up and are counted only once. Therefore, it has to be considered how many events produce at least one fragment that hits COMPACT.

Within the selection in figure A.9a, sub-windows were taken with COMPACT height and an effective width w_{eff}, representing the active area of COMPACT. For a given sub-window, the fraction of events with at least one spot in the sub-window on all

events was calculated. These fractions were evaluated for multiple center positions of the sub-window, and were used as weights for the dark-count-subtracted electronic count rate to produce the count rate distribution. Such convolutions were performed using effective widths of $w_{\text{eff}} = 13.4\,\text{mm}$, 15.5 mm and 19.7 mm, corresponding to the smallest, mean, and largest width of COMPACT in neutral position as found in section A.1.1. As an example, the convolved data for $w_{\text{eff}} = 15.5\,\text{mm}$ is shown in figure A.9b. The derived Gaussian widths when fitting equation (A.4) to the convolved NICE data are $\sigma = 6.6\,\text{mm}$, 6.8 mm and 7.4 mm and agree within the error bars with or are larger than the widths obtained from the fit to the COMPACT scan as shown in the subsection above (where $\sigma = 6.8\,\text{mm}$, 6.3 mm and 4.7 mm). This represents the expected behavior of a drifting neutral beam without additional focusing. Here, the x-axis on the NICE image was not artificially scaled to get the same beam width as in the fit to the COMPACT scan. Nonetheless, in the following, the effective width w_{eff} at the COMPACT position was assumed and the increase in the projected beam width at the NICE position is ignored. The systematic error introduced by subsequently assuming a too small effective width w_{eff} in the convolution procedure is estimated as additional 5 % on the detection efficiency for C_2F fragments.

Comparison of COMPACT and NICE detection efficiencies

Due to the mismatching x-axis, the efficiencies of the two detectors can no longer be compared using the fitted integrals as it was done for Ne^+ in equation (A.16). Instead, the detection efficiency for C_2F^+ fragments was estimated from the maxima in the normalized count rates R_{COMPACT} and R_{NICE} (compare figure A.9b) as derived in the COMPACT position scan and the NICE convolution, respectively,

$$\eta_{\text{i,COMPACT,C}_2\text{F}} = \eta_{\text{i,NICE}} \frac{\max(R_{\text{COMPACT}})}{\max(R_{\text{NICE}})}. \tag{A.18}$$

With the intrinsic single-particle detection efficiency of NICE of $\eta_{\text{i,NICE}} = 0.593(15)$ [36], the different effective widths $w_{\text{eff}} = 13.4\,\text{mm}$, 15.5 mm and 19.7 mm yield intrinsic efficiencies of $\eta_{\text{i,COMPACT,C}_2\text{F}} = 0.61$, 0.58 and 0.55. Taking into account the spread of the derived efficiencies for different widths, the systematic uncertainties due to mismatching x-axes (between w_{eff} and the NICE projection), and additional uncertainties in the procedure, a ∼15 % uncertainty on the COMPACT detection efficiency for C_2F fragments was estimated. The intrinsic detection efficiency for C_2F fragments thus is assumed as

$$\eta_{\text{i,COMPACT,C}_2\text{F}} = 0.58 \pm 0.09. \tag{A.19}$$

A.2.2.2 Linking detection efficiencies for neutral fragments and Xe^{2+}

Above, the detection efficiency of COMPACT for fragments from dissociative recombination of C_2F^+ was derived. As Xe^{2+} is much heavier and has a higher energy (900 keV) than the C_2F fragments (300 keV), the intrinsic detection efficiency for the

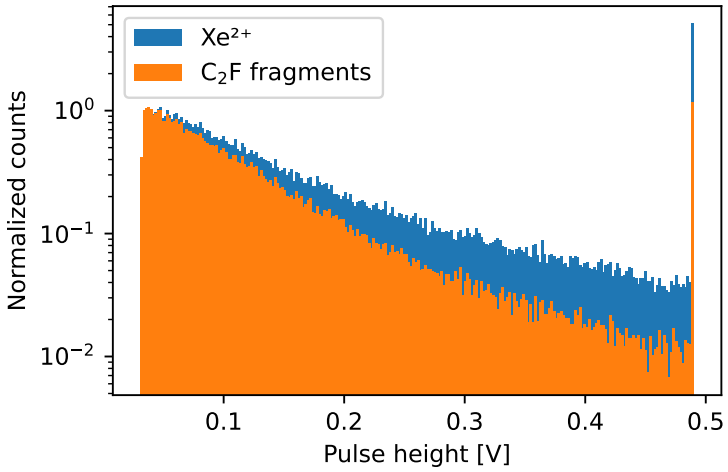

Figure A.10: Pulse Height Distributions (PHDs) for Xe^{2+} and C_2F fragments, respectively, impacting on COMPACT, recorded with the digitizer. Both distributions are scaled to 1 at low pulse heights.

different particles are not the same. To derive the intrinsic detection efficiency $\eta_{\mathrm{i,Xe^{2+}}}$ for Xe^{2+} from $\eta_{\mathrm{i,COMPACT,C_2F}}$, PHDs were recorded for impacting C_2F fragments and Xe^{2+} with COMPACT at the respective positions. Therefore, the electronic signal from COMPACT was no longer fed to the discriminator that was used for the regular measurements, but instead to a digitizer. The digitizer could analyze the electronic waveforms, and the pulse amplitudes were recorded, which enter the PHD. (In contrast, the discriminator could only count the electronic pulses.) From the PHDs, the fraction of events above the trigger threshold of the discriminator was estimated, as explained in the following. The relation of the two efficiencies for C_2F fragments and Xe^{2+} is determined by the fraction I of events above the trigger threshold of the discriminator and by the probability $(1 - P_0)$ that at least one secondary electron creates an avalanche in the MCP upon a particle hit on the converter (or side) plate. The intrinsic detection efficiency $\eta_{\mathrm{i,Xe^{2+}}}$ of COMPACT for Xe^{2+} can then be calculated by

$$\eta_{\mathrm{i,Xe^{2+}}} = \eta_{\mathrm{i,COMPACT,C_2F}} \cdot \frac{I_{\mathrm{Xe^{2+}}}}{I_{\mathrm{C_2F}}} \cdot \frac{(1 - P_{0,\mathrm{Xe^{2+}}})}{(1 - P_{0,\mathrm{C_2F}})}. \tag{A.20}$$

To obtain I and $(1 - P_0)$ for Xe^{2+} and C_2F fragments, the PHDs of the electronic signals at the MCP were recorded using the digitizer. The distributions are shown in figure A.10. For Xe^{2+}, the pulse heights are slightly shifted towards larger amplitudes, reflecting an larger number of secondary electrons released.

Modeling of the PHDs using equation (A.15), which relies on a Pólya distribution for secondary electrons reaching the MCP, allows to derive the probability $(1 - P_0)$ to produce at least one avalanche within the MCP after a particle hit on the converter electrode. During the beamtime campaign, the PHD f_1 for a single electron

hitting the MCP was not recorded. In [119], f_1 is described as 'monotonously decreasing exponential distribution', and in [118] as the sum of an exponential decay and a Gaussian. Here, as f_1 was not determined experimentally, it was assumed as exponential or double-exponential decay, respectively, in independent approaches. For these two distributions, the higher order f_k could be obtained analytically (in contrast to the sum of an exponential and a Gaussian, where f_k has to be obtained numerically). Taking the decay constants and amplitudes of the exponentials as fit parameters, as well as $\tilde{\gamma}$ and b for Xe^{2+} and C_2F fragments, equation (A.15) was fitted to the PHDs shown in figure A.10. Although the agreement between data and fit was reasonable, the fitting results involved large uncertainties due to the strong correlations of the fitting parameters. Constraining the parameters did not improve the results much. Therefore, the fits could not be used to reliably evaluate $(1 - P_0)$ and the fraction of events with pulse amplitudes below the trigger threshold. Instead, $(1 - P_0)$ was estimated from the findings in [119].

The Xe^{2+} product ions and C_2F fragments have energies corresponding to $\sim 7\,\mathrm{keV/u}$. This is a higher energy than for the particles presented in Table 1 in [119]. Here, it is assumed that $(1 - P_{0,C_2F}) = 0.85$, which is in line with the values reported in Table 1 in [119]. Since the PHDs in figure A.10 show overall stronger pulses for Xe^{3+} in comparison to the C_2F fragments, indicating more secondary electrons released, it can be assumed that the likelihood P_0 *not* to produce any avalanche in the MCP is lower for Xe^{2+}. Therefore, $(1 - P_{0,Xe^{2+}}) = 0.95$ is assumed here. The uncertainties on both values are estimated as $\sim 10\,\%$. The calculation of $\eta_{i,Xe^{2+}}$ from equation (A.20) is not sensitive on the actual values of $(1 - P_0)$, but rather on their ratio, which results as $(1 - P_{0,Xe^{2+}})/(1 - P_{0,C_2F}) = 1.12$ with an uncertainty of $\sim 14\,\%$.

To evaluate the fraction of events below the trigger threshold of the read-out electronics used in the regular measurements, which included the discriminator, the PHDs from figure A.10 (which were recorded with the digitizer) were approximated with a simple exponential,

$$F(h) = a\, e^{-bh} + c, \tag{A.21}$$

which agrees well with the measured data. However, the digitizer and the discriminator have different trigger thresholds. To estimate the discriminator threshold, the count rates R_{dig} and R_{disc} measured with the digitizer and discriminator, respectively, were compared with COMPACT in neutral position, detecting fragments from C_2F. From the exponential fit to the pulse height spectrum (according to equation (A.21)), the discriminator threshold h_{disc} could be inferred by numerically solving the relation

$$\frac{R_{\mathrm{disc}}}{R_{\mathrm{dig}}} = \frac{\int_{h_{\mathrm{disc}}}^{h_{\max}} F(h)\,\mathrm{d}h}{\int_{h_{\mathrm{dig}}}^{h_{\max}} F(h)\,\mathrm{d}h} = \frac{\int_{h_{\mathrm{disc}}}^{h_{\max}} (a\, e^{-bh} + c)\,\mathrm{d}h}{\int_{h_{\mathrm{dig}}}^{h_{\max}} (a\, e^{-bh} + c)\,\mathrm{d}h} \tag{A.22}$$

for h_{disc}. $h_{\max}$ was derived from the counts in the last overflow bin in the PHD. A discriminator threshold of $h_{\mathrm{disc}} = 39\,\mathrm{mV}$ was found, which is higher than the digitizer threshold of $h_{\mathrm{dig}} = 32\,\mathrm{mV}$.

With the deduced discriminator threshold, the fraction I of electronic pulses above the threshold could be calculated from the integrals over the PHD $F(h)$,

$$I_i = \frac{\int_{h_{\mathrm{disc}}}^{h_{\max}} F_i(h)\,\mathrm{d}h}{\int_0^{h_{\max}} F_i(h)\,\mathrm{d}h}, \tag{A.23}$$

where i represents either Xe^{2+} or C_2F fragments. This method relies on the extrapolation of the measured data towards lower pulse amplitudes, and therefore is prone to uncertainties due to the applied model. From the purely exponential fit, the fractions of events above the discriminator threshold are derived as $I_{C_2F} = 0.6$ for C_2F fragments and $I_{Xe^{2+}} = 0.7$ for Xe^{2+}. A relative uncertainty of 10 % generously reflects the possibility for a completely flat behavior below the threshold as well as for a much steeper increase. The calculation of $\eta_{\mathrm{i,Xe^{2+}}}$ from equation (A.20) is not sensitive to the actual values of I, but rather to their ratio, which is evaluated as $I_{Xe^{2+}}/I_{C_2F} = 1.17$ with an uncertainty of $\sim 14\,\%$.

The intrinsic detection efficiency of COMPACT for Xe^{2+} can then be calculated from equation (A.20) as

$$\eta_{\mathrm{i,Xe^{2+}}} = 0.76. \tag{A.24}$$

From error propagation, the total uncertainty is estimated as

$$\begin{aligned}\frac{\Delta\eta_{\mathrm{i,Xe^{2+}}}}{\eta_{\mathrm{i,Xe^{2+}}}} &= \sqrt{\left(\frac{\Delta\eta_{\mathrm{i,COMPACT,C_2F}}}{\eta_{\mathrm{i,COMPACT,C_2F}}}\right)^2 + \left(\frac{\Delta\left(\frac{1-P_{0,\mathrm{Xe^{2+}}}}{1-P_{0,\mathrm{C_2F}}}\right)}{\left(\frac{1-P_{0,\mathrm{Xe^{2+}}}}{1-P_{0,\mathrm{C_2F}}}\right)}\right)^2 + \left(\frac{\Delta(I_{\mathrm{Xe^{2+}}}/I_{\mathrm{C_2F}})}{(I_{\mathrm{Xe^{2+}}}/I_{\mathrm{C_2F}})}\right)^2} \\ &= 25\,\%,\end{aligned} \tag{A.25}$$

and thus

$$\Delta\eta_{\mathrm{i,Xe^{2+}}} = 0.25 \cdot 0.76 = 0.19. \tag{A.26}$$

In future experiments, the procedure to obtain the intrinsic detection efficiency could be improved if the PHD for *one* released secondary electron f_1 would be recorded by illuminating COMPACT with UV photons.

A.3 Total detection efficiencies

The total detection efficiency η of the COMPACT detector is the product of the geometric and intrinsic efficiencies as given in equation (A.1), i.e.

$$\eta = \eta_{\mathrm{g}} \cdot \eta_{\mathrm{i}}, \tag{A.27}$$

with the uncertainty

$$\Delta\eta = \sqrt{\left(\eta_\mathrm{i} \cdot \Delta\eta_\mathrm{g}\right)^2 + \left(\eta_\mathrm{g} \cdot \Delta\eta_\mathrm{i}\right)^2}. \tag{A.28}$$

With the values obtained in the previous sections A.1 and A.2, the total detection efficiencies of COMPACT for Ne^+ and Xe^{2+} ions under the conditions present in the experiments presented in this thesis can be obtained.

For the detection of Ne^+, $\eta_{\mathrm{g,Ne^+}} = 0.99 \pm 0.01$ and $\eta_{\mathrm{i,Ne^+}} = 0.75 \pm 0.25$, resulting in

$$\eta_{\mathrm{Ne^+}} = 0.74 \pm 0.25. \tag{A.29}$$

For the detection of Xe^{2+}, $\eta_{\mathrm{g,Xe^{2+}}} = 0.99 \pm 0.01$ and $\eta_{\mathrm{i,Xe^{2+}}} = 0.76 \pm 0.19$, and consequently

$$\eta_{\mathrm{Xe^{2+}}} = 0.75 \pm 0.19 \tag{A.30}$$

is concluded.

The uncertainties in the detection efficiencies were the main sources of uncertainty in the derivation of absolute MBRC presented in section 4.9 on page 55. In future experiments, the uncertainty of η can potentially be reduced by recording the PHD for *one* released secondary electron f_1 when illuminating COMPACT with UV photons. This could lead to a better interpretation of the recorded PHDs and improve the derivation of the intrinsic detection efficiency.

Bibliography

[1] A. Müller. 'Electron–ion collisions: Fundamental processes in the focus of applied research.' In: *Advances in Atomic, Molecular, and Optical Physics* 55 (2008), pp. 293–417 (cit. on p. 1).

[2] D. W. Savin. 'Can heavy ion storage rings contribute to our understanding of the charge state distributions in cosmic atomic plasmas?' In: *Journal of Physics: Conference Series*. Vol. 88. 1. IOP Publishing. 2007, p. 012071 (cit. on pp. 1, 2).

[3] H. A. Kramers. 'On the theory of X-ray absorption and of the continuous X-ray spectrum.' In: *The London, Edinburgh, and Dublin Philosophical Magazine and Journal of Science* 46 (275) (1923), pp. 836–871 (cit. on pp. 1, 5, 6).

[4] H. Massey and D. Bates. 'The properties of neutral and ionized atomic oxygen and their influence on the upper atmosphere.' In: *Reports on Progress in Physics* 9 (1) (1942), p. 62 (cit. on pp. 1, 7).

[5] A. Burgess. 'Delectronic Recombination and the Temperature of the Solar Corona.' In: *Astrophysical Journal, vol. 139, p. 776-780* 139 (1964), pp. 776–780 (cit. on p. 1).

[6] J. Mitchell, C. Ng, J. Forand, D. Levac, R. Mitchell, A. Sen, D. Miko, and J. W. McGowan. 'Dielectronic-recombination cross-section measurements for C^+ ions.' In: *Physical Review Letters* 50 (5) (1983), p. 335 (cit. on pp. 1, 8).

[7] P. Dittner, S. Datz, P. Miller, C. Moak, P. H. Stelson, C. Bottcher, W. Dress, G. Alton, N. Nešković, and C. Fou. 'Cross Sections for Dielectronic Recombination of B^{2+} and C^{3+} via 2s→2p Excitation.' In: *Physical Review Letters* 51 (1) (1983), p. 31 (cit. on pp. 1, 8).

[8] D. Belic, G. H. Dunn, T. Morgan, D. Mueller, and C. Timmer. 'Dielectronic recombination: A crossed-beams observation and measurement of cross section.' In: *Physical Review Letters* 50 (5) (1983), p. 339 (cit. on pp. 1, 8, 11).

[9] S. Schippers. 'Astrophysical relevance of storage-ring electron-ion recombination experiments.' In: *Journal of Physics: Conference Series*. Vol. 163. 1. IOP Publishing. 2009, p. 012001 (cit. on pp. 2, 11).

[10] C. Brandau, C. Kozhuharov, M. Lestinsky, A. Müller, S. Schippers, and T. Stöhlker. 'Storage-ring experiments on dielectronic recombination at the interface of atomic and nuclear physics.' In: *Physica Scripta* 2015 (T166) (2015), p. 014022 (cit. on p. 2).

[11] S. Schippers, E. Schmidt, D. Bernhardt, D. Yu, A. Müller, M. Lestinsky, D. Orlov, M. Grieser, R. Repnow, and A. Wolf. 'Storage-Ring Measurement of the Hyperfine Induced $^{47}Ti^{18+}$ ($2s2p\,^3P_0 \rightarrow 2s^2\,^1S_0$) Transition Rate.' In: *Physical Review Letters* 98 (3) (2007), p. 033001 (cit. on p. 2).

[12] C. Brandau and C. Kozhuharov. 'Storage-ring studies of dielectronic recombination as a tool for precision spectroscopy.' In: *Atomic Processes in Basic and Applied Physics* (2012), pp. 283–306 (cit. on p. 2).

[13] E. Lindroth, H. Danared, P. Glans, Z. Pešić, M. Tokman, G. Vikor, and R. Schuch. 'QED effects in Cu-like Pb recombination resonances near threshold.' In: *Physical Review Letters* 86 (22) (2001), p. 5027 (cit. on p. 2).

[14] C. Brandau, C. Kozhuharov, A. Müller, W. Shi, S. Schippers, T. Bartsch, S. Böhm, C. Böhme, A. Hoffknecht, H. Knopp, N. Grün, W. Scheid, T. Steih, F. Bosch, B. Franzke, P. Mokler, F. Nolden, M. Steck, T. Stöhlker, and Z. Stachura. 'Precise Determination of the $2s_{1/2} - 2p_{1/2}$ Splitting in Very Heavy Lithiumlike Ions Utilizing Dielectronic Recombination.' In: *Physical Review Letters* 91 (7) (2003), p. 073202 (cit. on p. 2).

[15] M. Lestinsky, E. Lindroth, D. Orlov, E. Schmidt, S. Schippers, S. Böhm, C. Brandau, F. Sprenger, A. Terekhov, A. Müller, and A. Wolf. 'Screened Radiative Corrections from Hyperfine-Split Dielectronic Resonances in Lithiumlike Scandium.' In: *Physical Review Letters* 100 (3) (2008), p. 033001 (cit. on p. 2).

[16] C. Krantz, N. R. Badnell, A. Müller, S. Schippers, and A. Wolf. 'Recombination of open-f-shell tungsten ions.' In: *Journal of Physics B: Atomic, Molecular and Optical Physics* 50 (5) (2017), p. 052001 (cit. on pp. 2, 8).

[17] A. Müller and S. Schippers. 'Unravelling the Mysteries of Matter Surrounding Supermassive Black Holes.' In: *Atomic Processes in Basic and Applied Physics* (2012), pp. 25–35 (cit. on p. 2).

[18] S. Schippers, M. Lestinsky, A. Müller, D. W. Savin, E. Schmidt, and A. Wolf. 'Dielectronic recombination data for astrophysical applications: Plasma rate-coefficients for Fe^{q+} (q= 7-10, 13-22) and Ni^{25+} ions from storage-ring experiments.' In: *International Review of Atomic and Molecular Physics* 1 (2) (2010), p. 109 (cit. on p. 2).

[19] O. Novotný, N. Badnell, D. Bernhardt, M. Grieser, M. Hahn, C. Krantz, M. Lestinsky, A. Müller, R. Repnow, S. Schippers, A. Wolf, and D. W. Savin. 'Electron–Ion Recombination of Fe XII Forming Fe XI: Laboratory Measurements and Theoretical Calculations.' In: *The Astrophysical Journal* 753 (1) (2012), p. 57 (cit. on p. 2).

[20] M. Hahn, N. Badnell, M. Grieser, C. Krantz, M. Lestinsky, A. Müller, O. Novotný, R. Repnow, S. Schippers, A. Wolf, and D. W. Savin. 'Electron–Ion Recombination of Fe^{12+} Forming Fe^{11+}: Laboratory Measurements and Theoretical Calculations.' In: *The Astrophysical Journal* 788 (1) (2014), p. 46 (cit. on p. 2).

[21] S. Schippers, T. Bartsch, C. Brandau, A. Müller, J. Linkemann, A. Saghiri, and A. Wolf. 'Experimental search for interference effects in the total $e^- + Sc^{3+}$ recombination rate.' In: *Physical Review A* 59 (4) (1999), p. 3092 (cit. on pp. 2, 11, 13, 112).

[22] S. Schippers, S. Kieslich, A. Müller, G. Gwinner, M. Schnell, A. Wolf, A. Covington, M. E. Bannister, and L.-B. Zhao. 'Interference effects in the photorecombination of argonlike Sc^{3+} ions: Storage-ring experiment and theory.' In: *Physical Review A* 65 (4) (2002), p. 042723 (cit. on pp. 2, 11, 13, 112).

[23] D. W. Savin, N. Brickhouse, J. Cowan, R. Drake, S. Federman, G. Ferland, A. Frank, M. Gudipati, W. Haxton, E. Herbst, S. Profumo, F. Salama, L. Ziurys, and E. Zweibel. 'The impact of recent advances in laboratory astrophysics on our understanding of the cosmos.' In: *Reports on Progress in Physics* 75 (3) (2012), p. 036901 (cit. on p. 2).

[24] B. D. Metzger. 'Kilonovae.' In: *Living Reviews in Relativity* 23 (1) (2020), p. 1 (cit. on p. 2).

[25] LIGO Scientific Collaboration and Virgo Collaboration et al. 'Multi-messenger observations of a binary neutron star merger.' In: *The Astrophysical Journal Letters* 848 (2) (2017), p. L12 (cit. on p. 3).

[26] D. Kasen, B. Metzger, J. Barnes, E. Quataert, and E. Ramirez-Ruiz. 'Origin of the heavy elements in binary neutron-star mergers from a gravitational-wave event.' In: *Nature* 551 (7678) (2017), pp. 80–84 (cit. on p. 3).

[27] M. Tanaka and K. Hotokezaka. 'Radiative transfer simulations of neutron star merger ejecta.' In: *The Astrophysical Journal* 775 (2) (2013), p. 113 (cit. on p. 3).

[28] D. Watson, C. J. Hansen, J. Selsing, A. Koch, D. B. Malesani, A. C. Andersen, J. P. Fynbo, A. Arcones, A. Bauswein, S. Covino, A. Grado, K. E. Heintz, L. Hunt, C. Kouveliotou, G. Leloudas, A. J. Levan, P. Mazzali, and E. Pian. 'Identification of strontium in the merger of two neutron stars.' In: *Nature* 574 (7779) (2019), pp. 497–500 (cit. on p. 3).

[29] A. Sneppen and D. Watson. 'Discovery of a 760nm P Cygni line in AT2017gfo: Identification of yttrium in the kilonova photosphere.' In: *Astronomy & Astrophysics* 675 (2023), A194 (cit. on p. 3).

[30] K. Hotokezaka, M. Tanaka, D. Kato, and G. Gaigalas. 'Tellurium emission line in kilonova AT 2017gfo.' In: *Monthly Notices of the Royal Astronomical Society: Letters* 526 (1) (2023), pp. L155–L159 (cit. on p. 3).

[31] A. J. Levan, B. P. Gompertz, O. S. Salafia, M. Bulla, E. Burns, K. Hotokezaka, L. Izzo, G. P. Lamb, D. B. Malesani, S. R. Oates, et al. 'Heavy-element production in a compact object merger observed by JWST.' In: *Nature* 626 (8000) (2024), pp. 737–741 (cit. on p. 3).

[32] N. Domoto, M. Tanaka, D. Kato, K. Kawaguchi, K. Hotokezaka, and S. Wanajo. 'Lanthanide features in near-infrared spectra of kilonovae.' In: *The Astrophysical Journal* 939 (1) (2022), p. 8 (cit. on p. 3).

[33] R. von Hahn, A. Becker, F. Berg, K. Blaum, C. Breitenfeldt, H. Fadil, F. Fellenberger, M. Froese, S. George, J. Göck, M. Grieser, F. Grussie, E. A. Guerin, O. Heber, P. Herwig, J. Karthein, C. Krantz, H. Kreckel, M. Lange, F. Laux, S. Lohmann, S. Menk, C. Meyer, P. M. Mishra, O. Novotný, A. P. O'Connor, D. A. Orlov, M. L. Rappaport, R. Repnow, S. Saurabh, S. Schippers, C. D. Schröter, D. Schwalm, L. Schweikhard, T. Sieber, A. Shornikov, K. Spruck, S. Sunil Kumar, J. Ullrich, X. Urbain, S. Vogel, P. Wilhelm, A. Wolf, and D. Zajfman. 'The cryogenic storage ring CSR.' In: *Review of Scientific Instruments* 87 (6) (2016), p. 063115. DOI: 10.1063/1.4953888 (cit. on pp. 3, 13, 16, 18, 19).

[34] H. Kreckel, O. Novotný, and A. Wolf. 'Astrochemical studies at the cryogenic storage ring.' In: *Philosophical Transactions of the Royal Society A* 377 (2154) (2019), p. 20180412 (cit. on p. 3).

[35] O. Novotný, P. Wilhelm, D. Paul, Á. Kálosi, S. Saurabh, A. Becker, K. Blaum, S. George, J. Göck, M. Grieser, F. Grussie, R. von Hahn, C. Krantz, H. Kreckel, C. Meyer, P. M. Mishra, D. Muell, F. Nuesslein, D. A. Orlov, M. Rimmler, V. C. Schmidt, A. Shornikov, A. S. Terekhov, S. Vogel, D. Zajfman, and A. Wolf. 'Quantum-state–selective electron recombination studies suggest enhanced abundance of primordial HeH^+.' In: *Science* 365 (6454) (2019), pp. 676–679. DOI: 10.1126/science.aax5921 (cit. on pp. 3, 22, 25).

[36] D. Paul, M. Grieser, F. Grussie, R. von Hahn, L. W. Isberner, Á. Kálosi, C. Krantz, H. Kreckel, D. Müll, D. A. Neufeld, D. W. Savin, S. Schippers, P. Wilhelm, A. Wolf, M. G. Wolfire, and O. Novotný. 'Experimental determination of the dissociative recombination rate coefficient for rotationally cold CH^+ and its implications for diffuse cloud chemistry.' In: *The Astrophysical Journal* 939 (2) (2022), p. 122 (cit. on pp. 3, 22, 25, 26, 58, 135, 138).

[37] N. Jain, Á. Kálosi, F. Nuesslein, D. Paul, P. Wilhelm, S. G. Ard, M. Grieser, R. von Hahn, M. C. Heaven, E. Miliordos, D. Maffucci, N. S. Shuman, A. A. Viggiano, A. Wolf, and O. Novotný. 'Near-thermo-neutral electron recombination of titanium oxide ions.' In: *The Journal of Chemical Physics* 158 (14) (2023) (cit. on pp. 3, 25).

[38] Á. Kálosi, L. Gamer, M. Grieser, R. von Hahn, L. W. Isberner, J. I. Jäger, H. Kreckel, D. A. Neufeld, D. Paul, D. W. Savin, S. Schippers, V. C. Schmidt, A. Wolf, M. G. Wolfire, and O. Novotný. 'Dissociative recombination of rotationally cold OH^+ and its implications for the cosmic ray ionization rate in diffuse clouds.' In: *The Astrophysical Journal Letters* 955 (2) (2023), p. L26 (cit. on pp. 3, 22, 25).

[39] Á. Kálosi, M. Grieser, L. W. Isberner, H. Kreckel, Å. Larson, D. A. Neufeld, A. E. Orel, D. Paul, D. W. Savin, S. Schippers, V. C. Schmidt, A. Wolf, M. G. Wolfire, and O. Novotný. 'Dissociative recombination of rotationally cold ArH^+.' In: *Physical Review A* 110 (2) (2024), p. 022816 (cit. on pp. 3, 11, 22, 25).

[40] A. Znotins. 'Electron recombination of rotationally cold deuterated triatomic hydrogen ions at the Cryogenic Storage Ring.' PhD thesis. Ruprecht-Karls-Universität Heidelberg, 2024 (cit. on pp. 3, 25).

[41] E. B. Menz. 'Preparation and Realisation of first Dielectronic Recombination Experiments at CRYRING@ESR.' PhD thesis. Friedrich-Schiller-Universität Jena, 2024 (cit. on pp. 3, 10, 71, 73, 75, 80–83, 92, 115).

[42] H. Spoon and J. Holt. 'Discovery of strongly blueshifted mid-infrared [Ne III] and [Ne V] emission in ULIRGs.' In: *The Astrophysical Journal* 702 (1) (2009), p. L42 (cit. on p. 3).

[43] J. P. Simpson, S. W. Colgan, R. H. Rubin, E. F. Erickson, and M. R. Haas. 'Far-infrared lines from H II regions: Abundance variations in the galaxy.' In: *Astrophysical Journal, Part 1 (ISSN 0004-637X), vol. 444, no. 2, p. 721-738* 444 (1995), pp. 721–738 (cit. on p. 3).

[44] D. Péquignot and J.-P. Baluteau. 'The identification of krypton, xenon, and other elements of rows 4, 5 and 6 of the periodic table in the planetary nebula NGC 7027.' In: *Astronomy and Astrophysics (ISSN 0004-6361), vol. 283, no. 2, p. 593-625* 283 (1994), pp. 593–625 (cit. on p. 4).

[45] K. Werner, T. Rauch, E. Ringat, and J. W. Kruk. 'First detection of krypton and xenon in a white dwarf.' In: *The Astrophysical Journal Letters* 753 (1) (2012), p. L7 (cit. on p. 4).

[46] T. Koizumi, Y. Awaya, A. Fujino, Y. Itoh, M. Kitajima, T. Kojima, M. Oura, R. Okuma, M. Sano, T. Seikioka, N. Watanabe, and F. Koike. '4d Photoionization of multiply charged Xe^{q+} (q= 1-3) ions.' In: *Physica Scripta* 1997 (T73) (1997), p. 131 (cit. on pp. 4, 95).

[47] N. Watanabe, Y. Awaya, A. Fujino, Y. Itoh, M. Kitajima, T. M. Kojima, M. Oura, R. Okuma, M. Sano, T. Sekioka, and T. Koizumi. 'Photoion-yield spectra of Xe^{2+} in the 4d-threshold energy region.' In: *Journal of Physics B: Atomic, Molecular and Optical Physics* 31 (18) (1998), p. 4137 (cit. on pp. 4, 95).

[48] M. Stobbe. 'Zur Quantenmechanik Photoelektrischer Prozesse.' In: *Annalen der Physik* 399 (6) (1930), pp. 661–715 (cit. on p. 5).

[49] A. Ichihara and J. Eichler. 'Cross sections for radiative recombination and the photoelectric effect in the K, L, and M shells of one-electron systems with $1 \leq Z \leq 112$ calculated within an exact relativistic description.' In: *Atomic Data and Nuclear Data Tables* 74 (1) (2000), pp. 1–121 (cit. on p. 5).

[50] V. Shabaev, V. Yerokhin, T. Beier, and J. Eichler. 'QED corrections to the radiative recombination of an electron with a bare nucleus.' In: *Physical Review A* 61 (5) (2000), p. 052112 (cit. on p. 5).

[51] A. Wolf. 'Wechselwirkung zwischen hochgeladenen Ionen und freien Elektronen in einem Ionenspeicherring: dynamische Reibung und Rekombination.' Habilitation Thesis. Ruprecht-Karls-Universität Heidelberg, 1992 (cit. on p. 6).

[52] L. H. Andersen and J. Bolko. 'Radiative recombination between fully stripped ions and free electrons.' In: *Physical Review A* 42 (3) (1990), p. 1184 (cit. on pp. 6, 7).

[53] L. H. Andersen, J. Bolko, and P. Kvistgaard. 'Radiative recombination between free electrons and bare carbon ions.' In: *Physical Review Letters* 64 (7) (1990), p. 729 (cit. on p. 7).

[54] A. Wolf, J. Berger, M. Bock, D. Habs, B. Hochadel, G. Kilgus, G. Neureither, U. Schramm, D. Schwalm, E. Szmola, A. Müller, M. Wagner, and R. Schuch. 'Experiments with highly-charged ions in the storage ring TSR.' In: *Zeitschrift für Physik D - Atoms, Molecules and Clusters* 21 (1991), S69–S75 (cit. on p. 7).

[55] H. Gao, D. DeWitt, R. Schuch, W. Zong, S. Asp, and M. Pajek. 'Observation of enhanced electron-ion recombination rates at very low energies.' In: *Physical Review Letters* 75 (24) (1995), p. 4381 (cit. on p. 7).

[56] A. Hoffknecht, C. Brandau, T. Bartsch, C. Böhme, H. Knopp, S. Schippers, A. Müller, C. Kozhuharov, K. Beckert, F. Bosch, B. Franzke, A. Krämer, P. Mokler, F. Nolden, M. Steck, T. Stöhlker, and Z. Stachura. 'Recombination of bare Bi^{83+} ions with electrons.' In: *Physical Review A* 63 (1) (2000), p. 012702 (cit. on pp. 7, 10, 91, 111).

[57] G. Gwinner, A. Hoffknecht, T. Bartsch, M. Beutelspacher, N. Eklöw, P. Glans, M. Grieser, S. Krohn, E. Lindroth, A. Müller, A. A. Saghiri, S. Schippers, U. Schramm, D. Schwalm, M. Tokman, G. Wissler, and A. Wolf. 'Influence of magnetic fields on electron-ion recombination at very low energies.' In: *Physical Review Letters* 84 (21) (2000), p. 4822 (cit. on pp. 7, 10, 91, 111).

[58] M. Hörndl, S. Yoshida, A. Wolf, G. Gwinner, and J. Burgdörfer. 'Enhancement of Low Energy Electron-Ion Recombination in a Magnetic Field: Influence of Transient Field Effects.' In: *Physical Review Letters* 95 (24) (2005), p. 243201 (cit. on pp. 7, 91, 111).

[59] M. Hörndl, S. Yoshida, A. Wolf, G. Gwinner, M. Seliger, and J. Burgdörfer. 'Classical dynamics of enhanced low-energy electron-ion recombination in storage rings.' In: *Physical Review A—Atomic, Molecular, and Optical Physics* 74 (5) (2006), p. 052712 (cit. on pp. 7, 91, 111).

[60] B. W. Shore. 'Dielectronic recombination.' In: *Astrophysical Journal, vol. 158, p. 1205* 158 (1969), p. 1205 (cit. on p. 7).

[61] S. Schippers. 'Experimente zur Photorekombination atomarer Ionen an Schwerionenspeicherringen.' Habilitation Thesis. Justus-Liebig-Universität Gießen, 2002 (cit. on pp. 7, 11).

[62] M. A. Levine, R. Marrs, J. Henderson, D. Knapp, and M. B. Schneider. 'The electron beam ion trap: A new instrument for atomic physics measurements.' In: *Physica Scripta* 1988 (T22) (1988), p. 157 (cit. on p. 8).

[63] W. Biela-Nowaczyk, F. Grilo, P. Amaro, and A. Warczak. 'L-Mn dielectronic recombination of cerium ions in a room-temperature EBIT.' In: *Journal of Physics B: Atomic, Molecular and Optical Physics* 57 (5) (2024), p. 055201 (cit. on p. 8).

[64] M. Schnell, G. Gwinner, N. Badnell, M. Bannister, S. Böhm, J. Colgan, S. Kieslich, S. Loch, D. Mitnik, A. Müller, M. Pindzola, S. Schippers, D. Schwalm, W. Shi, A. Wolf, and S. Zhou. 'Observation of trielectronic recombination in Be-like Cl ions.' In: *Physical Review Letters* 91 (4) (2003), p. 043001 (cit. on p. 8).

[65] C. Beilmann, P. Mokler, S. Bernitt, C. H. Keitel, J. Ullrich, J. C. López-Urrutia, and Z. Harman. 'Prominent higher-order contributions to electronic recombination.' In: *Physical Review Letters* 107 (14) (2011), p. 143201 (cit. on p. 8).

[66] G. Gribakin and S. Sahoo. 'Mixing of dielectronic and multiply excited states in electron–ion recombination: A study of Au^{24+}.' In: *Journal of Physics B: Atomic, Molecular and Optical Physics* 36 (15) (2003), p. 3349 (cit. on p. 8).

[67] V. Flambaum, A. Gribakina, G. Gribakin, and C. Harabati. 'Electron recombination with multicharged ions via chaotic many-electron states.' In: *Physical Review A* 66 (1) (2002), p. 012713 (cit. on p. 8).

[68] S. Schippers, D. Bernhardt, A. Müller, C. Krantz, M. Grieser, R. Repnow, A. Wolf, M. Lestinsky, M. Hahn, O. Novotný, and D. Savin. 'Dielectronic recombination of xenonlike tungsten ions.' In: *Physical Review A — Atomic, Molecular, and Optical Physics* 83 (1) (2011), p. 012711 (cit. on p. 8).

[69] N. Badnell, C. Ballance, D. Griffin, and M. O'Mullane. 'Dielectronic recombination of W^{20+} ($4d^{10}4f^8$): Addressing the half-open f shell.' In: *Physical Review A—Atomic, Molecular, and Optical Physics* 85 (5) (2012), p. 052716 (cit. on p. 8).

[70] K. Spruck, N. Badnell, C. Krantz, O. Novotný, A. Becker, D. Bernhardt, M. Grieser, M. Hahn, R. Repnow, D. W. Savin, A. Wolf, A. Müller, and S. Schippers. 'Recombination of W^{18+} ions with electrons: Absolute rate coefficients from a storage-ring experiment and from theoretical calculations.' In: *Physical Review A* 90 (3) (2014), p. 032715 (cit. on pp. 8, 10).

[71] K. Spruck. 'Dielectronic recombination experiments with tungsten ions at the Test Storage Ring and development of a single-particle detector at the Cryogenic Storage Ring.' PhD thesis. Justus-Liebig-Universität Gießen, 2015. DOI: 10.22029/jlupub-9693 (cit. on pp. 8, 22–24, 47, 68, 119, 130, 131).

[72] N. Badnell, K. Spruck, C. Krantz, O. Novotný, A. Becker, D. Bernhardt, M. Grieser, M. Hahn, R. Repnow, D. W. Savin, A. Wolf, A. Müller, and S. Schippers. 'Recombination of W^{19+} ions with electrons: absolute rate coefficients from a storage-ring experiment and from theoretical calculations.' In: *Physical Review A* 93 (5) (2016), p. 052703 (cit. on p. 8).

[73] D. Schwalm. 'Atomic and molecular astrophysics with heavy ion storage rings.' In: *Progress in Particle and Nuclear Physics* 59 (1) (2007), pp. 156–164 (cit. on p. 8).

[74] F. Hinterberger. *Physik der Teilchenbeschleuniger und Ionenoptik*. Vol. 2. Springer, 2008 (cit. on pp. 8, 9).

[75] R. Phaneuf, C. Havener, G. Dunn, and A. Müller. 'Merged-beams experiments in atomic and molecular physics.' In: *Reports on Progress in Physics* 62 (7) (1999), p. 1143 (cit. on p. 10).

[76] D. Bernhardt, C. Brandau, Z. Harman, C. Kozhuharov, A. Müller, W. Scheid, S. Schippers, E. Schmidt, D. Yu, A. Artemyev, I. Tupitsyn, S. Böhm, F. Bosch, F. Currell, B. Franzke, A. Gumberidze, J. Jacobi, P. Mokler, F. Nolden, U. Spillman, Z. Stachura, M. Steck, and T. Stöhlker. 'Breit interaction in dielectronic recombination of hydrogenlike uranium.' In: *Physical Review A—Atomic, Molecular, and Optical Physics* 83 (2) (2011), p. 020701 (cit. on p. 10).

[77] S. Schippers. 'Electron–ion merged-beam experiments at heavy-ion storage rings.' In: *Nuclear Instruments and Methods in Physics Research Section B: Beam Interactions with Materials and Atoms* 350 (2015), pp. 61–65 (cit. on p. 10).

[78] G. Kilgus, J. Berger, P. Blatt, M. Grieser, D. Habs, B. Hochadel, E. Jaeschke, D. Krämer, R. Neumann, G. Neureither, W. Ott, D. Schwalm, M. Steck, R. Stokstad, E. Szmola, and A. Wolf. 'Dielectronic recombination of hydrogenlike oxygen in a heavy-ion storage ring.' In: *Physical Review Letters* 64 (7) (1990), p. 737 (cit. on p. 10).

[79] S. Ali, I. Orban, S. Mahmood, Z. Altun, P. Glans, and R. Schuch. 'Electon–Ion Recombination Rate Coefficients for C II forming C I.' In: *The Astrophysical Journal* 753 (2) (2012), p. 132 (cit. on p. 10).

[80] I. Orban, P. Glans, Z. Altun, E. Lindroth, A. Källberg, and R. Schuch. 'Determination of the recombination rate coefficients for Na-like Si IV forming Mg-like Si III.' In: *Astronomy & Astrophysics* 459 (1) (2006), pp. 291–296 (cit. on p. 10).

[81] E. W. Schmidt, D. Bernhardt, A. Müller, S. Schippers, S. Fritzsche, J. Hoffmann, A. S. Jaroshevich, C. Krantz, M. Lestinsky, D. A. Orlov, A. Wolf, D. Lukic, and D. W. Savin. 'Electron-ion recombination of Si IV forming Si III: Storage-ring measurement and multiconfiguration Dirac-Fock calculations.' In: *Physical Review A—Atomic, Molecular, and Optical Physics* 76 (3) (2007), p. 032717 (cit. on p. 10).

[82] D. Bernhardt, C. Brandau, Z. Harman, C. Kozhuharov, S. Böhm, F. Bosch, S. Fritzsche, J. Jacobi, S. Kieslich, H. Knopp, F. Nolden, W. Shi, Z. Stachura, M. Steck, T. Stöhlker, S. Schippers, and A. Müller. 'Electron-ion collision spectroscopy: Lithium-like xenon ions.' In: *Physical Review A* 91 (1) (2015), p. 012710 (cit. on p. 10).

[83] W. Shi, S. Böhm, C. Böhme, C. Brandau, A. Hoffknecht, S. Kieslich, S. Schippers, A. Müller, C. Kozhuharov, F. Bosch, B. Franzke, P. Mokler, M. Steck, T. Stöhlker, and Z. Stachura. 'Recombination of U^{92+} ions with electrons.' In: *The European Physical Journal D-Atomic, Molecular, Optical and Plasma Physics* 15 (2001), pp. 145–154 (cit. on p. 10).

[84] M. Lestinsky, E. B. Menz, H. Danared, C. Krantz, E. Lindroth, Z. Andelkovic, C. Brandau, A. Bräuning-Demian, S. Fedotova, W. Geithner, F. Herfurth, A. Kalinin, I. Kraus, U. Spillmann, G. Vorobyev, and T. Stöhlker. 'First experiments with CRYRING@ ESR.' In: *Atoms* 10 (4) (2022), p. 141 (cit. on pp. 10, 14, 19).

[85] B. Zhu, A. Gumberidze, T. Over, G. Weber, Z. Andelkovic, A. Bräuning-Demian, R. Chen, D. Dmytriiev, O. Forstner, C. Hahn, F. Herfurth, M. Herdrich, P.-M. Hillenbrand, A. Kalinin, F. Kröger, M. Lestinsky, Y. Litvinov, E. Menz, W. Middents, T. Morgenroth, N. Petridis, P. Pfäfflein, M. Sanjari, R. Sidhu, U. Spillmann, R. Schuch, S. Schippers, S. Trotsenko, L. Varga, G. Vorobyev, and T. Stöhlker. 'X-ray emission associated with radiative recombination for Pb 82+ ions at threshold energies.' In: *Physical Review A* 105 (5) (2022), p. 052804 (cit. on p. 10).

[86] S.-X. Wang, Z.-K. Huang, W.-Q. Wen, C.-Y. Chen, S. Schippers, X. Xu, S. Sardar, N. Khan, H.-B. Wang, L.-J. Dou, S. Mahmood, D.-M. Zhao, X.-L. Zhu, L.-J. Mao, X.-M. Ma, J. Li, M.-T. Tang, R.-S. Mao, D.-Y. Yin, Y.-J. Yuan, J.-C. Yang, Y.-L. Shi, C.-Z. Dong, X.-W. Ma, and L.-F. Zhu. 'Dielectronic recombi-

nation rate coefficients of fluorine-like nickel.' In: *Astronomy & Astrophysics* 627 (2019), A171 (cit. on p. 10).

[87] Z. Huang, S. Wang, W. Wen, H. Wang, W. Ma, C. Chen, C. Zhang, D. Chen, H. Huang, L. Shao, X. Liu, X. Zhou, L. Mao, J. Li, X. Ma, M. Tang, J. Yang, Y. Yuan, S. Zhang, L. Zhu, and X. Ma. 'Absolute dielectronic recombination rate coefficients of highly charged ions at the storage ring CSRm and CSRe.' In: *Chinese Physics B* 32 (7) (2023), p. 073401 (cit. on p. 10).

[88] Z. Huang, N. Khan, S. Wang, W. Wen, H. Wang, W. Ma, L. Shao, H. Huang, X. Liu, D. Chen, X. Zhou, D. Zhao, H. Yang, L. Mao, X. Ma, J. Li, M. Tang, Y. Zhou, K. Yan, D. Yin, L. Yang, Y. Yuan, S. Zhang, L. Zhu, and X. Ma. 'Development of particle detectors for electron–ion collision spectroscopy with highly charged ions at the storage ring CSRe.' In: *Nuclear Instruments and Methods in Physics Research Section A: Accelerators, Spectrometers, Detectors and Associated Equipment* 1040 (2022), p. 167286 (cit. on p. 10).

[89] W.-L. Ma, S.-X. Wang, Z.-K. Huang, W.-Q. Wen, H.-B. Wang, D.-Y. Chen, X. Liu, X.-P. Zhou, H.-K. Huang, L. Shao, C. Liu, C.-Y. Zhang, C.-Y. Chen, L.-J. Mao, X.-M. Ma, J. Li, M.-T. Tang, K.-M. Yan, Y.-B. Zhou, D.-M. Zhao, Y.-J. Yuan, J.-C. Yang, X.-W. Ma, and L.-F. Zhu. 'Dielectronic recombination rate coefficients of carbon-like Kr^{30+}.' In: *Journal of Physics B: Atomic, Molecular and Optical Physics* 56 (9) (2023), p. 095203 (cit. on p. 10).

[90] S. Schippers. *Private communication.* 2024 (cit. on pp. 11, 69, 70, 79, 91, 104).

[91] A. Müller, D. Belić, B. DePaola, N. Djurić, G. Dunn, D. Mueller, and C. Timmer. 'Field effects on the Rydberg product-state distribution from dielectronic recombination.' In: *Physical review letters* 56 (2) (1986), p. 127 (cit. on p. 11).

[92] O. Novotný, H. Buhr, W. Geppert, M. Grieser, M. Hamberg, C. Krantz, M. Mendes, A. Petrignani, R. Repnow, D. W. Savin, D. Schwalm, J. Stützel, and A. Wolf. 'Dissociative Recombination Measurements of Chloronium Ions (D_2Cl^+) Using an Ion Storage Ring.' In: *The Astrophysical Journal* 862 (2) (2018), p. 166 (cit. on p. 11).

[93] V. Zhaunerchyk, R. Thomas, W. Geppert, M. Hamberg, M. Kamińska, E. Vigren, M. Larsson, A. Midey, and A. Viggiano. 'Dissociative recombination of $OPCl^+$ and $OPCl_2^+$: Pushing the upper mass limit at CRYRING.' In: *The Journal of Chemical Physics* 128 (13) (2008) (cit. on p. 11).

[94] A. Schlachter, J. Stearns, W. Graham, K. Berkner, R. Pyle, and J. Tanis. 'Electron capture for fast highly charged ions in gas targets: An empirical scaling rule.' In: *Physical Review A* 27 (6) (1983), p. 3372 (cit. on pp. 11, 12).

[95] M. Grieser, Y. A. Litvinov, R. Raabe, K. Blaum, Y. Blumenfeld, P. A. Butler, F. Wenander, P. Woods, M. Aliotta, A. Andreyev, et al. 'Storage ring at HIE-ISOLDE: Technical design report.' In: *The European Physical Journal Special Topics* 207 (2012), pp. 1–117 (cit. on pp. 14, 19).

[96] A. P. O'Connor, A. Becker, K. Blaum, C. Breitenfeldt, S. George, J. Göck, M. Grieser, F. Grussie, E. A. Guerin, R. von Hahn, U. Hechtfischer, P. Herwig, J. Karthein, C. Krantz, H. Kreckel, S. Lohmann, C. Meyer, P. M. Mishra, O. Novotný, R. Repnow, S. Saurabh, D. Schwalm, K. Spruck, S. Sunil Kumar, S. Vogel, and A. Wolf. 'Photodissociation of an Internally Cold Beam of CH^+ Ions in a Cryogenic Storage Ring.' In: *Physical Review Letters* 116 (11) (2016), p. 113002. DOI: 10.1103/PhysRevLett.116.113002 (cit. on pp. 15, 18, 19).

[97] C. Meyer, A. Becker, K. Blaum, C. Breitenfeldt, S. George, J. Göck, M. Grieser, F. Grussie, E. A. Guerin, R. von Hahn, P. Herwig, C. Krantz, H. Kreckel, J. Lion, S. Lohmann, P. M. Mishra, O. Novotný, A. P. O'Connor, R. Repnow, S. Saurabh, D. Schwalm, L. Schweikhard, K. Spruck, S. Sunil Kumar, S. Vogel, and A. Wolf. 'Radiative Rotational Lifetimes and State-Resolved Relative Detachment Cross Sections from Photodetachment Thermometry of Molecular Anions in a Cryogenic Storage Ring.' In: *Physical Review Letters* 119 (2) (2017), p. 023202. DOI: 10.1103/PhysRevLett.119.023202 (cit. on pp. 15, 18, 19).

[98] F. Grussie. 'Experimental studies of ion-neutral reactions under astrophysical conditions.' PhD thesis. Ruprecht-Karls-Universität Heidelberg, 2016. DOI: 10.11588/heidok.00021435 (cit. on p. 16).

[99] M. Grieser, V. C. Schmidt, K. Blaum, F. Grussie, R. von Hahn, Á. Kálosi, H. Kreckel, D. Müll, O. Novotný, F. Nuesslein, and A. Wolf. 'Isochronous mass spectrometry in an electrostatic storage ring.' In: *Review of Scientific Instruments* 93 (6) (2022) (cit. on p. 16).

[100] F. Grussie, A. O'Connor, M. Grieser, D. Müll, A. Znotins, X. Urbain, and H. Kreckel. 'An ion-atom merged beams setup at the Cryogenic Storage Ring.' In: *Review of Scientific Instruments* 93 (5) (2022) (cit. on p. 16).

[101] F. Grussie, L. Berger, M. Grieser, Á. Kálosi, D. Müll, O. Novotný, A. Znotins, F. Dayou, X. Urbain, and H. Kreckel. 'Merged-beams study of the reaction of cold HD^+ with C atoms reveals a pronounced intramolecular kinetic isotope effect.' In: *Physical Review Letters* 132 (24) (2024), p. 243001 (cit. on p. 16).

[102] F. Grussie, L. Berger, M. Grieser, Á. Kálosi, D. Müll, O. Novotný, A. Znotins, F. Dayou, X. Urbain, and H. Kreckel. 'Absolute rate coefficient measurements of the reactions of vibrationally cold HD^+ and H_3^+ ions with neutral C atoms.' In: *Physical Review A* 109 (6) (2024), p. 062804 (cit. on p. 16).

[103] Á. Kálosi, M. Grieser, R. von Hahn, U. Hechtfischer, C. Krantz, H. Kreckel, D. Müll, D. Paul, D. W. Savin, P. Wilhelm, A. Wolf, and O. Novotný. 'Laser probing of the rotational cooling of molecular ions by electron collisions.' In: *Physical Review Letters* 128 (18) (2022), p. 183402 (cit. on p. 18).

[104] F. Laux. 'Entwicklung von kapazitiven Positions-, Strom- und Schottkysignal-Messsystemen für den kryogenen Speicherring CSR.' PhD thesis. University of Heidelberg, 2011. DOI: 10.11588/heidok.00012435 (cit. on pp. 18, 57).

[105] S. Vogel. 'Developments at an Electrostatic Cryogenic Storage Ring for Electron-Cooled keV Energy Ion Beams.' PhD thesis. Ruprecht-Karls-Universität Heidelberg, 2016. DOI: 10.11588/heidok.00020262 (cit. on pp. 18, 19, 57, 58).

[106] F. Herrmann. In preparation. PhD thesis. Ruprecht-Karls-Universität Heidelberg (cit. on p. 18).

[107] *ESR Website*. https://www.gsi.de/work/forschung/appamml/atomphysik/anlagen_und_experimente/esr. Accessed: 13.06.2024 (cit. on p. 19).

[108] H. Poth. 'Electron cooling: theory, experiment, application.' In: *Physics Reports* 196 (3-4) (1990), pp. 135–297 (cit. on pp. 19, 32).

[109] A. Shornikov. 'An electron cooler for ultra-low energy cryogenic operation.' PhD thesis. Ruprecht-Karls-Universität Heidelberg, 2012. DOI: 10.11588/heidok.00013459 (cit. on pp. 19, 87).

[110] P. U. Wilhelm. 'First Studies of Low-Energy Electron Cooling of keV Energy Ion Beams at the Electrostatic Cryogenic Storage Ring CSR.' PhD thesis. Ruprecht-Karls-Universität Heidelberg, 2019. DOI: 10.11588/heidok.00026821 (cit. on pp. 19, 20, 35, 42, 43).

[111] U. Weigel. 'Cold Intense Electron Beams from Gallium Arsenide Photocathodes.' PhD thesis. Ruprecht-Karls-Universität Heidelberg, 2003. DOI: 10.11588/heidok.00004513 (cit. on p. 20).

[112] U. Weigel, D. Orlov, S. Kosolobov, D. Schwalm, A. Terekhov, and A. Wolf. 'Cold intense electron beams from LN2-cooled GaAs-photocathodes.' In: *Nuclear Instruments and Methods in Physics Research Section A: Accelerators, Spectrometers, Detectors and Associated Equipment* 536 (3) (2005), pp. 323–328 (cit. on p. 20).

[113] C. Krantz. 'Intense Electron Beams from GaAs Photocathodes as a Tool for Molecular and Atomic Physics.' PhD thesis. Ruprecht-Karls-Universität Heidelberg, 2009. DOI: 10.11588/heidok.00010009 (cit. on p. 20).

[114] C. Krantz, D. A. Orlov, J. Hoffmann, M. Lestinsky, O. Novotny, A. Jaroshevich, A. Terekhov, and A. Wolf. 'An ultra cold photoelectron gun for the Heidelberg TSR target section.' In: *Journal of Physics: Conference Series*. Vol. 192. 1. IOP Publishing. 2009, p. 012025 (cit. on p. 20).

[115] W. E. Spicer. 'Negative affinity 3–5 photocathodes: Their physics and technology.' In: *Applied physics* 12 (2) (1977), pp. 115–130 (cit. on p. 20).

[116] D. Paul. 'Electron recombination studies of rotationally CH^+ cold ions at the Cryogenic Storage Ring.' PhD thesis. Ruprecht-Karls-Universität Heidelberg, 2021. DOI: 10.11588/heidok.00030307 (cit. on pp. 21, 22, 25, 26, 35, 40, 43, 134).

[117] S. Pastuszka, U. Schramm, M. Grieser, C. Broude, R. Grimm, D. Habs, J. Kenntner, H.-J. Miesner, T. Schüßler, D. Schwalm, and A. Wolf. 'Electron cooling and recombination experiments with an adiabatically expanded electron beam.' In: *Nuclear Instruments and Methods in Physics Research Section A: Accelerators, Spectrometers, Detectors and Associated Equipment* 369 (1) (1996), pp. 11–22 (cit. on pp. 21, 81).

[118] K. Spruck, A. Becker, F. Fellenberger, M. Grieser, R. von Hahn, V. Klinkhamer, O. Novotný, S. Schippers, S. Vogel, A. Wolf, and C. Krantz. 'An efficient, movable single-particle detector for use in cryogenic ultra-high vacuum environments.' In: *Review of Scientific Instruments* 86 (2) (2015), p. 023303. DOI: 10.1063/1.4907352 (cit. on pp. 22–24, 119, 130, 131, 140).

[119] C. Krantz, O. Novotny, A. Becker, S. George, M. Grieser, R. von Hahn, C. Meyer, S. Schippers, K. Spruck, S. Vogel, and A. Wolf. 'Single-particle detection of products from atomic and molecular reactions in a cryogenic ion storage ring.' In: *Nuclear Instruments and Methods in Physics Research Section A: Accelerators, Spectrometers, Detectors and Associated Equipment* 851 (2017), pp. 92–102 (cit. on pp. 22–24, 48, 119, 120, 130, 131, 135, 140).

[120] A. Becker. 'Imaging of Neutral Fragmentation Products from Fast Molecular Ion Beams: Paving the Way for Reaction Studies in Cryogenic Environment.' PhD thesis. Ruprecht-Karls-Universität Heidelberg, 2016. DOI: 10.11588/heidok.00020213 (cit. on pp. 22, 25).

[121] K. Kühnel, C. Schröter, and J. Ullrich. 'Operating MCP detectors at cryogenic temperatures.' In: *Proceedings-EPAC Genoa, TUPC055* 106 (2008), p. 120 (cit. on p. 24).

[122] O. Siegmund, J. Vallerga, and B. Wargelin. 'Background events in microchannel plates.' In: *IEEE Transactions on Nuclear Science* 35 (1) (1988), pp. 524–528 (cit. on p. 24).

[123] G. Budker. 'An effective method of damping particle oscillations in proton and antiproton storage rings.' In: *Soviet Atomic Energy* 22 (5) (1967), pp. 438–440 (cit. on p. 32).

[124] G. Budker, N. Dikanskij, D. Pestrikov, I. Meshkov, V. Kudelainen, B. Sukhina, V. Parkhomchuk, and A. Skrinsky. 'Experimental studies of electron cooling.' In: *Part. Accel.* 7 (1976), pp. 197–211 (cit. on p. 32).

[125] J. Bechtel. 'Cooling force measurements with the phase shift method at the cryogenic storage ring CSR.' Bachelor's Thesis. Ruprecht-Karls-Universität Heidelberg, 2022 (cit. on p. 33).

[126] S. Saurabh. 'Collision studies with internally cold ion beams and merged electron beams in a cryogenic storage ring.' PhD thesis. Ruprecht-Karls-Universität Heidelberg, 2019. DOI: 10.11588/heidok.00026791 (cit. on pp. 34, 37).

[127] A. Shornikov, D. A. Orlov, C. Krantz, A. Jaroshevich, and A. Wolf. 'Maximum intensity, transmission limited cold electron beams from GaAs photocathode in the eV and sub-eV kinetic energy range.' In: *Physical Review Special Topics-Accelerators and Beams* 17 (4) (2014), p. 042802 (cit. on p. 35).

[128] F. Broetz, R. Trassl, R. McCullough, W. Arnold, and E. Salzborn. 'Design of compact all-permanent magnet electron cyclotron resonance (ECR) ion sources for atomic physics experiments.' In: *Physica Scripta* 2001 (T92) (2001), p. 278 (cit. on p. 66).

[129] A. Kramida, Y. Ralchenko, J. Reader, and NIST ASD Team. NIST Atomic Spectra Database (ver. 5.11), [Online]. Available: `https://physics.nist.gov/asd` [2024, August 12]. National Institute of Standards and Technology, Gaithersburg, MD. 2023 (cit. on pp. 68, 75, 76, 99, 101, 104).

[130] *AUTOSTRUCTURE*. `http://amdpp.phys.strath.ac.uk/autos/`. Accessed: 12.08.2024 (cit. on pp. 68, 78).

[131] N. Badnell. 'Dielectronic recombination of Fe^{22+} and Fe^{21+}.' In: *Journal of Physics B: Atomic and Molecular Physics* 19 (22) (1986), p. 3827 (cit. on pp. 68, 78).

[132] T. F. Gallagher. *Rydberg atoms (Cambridge Monographs on Atomic, Molecular, and Chemical Physics 3)*. Cambridge Univ. Press, 1994 (cit. on p. 69).

[133] S. Schippers, A. Müller, G. Gwinner, J. Linkemann, A. Saghiri, and A. Wolf. 'Storage ring measurement of the C IV recombination rate coefficient.' In: *The Astrophysical Journal* 555 (2) (2001), p. 1027 (cit. on p. 69).

[134] *Atomic Weights and Isotopic Compositions for Neon*. `https://physics.nist.gov/cgi-bin/Compositions/stand_alone.pl?ele=Ne`. Accessed: 01.11.2024 (cit. on p. 71).

[135] S. Singh, Z. Harman, and C. H. Keitel. *Private communication*. 2023 (cit. on pp. 78–80, 106–108).

[136] M. F. Gu. 'The flexible atomic code.' In: *AIP Conference Proceedings*. Vol. 730. 1. 2004 (cit. on p. 79).

[137] M. F. Gu. 'The flexible atomic code.' In: *Canadian Journal of Physics* 86 (5) (2008), pp. 675–689 (cit. on p. 79).

[138] *FAC 1.1.5 Manual*. `https://raw.githubusercontent.com/flexible-atomic-code/fac/release-pdf/manual.pdf`. Accessed: 05.12.2024 (cit. on pp. 80, 107).

[139] M. Grieser. *Private communication*. 2024 (cit. on p. 86).

[140] *Atomic Weights and Isotopic Compositions for Xenon*. `https://physics.nist.gov/cgi-bin/Compositions/stand_alone.pl?ele=Xe`. Accessed: 15.09.2024 (cit. on p. 95).

[141] E. Emmons, A. Aguilar, M. Gharaibeh, S. Scully, R. Phaneuf, A. Kilcoyne, A. Schlachter, I. Álvarez, C. Cisneros, and G. Hinojosa. 'Photoionization and electron-impact ionization of Xe^{3+}.' In: *Physical Review A—Atomic, Molecular, and Optical Physics* 71 (4) (2005), p. 042704 (cit. on p. 98).

[142] C. F. Fischer, G. Gaigalas, P. Jönsson, and J. Bieroń. 'GRASP2018—A Fortran 95 version of the general relativistic atomic structure package.' In: *Computer Physics Communications* 237 (2019), pp. 184–187 (cit. on p. 106).

[143] J. Prescott. 'A statistical model for photomultiplier single-electron statistics.' In: *Nuclear Instruments and Methods* 39 (1) (1966), pp. 173–179 (cit. on p. 130).

Danksagung

An dieser Stelle möchte ich mich bei den vielen Personen bedanken, ohne die diese Arbeit nicht zustandegekommen wäre.
Insbesondere bedanke ich mich bei Stefan Schippers, der dieses Projekt ermöglicht hat. Vielen Dank für die Betreuung meiner Arbeit, die fortwährende Unterstützung, die praktisch permanente Ansprechbarkeit und die Beantwortung meiner Fragen zur Physik der Elektron-Ion-Rekombination und darüber hinaus.
Vielen Dank an Markus Thoma für die Übernahme des Zweitgutachtens.
Klaus Blaum danke ich für die Aufnahme in seine Abteilung am MPIK.
Großer Dank gebührt Oldřich Novotný für die exzellente tägliche Betreuung und seine konstruktive, pragmatische und verlässliche Art. Die zahlreichen Gespräche über alle Aspekte des Experiments und der Datenanalyse waren extrem hilfreich. Danke auch für das gründliche Korrekturlesen dieser Arbeit.
Vielen Dank an Ábel Kálosi und Daniel Paul für die Einarbeitung am Elektronenkühler, dafür, dass sie auch während stressiger Strahlzeiten meine Fragen geduldig beantwortet haben und für die allgemein tolle Zusammenarbeit.
Vielen Dank an Suvam Singh und Zoltán Harman für die FAC-Rechnungen.
Manfred Grieser danke ich für die Berechnungen zu den Fokussiereffekten sowie für die Beantwortung aller Fragen zur Speicherringphysik.
Dem gesamten wissenschaftlichen und technischen CSR-Team danke ich herzlich für die überaus angenehme Arbeitsatmosphäre und die schnelle und unkomplizierte Hilfe in allen Belangen.
Danke an Aigars, Bhalchandra, Chris, Damian, Deepak, Felix, Jonas, Julia, Lisa, Lucia, Lukas, Marleen, Selina und Viviane für die schöne Zeit am Institut und für die Aktivitäten außerhalb des Instituts.
Vielen Dank an Pierre-Michel Hillenbrand für die Ermöglichung eines spannenden Nebenprojekts und zweier toller Forschungsaufenthalte.
Der gesamten Arbeitsgruppe Atom- und Molekülphysik aus Gießen danke ich dafür, dass es immer sehr angenehm war, zu Besuch zu kommen.

Versicherung

Ich erkläre: Ich habe die vorgelegte Dissertation selbstständig und ohne unerlaubte fremde Hilfe und nur mit den Hilfen angefertigt, die ich in der Dissertation angegeben habe. Alle Textstellen, die wörtlich oder sinngemäß aus veröffentlichten Schriften entnommen sind, und alle Angaben, die auf mündlichen Auskünften beruhen, sind als solche kenntlich gemacht. Ich stimme einer evtl. Überprüfung meiner Dissertation durch eine Antiplagiat-Software zu. Bei den von mir durchgeführten und in der Dissertation erwähnten Untersuchungen habe ich die Grundsätze guter wissenschaftlicher Praxis, wie sie in der „Satzung der Justus-Liebig-Universität Gießen zur Sicherung guter wissenschaftlicher Praxis“ niedergelegt sind, eingehalten.

Heidelberg, Februar 2025

Leonard Isberner